Amplitude and phase sonar calibration and the use of target phase for enhanced acoustic target characterisation

By

Alan Islas-Cital

A thesis submitted to The University of Birmingham for the degree of
DOCTOR OF PHILOSOPHY

School of Electronic and Electrical Engineering
College of Engineering and Physical Sciences
The University of Birmingham
Edgbaston
Birmingham
B15 2TT

October 2011

ABSTRACT

This thesis investigates the incorporation of target phase into sonar signal processing, for enhanced information in the context of acoustical oceanography. A sonar system phase calibration method, which includes both the amplitude and phase response is proposed. The technique is an extension of the widespread standard-target sonar calibration method, based on the use of metallic spheres as standard targets. Frequency domain data processing is used, with target phase measured as a phase angle difference between two frequency components. This approach minimizes the impact of range uncertainties in the calibration process. Calibration accuracy is examined by comparison to theoretical full-wave modal solutions. The system complex response is obtained for an operating frequency of 50 to 150 kHz, and sources of ambiguity are examined. The calibrated broadband sonar system is then used to study the complex scattering of objects important for the modelling of marine organism echoes, such as elastic spheres, fluid-filled shells, cylinders and prolate spheroids. Underlying echo formation mechanisms and their interaction are explored. Phase-sensitive sonar systems could be important for the acquisition of increased levels of information, crucial for the development of automated species identification. Studies of sonar system phase calibration and complex scattering from fundamental shapes are necessary in order to incorporate this type of fully-coherent processing into scientific acoustic instruments.

ACKNOWLEDGEMENTS

The author wishes to gratefully acknowledge the following people and institutions.

The Mexican National Committee for Science and Technology, for providing funding and making this possible.

My supervisor, Mr. Phil Atkins, for his warm encouragement, valuable advice, and unending patience. For providing multiple chances for improvement and personal growth. For his kindness and generosity. I remain indebted.

Dr. Trevor Francis, for developing the BEM models used in this work, and kindly sharing his knowledge and expertise.

Dr. Andrew Foo, for providing friendship, support and advice as a excellent colleague and mentor.

Dr. Rubén Picó and Ms. Nuria González. For their help in developing acoustic scattering models with COMSOL and for their friendship.

The staff in School of Engineering for all their support. Mr. Warren Hay, for machining some of the metallic objects used as targets. Ms. Mary Winkles, Ms. Clare Walsh and Tony, for all their help at various points during these years.

Ms. Yina Guo, for all her support, understanding and motivation. For making my life so much better during these challenging and exciting times.

Finally, to my parents Elizabeth and Cecilio, my brother Fabián and my sister Nadia. This is for you, I missed you much. Esto es para ustedes, los quiero y los extraño.

Table of Contents

LIST OF FIGURES

LIST OF TABLES

LIST OF SYMBOLS

A : System amplitude frequency response
A_r : Total received pressure amplitude
A_m : Reflection coefficient in the modal scattering solution formalism
A_w : Amplitude of received pulse travelling only in water (attenuation measurements)
A_s : Amplitude of received pulse travelling through specimen (attenuation measurements)
a : Sphere or cylinder radius
a_r : Received pressure amplitude at transducer aperture cell
a_{ratio} : System attenuation ratio
b: Complete, receive and transmit, transducer beam pattern factor
B : Circuit susceptance
B_w = Bandwidth
c : Speed of sound in water
c_{cp} : Compressed pulse
c_{env} : Compressed pulse envelope
C : Output of replica correlator (frequency domain)
C_{mot} : Motional capacitance in transducer electrical model
C_s : Shunt capacitance in transducer electrical model
C_v : Coefficient of variation
D_T : Transmitted beam pattern factor
D_R : Received beam pattern factor
f : Frequency
f_∞ : Generalized form function in the far field
F_{bs} : Target backscattering form function
f_{bs} : Target impulse response
G : Circuit conductance
H : System frequency response
H_r : Response of receiving transducer (attenuation measurements)
H_{MF} : Matched filter frequency response
h_{mf} : Matched filter impulse response
h_{scat} : Scatterer impulse response
h_m : Spherical Hankel function
I_r : Received sound intensity
I_i : Incident sound intensity
j : Imaginary number
j_n : Spherical Bessel function of the first kind.
J_n : Bessel function
k : Wave number
k_{const} : Proportionality constant
L : Scattering length
L_{cyl} : Finite cylinder length

L_{mot} : Motional inductance in transducer electrical model
L_{ss} : Propagation loss
L_s : Specimen length (attenuation measurements)
M_s : Transducer sensitivity
n : Index for individual echo contribution
N, M : Integers used in the ratio defining spectra separation in dual-frequency measurements
O_r : Receiver aperture function
p : Instantaneous sound pressure
p_a : Pressure averaged in the aperture of the transducer
p_{inc} : Pressure incident on the target (time domain)
p_{scat} : Pressure scattered from the target (time domain)
P_{inc} : Pressure incident on the target (frequency domain)
P_{scat} : Pressure scattered from the target (frequency domain)
p_r : Received pressure (time domain)
P_r : Received pressure (frequency domain)
p_t : Transmitted pressure (time domain)
P_t : Transmitted pressure (frequency domain)
P_o : Pressure amplitude at a reference distance
Q_M : Motional quality factor in the input admittance expression
R : Distance from receiver to target
R_{mot} : Motional resistance in the transducer electrical model
R_{coeff} : Boundary reflection coefficient
R_{in} : Input resistance in the transducer electrical model
RCP : Rate of change of phase
R_{rad} : Radiation and loss resistance in transducer electrical model
RX_w : Received pulse travelling only in water (attenuation measurements)
RX_s : Received pulse travelling through specimen (attenuation measurements)
s : Generalized time dependent signal
SD : Standard deviation
SD_{meas} : Standard deviation of measured differential target phase
t : Time
tx_{pulse} : A transmitted pulse in the time domain (attenuation measurements)
TX_{pulse} : A transmitted pulse in the frequency domain (attenuation measurements)
t_d : Time delay to target
T : Transmission coefficient through a boundary
T_{delay} : Propagation delay time
T_{emp} : Temperature in degrees Celsius
T_{pulse} : Pulse duration
TS : Target strength
u : Generalized monochromatic wave in space and time
u_o : Amplitude generalized monochromatic wave in space and time
U : Group velocity
v : Wave phase velocity

V_{in} : Input voltage into transducer electrical model
V_{out} : Output voltage out from transducer electrical model
V_{max} : Maximum amplitude of voltage applied to the transducer
V_{open} : Transducer open circuit voltage
V_r : Received voltage (frequency domain)
V_{ratio} : Ratio of received and transmitted voltage in backscattering measurements
v_t : Transmitted voltage (time domain)
V_t : Transmitted voltage (frequency domain)
w : Window function in the time domain
Y : Circuit admittance
y_n : Spherical Bessel function of the second kind
Y_n : Bessel function of the second kind

$\overline{X}$: Spatial matrix of sensitive cells in the transducer face

R, θ, ϕ : Spherical coordinate system

α : Attenuation coefficient in decibel per distance
β : Propagation phase constant
σ_{bs} : Target backscattering cross section
σ_c : Target backscattering cross section for concentrated (coherent) returns
σ_d : Target backscattering cross section for distributed (incoherent) returns
λ : Wavelength
ε_n : Newmann factor
ω : Angular frequency

φ_r : Received pressure phase at transducer aperture cell

φ : Phase of received signal
φ_{centre} : Phase of form function divided by dimensionless frequency ka
φ_s : Phase of received signal travelling through specimen (attenuation measurements)
φ_w : Phase of received signal travelling only in water (attenuation measurements)
Φ : System phase response
Φ_a : All-pass component of system phase response
Φ_m : Minimum phase component of system phase response
τ_g : Group delay
τ_p : Phase delay
ρ : Density of propagation media or target
μ : Spectral separation factor in dual-frequency measurements
μ_{mv} : Mean value
γ : Ratio between coherent and incoherent echo returns
ψ : Angle of incidence of plane wave on an elongated target with respect to major axis
Ω : Dispersion constant
Ω_ω : Angular frequency variable in the input admittance

1. INTRODUCTION

This chapter briefly introduces the use of sonar in oceanography and fisheries. A description of the current capabilities of acoustic tools for marine research is included, together with some of the challenges still open in the field. The concept of enhanced information level is presented as an important factor in the technological development of scientific sonar. The importance of sonar system calibration is stressed.

1.1 Background and importance of acoustical oceanography

The use of underwater sound as a non-invasive tool for the study and remote inspection of marine environments and their associated ecology is firmly established, both for oceanographic research (Medwin and Clay, 1998) and commercial applications, such as fisheries assessment (Misund, 1997, J. Simmonds and MacLennan, 2005). Sonar surveys can provide a wealth of information about population size, distribution patterns and migration behaviour, among other useful indicators. These investigations have been conducted on several fish species, particularly those with commercial value. Some examples are sardines (*Sardinops melanostictus*) in Japan (Aoki and Inagaki, 1993), orange roughy (*Hoplostethus atlanticus*) in New Zealand (Doonan et al., 2001), and cod (*Gadus Morhua L.*), in Canada (Lawson and Rose, 2000). It is clear that underwater acoustic surveys possess several advantageous characteristics such as being relatively economical to implement over larger volumes of water and longer periods of time, while remaining mostly non-intrusive and non-dependant on light or turbulence conditions. Nevertheless, room for improvement exists in their quality and applicability. This has been stressed by sustainability crises such as the

decline of the Baltic cod (Jonzén et al., 2002), that have dictated the urgent need for more reliable and efficient methods of evaluating aquatic habitats beyond mere detection, achieving capabilities for biomass estimation and species classification. Effectively, the scientific focus in fisheries has shifted from achieving maximum harvesting efficiency to optimal resource management (Godø, 2009a). This has led to a necessity of collecting increased amounts of data, not only aimed at characterizing individual objects, but guided by the exigencies of quantifying vast natural resources or surveying extensive areas of interest. Substantial improvements are then required in order to monitor and provide quantitative data on dynamic aquatic habitats, especially for ecosystem-based models (Koslow, 2009) and the management of resources facing sustainability issues.

1.2 Challenges of acoustical oceanography

The most persistent issue in sonar has been the interpretation problem, that is, the translation of received acoustic signals into meaningful and useful conclusions. For the case of fisheries acoustics, an aspect of acoustical oceanography, the desired outcome is usually biomass figures. This is a complex task, confronted by several sources of ambiguity, traditionally reserved exclusively for skilled sonar users. Early echo sounder displays typically consisted of echo returns printed on electro-chemical paper, producing a diagram of depth versus time (or distance), with fish shown as intensity variations in crescent or hyperbolic shapes (Lurton, 2002). Eventually, paper was replaced by colour electronic displays, as exemplified in Fig. 1, but the scrutinizing of sonar data output was still performed by visual examination and some reliance on prior knowledge. This approach, sometimes referred as the "fisherman's approach" (Zakharia et al., 1996) remains an approximate and largely subjective process, in which effectively construing a given sonar chart heavily depends on accumulated experience.

FIG. 1.1. Commercial echo sounder LCD display (from www.lowrance.com).

1.2.1 Quantitative methods

Efforts directed at achieving quantitative results led to the echo counter and the echo integrator, which are methods based on the analysis of compound echo signals, or collective target strengths (TS), over delimited spatial intervals (Misund, 1997). The echo counter, applicable to sparse distributions of fish, and the echo integrator, used to estimate stock size in high-density schools, are both based in the principle of linearity in fisheries acoustics,(K. G. Foote, 1983a) which allows the target strength of individual fish to be added together (J. Simmonds and MacLennan, 2005). Although these techniques have been substantially developed, they are still insufficient in achieving an optimal level of certainty. This is caused, in part, by the degree of arbitrariness present in the selection of the echoes to be processed, but also by the sheer complexity of underwater environments. Moreover, biomass density calculations rely inherently on measurements of the target strength of an individual organism. Consequently, an enormous amount of effort has been expended in the investigation of the target strength of relevant organisms. However, a level of uncertainty remains in the determination of this value, which becomes critical when added over large volumes.

1.2.2 Uncertainties in acoustical oceanography

Earlier works concerned with target strength determination tackled uncertainties originating from the sonar as a measurement system, and the propagation of the sound wave in the medium (Do and Surti, 1982). Knowledge of system parameters is necessary in order to account for uncertainties, such as the position and orientation of a specimen within the acoustic field, which can confuse the calculation of their actual size. In this case, indirect compensation can be achieved by deconvolving the beam-pattern factor from the echo level (Clay, 1983, Ehrenberg, 1979). In order to better approximate realistic target strength under field conditions, some researchers have favoured the implementation of *in situ* measurements. This has proven to be a feasible possibility, but faced by a variety of problems of its own, as described by (Ehrenberg, 1979), and more recently by (Kloser et al., 1997). Furthermore, the effects of fish dynamics such as swimming direction and attitude have also been examined (Henderson et al., 2007), along with other biological factors affecting TS measurement (Hazen and Horne, 2003), often focusing on the particular challenges involved in surveying single species, such as orange roughy (Kloser and Horne, 2003, Kloser et al., 1997) and Atlantic cod (Rose and Porter, 1996). Accumulated experience has impacted upon logistics and survey design considerations. For example, it has been recognized that acoustic estimations of distribution can be biased by fish behaviour, particularly their tendency to swim away from the approaching vessel, a reaction affected by several factors such as ship noise, fish species, location depth, and time of the day (Johannesson and Mitson, 1983, Soria et al., 1996).

Taking these and other reliability issues into consideration, acoustic surveys of marine biota, especially when species identification is attempted, tend to resort to complementing techniques for the verification of results. McClatchie et al., for instance, described several

alternative sampling methods such as visual observation by divers, and argued that their joint implementation with acoustic techniques can enhance the overall confidence level of the gathered data (McClatchie et al., 2000). It is envisioned that the advantages and disadvantages of specific technologies could be complemented with the adoption of multiple methods, for example, by validating acoustic measurements from the near-bottom dead zone with bottom trawls (Godø, 2009b). Nevertheless, the desirability of remote sensing has motivated attempts to develop fully automated acoustic means of classification, along with reliable quantitative acoustic methods. This drive has dictated the development of modern, scientific active sonar systems.

1.3 Enhanced information in active sonar

The evolution of acoustic technologies fits within a movement towards an information-rich research of the oceans, which has generated a converging interdisciplinary approach (MacLennan and Holliday, 1996) incorporating large sensor arrays, data fusion and various ground-truthing techniques (McClatchie et al., 2000). Currently, ambitious global-scale enterprises aim to revolutionize oceanographic research by providing interactive technological platforms for sampling and monitoring the world's waters, relying on state-of-the-art connectivity and vast communication networks (Delaney and Barga, 2009). In this broader context, enlarging the scope of sonar systems becomes crucial. Modern scientific sonar has reached capabilities for the acquisition of increased information, with broader frequency bandwidths for expanded spectral analysis and improved range resolution, and multiple beam arrays for enlarged spatial coverage (J. Simmonds and MacLennan, 2005). Broadband methods have had substantial success in identifying marine organisms through differences in their time-domain echo structure (W.W. L. Au and Benoit-Bird, 2003) or in their spectra

(Stanton et al., 2010). Furthermore, evidence has been found pointing out similar broadband discrimination strategies in dolphin and bat biosonar (Whitlow W.L. Au et al., 2009). Even in relatively simple commercial echosounders multiple discrete frequencies have been used. For example, dual-frequency systems are available, which combine two transmissions frequencies in order to obtain simultaneous resolution and propagation benefits. On the subject of sonar spatial coverage, dramatic increments have also been achieved through 3D sector scanners and multi-beam echosounders (Kenneth G. Foote et al., 2005), as exemplified in Fig. 1.2.

FIG. 1.2. Scientific multibeam echo sounder, Simrad ME70 (from www.simrad.com).

The approaches introduced above, in essence, increase the total level of energy injected into the medium, as an extension of the straightforward increment of the transmission peak power that directly improves the signal-to-noise ratio. The fundamental underlying relationship between energy and information (Tribus and McIrvine, 1971) underlies the direct connection between the interrogating signal's energy content and the information that can be recovered.

However, since signal power is limited by transmit pulse duration, hardware capabilities and non-linear effects, beam width by transducer size, and range resolution is constrained by bandwidth compromises (Lew, 1996), it would appear that this development direction cannot be sustained. Furthermore, techniques such as transmit waveform design, pulse compression, spread spectrum, and statistical methods substantially help in extracting more useful information from the received echoes, but these too are restricted to the actual content of the recovered amplitude.

1.4 Echo phase as an additional sonar parameter

An altogether different source of information could be tapped by fully taking into account the fact that echo signals possess a phase angle that is linked to the shape of the waveform. The phase of the echo is usually ignored in conventional active sonar; however, under the current paradigms it would be strongly desirable to fully exploit it. For example, it has been shown that the characteristics of the phase of a signal reflected from an object manifest many of its material properties (Mitri et al., 2008, Yen et al., 1990). This becomes especially relevant in achieving automatic acoustic species classification, where the notion of augmented information is particularly relevant (John K. Horne, 2000), and the use of phase has been explored as a feasible extra classifier parameter (P. R. Atkins et al., 2007a, Barr and Coombs, 2005, Braithwaite, 1973, Tucker and Barnickle, 1969).

Similarly to the gradual improvements associated with the analysis of echo magnitudes, the study of the complex scattering from fundamental finite shapes, such as spheres and cylinders can provide key insights into the mechanisms of echo formation and the connection between

phase and target characteristics. As previously discussed, translation of sonar survey data into useful biological parameters such as population abundance relies on a fundamental understanding of the scattering properties of individual animals (J. K. Horne and Clay, 1998). Again, this has been largely achieved for echo amplitude and target strength, for which an enormous body of work exists (Nash et al., 1987), whereas for the case of phase, a comparable literature is not available. The study of the role and applications of phase angle in acoustic scattering would then significantly expand the usefulness of acoustic remote sensing and fundamentally increase the amount of utilized information. Considerable advances in this direction can be obtained through the analysis of phase in the scattering from simple shapes, starting from a point scatterer, and gradually progressing towards more realistic geometries.

1.5 Importance of sonar system calibration

The acquisition of large amounts of acoustic data would be a futile task without reliable instrument calibration. The aims of calibration are twofold, first, to characterize and correct system effects which can distort measurements, and second, to establish reliable settings and references for repeatability and standardization. In summary, calibration serves as quality control for acoustic measurements, and development of these methods has greatly reduced errors in acoustic surveys (J. Simmonds and MacLennan, 2005). Furthermore, the accuracy level achieved during calibration directly impacts the accuracy of subsequent measurements. For this reason, the analysis of factors that degrade calibration precision has an immediate scientific value. Finally, although adaptation of calibration methodologies to modern sonar has largely been achieved, emerging technologies require suitable procedures. In this context, a calibration method for a phase-sensitive sonar system would seem necessary.

1.6 Research purpose and objectives

The present work concerns the continued investigation of target phase as a useful parameter for acoustic target characterisation and identification. Spectral techniques are applied to the measurement of target phase, isolating other phase shifts, such as the accumulation due to signal propagation. The design goal is to achieve a sonar system capable of assessing the amplitude and phase of target echoes. Central to this research is the development of a complete, amplitude and phase sonar calibration method, along with the evaluation of its capabilities and limitations. The performance and usefulness of the calibrated system is then explored using the scattering from objects with fundamental geometries, which allows for comparison between measured and predicted values. Consequently, some of the echo formation mechanisms that underlie a particular phase response can be examined. This approach follows the extensive literature on acoustic scattering, which has dealt with increasingly complex targets, from solid spheres to arbitrary shapes and composite bodies with contrasting densities. The emphasis is placed on the phase response of these objects, also as a stepping stone for more realistic targets that approximate marine organisms or physical features found in aquatic environments. As in the classic literature based on echo amplitude, this research was aimed to lead to improvements in target identification and characterization, which can also be applied to acoustic non-destructive testing and monitoring.

1.6.1 Research objectives

1. To investigate the suitability of using sonar target phase as an additional parameter for target identification and characterization.

2. To design and test a broadband active sonar system sensitive to complex acoustic scattering, and perform amplitude and phase measurements on relevant objects.

3. To examine phase measurements techniques aimed at isolating target-induced phase shifts, removing propagation and waveform effects.

4. To develop broadband active sonar calibration techniques that account for amplitude and phase and implement them on a scientific sonar system tested in a laboratory water tank.

5. To characterise the accuracy of the standard-target calibration method as applied in a broadband sonar system.

6. To evaluate the performance of tungsten carbide spheres commonly used as standard calibration targets.

7. To study the phase response of canonical scatterer geometries such as spheres, shells, finite cylinders and prolate spheroids, comparing it to theoretical solutions and numerical models.

1.6.2 Original contributions

Within this work significant and novel contributions have been put forward:

- Development and assessment of a broadband, filter-derived, matching network for transducer phase linearization.

- In-depth analysis of composition variability of tungsten carbide spheres with cobalt binder, using scanning electron microscopy, which revealed the occurrence of cobalt leaching processes.

- Analysis and performance comparison of tungsten carbide spheres with nickel binder as candidates for improved sonar standard calibration targets.

- Extension of the standard-target calibration method to include phase response, by means of dual-frequency transmissions and frequency-domain data processing.

- Usage of the dual-frequency target phase to more completely represent the acoustic scattering of canonical targets.

- Successful comparison of predicted and measured target phase responses of spheres, shells and cylinders.

1.6.3 Thesis structure

Chapter 2 – Review of methods and fundamental concepts related to the characterization of submerged targets using sonar, particularly addressing the importance of phase effects.

Chapter 3 – Literature review of the measurement and usage of signal phase, in acoustics applications in general, and in sonar for oceanography and fisheries in particular.

Chapter 4 – System design, experimental settings and data processing methods.

Chapter 5 – Introduction of the standard-target sonar calibration method. Analysis of variability sources, focused on the standard-targets. Detailed investigation on the physical characteristics of tungsten carbide spheres with cobalt and nickel binder.

- Some results concerning the error analysis of the standard-target sonar calibration (amplitude-only) were presented in the Oceans 2010 conference, in Sydney, Australia.

Chapter 6 - The phase response characteristics of electro-acoustical systems such as sonar are discussed. A phase response extension for the standard-target calibration method is proposed and detailed.

- The concept of filter-derived matching circuits was presented in the Acoustics 08 conference in Paris, France.

- The proposed phase calibration method forms the basis for a publication in the Journal of the Acoustical Society of America, Volume 130, Issue 4, pp. 1880-1887 (2011).

Chapter 7 – Scattering from relevant targets is presented and compared to theoretical models. Amplitude and phase obtained from the calibrated sonar system are analysed in terms of echo formation mechanisms and possible applications for enhanced target characterization.

- Results from the calibrated sonar system, using LFM pulses, were presented in the Oceans 2011 conference in Santander, Spain.
- Comparisons between measured backscattering data and numerical models will be presented in the Acoustics 2012 conferences in Nantes, France.

Chapter 8 – Summary, conclusions and further work.

2 ACOUSTIC CHARACTERIZATION OF UNDERWATER TARGETS

This chapter reviews some acoustic techniques utilized to characterize, assess and identify submerged targets. In the time domain, receiver operation is examined in terms of range resolution and signal-to-noise ratio. Spectral analysis in the frequency domain is introduced, with the form function serving as the acoustic transfer function of the target. Scattering from fundamental geometrical targets is covered, mainly as a foundation for the modelling of the scattering from marine organisms.

Sonar in acoustical oceanography is a remote sensing tool, in which the basic principle is the use of sound to extract information from a given environment or object located at a distance. Essentially, it involves applying or transmitting levels of energy, which upon interaction with the medium, cause a disturbance. The propagation of this disturbance, called a wave, then retrieves information to the observer (Blackstock, 2000). Extraction of this information constitutes a classical inverse-scattering problem. Often, in the ocean or in a more general sense (Werby and Evans, 1987), this is the most convenient or even the only possible way of learning about an object. In many ways a remote sensing system is analogous to a communications system, with the medium acting as the channel, and therefore its overall intelligibility largely depends on sufficiently high signal-to-noise ratio (SNR). In applications solely concerned with detection of static or moving targets, finding an optimal solution to the non-trivial task of recovering the signal from the noise floor is often enough to assure efficient

operation. Nevertheless, efforts to characterise or identify targets through remote sensing usually require increased levels of information and more sophisticated processing for a successful interpretation of raw data.

An active sonar system interrogates the medium by transmitting sound pulses of finite duration. These energy bursts propagate in the water and are partially reflected to the receiver upon encountering density discontinuities or inhomogeneities that constitute the targets. These sonar targets can display a wide range of shapes, dimensions, compositions and behaviours, depending on the context. In sonar for fisheries, oceanography and limnology, targets usually belong to the vast variety of aquatic animals and vegetation organisms, but they can also be sedimentary or geological features. In the area of defence and security, the task often involves differentiating between natural targets and man-made objects or intrusions that can pose a threat, such as a mine or a diver. These targets are likely to be found in reverberant and/or noisy environments, and often exhibit some degree of Doppler effects. Several different schemes have been essayed, with the objective of improving the capability of sonar systems to provide further details about detected targets. Data analysis and processing can be performed in the time domain, in the frequency domain, or in both. Various levels of sophistication have been implemented in the design of sonar system hardware and software, with the simplest strategies based on incoherent processing schemes.

2.1 Coherent and incoherent processing

Sound pressure waves propagating in the water, or their corresponding voltage variations in the receiver, can be expressed as time functions of sinusoidal form

$$p(t) = P_o \sin(\omega t - kR), \tag{2.1}$$

the expression corresponds to a travelling spherical wave of instantaneous pressure *p*, where *t* is time, ω is angular frequency, and P_o is the pressure amplitude at distance *R* (Medwin and Clay, 1998). The wave number, *k*, is defined as

$$k = \frac{\omega}{c} = \frac{2\pi}{\lambda}, \tag{2.2}$$

with λ as the wavelength.

The argument of the sinusoidal contains a temporal dependency, ωt, and a spatial, propagant phase, *kR* (L. Wang and Walsh, 2006). The pressure *p(t)* can also be represented in polar form as a phasor, such as

$$p(t) = P_o e^{j(\omega t - kR)}, \tag{2.3}$$

rotating in the complex plane at a rate ω over time (Carlson, 1986). The physical acoustical pressure is obtained by taking the real part of Eq. 2.3. Reflected sound waves, or echoes, arrive at the receiver with a time delay equal to the two-way path length,

$$t_d = \frac{2R}{c}, \tag{2.4}$$

where c is the speed of sound in water. Using an approximate value for c, a time-of-flight, range-based, sonar depiction of the probed environment emerges. In this time-domain representation discontinuities appear at locations referenced to their relative distance to the receiver, allowing for detection, ranging and tracking applications. While echo time delay can yield the target position, the main source of information about the target itself is found in the echo amplitude, since the amount of energy returned can be linked to its physical characteristics such as, most intuitively evident, size.

For many sonar systems, particularly simple commercial units, the joint usage of echo delay and amplitude suffices. These types of systems often ignore the phase of the received signal, relying only on the envelope. Traditional sonar receivers operating in this manner usually include an envelope detector after filtering and amplification. The resulting DC voltage value is then compared against a threshold, an operation that decides if the signal is displayed or discarded as noise. The sensitivity of the system is directly determined by the threshold value, which usually can be controlled by the user. Some basic echosounders are still based on this scheme, often displaying echo amplitude with intensity color codes on an LCD screen, as exemplified in Fig. 1.1. In general, echoes in underwater acoustics are formed by multiple,

often random, contributions. The summation of these acoustic components can occur at the target or targets, during propagation, or upon reception. Some of these factors will be briefly mentioned in the next paragraphs.

2.1.1 Coherent transducer operation

While traditional sonar processing could be considered incoherent in the sense that only echo amplitudes are taken into account, the receiver itself is not. Conventional transducers are inherently phase sensitive. Multiple echoes are added coherently at the transducer surface or aperture, which can be modelled as a 2-D arrangement of sensitive cells, where $\vec{X}$ represents an individual cell (Fink et al., 1990). For each time, *t*, the total time-dependent received pressure, $p_r(t)$, is the linear superposition of the individual contributions over the receiver aperture function, $O_r(\vec{X})$. Expressed as an integral

$$p_r(t) = \int O_r\left(\vec{X}\right) p_a\left(\vec{X}, t\right)\, d\vec{X} \,. \tag{2.5}$$

Each contribution originating from within the resolution cell is made of an amplitude a_r and phase φ_r, such that

$$p_a\left(\vec{X}, t\right) = a_r\left(\vec{X}, t\right) \cos \varphi_r\left(\vec{X}, t\right). \tag{2.6}$$

This averaged pressure is incorporated in the definition of the transducer receive sensitivity, expressed as a function of angular frequency, $M_s(\omega)$ (Bobber, 1970, P.L.M.J. van Neer et al., 2011b), such as

$$M_s(\omega) = \frac{V_{open}(\omega)}{p_a(\omega)}, \tag{2.7}$$

where V_{open} is the transducer open circuit voltage.

In ultrasound imaging, random phase returns known as speckle noise, are an important performance issue. Reduction of speckle noise has been attempted through phase filtering (Kim et al., 1990), or compounding methods (Martin E. Anderson et al., 1998) intended to minimize unwanted noise correlation, such as phase-insensitive transducers and random-phase screens (Laugier et al., 1990). The averaged total echo, in a single transducer or array element is the basic quantity most commonly used, although phase differences between half-beams in a split-beam system are used to determine arrival angle (Ehrenberg, 1979).

2.1.2 Echoes from multiple targets

In sonar and sediment analysis, echoes arriving at the same time, or nearly the same time, at the receiver pose problems for single-target resolution (K. G. Foote, 1996, Stanton and Clay, 1986). Again, linear superposition of each individual target echo, *n*, is assumed. In the case of fisheries acoustics the assumption of linearity was experimentally proven by Foote, based on measurements of fish aggregations under controlled conditions (K. G. Foote, 1983a).

Taking into account its backscattering cross section of each target, σ_{bs}, and the transmitted and received beam pattern factors, D_T and D_R, we obtain a total received pressure of

$$p_r(t) = \sum b_n \sigma_{bs_n}^{1/2} \mathrm{e}^{i\phi_n} , \tag{2.8}$$

where ϕ_n is the phase of the nth echo, and the complete beam pattern factor is $b_n = D_{Tn} D_{Rn}$ (K. G. Foote, 1996). The beam pattern variables correspond to the direction of the nth target. Since the backscattering cross section is originally defined as a ratio of sound intensities, a square root operation is needed when using pressures. The pressure resulting from Eq. 2.8 is then a coherent summation of echoes and noise. For an aggregation of unresolved scatterers, returns are spatially compounded and fluctuate from ping-to-ping. Random phases interfere and result in a "smeared" total echo (Stanton and Clay, 1986) with exacerbated statistical variance (D. A. Demer et al., 2009). Analogous phase dispersion conditions (K. G. Foote, 1996) are common and can be found in radar (Dunn et al., 1959), sediment analysis, interferometric swath bathymetry (Jin and Tang, 1996, Llort and Sintes, 2009, Matsumoto, 1990), medical ultrasound and grain-level non-destructive testing (Bordier et al., 1992). For the case of a fish school, the resulting statistics of overlapping echoes amplitudes are those of a Gaussian process that can be represented by a Rayleigh distribution (Deuser et al., 1979, J. Simmonds and MacLennan, 2005). This statistical distribution scenarios where narrow band signals of comparable amplitudes are combined in a single observation (Lurton, 2002).

As an additional note, it has been suggested that frequency-dependant target phase response can be useful in determining if multiple scatterers are present, since their apparent target position, or scattering centres, would shift distinctly as a function of frequency (K. G. Foote, 1996). On the other hand, a point scatterer appears fixed in position for the entire bandwidth, and multiple point scatterers maintain a constant interference pattern. The concept of scattering centres, based in the geometrical theory of diffraction, has been applied to model complex radar targets (Ross and Bechtel, 1968).

2.1.3 Echoes from a single target

Acoustic returns from a resolved target in the ocean are prone to strong variability due to a multitude of factors. Under these conditions, fundamental quantities such as target strength are often considered as stochastic variables (J. Simmonds and MacLennan, 2005). In the case of an echo originated from a single fish, the backscattered cross section formed of components concentrated in a principal scattering feature, σ_c, such as the swimbladder, and distributed components, σ_d, originated in other features. The distributed contributions have random phase that adds incoherently, while the concentrated contributions possess the same phase and thus are summed coherently. A ratio between coherent and incoherent energies is then defined in terms of the two types of backscatter cross sections, yielding a measure of the level of randomness (Clay and Heist, 1984),

$$\gamma = \frac{\sigma_c}{\sigma_d} . \tag{2.9}$$

Clay and Heist fitted a Rician Probability Density Function (PDF) to the scattering of individual fish, by varying the ratio of concentrated (coherent) to distributed (incoherent) components that form the far field returns (Clay and Heist, 1984). This PDF is appropriate since it appears when noise is superposed on a coherent signal (Lurton, 2002). It is expected that phase discrepancies are more marked in larger fish with distributed anatomical features, while smaller bodies appear as more concentrated sources. In higher resolution regimes, targets deviate further from the ideal point scatterer and appear increasingly distributed.

2.1.4 Multiple paths

Multiple reflections occurring on the two-way propagation path can also introduce random amplitude and phase fluctuations (Lurton, 2002). When these paths are close in length, they generate nearly coincident echoes that are difficult if not impossible to separate. Micro multi-path perturbations, caused by the presence of small scatterers in the propagation path, add further variation, known as dispersion, a separation of the radiation components which can occur in the time, frequency or space domains.

2.2 Linear systems approach to acoustic scattering

Underwater acoustics can be studied as a linear systems problem (K. G. Foote, 1983a, Tolstoy and Clay, 1966), where the relationship between the transmitted and received wave can be determined by a linear relationship. Besides the transfer function of the sonar system itself, a particular transfer function can also be established for any given target, with the incident pressure wave as the input and the scattered wave as the output. Knowledge of the system

and target transfer functions allows forward prediction of the scattered signal. In the time domain the transfer function becomes the impulse of response of the scatterer, $h_{scat}(t)$, and its convolution with the transmitted signal yields the received pressure, such that

$$p_r(t) = \int_{-\infty}^{\infty} p_{inc}(\tau) h_{scat}(t-\tau) d\tau \,, \tag{2.10}$$

where the response depends on target parameters such as dimensions, geometry, and composition (Roberts and Jaffe, 2007).

2.2.1 The matched-filter receiver

An important shortcoming in incoherent processing is noise performance, since noise rejection becomes heavily dependent on system gain and linear filter efficiency. In order to achieve optimal SNR in active sonar, the *a priori* knowledge of the transmitted waveform can be incorporated into the processing strategy. This is best illustrated by the ideal point scatterer case, where the reflected echo is a delayed, attenuated copy of the transmitted pressure signal, p_t, such as

$$p_r(t) = A(R,\alpha)\, p_t\left(t - \frac{2R}{c}\right), \tag{2.11}$$

where $2R/c$ is the two-way propagation time, with R as the range and c as the speed of sound. The amplitude of the received signal, A, is a function of range and the associated propagation loss mechanisms, as expressed by the attenuation coefficient, α, in units of decibel per distance. The phase of this echo is identical to that of the transmitted function and therefore, perfectly correlated to it, whilst noise would be uncorrelated or very poorly correlated. This principle is the basis for the correlator or matched filter receiver, which is the optimum filtering strategy for noise performance. Therefore, by definition a matched filter receiver is intrinsically coherent. Furthermore, it has been suggested that phase information could even have a more important role than amplitude in matched filtering (Horner and Gianino, 1984), and this has led to the incorporation of phase-only filters in active sonar (Chan and Rabe, 1997).

The impulse response of the matched filter, $h_{mf}(t)$, is designed to be complementary to that of a signal, $s(t)$, such as (Turin, 1960)

$$h_{mf}(t) = k_{const}\, s\left(t_0 - t\right), \tag{2.12}$$

where k_{const} and t_0 are constants. The response of the matched filter is a time-reversed version of the relevant signal, or, equivalently, its complex conjugate in the frequency domain,

$$H_{MF}(\omega) = k_{const} S^{*}\left(\omega\right) e^{-j\omega t_0}. \tag{2.13}$$

Relevant signals arriving at the receiver are usually matched to a replica of the transmission, therefore, this processor is also called a replica correlator. However, targets other than ideal point scatterers induce phase effects due to their finite dimensions and physical characteristics. This causes a mismatch and, strictly, the processing is not fully considered a matched filter since the filter is not perfectly matched to *s(t)*. The response of a true matched filter includes the characteristics of each specific target, which is impractical for most cases. Nevertheless, it has been pointed out that the mismatch yields information about the scatterer, often represented as multiple features in the time domain (Dezhang Chu and Stanton, 1998). This has been applied to the study of scattering from fish (W.W. L. Au and Benoit-Bird, 2003, Barr, 2001) and zooplankton (Andone C. Lavery et al., 2010). Identification of submarine echoes through their temporal structure is also feasible (Lurton, 2002).

2.2.2 Target resolution and chirp transmissions

As previously discussed, higher bandwidth and, therefore, higher resolution of scatterers is part of the trend towards increased information in sonar and non-destructive testing. Resolution refers to the ability to distinguish two closely located targets, or individual reflectors within a complex object. In active sonar, this usually refers to range resolution in particular. Intuitively, it can be seen that a finer probing signal, such as a short pulse, allows for higher resolution than a longer signal, which covers an extended segment. Linear-Frequency Modulated (LFM) pulses, for example, well-established in the design of pulse-compression or chirp radars (Skolnik, 1962), are viable in the absence of Doppler effects, and can be optimally applied in static scenarios such as in non-destructive testing, where the enhanced energy content is beneficial for highly-absorbent media (F. Lam and Szilard, 1976).

Due to the complementary nature of the phase spectrum, pulse compression also occurs with a matched filter approach as applied to broadband signals (Ramp and Wingrove, 1961). This scheme is widely used to maximize range resolution while maintaining good signal-to-noise ratio. Unlike a narrow-band signal, where resolution is dictated by the pulse length, in pulse compression it is approximately proportional to bandwidth (Turin, 1960). Therefore, the trade-off between resolution and signal-to-noise ratio is largely avoided. Pulse compression techniques have been applied for high-resolution scattering studies of, for example, zooplankton (Dezhang Chu and Stanton, 1998). This allows for separation of distinct echo contributions or highlights, which can be useful for target identification (W.W. L. Au and Benoit-Bird, 2003, Barr, 2001). Chirp signals, such as Linear Frequency Modulated (LFM) pulses, have been used in conjunction with pulse compression methods. This is developed in more detail in Appendix A.3.

2.2.3 The form function

The transfer function of a resolved target depends on its size, composition, and orientation. In acoustical oceanography this is often expressed as a complex acoustical scattering length, *L* (Medwin and Clay, 1998),

$$L(\theta,\phi,f)=\frac{P_{scat}}{P_{inc}}\left[R\,10^{\alpha(f)R/20}\right], \tag{2.14}$$

where α is the attenuation coefficient in decibels per unit distance, P_{inc} and P_{scat} are the Fourier transforms of the incident and scattered pressures, respectively, and the range R and associated angles are depicted in Fig. 2.1.

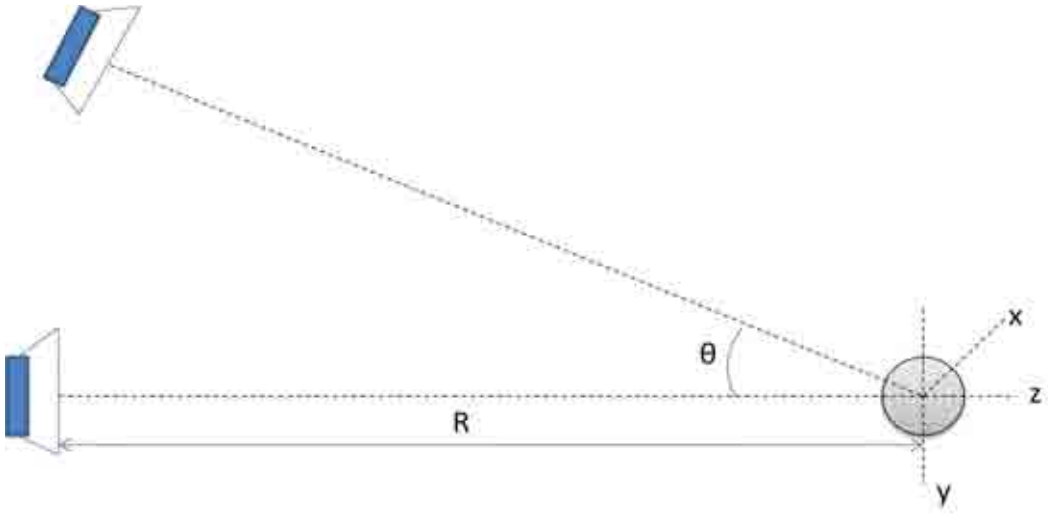

FIG. 2.1. Scattering geometry, in spherical coordinates R, θ (angle ϕ coming out of the plane) and Cartesian coordinates x, y, z. For monostatic backscattering setup θ = 180°.

The squared absolute value of the scattering length is equal to the cross section, called the backscattering cross section when limited to the backscattering direction, $\sigma_{bs}(f)$,

$$\sigma_{bs}(f) = \left|L(0,0,f)\right|^2 . \tag{2.15}$$

The form function is a related quantity, normalized to the characteristic dimension of the target, a, and measured in the far field (Fraunhofer zone (Lurton, 2002)),

$$F_{bs}(f) = \frac{a}{2} L_{bs} \,. \tag{2.16}$$

The form function, evaluated in a monostatic, backscattering arrangement, can be expressed in the electrical equivalents of the pressure in the electro-acoustical system. With *H(f)* as the system frequency response (including propagation losses), and $V_r(f)$ and $V_t(f)$ as received and transmitted voltages respectively, the form function is defined as (Stanton and Chu, 2008)

$$F_{bs}(f) = \frac{V_r(f)}{V_t(f) H(f)} \,. \tag{2.17}$$

The target strength (TS) describes the acoustic reflectivity of a target as a decibel ratio such as

$$TS = 10 \log\left(\frac{I_r}{I_i}\right) = 20 \log\left(\frac{p_r}{p_{inc}}\right), \tag{2.18}$$

where I_i and p_i are incident intensity and pressure, and I_r and p_r are reflected quantities. This assumes a locally plane incident wave, and spherical scattering measured at a 1 m distance.

2.3 Marine organism scattering

Life forms inhabiting the ocean present varied shapes, compositions and behavioural patterns. Even if fish in general have an elongated body, other biological features such as the swimbladder are often equally or even more important in echo generation. Zooplankton species, on the contrary, differ wildly in their characteristics and have highly irregular bodies (Stanton and Chu, 2000). Both categories are often encountered in aggregations organized in periodic, semi-periodic or random patterns, which need to be measured in the average sense.

2.3.1 Target strength measurements

An important research effort in acoustical oceanography has been the study of the empirical and theoretical acoustic properties of marine organisms and their constituent parts. Substantial early work was conducted by Haslett, who investigated the acoustic properties of fish through backscattering experiments. He obtained reflection coefficients of fish bone and tissue immersed in fresh water, using both short and long pulses (Haslett, 1962). This relatively simple experimental setup (backscattering in a laboratory tank lab) provides valuable information on the composition of inert objects, and has since been replicated with slight variations. The target strength of a whole fish is much more complicated, with aspect angle playing a crucial role along with other biological variables relative to the species and life stage of the animal. Numerous measurements of the target strength of acoustic cross section of fish have been conducted *ex situ*, with dead fish, tethered or caged live fish, rotating in the yaw, roll or pitch planes (Haslett, 1969, K. Huang and Clay, 1980, McClatchie et al., 1999). A holistic scientific approach that takes into account biological characteristics and the underlying physical processes of echo formation has been advocated as a route towards achieving predictive capabilities (MacLennan and Holliday, 1996).

2.3.2 Marine organism scattering modelling

The theoretical aspect of the effort to study fish and zooplankton scattering has produced models with different degrees of complexity to represent underwater targets, usually stemming from fundamental geometrical shapes that are well understood mathematically. Models are crucial for the achievement of predictive capabilities through inversion and they are also useful to study the separate influence of parameters such as composition, size and orientation. These models have been verified and tested against empirical trials, in a joint

approach that seems most suitable to the nature of the problem (J. K. Horne and Clay, 1998). Although the relevant targets are often complex, inhomogeneous, composite bodies, simple models can often describe their scattering to a satisfactory level or offer the foundations for more exact representations. Spheres, spheroids and cylinders, solid or fluid-filled have been used in several studies to model plankton, fish, or their constituent parts (Clay and Horne, 1994, J. K. Horne and Clay, 1998, Medwin and Clay, 1998, J. Simmonds and MacLennan, 2005). Elastic effects are very relevant since density contrasts of objects submerged in water is not so great as to be considered strictly rigid (Faran, 1951, R. Hickling, 1962a). Therefore, elastic effects often play a dominant role in the overall scattering response, particularly at the intermediate frequency ranges, commonly used in sonar for fisheries and oceanography, where wavelength is comparable to target dimensions.

2.3.2.1 Acoustic models of fish

Acoustic models for fish have traditionally been based on elongated shapes that coarsely mimic their anatomy. Model evolution has advanced from spheres and solid cylinders towards prolate spheroids, which more closely resemble fish shape. Higher resolution models that involve digitizing the specimen shape and properties have also been developed, either as an assemblage of point scatterers (Nash et al., 1987) or as fully-3D, mesh-based representations.(K. G. Foote and Francis, 2002, Jech and Horne, 2002) Accurate digital visualizations of fish anatomy and their internal structure are have often been achieved by dissection and X-ray.

A system with enhanced range-resolution capability, often relying on pulse compression techniques (Dezhang Chu and Stanton, 1998), can discern different constituents of the specimen, which may have specific acoustic properties. For fish without swimbladder, such as the Atlantic mackerel (*Scomber scombrus)*, the overall echo results from the superposition of individual contributions from tissue, skeleton, skull (Nesse et al., 2009), with interference effects likely to occur (Nash et al., 1987). These features have to be included into a model in order to achieve greater accuracy. Again, progress has been largely gained by means of studies of these individual anatomical features. Similarly, separate models have been fitted to each part. Gorska *et. al.* (Natalia Gorska et al., 2005), for example used the Distorted Wave, Born-Approximation (DWBA) (Stanton et al., 1998a) for fish flesh, and the Modal-Based, Deformed Cylinder Model (MB-DCM) (Stanton, 1988a, b, 1989) for bone, in order to simulate the complete response of Atlantic mackerel. Since the density of fish flesh is relatively close to that of water, scattering is weak and the DWBA model applies, while the MB-DCM model is well suited for finite rigid and elastic cylinder-like shapes, such as the backbone.

2.3.2.2 The acoustic role of the swimbladder

The modelling of fish swimbladders has been of special importance in fisheries acoustics. This anatomical feature, present in many commercially-valuable species, which mainly use it for the control of buoyancy, has a dominant contribution to scattering at lower frequencies, due to its contrasting density and resonant characteristics (K. G. Foote, 1980). The resonant frequency is related to the size of the swimbladder and, therefore, to the size of the fish. However, equating resonant peaks in the spectrum of received echoes to a fish dimensions

becomes complicated as other factors such as depth-dependent pressure also play a role (N. Gorska and Ona, 2003). Nevertheless, the differentiation (or proportion estimation in mixtures) of fish, with and without swimbladder, through their acoustics has been proven feasible, since this is a case of stark contrast in the amplitude of the returns (Coombs and Barr, 2004). In particular, the lower-frequency swimbladder resonance has served as a differentiator against fish without swimbladder and zooplankton (Stanton et al., 2010).

Scattering from the swimbladder is also affected by the fluid inside. If this organ is filled with a material close to the density of water, its reflective properties will be strongly diminished, as is the case of the deep-water dwelling orange roughy (*Hoplostethus Atlanticus)*, which have wax esters in their swimbladders. Barr took advantage of this distinction in acoustic properties to separate orange roughy from black oreos (*Allocytus niger)* and smooth oreos (*Pseudocyttus maculatus),* from mixed stocks in deep waters around New Zealand (Barr, 2001). The physical nature of the swimbladder results in an acoustic behaviour close to that of a reflector, with amplitude outliers and resonance. Furthermore, the swimbladder is also an acoustically-soft scatterer, with acoustic impedance lower than the medium. This causes a phase reversal that can also be useful for identification purposes. The distinct acoustic characteristics of the swimbladder have suggested the use of hybrid models such as the Kirchhoff Ray Model (KRM), which models the swimbladder with Stanton's cylinder model for lower frequencies, and the Kirchhoff approximation for the external shape at higher frequencies (J. K. Horne and Clay, 1998).

2.3.2.3 Acoustic models of zooplankton

Due to the diversity in zooplankton species, various models have been used to simulate their acoustic scattering, always linked to the particular animal morphology (K. G. Foote, 1998). The simplest model is the low-contrast fluid filled sphere, as originally developed by Anderson (Victor C. Anderson, 1950) and re-examined by Feuillade and Clay (Feuillade and Clay, 1999). However, this approach is limited, mostly applying to nearly spherical classes of zooplankton. In order to account for other types of scattering for example from specimens bearing elastic shells or gas inclusions, Stanton studied individual contributions by means of a high-resolution pulse-compression system (Dezhang Chu and Stanton, 1998, Stanton et al., 1998b). In general, knowledge of the relevant scattering mechanisms and prevalent target physical characteristics allows selection of the optimal model.

It is known that weakly-scattering organisms, with density close to that of the surrounding medium, allow for sound penetration, causing interference patterns between the entrance and exit boundaries. A simple two-way ray scattering model, based on a straight cylinder geometry, has been developed to include this behaviour (Stanton et al., 1993b). In a more precise approach, the Distorted Wave Born Approximation (DWBA) has been applied to weakly scattering bodies (Stanton et al., 1998a). The term “distorted wave” refers to the fact that the wave suffers phase perturbations as it encounters sound speed variations within the scatterer (D. Chu and Ye, 1999). An advantageous characteristic of the DWBA is its versatility to cover inhomogeneous bodies with arbitrary dimensions and shapes. For example, it has been used with a bent cylinder geometry for euphausiid (*Meganyctiphanes norvegica)* and with a prolate spheroid for copecod (*Calanus finmarchicus)* (Stanton and Chu, 2000). Higher-resolution 3-D representations have been achieved through computerized scans incorporated into the DWBA formulation (A. C. Lavery et al., 2002). Furthermore, this

model is not restricted in angle of orientation and has been implemented to predict scattering from *in situ* zooplankton aggregations, which exhibit random size and orientation distributions (Stanton et al., 1998a). Further improvements in the DWBA is the more detailed inclusion of phase variability due to stochastic and behavioural causes, or composition changes along the body of larger organisms, not necessarily plankton, such as krill (D.A. Demer and Conti, 2003, Jones et al., 2009). Finally, it is noted that some researchers have preferred an empirical approach to the prediction of scattering from zooplankton, deriving approximations from experimental data relating acoustic cross section to length. They argue that models based on detailed morphology are very complicated and can fail due to insufficient knowledge of physical parameters of organisms (Andreeva and Tarasov, 2003).

2.3.2.4 The role of target orientation

Target aspect angle is one of the parameters with a stronger impact on fish target strength, particularly vertical tilt for downward-looking echosounders, but also roll angle (Misund, 1997). For objects large or comparable to the wavelength this factor must be included in the determination of the target strength, along with the specimen dimensions and the scattering frequency response (Love, 1977). In general, the interacting effects of unknown target orientation and composition present one of the most serious challenges for acoustic data interpretation (Roberts and Jaffe, 2007). Since fish and other marine organisms possess elongated, highly-directive shapes, orientation is especially important, and random tilt within a school is averaged and considered within scattering models (Coombs and Barr, 2004, Stanton et al., 1993a, Traykovski et al., 1998). The impact of tilt angle can be partly explained with geometrical arguments, as the insonified section changes in apparent size.

However, wave interference effects also play an important role, as illustrated in Fig. 2.2, where phases can add constructively or destructively.

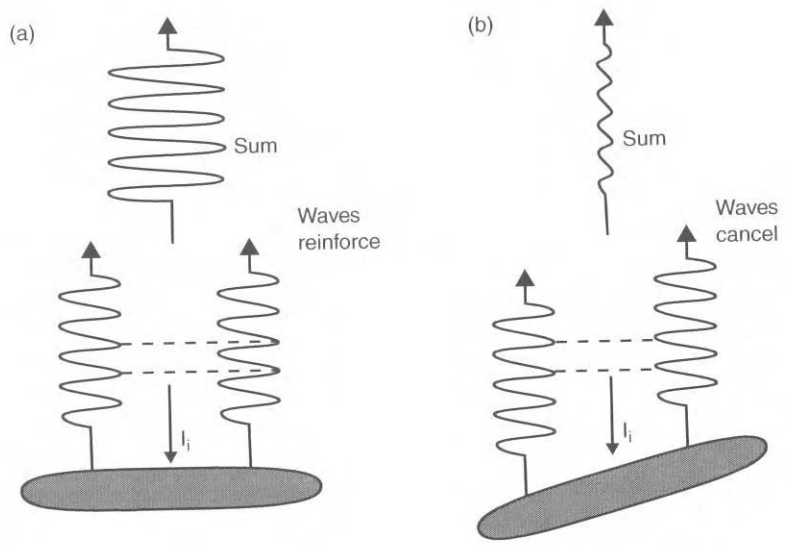

FIG. 2.2. Target orientation phase effects (From (J. Simmonds and MacLennan, 2005)). (a) Constructive interference. (b) Destructive interference.

Automatic determination of target orientation from the acoustic scattering is an important problem. Classic applications can be military, since inferring submarine orientation would expose its travelling direction. Although orientation (in tilt, roll, and yaw) is obviously connected to fish swimming direction (Henderson et al., 2007), determining orientation has an intrinsic value, even for static organisms, connected to behaviour and as a parameter for survey data interpretation (Stanton et al., 2003). Broadband transmissions have been used to determine target orientation. Martin Traykovski *et. al.* used a feature extraction approach in order to estimate the orientation of Antarctic krill (Martin Traykovski et al., 1998). Inversion was achieved by comparing measured broadband spectral signatures to empirical and theoretical model spaces, by means of the Covariance Mean Variance Classification scheme.

The high-resolution capacity of broadband transmissions has also been used for the same purpose, with an inversion based on the correlation between compressed pulse length and orientation (Stanton et al., 2003). The underlying physics is based on the resolution of individual scattering features along the fish body. At broadside incidence all the contributions arrive nearly simultaneously, combining in a single, relatively narrow, received pulse. As the target tilts contributions from distinct points tend to arrive separately, thus lengthening the received pulse. This phenomenon has also been observed in the scattering of Hawaiian lutjanid snappers, with an increased number of temporal highlights and correspondingly larger pulse length at off-axis incidence (W.W. L. Au and Benoit-Bird, 2003). More recently, this principle has been further pursued to study the orientation of salmon tethered at the bottom of a shallow river, with joint echo envelopes and Didson imaging analysis (Burwen et al., 2007).

2.3.3 Fish and zooplankton species identification using sonar

Several research efforts have been directed to attain classification of submerged targets, all of them grounded in the basic tenet of recognizing a particular set of characteristics in the backscattered echo signal, resulting from its interaction with the object. In a general approach related to pattern recognition techniques, the amplitudes of the received echoes are submitted to analysis methods in search of distinguishing cues or features, in the time domain or in the frequency domain. Many of these methods have sought to extract these estimators from the output of conventional sonar systems, subjecting these signals to additional analyses and techniques such as image processing (LeFeuvre et al., 2000, Lu and Lee, 1995) or neural networks (Azimi-Sadjadi et al., 2000), sometimes inspired or compared against the performance of biological sonar (Whitlow W. L. Au, 1994). These and other works have shown that acoustic species classification is feasible but challenging, with success rates higher

in particularly suitable conditions, such as large sample sizes in localized surveys (Misund, 1997). However, as Horne (John K. Horne, 2000) pointed out, the large number and variety of different approaches to acoustic species identification may in turn indicate the vast aquatic biodiversity, which distinct anatomies and behaviours requiring special treatment. In order to increase the performance of classifying methods, further estimators have been sought in the processing of received signals, with the intent of relating them to real features in the investigated targets. It has been accepted that classification based only on a single parameter, such as target strength, is very difficult (Burwen et al., 2007). Often these estimators are stochastic, arising from multiple ensemble recordings of the echoes. Other researchers have focused on the random nature of sonar signals by employing statistical analysis tools. For instance, Hoffman used Bayesian decision rules and likelihood ratios to classify spherical targets (Hoffman, 1971), Fernandes utilized classification trees for the classification of fish schools (Fernandes, 2009). Canonical correlation analysis has also been used, for example, in the classification of man-made target seen an multiple aspect angles (Pezeshki et al., 2007). Other workers have turned their attention to the proven practical success of animal sonar, especially that of dolphins and bats, in the discrimination of targets, even when buried under sediment.(Roitblat et al., 1995) Various connections between animal echolocation and current data processing techniques have been examined (Altes, 1995). For example, it is thought that dolphins might be applying processing techniques related to time-frequency analysis, which would allow them to extract features both from temporal and spectral cues (Muller et al., 2008). Furthermore, the enhanced temporal resolution capabilities of bat (Yovel et al., 2011) and dolphin (Imaizumi et al., 2008) broadband transmissions is fully recognized, although the actual imaging representation used by the animals has not been decided (Whitlow W.L. Au and Simmons, 2007).

2.3.3.1 Broadband approaches to species identification

The usefulness of broadband techniques was recognized early on, with Chestnut *et al* contrasting broadband biosonar and human speech perception to traditional narrowband echosounders (Chestnut et al., 1979). They measured the broadband spectral response of the targets to be classified, analysing the energetic content of the spectrum as well as the reflection coefficients in an all-pole model of the transfer functions obtained through a linear prediction method. Application of statistical methods to broadband or multi-frequency spectra has also been proposed. Recently, Demer *et. al.* presented a method for pre-classification of general target classes, useful for distinguishing fish from the seabed, before model-based identification can be applied (D. A. Demer et al., 2009). They applied a measure of variability to each echogram pixel, based on the ratio between coherent and incoherent contributions in overlapping echoes (Eq. 8). Targets near the ocean bottom, or buried (partially or completely) in sediment have received considerable attention, due in part to military mine-detection applications, but also the increasing interest in ocenographical archaeology.

Transmission of a least two discrete frequencies affords the method of acoustic differencing, which returns the difference of mean volume-backscattering between the two components. Ideally, acoustic differencing could detect the change in acoustic behaviour in shifting from Rayleigh to geometric scattering, which sets the approximate frequency range as a function of the size of the relevant target. This method has been applied to mixed stocks in the ocean, as exemplified by the work of Logerwell and Wilson (Logerwell and Wilson, 2004) and other works that use state-of-the-art systems (Stanton et al., 2010). Recently, Korneliussen *et. al.* proposed systematic procedures for the efficient acquisition and processing of multifrequency acoustic data (Korneliussen et al., 2008).

Besides discretized multiple frequencies, the continuous broadband spectrum has been used for species identification, sometimes as the input for discriminant analysis performed by neural networks (E. J. Simmonds et al., 1996, Zakharia et al., 1996). Other approaches are more reliant on the underlying physics of the features found in the spectra of finite objects. Mature knowledge of echo formation mechanisms has facilitated the task of using spectra to identify targets, by means of spectral signature comparison to predicted values. On a fundamental level, physical characteristics of the scatterer will be imprinted in its spectrum, constituting a signature that can be classified in terms of geometry and composition. This has been achieved for the case of simple targets such as spheres, shells and cylinders, by means of their form function (Dardy et al., 1977, S.K. Numrich et al., 1982). Particularly tell-tale features found in the form function of many objects are the mechanical resonances, seen as distinctive peaks or notches in the magnitude representation.

2.3.3.2 Target phase for acoustic target identification

In general, target strength alone has proven insufficient to discriminate between similar acoustics, since disparaging targets can present the same TS under differing conditions. In this context, target phase has been explored as an additional source of information for acoustic target identification. (Deuser et al., 1979) for example, analysed several statistical parameters obtained from backscattered waveforms, such as the average intensity and energy, and number of peaks above set thresholds. They noted that the data can be represented by its in-phase and quadrature components, but limited their analysis to the envelope, since the application would not retain phase information. Most early workers also confined classification parameters to the statistics of the envelope function. Another example is Gyrin,

who mentioned estimators obtained from the complex Fourier spectra but did not use them (Giryn, 1982). Similarly, Chestnut and his co-workers pointed out that the phase of the spectrum holds valuable information as well (Chestnut et al., 1979). Furthermore, work performed in New Zealand by Barr and Coombs used echo signal rate-of-change of phase parameter to separate echoes from gas-filled swimbladders in fish and resonant bubbles, thus improving the precision of biomass estimations (Barr and Coombs, 2005).

Another way to enhance the information content of sonar signals was pioneered in the late 1960s and early 1970s by workers in the University of Birmingham (Braithwaite, 1973, Tucker and Barnickle, 1969), and consists in taking into account the phase angle of the reflected complex signal and the fact that it undergoes a 180° shift when impinging upon an acoustically 'soft' boundary. In these early works, dual-frequency transmissions were introduced because the time-axis asymmetry of such a pulse, allowed for easier detection of polarity reversals in the time domain, as illustrated in Fig. 2.3. In the ocean, acoustically ‘soft’ objects abound, and tend to be biological in nature, such as the tissue and flesh of some marine animals and algae, and water-air boundaries such as gas-filled swimbladders. In principle, detection of these phase shifts could allow for classification of objects with clearly diverging ‘soft’ and ‘hard’ characteristics, such as fish and rocks. More recently, this approach was further developed by Atkins *et al.*, with a study that tackled the practical obstacles in the measurement of target phase (P. R. Atkins et al., 2007a). Using a dual-frequency transmission, in the manner of Tucker and Barnickle, and testing different types of waveforms for optimal performance, this work reported positive results in the identification of krill (euphausiid), while admitting the need for more resolution.

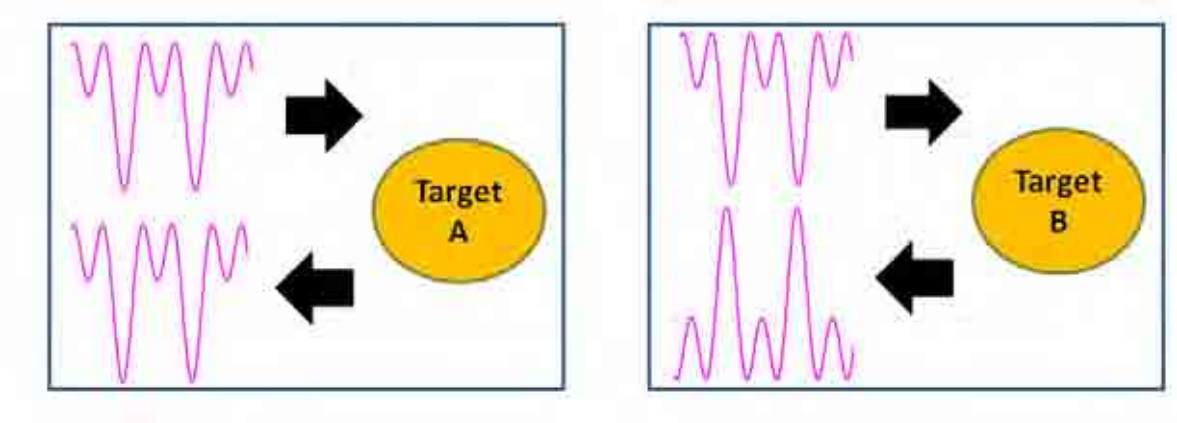

FIG. 2.3. Left, no phase shift. Target A acoustic impedance greater than the medium. Right, polarity reversal. Target B acoustic impedance less than the medium.

2.4 Acoustic scattering of canonical geometrical targets

Underlying mechanisms behind the transmission, diffraction, and reflection of a sound wave on solid a bodies have been extensively studied in the past. Size, relative to wavelength, determines the principal acoustic phenomena. In general, most target responses can be separated into three main frequency sections, exhibiting similar features in the form function (Brill et al., 1991). Scattering from targets much smaller than the wavelength ($ka << 1$), i.e. Rayleigh scattering, presents a power law dependence with frequency (J. Simmonds and MacLennan, 2005). In this low *ka* regime diffraction is dominant. As the relative size of the target increases specular reflection becomes the main echo contribution, with an oscillatory behaviour caused by interaction with diffraction-induced peripheral waves. This is the rigid region. As the frequency increases, diffraction effects are weakened and elastic surface waves are excited, entering into the resonant region, superimposed on the appropriate background. At even higher frequencies ($ka >> 1$) the response tends to the geometrical acoustics limit, where the ray approximation applies. The complicated interaction arising from targets in the elastic regime have been investigated using simple geometries. For example, spheres, shells

and finite cylinders have often been chosen as benchmark cases, due to their manageable analytical expressions for theoretical solutions and their usefulness as building blocks for more complex structures.

2.4.1 **Sound scattering solution approaches**

Solution to the wave scattering from these finite targets can be accomplished through several methods, with the form function commonly used to represent the scattering of these targets in the frequency domain.

2.4.1.1 **Kirchhoff method**

An approach based on geometrical optics as a high frequency approximation is the Kirchhoff approximation used to solve the Helmholtz-Kirchhoff integral. This method assumes a perfectly rigid, homogenous object and no diffraction effects, with each differential components of the insonified area acting as individually reflecting facets (Dietzen, 2008, Medwin and Clay, 1998). The Kirchhoff ray approximation is exclusively based on the geometry of the target and its surface composition and internal structure are not considered. Resonances that may occur due to physical or mechanical properties are thus ignored. This is an important limitation for underwater acoustics, since an object submerged in water seldom behaves as an impenetrable rigid body (Gudra et al., 2010).

2.4.1.2 **Exact analytical solutions**

The exact theoretical scattering of a penetrable object, which include diffraction and resonant effects related to surface waves and elasticity can be achieved through modal or normal-mode solutions, as first described by Rayleigh. In general, the solution of the scalar wave equation in the relevant coordinates is obtained, and the appropriate boundary conditions are applied. Incident waves and resulting scattered pressures are expressed as the expanded summation of spherical Bessel functions and Legendre polynomials. This mathematical development became widely applied with the advent of computers, as demonstrated early on by Hickling (R. Hickling, 1962a), followed by Rudgers (Rudgers, 1969). However, closed solutions of this nature are only feasible for geometries defined in a set of coordinates that allow for separation of variables. Moreover, for elastic bodies the scalar wave equation becomes a triple coupled equation, only separable in the cases of simple, highly symmetrical geometries, namely the sphere, infinite cylinder and infinite rectangular slab (Partridge and Smith, 1995).

2.4.1.3 **Approximations for more complex geometries**

Scattering from finite elastic targets has to be calculated through numerical methods or approximated using simpler solutions (Partridge and Smith, 1995). Alternative solutions for axy-symmetric finite objects with rigid, soft and fluid boundary conditions have been provided by the Fourier Matching Method (FMM) (Reeder and Stanton, 2004). Fully-elastic scattering from arbitrary finite objects has most successfully been solved with the transition matrix (T-matrix) approach (Waterman, 1969), or approximated with the Boundary Element Method (BEM) and Finite Element Methods (FEM). In particular, FEM models, often implemented in COMSOL (Comsol Inc., Palo Alto, USA), have been applied to more realistic situations beyond free-field conditions, where targets are near a boundary (LaFollett et al.,

2011), or in contact with sediment (Williams et al., 2010). This approach has a recent impetus in relation to the detection of mines or UXOs (UneXploed Ordnances) (Lim, 2010).

2.4.2 Elastic resonances, normal modes and circumferential waves

The phenomenon of resonances in the scattering from elastic bodies is very significant and has received an important amount of attention. Hickling noticed the occurrence of resonances in the form of trailing echoes or ringing seen in the pulses reflected from a solid sphere (Robert Hickling, 1962b). He correctly identified the cause to be both geometric diffraction and elastic vibrations. Furthermore, the idea of separate specular and resonant returns was also introduced. The relationship between resonances and normal modes of free vibration had already been investigated by Faran (Faran, 1951). He noted that the frequency locations of the resonances were very close to those of normal modes of free vibrations, with only slight differences due to the coupling to the medium (Uberall et al., 1977). Faran also emphasized the role of shear waves, linking resonant characteristics to material composition parameters, particularly the elastic moduli. This connection has been exploited in non-destructive testing techniques that examine resonances in order to assess the condition and physical properties of a sample. Variations of this approach, generally denominated resonant ultrasound spectroscopy (RUS) (Fraser and LeCraw, 1964, Zadler et al., 2004b), have been applied to several materials, either with the specimen in contact with ultrasonic transducers (Yaoita et al., 2005) or via optic interferometry (Deneuville et al., 2008). The same principle has been applied in underwater acoustics for the evaluation of the elastic parameters of tungsten carbide spheres used as standard sonar calibration targets (MacLennan and Dunn, 1984).

Experimental investigations of target resonances involved in scattering can rely on a sophisticated theoretical framework, known as the resonant scattering theory (RST) and originated from nuclear physics (Flax et al., 1981, Uberall et al., 1996). The fundamental physical interpretation of RST encompasses sustained oscillatory processes in general, with particular applications to acoustic and electromagnetic scattering (Uberall et al., 1985). RST has shown that modal resonances occur at the onset of constructive or destructive interference between surface waves circumnavigating the object. This condition is reached at specific discrete frequencies called eigenfrequencies, when these peripheral waves match phases (Uberall et al., 1977). For elongated objects such as cylinders and prolate spheroids these iterative waves follow helical paths (Uberall et al., 1985). The observed surface wave types are manifold, including Franz, Lamb, Rayleigh, Whispering Gallery, and Stoneley waves (Uberall et al., 1996, Veksler, 1996).

2.4.3 Solid spheres

Spherical targets are an extremely important benchmark scatterer with applications in modelling and sonar calibration. The problem of predicting the acoustic scattering from a sphere in water is classic, and has been solved in various ways. Analysis has been restricted to the cases where the spherical target is larger or comparable to the wavelength.

2.4.4 Kirchhoff approximation

Application of the Kirchhoff method to the sphere is not ideal, due to the diffraction effects that, in the rigid case, generate Franz waves around the circumference (S. K. Numrich and Uberall, 1992, Rudgers, 1969), as illustrated by Feuillade (Feuillade, 2004). Nevertheless, predictions from the Kirchhoff method are acceptable for rigid spheres insonified at high

frequencies, tending asymptotically to the geometrical scattering constant. The form function in the far field, f_∞, for a rigid sphere, obtained from the Kirchhoff integral is (Dietzen, 2008)

$$f_\infty = \frac{-i2\pi a^2}{\lambda} \int_0^{\pi/2} \cos\theta e^{-i2ka\cos\theta} \sin\theta \, d\theta \,, \tag{2.19}$$

where λ is the wavelength, k is the wave number, a is the sphere radius and θ is an angle from the spherical coordinate system illustrated in Fig. 2.1.

2.4.5 Modal solution

Solutions to the scattering of solid spheres in water, including both geometric (rigid) diffraction and elastic effects were first given in Faran's seminal 1951 paper (Faran, 1951). This approach was related to the normal-mode solutions developed by Lord Rayleigh for small scatterers relative to wavelength (Rayleigh scattering). Following the notation of Hickling (Robert Hickling, 1962b) and Goodman and Stern (Goodman and Stern, 1962), an incident plane wave P_{inc} of amplitude P_o can be expressed as

$$P_{inc}(ka) = P_o \sum_{m=0}^{\infty} i^m (2m+1)\, P_m(\cos\theta)\, j_m(ka)\,, \tag{2.20}$$

where a is the sphere radius, and the subscript m indicates individual partial waves forming the total field, with corresponding m_{th} Legendre polynomial, P_m, and spherical Bessel function of the first kind, j_m. The acoustic variables can alternatively be expressed in

frequency or dimensionless frequency, *ka*. The scattered pressure wave, measured in the far-field, P_{scat}, is

$$P_{scat}(ka) = \sum_{m=0}^{\infty} A_m P_m(\cos\theta)\, h_m(ka), \tag{2.21}$$

with spherical Hankel functions, h_m, and reflection coefficient, A_m, calculated from a set of linear equations after appropriate boundary conditions are applied. The incident and scattered pressure can be then used as the input and output quantities, respectively, that define the transfer function of the sphere, expressed as its normalized form function in the far-field,

$$f_{\infty}(ka) = \left(\frac{2R}{a}\right)\frac{P_{scat}(ka)}{P_{inc}(ka)}, \tag{2.22}$$

where the complete symmetry of the sphere precludes dependence on the angle of incidence. Although the form function in Eq. 2.22 is complex, often only its modulus is presented.

2.4.6 Fluid-filled shells

Fluid-filled shells are important in acoustical oceanography, particularly for modelling zooplankton, fish swimbladders and bubbles. Solutions of the scattering originated in a spherical shell take various forms, depending on the shell thickness and composition, as well on the fluid within (Diercks and Hickling, 1967). An early theoretical treatment for a fluid sphere was performed by Anderson (Victor C. Anderson, 1950), in terms of a modal series expansion. Anderson's work was later revisited and found to be consistent with the theory of

Faran (Feuillade and Clay, 1999). Scattering from a fluid sphere can be expressed by Eq. 2.21, setting the appropriate boundary conditions for the calculation of the A_m coefficients. Further complexity arises from the interaction between the external layer and the fluid inside, with an stronger coupling as thickness decreases. Density contrasts are defining in determining the ensuing echo formation mechanisms. A water-filled thin-shell, for example, allows for sound penetration and sustains compressional waves causing multiple internal reflections from the concave back end (R. Hickling, 1964). An air-filled shell such as a bubble, presents a high-density contrast that forbids sound penetration. Another consequence is that the lower acoustic impedance of the air, as compared to the surrounding water, produces a phase reversal, as the sign of the reflection coefficient becomes negative. Variations in the mismatch between the internal and external acoustic impedance, given by the index of refraction can produce focusing effects, analogous to an spherical lens (Folds, 1971). This can have useful applications for the design of highly reflective targets that can act, for example, as aids for recovering acoustic buoys or as contrast agents in ultrasound imaging (Allen et al., 2001). For an elastic shell, flexural waves travelling along circumferential paths in the surface need to be considered. Elastic effects and mechanical resonances are fully addressed by the Faran model, and are similar to those occurring on a solid elastic sphere. The elastic response is also superimposed on a background, found to be soft for thin shells at lower frequencies and rigid for thick shells at higher frequencies (Werby, 1991). However, unlike the solid case, a mid-frequency enhanced resonant response has been observed and investigated for thin shells. These resonances have been found to be caused by anti-symmetric Lamb waves (also called Stoneley waves) (Kaduchak and Marston, 1993).

2.4.7 Infinite and finite cylinders

Solid elastic truncated cylinders have been used as an approximation for the elongated shape of fish. An isotropic cylinder, with circular cross section is depicted in Fig. 2.4.

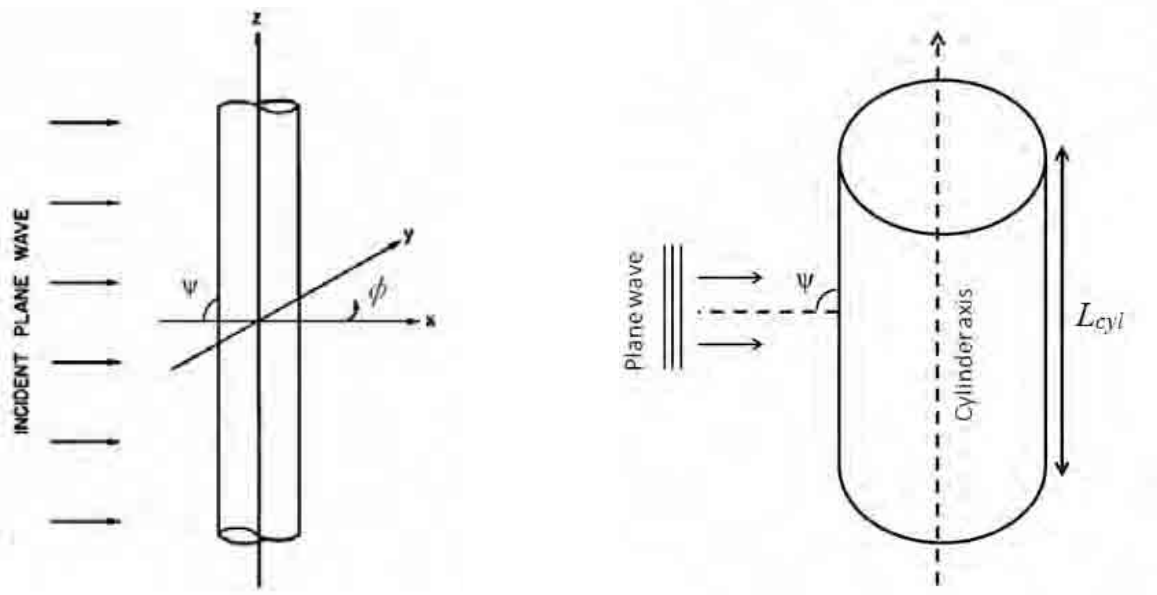

FIG. 2.4. Schematic depiction of plane wave incidence on a circular cross section cylinder. Left, infinite cylinder (Faran, 1951). Right, finite cylinder of length L_{cyl}. Plane wave incidence forms an angle ψ relative to the normal of the cylindrical axis.

The length of cylinder, relative to the wavelength of the incident signal, is defined in terms of the Fresnel zones, whereas the object has to be contained within the innermost cross section (Stanton, 1988b). This raises two situations where either the finite, or infinite, length cylinder case apply more closely, such as, $L_{cyl} << \sqrt{R\lambda}$, for a finite cylinder and, $L_{cyl} >> 2\sqrt{R\lambda}$, for an infinite cylinder. If the length is larger than the first Fresnel zone it can be considered "infinite" and end effects ignored. Compared to the infinite cylinder, which is essentially a

two-dimensional problem, the finite length cylinder is a much more complicated scatterer. The main problem faced in the case of the truncated cylinder is the diffraction effects occurring at the ends. These effects cannot be properly predicted by modal solutions or ray acoustics approximations. Stanton developed such an approximation calculating the volume flow for discrete sections along the length, assuming them to be equivalent to those of an infinite cylinder. He adapted this solution, sometimes referred as the Modal-Based Deformed Cylinder model (MB-DCM), to the case of fluid finite cylinders (Stanton, 1988a), elastic finite cylinders (Stanton, 1988b), and deformed cylinders and spheroids (Stanton, 1989).

Predicting scattering at different angles of incidence relative to the cylinder axis is directly relevant for investigating the effects of fish orientation. This problem was first solved for the infinite elastic cylinder, assuming plane wave incidence (Flax et al., 1980). These studies showed the presence of various circumferential waves, as well as helical Franz waves. Also, beyond a critical angle of incidence given by the longitudinal and shear wave coupling, axially-propagating waves ensue. Effects of oblique-incidence scattering on infinite cylinders have received significant attention (Fan et al., 2003, Mitri, 2010), along with the more realistic problem of scattering from a finite cylinder. In this respect the Deformed Cylinder Model (DCM) has proven insufficient, since its range of validity is limited near broadside incidence (Partridge and Smith, 1995). Solutions based on the T-Matrix method have been advanced for truncated cylinders with hemispherical end caps for a few angles of incidence (Hackman and Todoroff, 1985, S.K. Numrich et al., 1981). In parallel, several studies have been concerned with cylinders of non-circular cross sections, both as solid bodies and fluid-filled shells (Chinnery and Humphrey, 1998). Latest efforts for the prediction of directivity patterns from elastic finite cylinder have been conducted through Finite Element (FE)

numerical modelling. Some of these studies have been motivated by the need for acoustic identification of unexploded ordnances (UXOs). In this context, FE modelling conducted in COMSOL has reached a considerable level of maturity, with good agreement between the measurements and predicted scattering of a finite elastic cylinder rotated in the free field (Lim, 2010). Current research objectives in this area involve scattering simulation of cylinders near flat boundaries (LaFollett et al., 2011).

2.4.8 Prolate spheroids

The prolate spheroid has been found to be the closest fit to swimbladder scattering, from the simple geometrical models (Benoit-Bird et al., 2003). As mentioned previously, in zooplankton scattering this geometry is also relevant and has been used to a low-resolution representation for copecods as computed through the DWBA model (Stanton and Chu, 2000). Exact solutions for an elastic prolate spheroid have been achieved, since this geometry still allows for separation of variables in a wave equation expressed in spheroidal coordinates (Silbiger, 1963, Skudrzyk, 1971, Spence and Granger, 1951). These modal solutions have also been adapted for fluid prolate spheroids (Furusawa, 1988). Furthermore, several theoretical scattering studies exist, based for example, in the resonance scattering theory (Uberall et al., 1987) and the T-Matrix solution (Werby and Evans, 1987).

3 SONAR TARGET PHASE INFORMATION

This chapter briefly reviews the usage of signal phase information to calculate range, velocity and dispersion. The concept of target-induced phase, or, more succinctly, target phase, is explored in the context of applications in ultrasound, radar and sonar for fisheries and acoustical oceanography. Target phase measurement methods are described.

3.1 Applications of signal phase information

Signal phase is important in signal processing in general (Spagnolini, 1995), since it contains essential information about the process that originated it. As previously mentioned, phase has been used as an additional source of features which can be extracted for classification. Besides target identification tasks, this approach has also been adopted in speech analysis for the classification of audio utterances (Paraskevas and Chilton, 2004). In particular, it has been advanced that phase contains information about 'location' in domains such as time and space (Oppenheim and Lim, 1981). For image processing, this results in enhanced intelligibility of features, while in applications such as ultrasound imaging, sonar and radar, phase is intrinsically linked with time, which translates into distance information. This has proven advantageous for radar and ultrasound rangers, since the simpler and widespread time-of-flight method has often been insufficiently accurate. In broadband signal propagation phase characteristics, expressed as group velocity, have been used to study dispersive behaviour. However, the analysis of the phase characteristics induced by targets and inhomogeneities is scarce in radar, ultrasound and sonar literature.

In a simplified narrative it could be noted that in order to evaluate one of the parameters associated with phase (dispersion, range, or target phase), an approximation of the others is made. In this way, for phase-based range measurements, sound speed is estimated and target-induced phase is not considered. Likewise, in dispersion experiments range is fixed and target effects ignored. Finally, for the case of target-induced phase determination, sound speed is estimated and range is removed via processing. These assumptions have variable impact on measurements, addressed in the specific experiment (H. Wang and Cao, 2001).

3.1.1 Phase-based time-delay measurements

Phase information has been used to determine time delay, and, consequently, range. This has been particularly suitable for various situations, such as in the generalized multipath channel problem, where processing of phase spectra compare favourably to corresponding time-domain operations. Piersol, for example, showed that the time delay between arrivals originated in two sound sources could be estimated from the cross-spectrum phase by means of regression techniques (Piersol, 1981). This proved advantageous for a reduced variability in the presence of uncorrelated and correlated noise. However, in severely reverberant environments this method suffers from fluctuations in the spectrum, that could impede attainment of the Cramer-Rao (Lurton, 2002) lower bound if the power spectrum is used as the weighting function (Zhao and Hou, 1984). Phase information has also been shown to be crucial for the identification of superimposed echoes not separable by gating. This is particularly problematic for systems with constraints in range-resolution, such as limited waveform choice. Distinction of underlying individual arrivals has been achieved through both the phase spectrum (sometimes calculated with the Maximum Entropy Method (Yao and Ida, 1990)) and the complex cepstrum (Hassab, 1978).

When only direct specular returns are considered and signal decomposition is not required, the problem reduces to the accurate measurement of the time lapse between transmission and reception. Although range measurements are conceptually simpler, challenges reside in the level of accuracy achieved and the distances covered. The most straightforward approach, namely the time-of-flight measurement, is still extensively used but its precision is limited by the sharpness of the probing pulse, and, thus, system bandwidth (Yang et al., 1994). More accurate measurements have been achieved with phase-based methods, where distance is determined from phase differences at two points. However, since phase values are modulo 2π an ambiguity occurs for ranges, R, larger than half the wavelength, λ. This uncertainty has been resolved by transmitting two or more frequency components, for applications in ultrasound (C. F. Huang et al., 1999, Kimura et al., 1995, Yang et al., 1994), radar (Amin et al., 2006, Skolnik, 1962, Yimin Zhang et al., 2008) and sonar (Assous et al., 2010).

For a continuous wave signal, $s_1(t)$, with a single frequency, f_1, range, R, is related to the phase of the received signal, $\varphi_1(t)$, as follows

$$\varphi_1(t) = \frac{4\pi f_1 R}{c}, \tag{3.1}$$

with wave speed c assumed to be constant and non-dispersive. Use of a second signal $s_2(t)$ with frequency f_2, and a corresponding phase

$$\varphi_2(t) = \frac{4\pi f_2 R}{c}, \tag{3.2}$$

allows for range determination by subtraction, such as

$$R = \frac{c}{4\pi(f_2 - f_1)}\left[\varphi_2(t) - \varphi_1(t)\right]. \tag{3.3}$$

Alternative to the measurement of individual phases, with its difficulties due to unwrapping issues, direct extraction of the difference can be achieved with a multiplication of the complex conjugate of the lower frequency signal by the higher frequency signal (Amin et al., 2006),

$$s_2(t)s_1^*(t) = |s_1||s_2|e^{\left[j(\varphi_2(t)-\varphi_1(t))\right]}. \tag{3.4}$$

Again, in this approach echoes are considered to be purely specular, and without target-induced phase effects. The maximum unambiguous range is determined by the frequency difference, such as (Yimin Zhang et al., 2008)

$$R_{\max} = \frac{c}{2(f_2 - f_1)}. \tag{3.5}$$

This method has demonstrated improved resolution, which can be even finer with more frequencies utilized in a manner analogous to a Vernier gauge (Assous et al., 2010). Error sources are mainly due to phase noise, which could be ameliorated in part with the adoption of direct digital frequency synthesizer algorithms (K. N. Huang and Huang, 2009).

3.1.2 Phase-based velocity and dispersion measurements

Wave velocity has been measured through the phase shifts occurring on the acoustic path. This has been applied to the classic problem of accurate estimation of sound speed in water, with steady-state signals and phase calculated by comparison against a reference signal, in highly-controlled conditions (Barlow and Yazgan, 1966). The accuracy and consistency of

these results compared favourably to other works. However, largely the focus of velocity measurement experiments has been placed in the more prevailing condition of dispersive propagation, where wave velocity varies as a function of frequency (Brillouin, 1960). Sachse and Pao (Sachse and Pao, 1978) listed the possible causes of dispersion, three of them being geometric dispersion occurring at boundaries, attenuation in the material due to the composition of the specimen, and scattering dispersion in aggregations of inhomogeneities. A broadband pulse travelling in a dispersive medium will suffer distortion, as its frequency components are affected by different amounts. This is analogous to the signal distortions occurring in a dispersive system such as an electrical network with resonant elements. In the time domain, dispersive distortion changes the waveform from the original transmitted shape.

Using the definitions and notation of Ting and Sachse (Ting and Sachse, 1978) a plane monochromatic wave, moving in space, *x*, and time, *t*, is described as

$$u(x,t) = u_o e^{i(\omega t \pm kx)}, \tag{3.6}$$

where u_o is the amplitude. The derivative of position versus time, yields the phase velocity, *v*, such that

$$v = \frac{dx}{dt} = \frac{\omega}{k} = f\lambda . \tag{3.7}$$

Eq. 3.7 effectively describes a dispersion relationship between angular frequency and wave number,

$$\omega = \Omega(k) = vk = ck \tag{3.8}$$

for the specific case where no dispersion exists (or is considered), phase velocity, *v*, becomes synonymous with the speed of sound *c*.

A wave packet has envelope that moves with a group velocity *U*, such that

$$U = \frac{d\omega}{dk} = \frac{d(vk)}{dk} = v + k\frac{dv}{dk}. \tag{3.9}$$

It can be seen that group velocity is only equal to phase velocity when velocity is a constant with respect to wave number. While group velocity has been connected to the rate of information or energy transportation (Biot, 1957), physical interpretation is not always intuitively evident, particularly in the presence of anomalous dispersion phenomena.

Dispersion, and attenuation are the parameters usually measured for the estimation of acoustic properties of materials. Estimation of these quantities is useful in areas such biological tissue characterization and non-destructive testing, with applications in the analysis of a variety of specimens such as composite and porous materials (Sachse and Pao, 1978), polystyrene suspensions (Peters and Petit, 2003), sandy marine sediment (K.I. Lee, 2007), plant leaves (Sancho-Knapik et al., 2011), and acoustic panels (Humphrey et al., 2008, Piquette and Paolero, 2003), to mention a few. Determination of dispersion and attenuation is often achieved in a through-transmission, pitch-catch, arrangement, in which the change suffered by a wave traversing a specimen is examined, and compared to transmission in its absence. While the energy reduction, attenuation, caused by an object is relatively straightforward to assess, its dispersive characteristics present a more considerable experimental challenge. Broadband phase spectroscopy, as introduced by Sachse and Pao (Sachse and Pao, 1978), relies on Fourier techniques to measure the phase spectra and extract phase and group

velocity. While they initially used two transducers in intimate contact with a solid specimen, their technique has been applied to measurements of specimens immersed in water.

If two measurements are performed in a water tank, one with a specimen of thickness L between the transducers, and another without the specimen, the spectra of the two received signals can be used to calculate dispersion. A transmitted pulse $tx_{pulse}(t)$, with Fourier transform $TX_{pulse}(\omega)$, is transmitted, alternatively, solely through the water and through the specimen, with the corresponding receiving signals $RX_w(\omega)$, and $RX_s(\omega)$, such as

$$RX_w(\omega) = A_w(\omega)e^{-j\varphi_w(\omega)}, \tag{3.10}$$

and

$$RX_s(\omega) = A_s(\omega)e^{-j\varphi_s(\omega)}, \tag{3.11}$$

where A_w, A_s are the recorded amplitude spectra, and φ_w, φ_s the recorded phase spectra. Following He's formulation (P. He, 1999), the signal-only propagating through the water depends on the spectrum of the transmitted pulse, $TX_{pulse}(\omega)$, the distance between the transducers R, and the response of the receiving transducer, $H_r(\omega)$,

$$RX_w(\omega) = TX_{pulse}(\omega)e^{-R(\alpha_w(\omega)+j\beta_w(\omega))}H_r(\omega), \tag{3.12}$$

with $\alpha_w(\omega)$ and $\beta_w(\omega)$, as the attenuation and propagation phase constant, respectively. The propagation constant is the imaginary part of a complex wave number in which the attenuation coefficient is the real part. The signal through the specimen also depends on the

thickness, L_s, and the transmission coefficients of the two interfaces, T_1 and T_2, such as

$$RX_s(\omega) = TX_{pulse}(\omega) e^{-(\alpha_w(\omega)+j\beta_w(\omega))(R-L_s)} e^{-(\alpha_s(\omega)+j\beta_s(\omega))L_s} T_1 T_2 H_r(\omega). \tag{3.13}$$

This applies to the first part of the received pulse, prior to the arrival of secondary reflections. From these equations, the propagation constant, β_s, can be determined,

$$\beta_s = \frac{\varphi_s(\omega) - \varphi_w(\omega)}{L_s} + \beta_w, \tag{3.14}$$

for simplicity, phase deviations due to the sample window are not considered here. This is related to phase velocity, by

$$\beta_s = \frac{\omega}{v(\omega)}, \tag{3.15}$$

resulting in an expression that is only a function of phase, frequency and thickness,

$$\frac{1}{v_s(\omega_o)} - \frac{1}{v_s(\omega)} = \frac{\varphi_w(\omega_o) - \varphi_s(\omega_o)}{\omega L_s} - \frac{\varphi_w(\omega_o) - \varphi_s(\omega_o)}{\omega_o L_s} \tag{3.16}$$

with ω_o as a reference angular frequency, and v_s as the phase velocity in the specimen.

An alternative approach has been suggested, in which the need to remove the specimen and estimate the phase spectra in water is precluded, thus, with only a single measurement required (H. Wang and Cao, 2001). This method is in a way analogous to dual-frequency range calculations, and relies on detection of second signal, arriving from an internal

reflection in the specimen (from the exit interface back to the entrance interface, and onward to the receiver). Velocity is calculated from phase differences, such that

$$v(\omega) = \frac{2\omega L_s}{\varphi_1(1) - \varphi_2(\omega)}. \tag{3.17}$$

Although not presented, the methods reviewed also yield attenuation estimates. An alternative is the extraction of attenuation characteristics from dispersion, or vice versa. This can be attained through their fundamental inter-dependence, expressed by the Kramers-Kronig relationship, for linear, causal systems and unbounded waves (C.C. Lee et al., 1990).

3.1.3 Target-induced phase measurements

The phase of a reflected signal has been used to investigate characteristics of the reflecting surface, boundary or scattering object. That is, upon interaction with a waveform, targets imprint phase shifts on the returning echoes, thus conveying information alongside amplitude. However, some difficulties lie in the fact that phase also contains range and velocity information, as we discussed previously. In many cases, phase differences rather than absolute values are examined. The formulation of these differences can be done in various ways, depending on the application. For example, phase gradients have been measured with a pair of microphones placed in front of a reflecting surface. Phase differences at the two receivers are used to calculate the boundary impedance, a useful parameter in the characterization of, for example, soil (Daigle, 1987) and porous materials (Legouis and Nicolas, 1987). Broadband ultrasonic phase spectroscopy methods, have also been applied to the detection and characterization of flaws (Mercier et al., 1993). Particularly, phase information has been linked to the mechanical resonances of targets, sometimes as an aid to

emphasize their presence (Maze, 1991) or elucidate underlying echo formation mechanisms. Sensitivity to resonances has been explored through the phase angle of the form function of spheres and cylinders (Mitri, 2010, Mitri et al., 2008, Yen et al., 1990).

In marine target identification, echo phase has been also explored in a complementary manner to amplitude, as briefly mentioned previously. The potential of this was recognized early on, in the context of species identification schemes (Chestnut et al., 1979, Deuser et al., 1979, Giryn, 1982), although a more widespread adoption has not occurred due in part to limitations in scientific and commercially-available instruments. A considerable effort was conducted by Barr and Coombs, who used rate-of-change of phase as an additional descriptor to fit discriminate fish and plankton species (Barr and Coombs, 2005). They developed complex target strength versus rate-of-change of phase plots, for single targets, both modelled and measured with a 38 kHz echosounder. The models could then be fitted to patterns found in these plots by modifying length and tilt angle variables. Since the results of this work were promising, with modelled and experimental complex plots showing resemblance, Barr and Coombs called for the development of calibrated phase-sensitive sonar systems. More recently, Demer *et al.* have also advocated these technologies (D. A. Demer et al., 2009).

Although some investigations of phase as a target descriptor have been heuristic, acoustic phenomena causing phase shifts have been recognized at a physics-based level. One of such phenomena was indicated by Lord Rayleigh and involved phase distortions at angles of incidence larger than the critical angle (Arons and Yennie, 1950). Another example is the 180° degree shift that ensues when an acoustic wave strikes upon a boundary of lower acoustic impedance than the initial media. This polarity reversal is manifested in the reflection coefficient,

$$R_{coeff} = \frac{\rho_2 c_2 - \rho_1 c_1}{\rho_2 c_2 + \rho_1 c_1}, \tag{3.18}$$

where ρ_2 and c_2 refer to second medium density and sound speed, and ρ_1 and c_1 to the surrounding medium, i.e., water in fisheries applications, but also potentially defining different sediment layers. This was the basis of a fish and plankton identification scheme (Braithwaite, 1973, Tucker and Barnickle, 1969), described in Section 2.3.3.

3.2 Coherent and incoherent scattering from a single target

As in the case of multiple-scattering regimes, phase variations within an echo from a single target can also be understood in terms of coherency. This can have important implications for target detectability, as phase effects modulate echo amplitude beyond predictions from ray propagation models. As previously mentioned in the context of orientation of elongated targets, the phases of echoes generated at different points along the length of the body can interact constructively or destructively. Effects can be severe, with large substantial changes potentially produced by small rotations. In classic radar theory, these phenomena is referred as scintillation noise, and the complexity of the resulting wave interference patterns presented challenges for the continuous tracking of highly-dynamic targets (Dunn et al., 1959). The term ‘scintillation’ is also used in underwater acoustics in the scintillation index. In that context, it represents the temporal fluctuations of a signal due to spatial coherence degradation, caused by relative motion in the source or receiver, or random scattering along the propagation path (Cotté et al., 2007).

In general, interference effects in a single target become important as the object deviates from the ideal point scatterers and presents and extended surface or volume. Backscattering from an ideal point scatterer, $p_{scat}(t)$, appears as a single return generated at a single distance from the receiver, R, at time, t_0, such as

$$p_{scat}(t) = \frac{s_o(t-t_0)}{R^2} * f_{bs}(t), \tag{3.19}$$

where s_o is the transmitted signal and f_{bs} is the impulse response of the target. This expression contains the two-way spreading losses of the incident and scattered waves, hence the squared range term. Upon matched filter processing, the signal envelope in the time domain yields a sinc-like function at the output, due to the rectangular spectrum of the pulse and their Fourier transform relationship. However, realistic scatterers tend to generate multiple returns arriving at different times (Chu and Stanton, 1998). Complex targets have been modelled, both in radar (Rihaczek and Hershkowitz, 1996) and sonar (Clay and Heist, 1984, Lacker and Henderson, 1990), as a conglomeration of reflecting scattering points or glints, that produce individual returns with delays proportional to their relative location within the object.

This intuitively-simple model, constructed from point scatterers with assumed fixed locations, is challenged by various factors. Again, wave interference complicates the response. Also, the choice of an appropriate density and weighting of the point scatterers is not straightforward. A closely-related simplification has also been advanced, based on the use of a few, dominant scattering centres each with its own amplitude and phase (Gaunaurd, 1985,

Lacker and Henderson, 1990, Ross and Bechtel, 1968). This representation can also fail in the assumption of static scattering centres firmly fixated within the target. This is not the case in the presence of dispersion effects that seem to shift the apparent origin of the reflection. An example of this situation is found in cavity-like reflectors, as termed in radar (Rihaczek and Hershkowitz, 1996), which store energy from the incident wave before returning it to the receiver. In acoustic scattering a parallel can be found in resonant objects such as elastic spheres, which hold energy in the form of ringing, caused by circumnavigating surface waves.

Since phase information contains time delay characteristics, the frequency-dependent phase of the acoustic form function has been linked to the relative position of a phase centre within an extended scatterer. Movement of the phase centre is then seen as a phase modulation in the received signal (Rihaczek and Hershkowitz, 1996). In sonar, Hickling arrived to this conclusion after studying the complex scattering from solid elastic spheres (R. Hickling, 1962a, Robert Hickling, 1962b). He interpreted the target phase behaviour as the relative position of the phase centre, φ_{centre} ,along the sphere diameter, such as

$$\varphi_{centre} = \frac{-angle(f_{bs})}{ka}, \tag{3.20}$$

with radian units.

For a rigid response an acoustic “bright spot” could be said to move towards the back of the sphere (far side from transducer along the z axis in Fig. 2.1), as frequency increased. This was previously observed in an air-acoustics experiment performed on rigid spheres (Wiener,

1947). For Hickling this characteristic showed a gradual change from full target cross section reflection at low frequencies, to localized geometric reflection at higher frequencies. However, this physical explanation does not apply in a straightforward manner for an elastic behaviour, which exhibits discontinuous phase jumps in Eq. 3.20. This usage of the phase information was adopted in the study of microcalcifications with ultrasound, where these inhomogeneities are modelled as hydroxyapatite spheres in a fluid (Martin E. Anderson et al., 1998). The observed disjunction in the phase spectra, due to elastic effects, is equated to temporal (or spatial) incoherence. In other words, incoherent acoustic scattering from an extended target arises not only from the presence of various highlights in the body geometry, but also from dispersive effects that shift the apparent acoustic source. The resulting level of incoherence is contained in the signal's phase spectrum. This is closely related to the assessment of diffuse acoustic fields, where phase accumulation exceeds that of a direct field in that case (L. Wang and Walsh, 2006).

Localization of the frequency-dependent acoustic position within a scattering body can also be applied to active radiator. This analogous phenomenon was investigated in transducer characterisation, focused on high-fidelity loudspeakers, by Heyser. He also linked dispersive behaviour to a time delay larger than that due to simple signal propagation and modelled the resulting spatial spread of the acoustic source as an array of ideal sources with a frequency-dependent position (Heyser, 1969a, b, Heyser, 1984). Using a generalized system analysis, Lyon identified deviations in the unwrapped phase trend, away from the linear response due to transmission (H. He and Lyon, 1996, Lyon, 1983). Again, added phase shifts were proven to be due to modal resonances, studied through the poles and zeroes of the transfer function.

From various converging perspectives then, temporal and spatial coherence in scattering and radiation has been explained in terms of dispersive effects and elastic resonances.

3.3 Target echo phase in biosonar

The potential significance of target echo phase has also been explored in the context of bat and dolphin biosonar. For bats, sensitivity to phase has been investigated in relation to their superior range resolution, or hyperacuity, and discrimination performance. Modelling bat sonar as an ideal correlation receiver, Moss and Simmons (Moss and Simmons, 1993) found evidence of the animal's sensitivity to echo phase, measured in reference to the transmitted signal, and linked to detection performance of jittering point targets. However, these results have been highly controversial, particularly in relation to the validity of the reported 10 ns time resolution threshold, which indicates complete, coherent utilization of the echo information (Beedholm and Mohl, 1998, Schornich and Wiegrebe, 2008). An alternative model that does not utilize complete phase information is a semi-coherent matched filter, which relies on the cross-correlation envelope (Yovel et al., 2011).

3.4 Target phase measurements

The meaningful and correct interpretation of the phase component of an acoustic signal presents considerable more obstacles than amplitude, and this difficulty is partly the reason for its relative neglect. For one part, measuring the phase of the target is an inherently ambiguous task since the value can go through multiple full 2π rotations, and consequently needs to be unwrapped. Furthermore, it has been mentioned that, as a signal advances through the propagation media, phase angle accumulates in proportion to the distance

travelled. In system analysis, the accumulated phase trend in itself can reveal important information (Lyon, 1983, 1984, L. Wang and Walsh, 2006). However, in order to uncover the effects solely attributable to a scatterer, the linear component must be removed.

3.4.1 Linear range correction

As previously discussed, a sound signal propagating through non-dispersive space will introduce a phase change that is linearly related to frequency, thus yielding a flat group delay (Brillouin, 1960). In this situation, removal of the appropriate linear phase term uncovers the phase response due to the process under test. In some cases, exact spatial correspondence may not be important, as delay is introduced in order to express signals relative to an specific reference point (Humphrey et al., 2008). However, other applications are concerned with determining the "true acoustic position" (Heyser, 1984) of a system. Removal of the linear phase propagation factor can be complicated, particularly in the cases where the exact distance has to be known. Furthermore, accumulated phase is most often 'wrapped', that is, constrained within the values of $-\pi$ to π. This is due to the definition, which includes the arctangent function, such as the phase of a complex signal, $S(\omega)$, is

$$\varphi(\omega) = \tan^{-1}\left[\frac{\mathrm{Im}(S(\omega))}{\mathrm{Re}(S(\omega))}\right], \tag{3.21}$$

with the ratio of the imaginary, Im, and real , Re, components. However, the true values are not limited to this interval.

3.4.2 Phase unwrapping

Wrapped phase presents drastic jumps, usually resulting in a saw tooth appearance (Lyon, 1983). This form is awkward to manipulate and, more importantly, to interpret. For this reason, unwrapping algorithms, which revert this format, are used in various applications in order to smooth phase plots. Wrapping discontinuities have been referred as "extrinsic" since they originate in the processing, and do not belong to the signal itself (Paraskevas and Chilton, 2004). Phase unwrapping is a challenging tasks in signal processing, and a large number of publications have been dedicated to it (Gdeisat and Lilley, 2011). In the case of target echo phase, the usual obstacles, such as noise and low frequency resolution, are present. These issues are known to cause spurious phase jumps which confuse the unwrapping process and add ambiguity. Furthermore, unwrapping is an accumulative operation in which a single error, carried over the entire domain, can produce a drastically different result. For this work, a simple approach was adopted, using the Matlab 'unwrap' function, in line with other investigations of target phase in sonar (Mitri et al., 2008). This function is a conventional, one-dimensional phase unwrapper, which adds a factor of $\pm 2\pi$ when adjacent array elements have a phase difference larger than π radians. An example of a wrapped and unwrapped phase using this function is presented in Fig. 3.1.

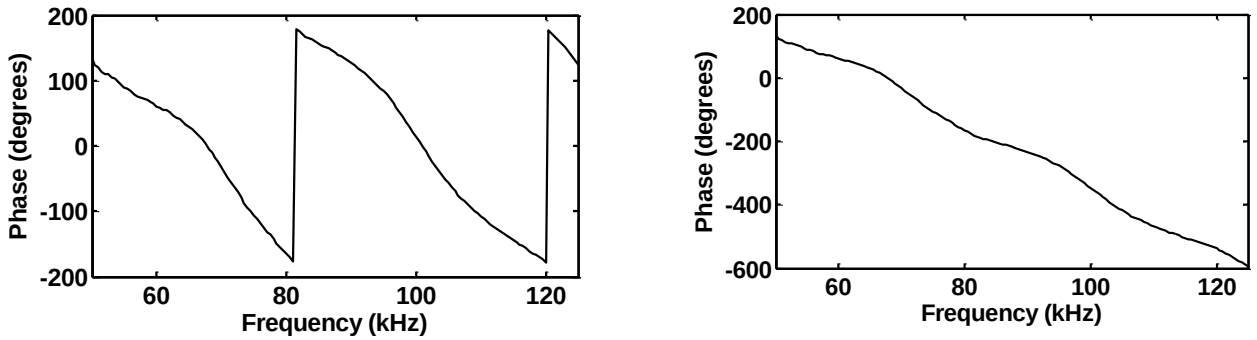

Figure 3.1. Wrapped (left) and unwrapped (right) phase.

3.4.3 Rate-of-change of phase

Examination of the rate-of-change of phase is also a viable option to uncover target-induced shifts. As previously discussed, the phase of a signal propagating in a non-dispersive medium is linear with respect to frequency. A derivate operation, then, removes the linear slope caused by propagation and the residual phase variation is attributable to the target. This has been used to uncover or highlight echo formation mechanisms in elastic scattering (Mitri et al., 2008, Yen et al., 1990). It was also mentioned how the rate-of-change of phase against time has served as a feature for fish species classification (Barr and Coombs, 2005). In radar, rate-of-change of phase against frequency, with constant time and position, can be used as an indication of target range (Skolnik, 1962).

3.4.4 Dual-frequency transmissions

The concept of transmitting dual or multiple frequencies in order to account for range ambiguities in phase information has found applications in ranging techniques, as discussed previously. Target phase can be calculated from the relative backscattered phases of a transmission pulse, v_t , composed of two frequencies, a lower f_1, and a higher $f_2 = \mu f_1$, expressed in the time domain as (P. R. Atkins et al., 2007a)

$$v_t = \frac{V_{\max}}{2}\cos\left(2\pi f_1 t\right) + \frac{V_{\max}}{2}\cos\left(2\pi\mu f_1 t\right), \tag{3.22}$$

where t is time, and V_{max} is the maximum amplitude of the voltage applied to the transducer. The spectral separation factor μ is usually defined as a ratio of integers such as

$$\mu = \frac{N}{M}, \tag{3.23}$$

where N and M are small, typically within the range of 1-10, and N > M so that $\mu > 1$.

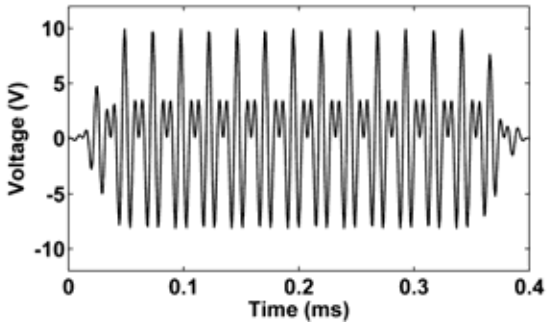

FIG. 3.2. Dual-frequency pulse, p_t, with frequency components f_1 = 82 kHz and f_2 = 123 kHz.

Range dependencies are cancelled following the method of (P. R. Atkins et al., 2007a). After the received echo is windowed in time, sub-band correlators isolate the two frequency components to be compared, p_{r1} corresponding to the lower frequency and p_{r2} to the higher frequency. This pair of complex-valued components can be expressed as

$$p_{r1} = P_{r1} e^{j(k_1 R + \varphi_1)}, \tag{3.24}$$

$$p_{r2} = P_{r2} e^{j(k_2 R + \varphi_2)}, \tag{3.25}$$

where φ_1 *and* φ_2 are the target phases at each frequency, R is the range from the transmitter to the target, P_{r1} and P_{r2} are the peak received pressures, and k_1 and k_2 are the wave numbers in the water. In practice, this results in two receiver channels centered on frequencies separated

by the factor μ, as exemplified in Fig. 3.3 for the case of the pulse presented in Fig. 3.2 (f_1 = 82 kHz and f_2 = 123 kHz). The bandwidth of the signals will be determined by the amplitude weighting function applied to the transmission signal whilst the amplitudes will be influenced by the variations of the form function as the desired calibration bandwidth is covered with a series of stepped-frequency transmission pulses. In parallel to the processing of the measured data, the predicted phase response is calculated using the Goodman and Stern (Goodman and Stern, 1962) model.

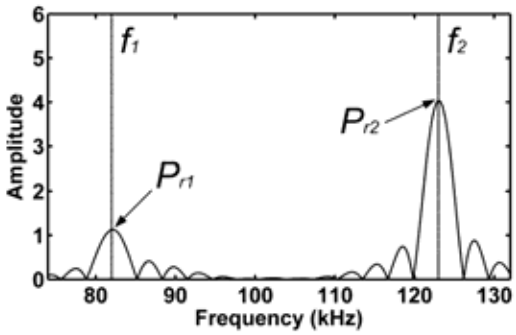

FIG. 3.3. Spectral magnitude components of a received echo from a 30-mm-diameter tungsten carbide sphere insonified by a dual-frequency pulse composed by f_1 = 82 kHz and f_2 = 123 kHz (spectral separation μ = 3/2 = 1.5).

The next step in the determination of target phase is to scale the lower frequency component by μ and multiply it by the complex conjugate of the higher frequency component, such as

$$p_{r1scaled}\, p_{r2}^{*} = P_{r1}^{\mu} P_{r2} e^{j\mu(k_1 R+\varphi_1)} e^{-j(k_2 R+\varphi_2)}, \tag{3.26}$$

$$p_{r1scaled}\, p_{r2}^{*} = P_{r1}^{\mu} P_{r2} e^{j(\mu\varphi_1-\varphi_2)}. \tag{3.27}$$

With this mathematical manipulation the range factor R is removed and a phase difference term, scaled by μ and corresponding solely to the target remains, such that

$$angle\left(p_{r1scaled}\, p_{r2}^{*} \right) = \mu\varphi_1 - \varphi_2 = \frac{N\varphi_1 - M\varphi_2}{M}, \tag{3.28}$$

where the "angle" operator yields a phase angle defined in the four quadrants In the case of an ideal point scatters (as in the equations in (P. R. Atkins et al., 2007a)), this results in the elimination of the separation factor from the resulting expression.

4 SYSTEM DESIGN AND EXPERIMENTAL METHODS

This chapter details the design and construction of a sonar platform capable of measuring target phase reliably. Operational settings and experimental conditions for water tank monostatic acoustic measurements are described. Data processing methods are described.

4.1 Sonar system overview

Sonar measurements were performed in the far-field region, under free-field conditions, i.e., assuming the medium to be homogeneous, isotropic, and boundless (Bobber, 1970). However, these conditions are not fully attainable in realistic situations, particularly in a reverberant water tank laboratory. Measures were taken in order to best approximate free-field conditions, as described below. All experiments were performed in the water tank at the University of Birmingham, with concrete walls and dimensions of 8.48 m in length, 3.95 m in width and 3.04 m in depth. The transducer was a TC-2130 piezoelectric transducer (Reson, Slangerup, Denmark), used as both transmitter and receiver, in a duplexed mode. Maximum hydrophone and projector sensitivities at 104 kHz were -182 dB re 1V/μPa and 157 dB re 1μPa/V respectively. The beam width in both planes is approximately 30°. A data acquisition card was used to convert the transmit pulses generated in Matlab into analogue waveforms, and to digitize the received backscattered echoes. The chosen kit was the National Instruments M-series 6251 model (National Instruments, Austin, TX), which has eight differential 16-bit analogue inputs, with a sampling rate of 1.25 MS/s on a single-channel, two 16-bit analogue outputs, and twenty four digital I/Os.

Pulses were generated and captured through a MATLAB (The Mathworks, Natick, USA) script, interfaced to the data acquisition card through the NI-DAQmx software. Signal generation and acquisition tasks were synchronized with internal clock signals. Two additional analog input channel were set up for recording battery voltage. Besides the analog channels, digital lines were configured for duplexing and motor control. The sampling frequency was 1.25 MHz with 2^{14} samples per channel (transmit and receive), yielding a total collection time of around 13 ms. The maximum dynamic range of the analog input channel was set in software in a flexible manner. For smaller targets (e.g. 15, 20, and 30 mm tungsten carbide spheres), a range of ±0.20 V was enough to capture the echoes without clipping. For larger sizes ranges of ±0.50 V and ±1.0 V were selected. A maximum voltage, V_{max}, of 10 V was sent from the digital to analog converter into the transmitter amplifier (gain ~ 3x).

Amplifiers, low-pass filters and a RX/TX switch control were custom-built, with the main aim of enhancing noise performance. Transmit and receive circuitry were designed to be fully differential. The differential amplifier in the return path (low-level signal) was battery-powered in order to avoid power-line noise. Four 12 V lead acid, deep cycle batteries, RT12120 (Ritar Power, Shenzhen, China), provided stable +12 V and -12 V voltage references using linear regulators. The experimental and hardware configurations are depicted in Figs. 4.1 and 4.2 respectively. More detailed design notes and system descriptions are given in the Appendix.

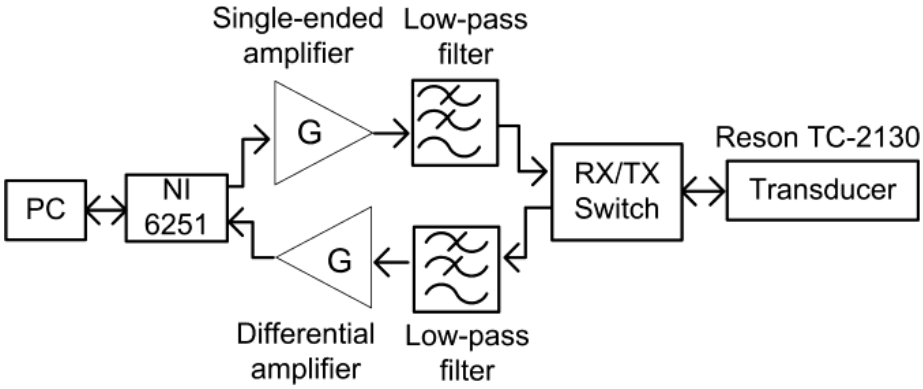

FIG. 4.1. Schematic of the complete electrical system. Signal generation and data acquisition operations are both performed through the NI 6251 data acquisition card. The sonar signal flow was controlled with the RX/TX switch, with logic signals also sent from the NI 6251. Amplifiers and filters were optimized for low-noise performance.

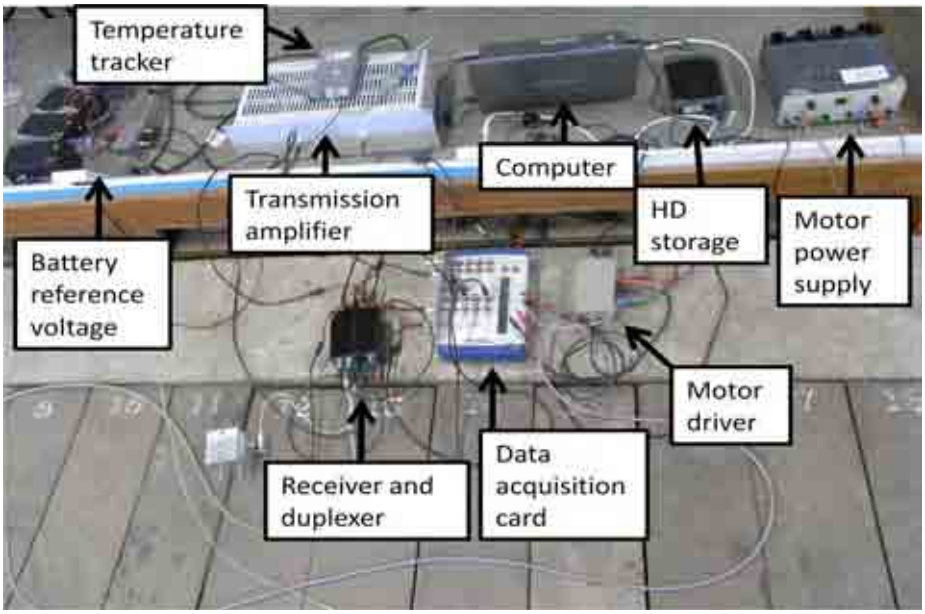

FIG. 4.2. Sonar system hardware and supporting electronics

4.2 Static target suspension

Targets were suspended with braided fishing lines made from high-modulus polyethylene fibres (Pure Fishing, Spirit Lake, IA) which exhibit minimum stretch, in order to prevent elongation and thus guaranteeing a stable depth position. They were attached to an XY table (spheres and shells) or the rotation device (cylinders and spheroid) for alignment within the main acoustic lobe. This was a substantial improvement from the previously used nylon strings, whose length was measured to change as much as 18 mm after being taken out from the water for about 12 hours, probably caused by water adsorption. To maintain strict equivalence in string length among the different targets, corrections were performed with the adjustment screw and verified prior to every trial. The suspension rig is shown in Fig. 4.3.

FIG. 4.3. Target suspension rig mounted on the X-Y table.

The minute impact of the supporting net on the backscattering was disregarded, in the same manner as Feuillade et al., due to its low target strength and the fact that when spread over the sphere it presents a rather diffuse target (Feuillade et al., 2002a). Further confirmation of this assumption can be found in the work of Welsby and Goddard, who investigated and compared the effects of various sphere supporting schemes, arriving to the conclusion that the presence of bubbles on the material can be most influential in modifying target strength (V. G.

Welsby and Goddard, 1973). The effect of bubbles is particularly strong for acoustic measurements of fish in a water tank. If the specimen is exposed, air can be attached to the skin or become trapped in the gills, even dominating the scattering, as reported by (Nesse et al., 2009). More recently these notions have been revisited (Hobæk and Nesse, 2006). The impact of bubbles in metallic spheres and cylinders was also observed, and targets were submerged for as a long as a week in order to ensure dissolution. They estimated that the influence of a nylon supporting net could be important, especially situations where the target is seen from the side. In this respect, scattering variations were observed upon rotation of a sphere, which were reduced with a thinner nylon stocking support. In the case of the present work, the thin fibres used were expected to induce less aspect-dependant variation. However, the remaining effects of the support net, particularly caused by knots, is not known accurately and is subject for further investigation.

4.3 Acoustic beam localization

The experimental procedure follows the accepted practice of supporting a standard-target within the main-lobe of the transducer (K.G. Foote et al., 1987). From the directivity characteristics of the transducer it follows that parting from the transducer axis will affect the amplitude and phase of the received voltage (Han Zhang et al., 1998). The centring of the target can be achieved by careful mechanical or optical alignment as done in the experimental settings of Neubauer *et al.* (Neubauer et al., 1974), yet this method does not comprise the system as a whole, excluding the effect of the transmitter and receiver electronics. Therefore, the directional properties of the complete system, or effective directivity characteristics (Bamber and Phelps, 1977), were obtained by moving a target across the acoustic field and thus delineating its three dimensional shape as a function of position and echo amplitude.

This approach ensures that the artefacts of the equipment are taken into account in real-time when the beam is profiled. An X-Y table, shown in Fig. 4.4, was controlled through RS-232 communication, positioning the target in 5 mm steps, at right angles to transducer beam axis. An linear frequency modulated pulse (LFM) was used for insonification, with the backscattered signal matched filtered, and the target strength calculated for each location. The resulting 3D representation of the acoustic beam is presented in Fig. 4.5.

FIG. 4.4. Left, X-Y table control display. Right, X-Y table and supporting frame.

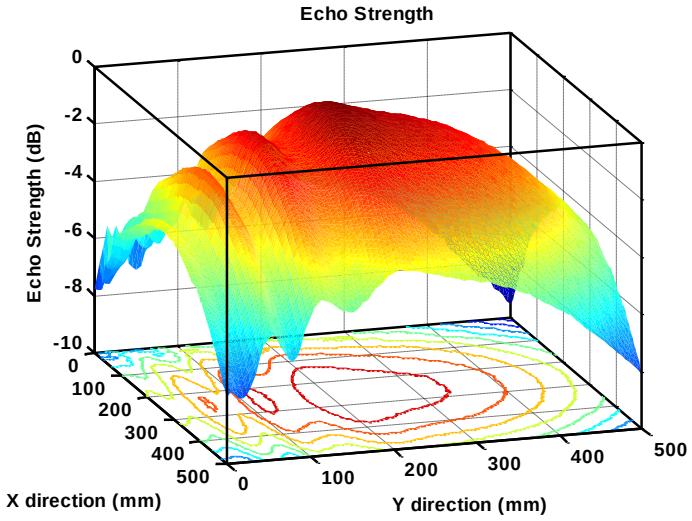

FIG 4.5. Transmit-receive beam characteristic obtained by scanning a 20 mm target sphere through the field at a range of 2.17 m. Vertical axis is the (normalised) echo strength measured from the peak amplitude of the matched filter output for a LFM transmission.

4.4 Target rotation

In order to study the effects of target orientation, a rotation system was built. A stepper motor with a 1.8° angular resolution was attached to a rotating arm and controlled digitally from the NI-6251 data acquisition card, allowing for position control during measurements. The mechanical system is shown in Fig. 4.6, with more design details included in Appendix A.5.

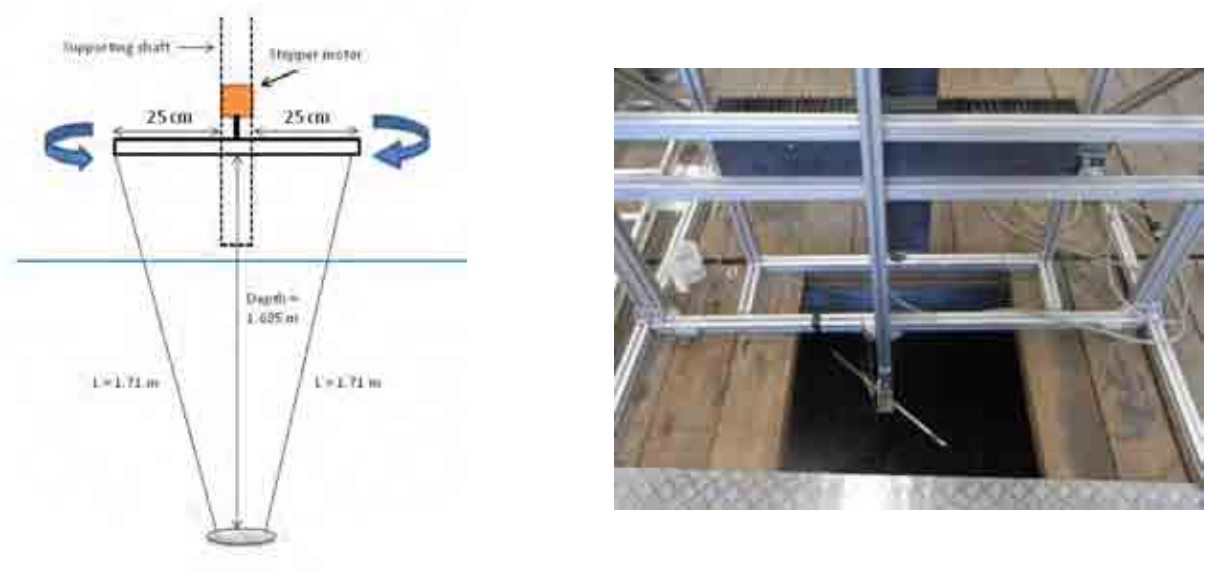

FIG. 4.6 Suspension system for rotation of targets.

Schematic diagram (Left). Picture of rotation device attached to the XY table frame (Right).

Stabilization periods were allowed after initial immersion, and after each arc segment was completed. The rotation stabilization period was of the order of minutes, depending on the arc length performed. Targets (cylinders and a prolate spheroid) were supported with string loops from the ends Although the strings were measured to be equal, slight differences could have potentially remained, introducing an unwanted tilt in the horizontal plane (normal to the bottom). Visual verification was attempted after immersion, but this was prone to parallax errors. Optimally, validation could be implemented by properly-aligned underwater cameras or laser rangers. For the purposes of this work, the described system was deemed sufficient.

4.5 Reverberation

As a case of room acoustics, test tanks are usually marked by reverberation, which is akin to a diffuse noise field (Piersol, 1981), formed by the multiplicity of echoes returned from the boundaries. Adoption of an anechoic underwater chamber is often not viable due to costs or difficulties in refurbishing existing facilities. An initial approach for reverberation reduction was to record the signals without the target being present, for post-processing coherent subtraction. Substantial improvement was achieved, but destructive and constructive interaction of remaining multi-paths was enough to cause oscillatory distortions. A second approach was to encase the transducer in a frame padded with polyurethane acoustic absorber tiles (Applied Polymer Technology Limited, Ross On Wye, United Kingdom). According to the manufacturer, each tile would provide a typical fractional power loss of around 80%. Individual tiles, 30 mm thick and with an area of 305 mm squared, were attached to the isolating cage, as pictured in Figs. 4.7 and 4.8, resulting in an overall reverberation reduction of approximately 40 dB within the measurement range window. Furthermore, transmitter and targets were located midway from any boundary in the tank, as depicted in Fig. 4.9 and 4.10.

FIG. 4.7. Sound absorbing frame.

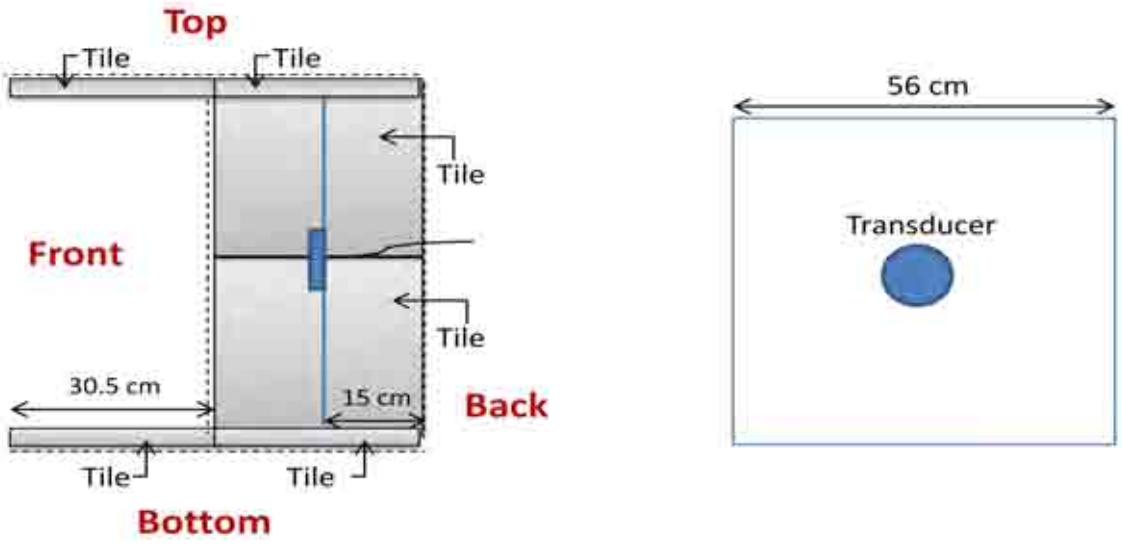

FIG. 4.8. Left, side view drawing of absorbing frame. Right, transducer mounting plate.

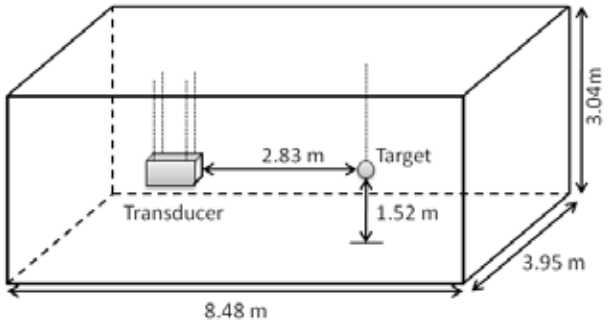

FIG. 4.9. Schematic location of transducer and a spherical target, as used during calibration.

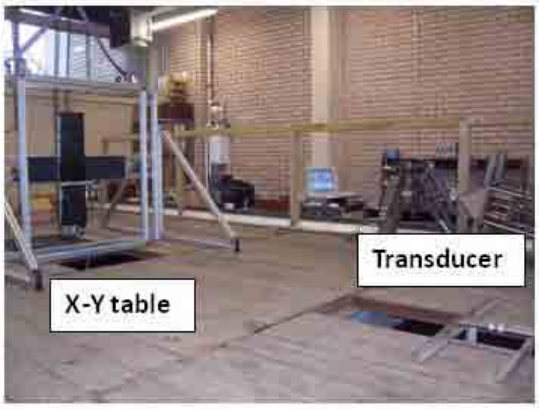

FIG. 4.10. X-Y table and transducer arrangement in the laboratory tank.

4.6 Immersion medium characteristics

4.6.1 Water salinity

Salinity, expressed in oceanography as grams/Litre (g/L) or parts per thousand (ppt), can be loosely defined as the amount of salts dissolved in a given volume of water, or more precisely, the inorganic matter without halogens in 1 kg of water (McCutcheon et al., 1993). This quantity, whose fluctuations are subject to a complex interaction of natural and artificial processes, is one of the main descriptors in hydrological studies. In this respect, the tap water contained in the laboratory tank can be classified as "fresh," since it falls inside the salinity range of rivers, streams and some lakes. Since salts dissolved in the water are major contributors of charged particles, there is a direct connection between electrical conductivity and salinity. For the world oceans, this relationship has been established by the Practical Salinity Scale (PSS) 1978, an international scale, referenced to the composition of standard seawater. However, no such definition exists for fresh water, and the determination of salinity is nuanced by disparities in chemical composition. Acknowledging the lack of a firm equivalence between electrical conductivity and dissolved salts, conductivity itself, in units of μs/cm, often suffices as a direct indicator of ion concentrations in fresh water. However, to aid consistency and account for temperature dependence, it is advised to use the specific conductance, a value corrected to a reference temperature of 25 ℃ (Radtke et al., 2005). Conductivity meters can also incorporate automatic conversion features. For this work, a Mettler-Toledo (Mettler-Toledo Ltd., Leicester, UK) S30 meter (accuracy of ±0.5%), was used to measure the conductivity of eight water samples obtained from different locations in the tank using a plastic pipette. This yielded an average conductivity value of 166.30 μS/cm, and salinity of 0.11 ppt.

4.6.2 Temperature

The volume contained in the water tank (over 100,000 litres) will constrict or at least slow down temperature changes over time, rendering the laboratory tank thermal properties relatively constant. Temperature was monitored with a platinum resistor sensor connected to a Tracker 220 (TMS Europe, Bradwell, United Kingdom) that specifies an uncertainty of ±0.075 °C. The temperature tracking device was connected to the computer, a Toshiba laptop, through serial communication using a Dynex DX-UBDB9 USB-serial adapter (Dynex, Richfield, USA). The temperature was recorded at every frequency step, for a stepped-up procedure, and stored together with its associated backscattering data. The temperature values were used in the calculation of the sound speed in the water, which is in turn an input to the Goodman and Stern computer model, as introduced in Section 2.4.5. This ensured that the modelled form function corresponded to prevailing experimental conditions.

4.6.3 Density

Density was calculated as a function of temperature, T_{emp}, in ℃, and salinity, S, in ppt, which are the independent parameters. Density, ρ, is given in kg/m^3 such as (McCutcheon et al., 1993)

$$\rho(T_{emp}) = 1000\left[\frac{1-\left(T_{emp}+288.9414\right)}{508929.2\left(T_{emp}+68.12963\right)\left(T_{emp}-3.9863\right)^2}\right], \tag{4.1}$$

and

$$\rho(T_{emp}, S) = \rho(T_{emp}) + \mathrm{A}S + \mathrm{B}S^{3/2} + \mathrm{C}S^2, \tag{4.2}$$

with

$$A = 8.24493x10^{-1} - (4.0899x10^{-3})T_{emp} + (7.6438x10^{-5})T_{emp}{}^{2} - (8.2467x10^{-7})T_{emp}{}^{3} + (5.3675x10^{-9})T_{emp}{}^{4}$$

$$B = -5.724x10^{-3} + (1.0227x10^{-4})T_{emp} - (1.654x10^{-6})T_{emp}{}^{2}$$

$$C = 4.831x10^{-4}.$$

If salinity is fixed at 0.11 ppt and temperature is varied over the relevant range, the resulting variation in density is only of about 1.5 kg/m^3, or 0.15%, shown in 4.11.

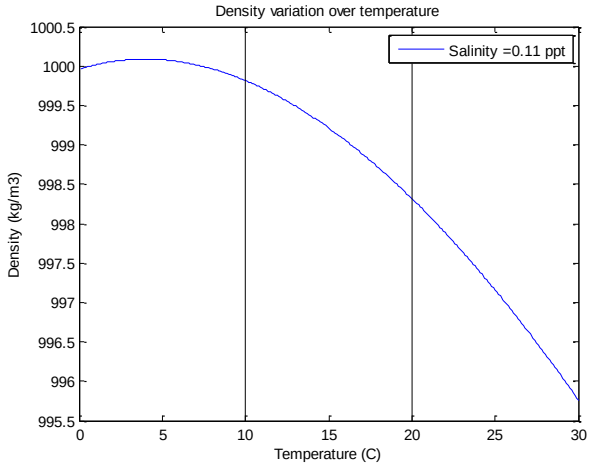

FIG. 4.11. Density variation as a function of temperature calculated using Eq. 4.2 for a salinity of 0.11 ppt.

4.6.4 Sound speed

The velocity of sound waves in water has an effect on the backscattering form function. Inaccuracies in sonar calibration can be in part ascribed to the incorrect estimation of its value (Miyanohana et al., 1993). In order to compute the speed of sound from salinity and temperature, the UNESCO equation (Fofonoff and Millard Jr., 1983) was used. This expression has been recently corrected in its lower salinity region by (Leroy et al., 2008), to include fresh water, and therefore it was adopted in the present work.

4.7 Data processing methods

4.7.1 Transmission signals

In general two measurement methods were used, based on two types of transmission signals, narrowband stepped-frequency continuous waves, and broadband chirps.

4.7.2 Stepped dual-frequency transmissions

A steady-state regime (Neubauer et al., 1974) was approximated with sinusoidal bursts of 400 μsec duration, corresponding to a pulse length in the water of about 0.59 m, much larger than the spheres' diameter. This procedure is slower but has better noise performance due to the higher energy of the transmitted signal at a given frequency. Backscattering measurements were taken in the frequency range of 50 to 150 kHz, with frequency steps ranging from 10 Hz to 1000 Hz, but most usually 500 Hz. In order to improve the SNR of the received signal, 50 pings were averaged in time. The transmission signal consisted of two sinusoidals at different frequencies. These dual-frequency signals were used for phase calibration, as will be detailed in the following chapter.

4.7.3 Linear-frequency modulated (LFM) chirps

The second method was to transmit short broadband pulses, namely an LFM chirps, shown in Fig. 4.12. This was faster but poorer in noise performance. However, these signals provided enhanced time resolution, in conjunction with a pulse-compression technique. This is explained in more detail in Appendix A.3.

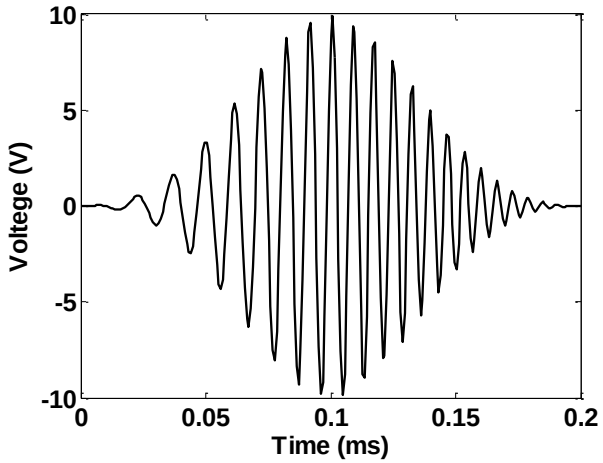

FIG. 4.12. LFM transmitted chirp. Frequency range from 50 to 180 kHz.

4.7.4 Receiver processing

For each transmitted signal, the received, time-averaged echo, $p_r(t)$, was extracted from the raw data by means of a Tukey window (taper-to-constant ratio = 0.39) in order to ameliorate truncation effects due to gating. This is depicted in Fig. 4.13, where the window (in red) is scaled down. The multiplication of the entire received time series with the window function is then Fourier transformed, resulting in the echo spectrum $P_r(\omega)$. Discrete Fourier transforms used the Matlab 'fft' function and were performed with 125000 points for a frequency resolution of 10 Hz. Windowing and subsequent frequency-domain are repeated for each frequency bin in the continuous wave, stepped-frequency case, whilst for the broadband case a single echo yields the entire relevant bandwidth. In general, the processor is structured as a correlation receiver or replica correlator, shown in schematic form in Fig. 4.14.

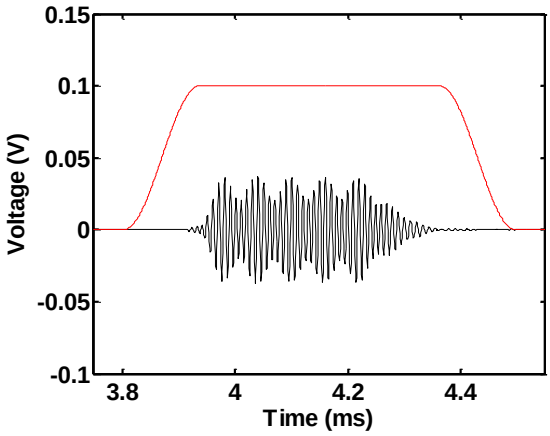

FIG. 4.13. Received echo windowing.

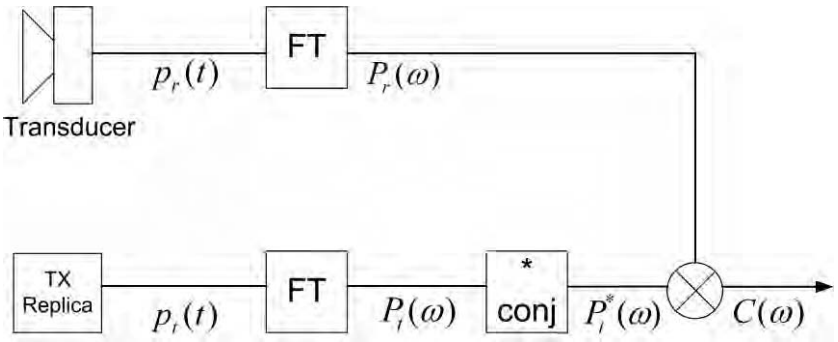

FIG. 4.14. Receiver matched filter processing.

The digital transmission signal, $p_t(t)$, serves as the replica. Cross-correlation spectrum, $C(\omega)$, is obtained by multiplying the complex conjugate of the replica spectrum, $P_t(\omega)$, with the received echo spectrum $P_r(\omega)$. This is a non-ideal matched filter that produces a compressed pulse (Dezhang Chu and Stanton, 1998), used for time-domain representation. In order to achieve this, the output of the correlator is converted into the time domain by means of an inverse Fourier transform, such as,

$$c_{cp}(t) = \Im^{-1}\{C(\omega)\}. \tag{4.3}$$

Then the matched filter or compressed pulse envelope, $c_{env}(t)$, is computed through the absolute value of its analytic function, obtained through the Hilbert transform, such as (W.W. L. Au and Benoit-Bird, 2003)

$$c_{env}(t) = \left| Hilbert\left(c_{cp}(t)\right)\right|. \tag{4.4}$$

Since the analytic signal magnitude is related to the rate of energy arrival (Gammell, 1981) this representation is most suitable for visualizing distinct echo contributions in the time domain.

5 STANDARD-TARGET CALIBRATION METHOD

The implementation of the well-established method of standard-target sonar calibration is described. Broadband amplitude calibration results are presented. The accuracy and repeatability of the procedure are explored, along with the error sources potentially degrading its outcome. Particularly, variability induced by the standard-targets is examined, with detailed tests on the material composition of tungsten carbide spheres.

Sonar, as a measurement instrument, requires system calibration in order ensure correctness and adherence to accepted international standards. Furthermore, before the physical significance of target echoes can be successfully interpreted, it is imperative to address the effects of the entire sonar system including both the transducer and the electronic components. A calibration process that accounts for amplitude and phase is required in order to ensure accurate and valid measurements (P. R. Atkins et al., 2007a, P. R. Atkins et al., 2007b, Barr and Coombs, 2005). In fisheries research and acoustical oceanography, the standard-target sonar calibration method (K.G. Foote et al., 1987) is well-established, but in its current implementation it does not consider phase, examining only the scattering amplitude of the reference target. This primary calibration method is also fundamentally based on a deconvolution operation, using a calculation of the acoustic backscattering from an standard target as the reference. This computation is obtained from a theoretical model based upon full-wave analysis solutions (Kenneth G. Foote, 1982, Stanton and Chu, 2008), initially developed by Faran (Faran, 1951) and Hickling (Robert Hickling, 1962b), and restated correctly by Goodman and Stern (Goodman and Stern, 1962). This modal solution for

spheres was mentioned in Section 2.4.5. The acoustic form function is deconvolved from the measured signal either in the time domain (Feuillade et al., 2002b) or with a complex division in the frequency domain (Stanton and Chu, 2008). The standard-target method permits the determination of the complete system response, without incurring in the additional uncertainties associated with the use of a reference hydrophone. The importance of the integral system, black box approach is emphasized, since a separate characterization of components (as in the hydrophone calibration schemes reviewed above) could lead to error compounding (K. G. Foote et al., 2007). This procedure is routinely implemented before sonar measurements, with spherical reference targets usually made from electrolytic-grade copper, aluminium alloys or tungsten carbide. It has been successfully adapted for *in situ* implementation on board scientific vessels, as illustrated in Fig. 5.1, as well as for multibeam (Kenneth G. Foote et al., 2005, Ona et al., 2009) and parametric sonar systems (K. G. Foote et al., 2007).

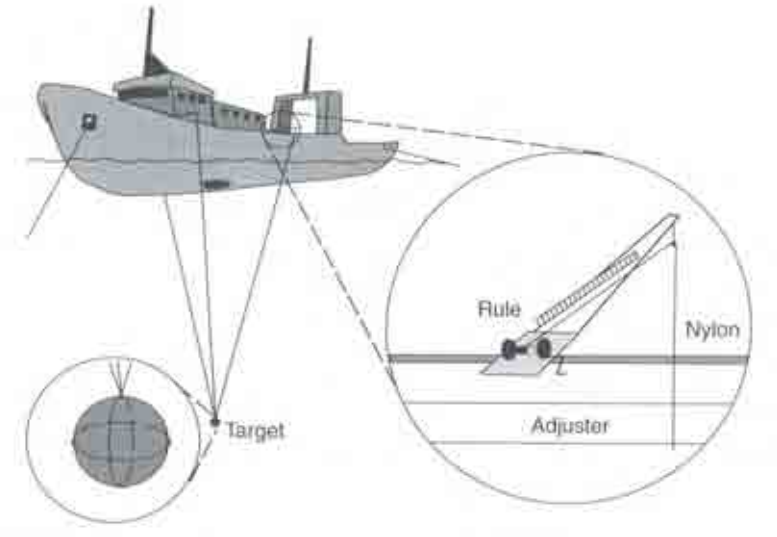

FIG. 5.1. Target support for standard-target calibration on board a vessel (From (Foote, 1983b) and (J. Simmonds and MacLennan, 2005)).

5.1 Standard-target calibration accuracy

Performance and accuracy of system calibration impacts directly on the accuracy and validity of sonar measurements. For this reason, efforts have been made to identify and reduce specific sources of ambiguity. Foote established that an accuracy level of 0.1 dB is attainable for narrow band calibration (Foote, 1982), with careful consideration of the variability factors involved. In this context, the first concern is selection of the most suitable standard-target. For this purpose, tungsten carbide spheres have been advanced as high-quality targets, mainly due to their hardness, robustness and corrosion resistance (Kenneth G. Foote and MacLennan, 1984, MacLennan and Dunn, 1984). These spheres are built as ball bearings (Spheric Trafalgar, Ashington, United Kingdom) with high standard specifications, and usually contain 6% cobalt, which serves as binder in the sintering process. Tungsten carbide spheres with 6% cobalt will be labelled with the abbreviation 'TC/Co.'

For this work, calibrations in the frequency range from 50 to 125 kHz were performed using small tungsten carbide spheres, most often 20 mm or 22 mm in diameter. An even smaller sphere of 15 mm in diameter was not favoured because it TS is significantly below the optimal value of -40 dB (K. G. Foote, 1990). This choice is consistent with the preference for targets devoid of elastic resonances in the frequency range. It has been advanced that the resonances pose the most serious challenge for the maintaining accuracy, due to the rapid variations in the backscattered signal characteristics, manifested as a series of deep nulls along the frequency axis. However, it is acknowledged that for larger bandwidths this is not feasible and some resonances will be present. Therefore, in order to minimize their detrimental effects, the idea of separating the specular and resonant parts in the echo has been developed (Dragonette et al., 1981, Stanton and Chu, 2008), as well as the use of the joint

response of multiple spheres (Philip R. Atkins et al., 2008a). In both approaches sensitivity to resonances is reduced. Alternatively, multiple spheres can be used separately in order to cover different discrete frequencies or span a continuous band (K. G. Foote, 1990, Miyanohana et al., 1993). Nesse *et. al.* adopted a more direct approach, manually removing resonant notches from the data and replacing them with bridging lines (Nesse et al., 2009). In contrast, the acoustics of the targets used for calibration were determined by their rigid response, largely insensitive to material parameters. In order to evaluate calibration precision a second set of acoustic measurements was performed after the system response was extracted. This also allowed for examination of the role of material parameters. Agreement between measured and modelled TS is presented in Fig. 5.2, for the case of TC/Co spheres exhibiting rigid behaviour.

For amplitude calibration, the procedure closely follows accepted practice as described publications by Foote (Kenneth G. Foote, 1983b) and many other workers in the field. More details are presented in the following chapter, when the extension to include the phase response is introduced. Although both amplitude and phase are obtained in parallel, they are presented separately for clarity. The error was estimated from the difference between the measured and modelled responses, using RMS values calculated for the entire bandwidth.

5.1.1 Rigid response

Modelled and measured TS plots for smaller TC/Co spheres exhibiting rigid scattering are shown in Fig. 5.2. RMS errors were calculated from differences between measured and modelled TS plots in dB. These errors were approximately 0.32 dB for the 15 mm sphere, 0.14 dB for the 20 mm, 0.20 dB for the 22 mm and the 25 mm. It is clear that the lower TS of the 15 mm warrants a higher error. The best agreement is found for the 20 mm sphere, which was the same sphere used to extract the system response applied in the results of Fig. 5.2. This is due to reduced variability factors. The reported values are comparable to the potential, narrow-band, accuracy of 0.1 dB (Kenneth G. Foote, 1983b). Other broadband agreement results reported in the literature are similar. For example, Nesse *et al.* estimated an RMS error of 0.12 dB across a bandwidth of 165 kHz, also using a 22-mm-diameter TC sphere, although with a frequency resolution of 1 kHz (Nesse et al., 2009), while a 500 Hz step was used in for the results of Fig. 5.2. However, addition of random errors after repeated measurements resulted in a total RMS error of ±2.3 dB in the case of Nesse, much larger than our corresponding error estimation.

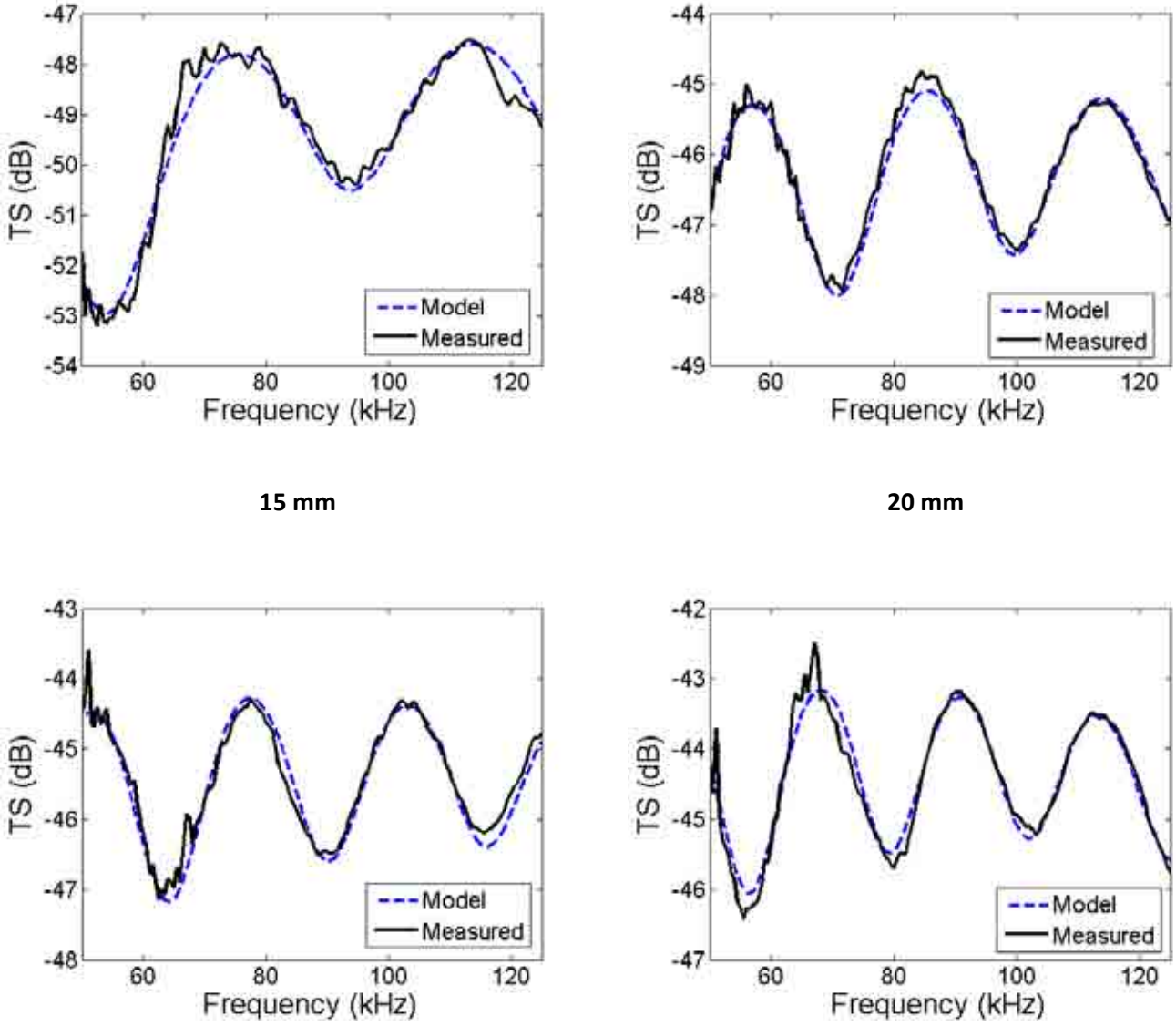

FIG. 5.2. Modelled and measured TS for tungsten carbide spheres with 6% cobalt binder.

Sphere diameter is indicated below each panel.

5.1.2 Elastic response

Spheres exhibiting at least one elastic resonance are presented in Fig. 5.3. As discussed in Section 2.4.2 elastic resonances excited by the incident pressure wave are determined by the dimensions and composition of the object. Since the diameter is known with high precision, lack of agreement with predicted resonance locations is mostly due to the lack of knowledge concerning the exact composition of the spheres. In order to obtain the best agreement, the elastic parameters were optimized through a multivariate minimization routine.

Table 5.1. Tungsten carbide spheres density measurements.
Values from manufacturer's specifications given on the top of each column.

Sphere diameter (mm)	**Density (kg/m^3)**	
	Cobalt binder (Spec.=14947)	**Nickel binder** (Spec.=14968)
15 mm	14936	15005
20 mm (A)	14932	---
20 mm (B)	14963	---
20 mm (C)	14956	---
22 mm	14931	14989
24 mm	14954	15039
25 mm	14862	---
30 mm	14925	15022
40 mm	14907	---
50 mm	14892	---

The nominal values that served as starting point were those given by MacLennan (MacLennan and Dunn, 1984) in terms of density (14900 kg/m^3), longitudinal (compressional), C_L = 6853 ± 19 m/s, and transverse (shear), C_T = 4171 ± 7 m/s, wave speeds in the solid. Density was measured for every sphere with a mass less than the maximum capacity of the available scales. For spheres with less than 210 g a Sartorius A210P (Sartorius, Goettingen, Germany) electronic scale was used, which reports a standard deviation of ±0.0001 g. For heavier spheres the following weighting instruments were available, Ohaus GT480 (Ohaus, Norfolk, United Kingdom), PM600 and PM3000 (Mettler-Toledo, Columbus, USA). Besides the tungsten carbide spheres with cobalt binder, spheres with nickel binder were also purchased. Density measurements for both types are given in Table 5.1 (rounded to the closest integer). Although all the balls share a common manufacturer, density deviations are clear, with the a mean value of the cobalt binder case of 14926 kg/m^3 and a standard deviation of 31 kg/m^3. Composition variability and deviation will be examined more closely in the next section.

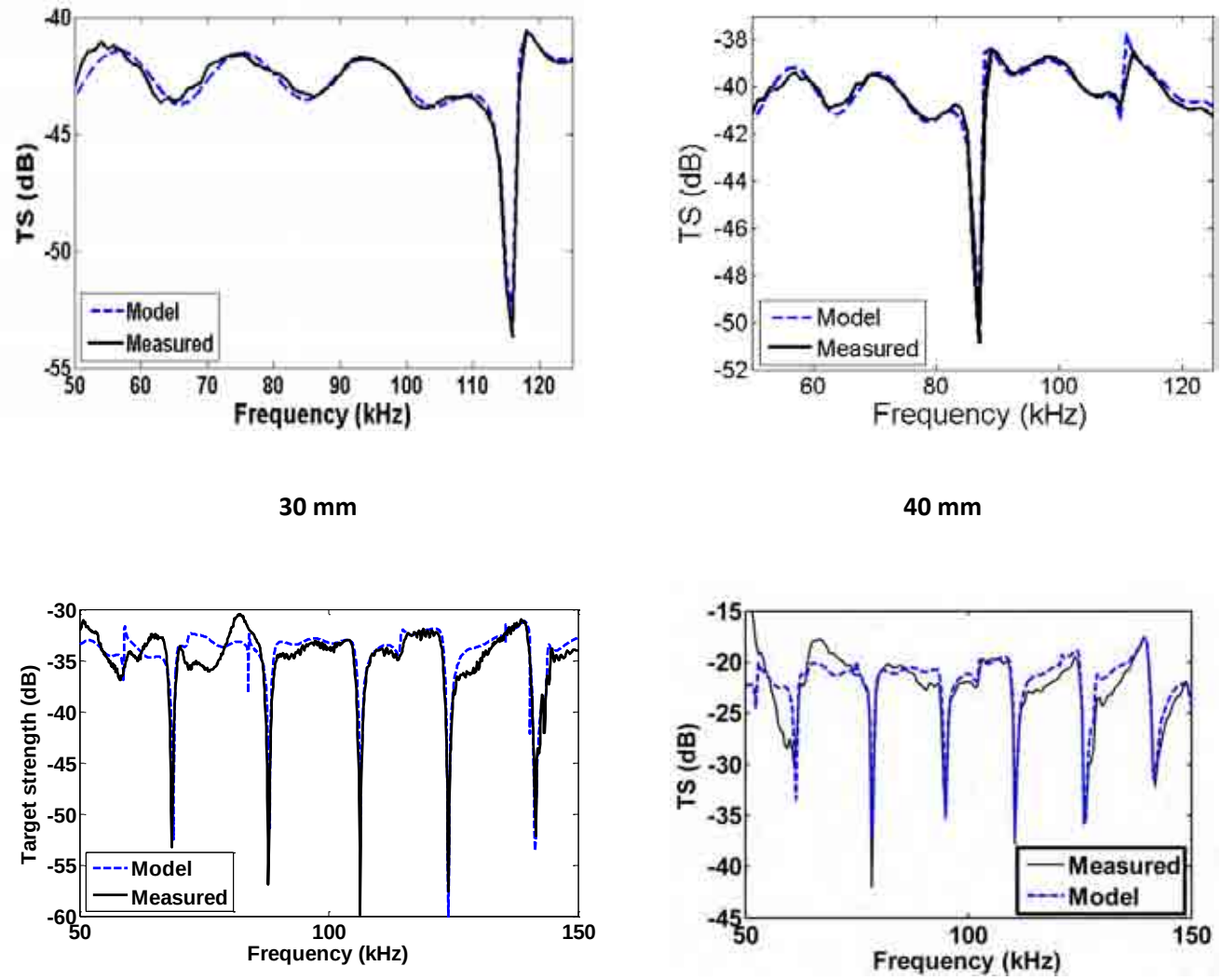

FIG. 5.3. Modelled and measured TS for tungsten carbide spheres with 6% cobalt binder. Sphere diameter is indicated below each panel.

As expected, the agreement RMS error corresponding to the plots in Fig. 5.3 was much larger. The parameters used for the 30 and 40 mm modelling are presented in Table 5.2. For the larger spheres, where density measurements were not possible, nominal values were used. The error for the 30 mm sphere, with a single resonance is 0.37 dB, for the 40 mm sphere 0.40 dB and

for the 75 mm, measured up to 150 kHz and containing several resonances 1.76 dB. Optimisation was achieved with the alignment of the location of resonances by modifying elastic parameters, manually and with a multivariate minimization algorithm. The presence of multiple resonances in the response complicates the selection of the appropriate cost function for minimization. Furthermore, different resonances are caused by specific modes and their sensitivity to a particular parameter may vary. For tungsten carbide spheres the lowest frequency resonant notch (located at approximately 116 kHz in the 30 mm sphere) is known to be due to a oblate-prolate spheroidal mode of vibration, S_{21}. The subscript '2' refers to the second term of the partial wave series expansion, whilst '1' corresponds to the fundamental (Neubauer et al., 1974). This resonance is very strongly sensitive to shear wave speed, and not very responsive to the longitudinal wave speed or density. Exact determination of shear speed is then crucial for calibration accuracy. This and other error sources are examined next.

Table 5.2. Optimized shear and compressional wave speed values for some targets, along with measured density.

Sphere	**Shear wave speed C_T (m/s)**	**Compressional wave speed C_L (m/s)**	**Density (kg/m^3)**
24 mm TC / Nickel	4130	6750	14954
24 mm TC / Cobalt	4175	6885	15039
25 mm TC / Cobalt	4167	6850	14862
30 mm TC / Cobalt	4171	6856	14925
30 mm TC / Nickel	4125	6750	15022
40 mm TC / Cobalt	4173	6875	14907

5.2 Standard-target calibration degradation factors

Factors lowering the optimal accuracy of the standard-target calibration factor have been analyzed mostly for spot-frequency calibrations performed at traditional echosounder frequencies such as 38 and 120 kHz. The importance of these issues varies according to the specific experimental conditions, but they can be broadly classified in errors related to the medium, the system and the target.

5.2.1 Immersion medium error sources

The characteristics of the surrounding medium determine the propagation of sound and, consequently, influence target strength. This is taken into account in the backscattering model through the parameters of water density and sound speed. However, these quantities depend on salinity and temperature, measured as described in Section 4.6, and with a fixed value of 0.11 ppt used. At this salinity, sound speed and target strength are shown in Fig. 5.4, as a function of temperature.

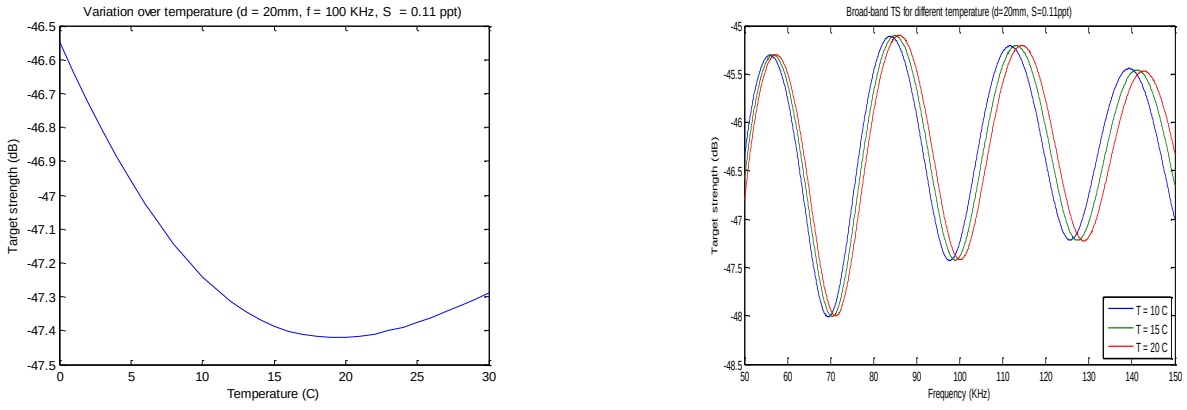

FIG. 5.4. Effects of temperature in modelled target strength, at 100 kHz (left) and across bandwidth (right).

It can be noted that the complete temperature range encompasses nearly 1 dB variation, however, within the likely temperatures found in water tank (14 to 17 ℃), this is much less. However, it can also be seen that temperature change actually shifts the TS response in frequency by approximately 1 kHz per 5 ℃ step.

5.2.2 System error sources

As is the case in most measurement exercises, the precision achieved in a task is ultimately limited by the resolution, accuracy and stability of the instrument itself. For a sonar, this comprises the transducer and independent linear devices such as the filters and amplifiers. In practice, ambient conditions, power source fluctuations or gain drifts can shift the output significantly, especially when signals are close to the noise floor. Such errors can skew a calibration outside the desired tolerance, and large discrepancies can be ascribed to stability problems (Vagle et al., 1996). To address this issue, a series of broad-band continuous measurements were conducted. First, to assess the levels and nature of noise, records were taken without a transmit signal being sent (passive mode). These records consisted of raw data from the transducer into the A/D, evaluated at a given point in time, and without using a matched filter. It can be seen in Fig. 5.5 that the noise floor lies on top of a small negative DC offset, arising from marginal unbalance of the differential channels. This plot shows the Gaussian distribution fit to the typical measured system noise, exhibiting a mean of -8.3 mV and a standard deviation of 3.03 mV (in a 300 kHz passive sonar bandwidth).

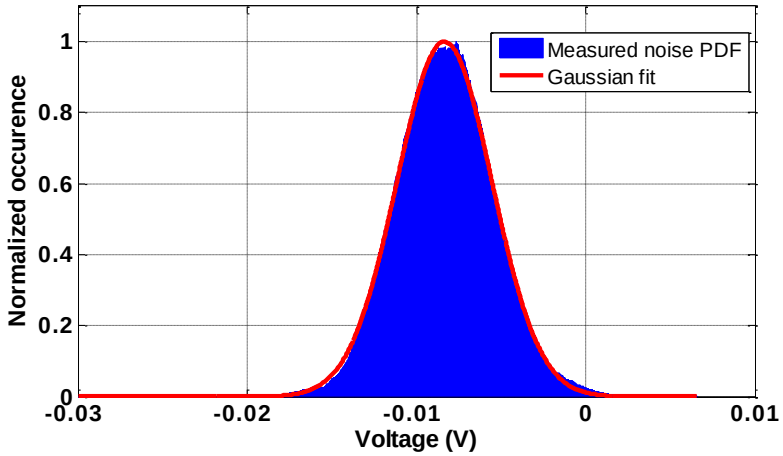

FIG. 5.5. Passive sonar receive noise distribution with Gaussian fit.

Secondly, it was crucial to ensure low overall system noise and drift. For this purpose the echo strength was recorded by pinging repeatedly at a fixed target, in this case the back wall, over an extended period of time. Stability tests of the same character were also performed by (Kenneth G. Foote et al., 2005). The maximum amplitude of the matched filter (compressed pulse) envelope, corresponding to the specular return, was chosen as the relevant quantity, since it contains energy components from the entire bandwidth. The statistical variable mainly used to represent changes in the acoustic monitoring was the coefficient of variation, C_v, expressed as a percentage and defined as

$$C_v = \frac{SD}{|\mu_{mv}|}, \tag{5.1}$$

where SD is the standard deviation and μ_{mv} is the mean value. The standard symbol for standard deviation, σ, was avoided because of its association with acoustic cross-section in the related sonar literature.

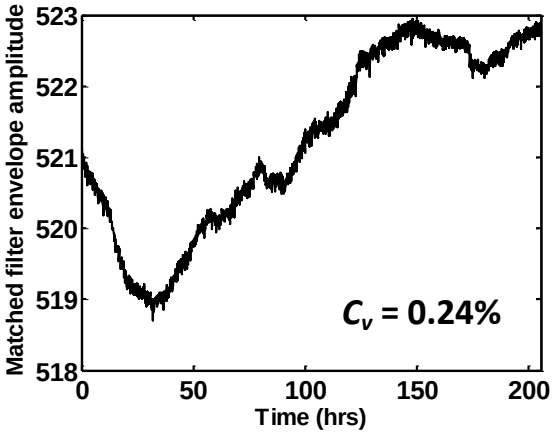

FIG. 5.6. Stability measurements from the back wall. Maximum amplitude of the matched filter envelope (specular reflection) monitored over time.

After one week of measurements performed every 30 minutes, C_v for back wall measurements is 0.24%. The apparent non-stationary characteristics of the back wall echo amplitude time series could be attributed to some degree to temperature dependence. The correlation coefficient with the associated temperature data is 0.85, which is statistically significant and supports the assumption. The receiver battery power remained constant throughout the trial, with an standard deviation of only 3 mV out of a nominal value of 12 V. The observed long-term variation is then not considered problematic for the experiments performed.

5.2.3 Target error sources

As previously discussed, knowledge of the material parameters of the standard-targets is relevant to the calibration, particularly in relation to the sharp resonant features exhibited by most targets. Although nominal values are available, it is known that variations in manufacturing, undermine their applicability. Significant deviations in density were already noted. Furthermore, it has been established that uncertainties in the amount of cobalt content

can also have an impact, since this element is known to alter the elasticity of tungsten carbide (MacLennan and Dunn, 1984). For this reason it was deemed useful to obtain a more precise value within its 5 - 7% stated tolerance.

5.2.3.1 Cobalt content measurements

Spectroscopic elemental analysis was performed on the surface of the spheres with a Phillips XL 30 Scanning Electron Microscope (SEM). Admittedly, this approach is not optimal for SEM samples, due to the convex, unpolished test areas. However, only an indication of relative, comparable cobalt content was sought, and not exact rigorous figures. For this purposes, the SEM strategy, first suggested by Dr. Kenneth Foote, was deemed useful. Measurement validity is suggested by Fig. 5.7, where measured density vs. cobalt content percentages fit well with a linear interpolation obtained from published metallurgical data (Gerlich and Kennedy, 1979).

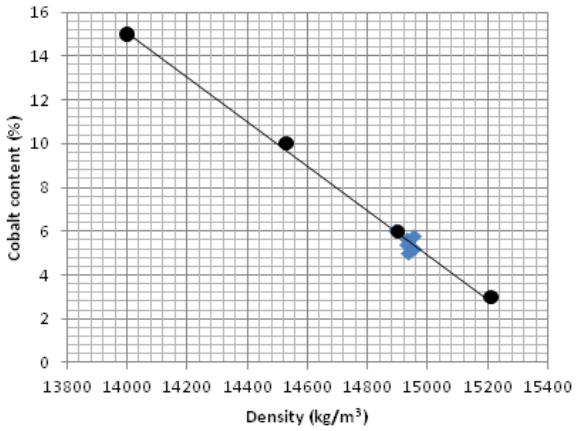

FIG. 5.7. Relationship between density and cobalt content in tungsten carbide with cobalt binder. Line is fitted to the black circles, which are values from (Gerlich and Kennedy, 1979). Measured data points (in blue) are seen grouped near 14900 kg/m^3 density.

Initially, no traces of cobalt were detected in some of the spheres, namely the ones that had been most extensively used in the tank. It became clear that a cobalt-leaching phenomenon had occurred, due to prolonged exposure to the slightly chlorinated water of the laboratory tank. Even though tungsten carbide is more impervious to corrosion than other alloys, it is still vulnerable to cumulative attack by corrosive liquids (Biernat Jr., 1995). This process is often electrochemical, with a saline or chlorinated fluid acting as an electrolyte and causing the cobalt to be extruded from the material (Biernat Jr., 1995). This was verified in two ways. First, the 40 mm sphere, that previously had showed 4.29% of cobalt, was submerged in the tank for approximately 90 hours. Afterwards, a second SEM experiment provided evidence of an unequivocal decrease to 2.48% (standard deviation 0.29%). Secondly, one of the spheres that originally presented no cobalt on the surface was cut, as pictured in Fig. 5.8, and its interior observed with the microscope. Confirmation was found in the cut surface of one hemispheres, with 5.39% cobalt. Moreover, it was established that the cobalt percentage clearly diminishes nearer the edge, as Fig. 5.9 shows.

FIG. 5.8. Cut hemisphere of 20 mm (A) TC/Co sphere.

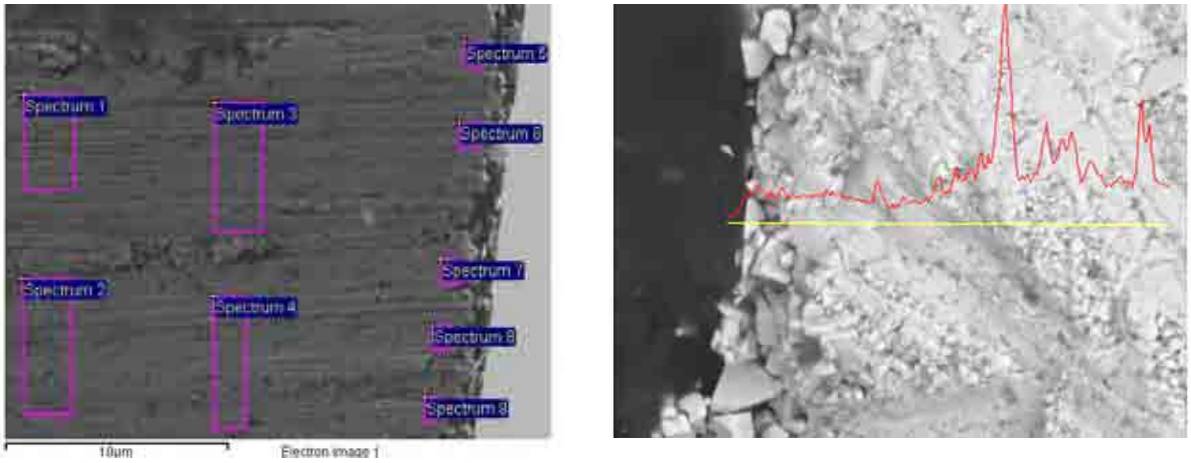

FIG. 5.9. Left, SEM image of cut hemisphere, with the averaged analysis areas shown. Right, the red line corresponds to relative cobalt content gradient.

Since cobalt leaching appears to be very superficial, a significant change on the overall properties of the sphere does not seem to occur. Also, because it happens on the granular level, it would appear improbable that it influences acoustic scattering. However, the existence of an alternative standard-target more suitable for the corrosive conditions of the sea is noted, namely, tungsten carbide spheres cemented with nickel binder, which have superior corrosion resistance (Aw et al., 2008). The improvement in corrosion resistance found in nickel-based tungsten carbide spheres was obvious during the acoustic experiments. The difference between the two types of tungsten carbide spheres can be clearly noticed in Fig. 5.10. The potential of these spheres to serve as improved sonar calibration targets in the following section. A stability comparison is presented, and the acoustic detection of the visible superficial corrosion degradation (less than 1 mm in depth) is considered.

FIG. 5.10. Corrosion performance compared after approximately equal immersion time. Left, cobalt-binder tungsten carbide sphere. Right, nickel-binder tungsten carbide sphere.

5.3 Acoustic monitoring of corrosion of tungsten carbide spheres

The purpose of this investigation was twofold. Firstly, to explore the possibility of monitoring subtle, corrosion-induced target changes via acoustic backscattering. Secondly, to compare the performance as calibration targets of tungsten carbide spheres with nickel and cobalt binder. Material properties of an object can be assessed and monitored through acoustic backscattering measurements. A slightly corroded surface presents a randomly enhanced roughness and higher chance for the adhesion of contaminant particles. However, it was not known if the acoustic system could be sensitive to these subtle changes in a verifiable manner.

Acoustic remote evaluation or monitoring assumes that a physical change in the object under test will be carried back to the receiver by the diagnostic wave. This is often achieved

through resonance evaluation, since their location is determined by the physical properties of the object. Applications such as Resonant Ultrasound Spectroscopy (RUS) (Zadler et al., 2004a) have been successful in determining elastic moduli acoustically. Theoretical frameworks such as Resonant Scattering Theory (RST) (Flax et al., 1978), have facilitated a meaningful interpretation of resonance phenomena in acoustic scattering, by formalizing relationships between surface waves and normal modes of vibration. After a resonance has been detected and identified, one approach is to calculate parameters such as bulk speeds by using theoretical models and minimization techniques (Tesei et al., 2008). The majority of acoustic NDT experiments and applications have been aimed at detecting flaws, cracks, or thickness discontinuities in the specimen. However, microscopic NDT ultrasonic techniques have also been used to evaluate concrete and steel grain size (O'Donell and Miller, 1981), while less works have been devoted to the detection of signs of fatigue and the onset of corrosion (Anson et al., 1995). For the specific case of severe corrosion-induced flaws similar approaches have been adopted, while corrosion monitoring has been attempted through the measurement of acoustic emission (Cole and Watson, 2005), combined acoustical-visual inspection (Doane et al., 2006), and wavelet transformation of corrosion potentials (Montes-García et al., 2010).

5.3.1 Experiment

In order to detect corrosion-induced changes in the backscattered acoustic signals it is necessary to separate other processes that may be happening concurrently. The sonar system used in the present work operates as described in Chapter 4. Transmission signals were linear-frequency modulated (LFM) pulses encompassing a frequency from 50 kHz to 180 kHz. For long term monitoring a measurement was performed every 30 minutes, with the

average of 10 pings recorded together with water temperature and receiver battery voltage. The targets to compare were a 30 mm-diameter tungsten carbide sphere with nickel binder (30mm TC/Ni) and a 24 mm-diameter tungsten carbide sphere with cobalt binder (24mm TC/Co). Targets were placed at the same location. In order to ensure stable targets and equivalent conditions the spheres were given the same stabilization period of one week prior to measurements. Bubbles that might have formed in the surface during immersion are expected to dissolve in this time frame (Hobæk and Nesse, 2006). After immersion, long-term monitoring was not interrupted and the water tank was not disturbed.

5.3.1.1 Time-domain corrosion monitoring

The main indicator used was the envelope of the matched filter (compressed pulse) as used in the stability discussion presented in Section 5.2.2. Any variation introduced by corrosion should be above the level of system drift, with an estimated coefficient of variation of 0.24% based on back-wall reflections over 200 hours. For target monitoring, in addition to the specular reflection, a second arrival ascribed to a circumferential wave was also recorded, as shown in Fig. 5.11.

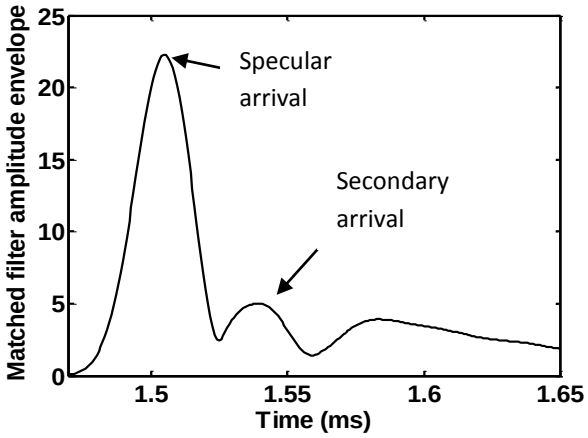

FIG. 5.11. Matched filter envelope of echo from 30 mm TC/Co sphere.

A comparison of the specular amplitude time series of both targets is presented in Fig. 5.12. A clear increasing trend can be noticed in the 30 mm TC/Co (right panel) sphere that is not present in the TC/Ni sphere (left panel). For approximately equal time scales, the coefficients of variation were substantially different, C_v = 0.62% for the 30 mm TC/Co and C_v = 0.058% for the 24 mm TC/Ni. This suggests a sensitivity to the gradual corrosion of the surface of the cobalt tungsten carbide sphere. However, the small increment in amplitude in the backscattered signal appears is not readily explainable, since a rougher target surface would be likely to induce more scattering. Temperature remained fairly constant during both trials, with a mean value of 17.10° and a coefficient of variation of 0.07%. Correlations between temperature trends were negligible.

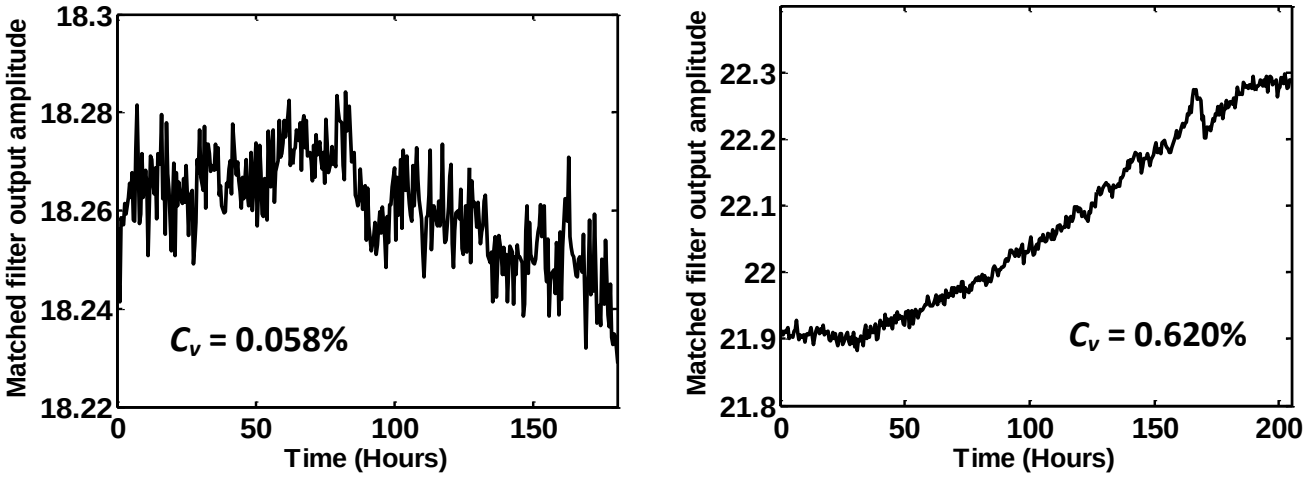

FIG. 5.12. Specular reflection monitoring using an LFM pulse, and presenting the maximum amplitude of the matched filter envelope.

Time axis starts after a 1 week immersion stabilization period.

Left panel, 24 mm TC/Ni sphere. Right panel, 30 mm TC/Co sphere.

In addition to the specular amplitude, a secondary arrival was also monitored. Since corrosion effects occur in the surface of the target, these waves, which circumnavigate the sphere, could sensitive to this deterioration (Anson et al., 1995). Monitoring results of the amplitude of this second arrivals are presented in Fig. 5.13, with an even greater difference.

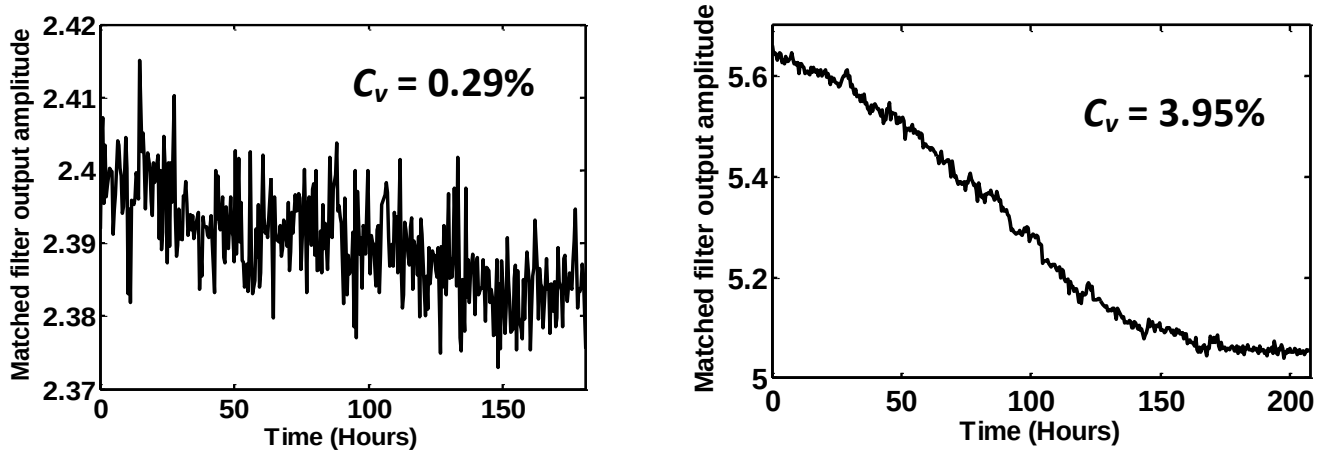

Fig. 5.13. Secondary arrival monitoring. using an LFM pulse, and presenting the maximum amplitude of the matched filter envelope.

Time axis starts after a 1 week immersion stabilization period.

Left panel, 24 mm TC/Ni sphere. Right panel, 30 mm TC/Co sphere.

5.3.1.2 Frequency-domain corrosion monitoring

The location of the resonance in the spectrum was also measured and monitored over time. For the 30 mm sphere three spheroidal resonances are exhibited in the frequency range, as shown in Fig. 5.14.

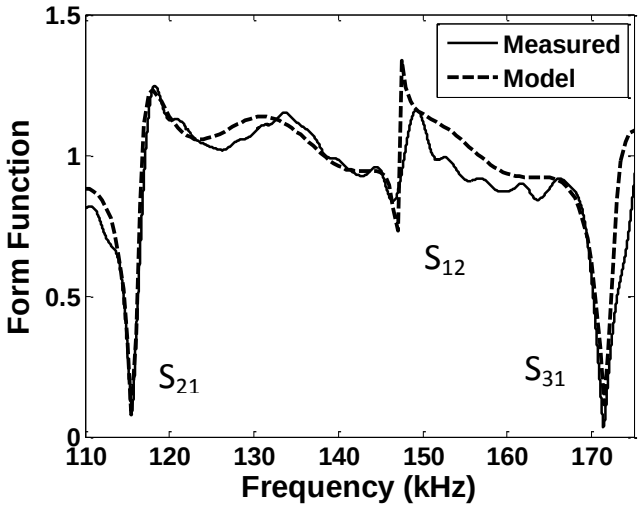

Fig. 5.14. Resonances of the 30 mm tungsten carbide sphere with nickel binder.

Along with the location of notch minima, the adjacent 3 dB points were also examined. It has been proposed that surface cracks could lower the quality factor of the resonance, as they tend to dissipate the energy (Hsieh and Khuri-Yakub, 1992). Resonance monitoring in the frequency domain is presented in Fig. 5.15. It can be noticed that no trends appear for the TC/Co sphere after an stabilization period, whilst the TC/Ni sphere exhibits a change in the central notch frequency, and a narrowing of the quality factor. Discernible variations could be ascribed to corrosion induced changes in the sphere. However, the exact acoustic mechanisms are not known unambiguously. More trials should be conducted in order to verify repeatability. Furthermore, additional acoustic indicators could also be examined. For this purpose, the dual-frequency target phase was found to lack the necessary resolution.

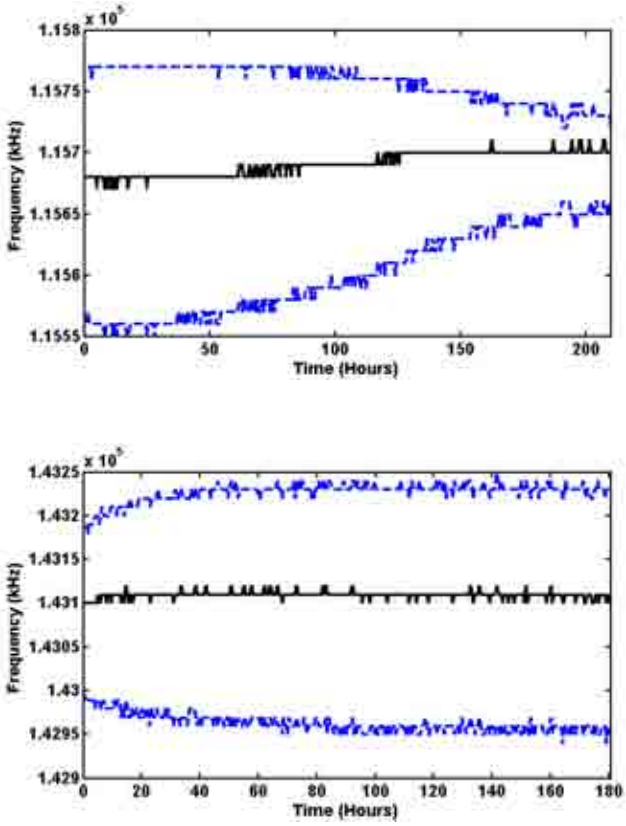

Fig. 5.15. S_{21} resonance frequency location and 3 dB points (in blue).

Top, 24 mm TC/Ni. Bottom, 30 mm TC/Co.

5.4 Summary

The standard-target sonar calibration method has been introduced. Accuracy and constraints have been explored, examining the sources of error degrading the outcome of the procedure. Particularly, dependence on the elastic properties of the standard- targets has been discussed, with an assessment of composition parameters of tungsten carbide spheres in relation to acoustic performance. Density has been computed from mass measurements and the amount of cobalt content has been estimated with SEM spectroscopy. It has been established that spheres containing cobalt binder are more vulnerable to corrosion than spheres made with nickel binder. Potential for acoustic detection of surface contamination has been explored.

6 SYSTEM PHASE RESPONSE CALIBRATION

This chapter is concerned with the phase response of electro-acoustical systems, describing phase distortion issues that can lead to performance degradation. The concepts of group delay and minimum phase systems are introduced. Phase distortion correction approaches are reviewed. Filter-derived transducer matching networks are developed for phase response linearization. An extension to the standard-target calibration method, using dual-frequency processing to include phase response is presented.

6.1 System phase distortion

The dynamics of a linear electro-acoustic system can be described in the frequency domain through its frequency or system response (Heyser, 1969a, Papoulis, 1962), a complex variable composed of an amplitude and a phase, such as

$$H(f) = A(f)e^{j\Phi(f)}, \tag{6.1}$$

where *A(f)* is the amplitude response or gain and *Φ(f)* is the phase response.

The practical importance of the phase response of electroacoustical systems was first acknowledged in the field of audio engineering, particularly in relation to fidelity issues in high quality audio reproducers (Wiener, 1941). Some attention was also given to phase distortion issues in communications engineering, for instance in the development of facsimile

and television technology (Wheeler, 1939). In audio engineering it was found that resonant elements within the system, i.e. the loudspeaker, were the main sources of phase distortion (Ashley, 1966). However, phase was relatively disregarded, in part due to the relative difficulty of its experimental estimation (Wheeler, 1939), but also due to a long-standing controversy on human auditory perception of phase (Stodolsky, 1970). In this context, it was established that if phase could be detected by a human listener it would be through its slope characteristics, or group delay, rather than absolute shifts (Tappan, 1965). Although it was later shown that the perception of group delay distortion was often negligible for practical purposes (Blauert and Laws, 1978), the concept is useful in the analysis of phase distortion in general. On a related note, the fact that human listeners are mostly unaware of phase shifts occurring in an audio signal has proven useful for steganography. In these applications, data is covertly encoded within the phase spectrum of a seemingly-innocuous signal, which can be transmitted without arousing suspicion for later recovery (Meghanathan and Nayak, 2010).

6.1.1 Group delay

Group delay, τ_g, is usually defined as the negative of the derivative of the phase response with respect to frequency, such as (Heyser, 1969b)

$$\tau_g(\omega) = -\frac{d\Phi(\omega)}{d\omega}. \tag{6.2}$$

A related quantity, phase delay τ_p, is defined as

$$\tau_p(\omega) = -\frac{\Phi(\omega)}{\omega}, \tag{6.3}$$

where group delay corresponds to the delay of the envelope of a wave packet and phase delay to that of the carrier, with both in units of time. These expressions have been recently challenged and an alternative definition based on Taylor series expansion has been advanced (Zhu et al., 2009). The derivative operation was found to introduce inherent accuracy and resolution issues that limit its usefulness for fast synchronization applications such as Global Positioning Systems (GPS) receivers. In many applications group delay is determined using a discrete step aperture technique for the differential calculations. Step size selection can exacerbate noise and cause a compromise between accuracy and resolution (Zhu et al., 2009). As discussed in the context of dispersive behaviour, a distortionless acoustic measurement system possesses a phase response which is linearly related to frequency (Papoulis, 1962),

$$\Phi(\omega) = -\omega T_{delay}, \tag{6.4}$$

where T_{delay} is the propagation delay time. That is, the signal its delayed, in its entirety, by a constant amount of time T_{delay}. In this case, both group and phase delay correspond to the propagation interval of the signal through the system(Heyser, 1969b, Preis, 1982), such as

$$\tau_p(\omega) = \tau_g(\omega) = T_{delay}. \tag{6.5}$$

Deviations from a constant group delay, which occur in dispersive networks (Heyser, 1969a), or media (Brillouin, 1960), as previously mentioned, amount to phase distortions that imply

fidelity degradation. That is, when the frequency components of a signal are delayed by disparate amounts of time the original shape of the waveform is modified, a phenomenon commonly encountered in systems with resonant transducer elements (Blauert and Laws, 1978). It has been noted that most practical electronic systems introduce some degree of phase distortion (Zhu et al., 2009). In these conditions, physical interpretation of group delay and its implication on practical systems can be ambiguous. An intuitive explanation has been elusive, particularly in general cases of anomalous dispersion, where a negative group delay may appear to violate the principle of causality (Heyser, 1969b). The relationship between group delay and signal propagation delay was already explored within the related discussion of spatial coherence, Section 3.2, where the concept of frequency-dependent apparent radiator position was introduced. Equalization of these distortion phenomena is constrained by minimum and non-minimum phase system behaviour.

6.1.2 Minimum phase and non-minimum phase systems

Minimum phase functions are a class of causal functions in which the phase, $\Phi(\omega)$, can be uniquely determined from the amplitude, $|H(\omega)|$ (Papoulis, 1962). A minimum phase system has the lowest possible phase shift (or delay), for a given magnitude response (Preis, 1982). In other words, these systems are fastest in returning or releasing energy, with a speed only restrained by causality (McDaniel and Clarke, 2001, Preis, 1982). On the contrary, a non minimum phase system will contain excess shifts due to all pass (pure delay) positive components (Heyser, 1969b). Another consequence of minimum phase systems, due to causality, is that the zeroes of its transfer function (expressed as a rational function) lie outside the upper half of the complex frequency plane (McDaniel and Clarke, 2001). This ensures that the inverse of the minimum phase response is also causal and minimum phase.

The overall phase of the mixed phase response (Cahill and Lawlor, 2008) can then be decomposed in the minimum phase components Φ_m, plus all-pass components Φ_a, such as

$$\Phi(\omega) = \Phi_m(\omega) + \Phi_a(\omega). \tag{6.6}$$

As pointed out before, an equalization scheme for a minimum phase system is insufficient when additional all-pass components are encountered (Blauert and Laws, 1978). Identification of delay contributions is possible through the relationship between amplitude and phase in minimum phase systems, defined by the Hilbert transform. If the attenuation ratio of the system response is

$$a_{ratio}(\omega) = -\ln|H(\omega)|, \tag{6.7}$$

then the phase is related to it through the Hilbert transform,

$$a_{ratio}(\omega_o) = \frac{1}{\pi}\int_{-\infty}^{\infty}\frac{\Phi(\omega)}{\omega-\omega_o}d\omega, \tag{6.8}$$

and

$$-\Phi(\omega_o) = \frac{1}{\pi} \int_{-\infty}^{\infty} \frac{a_{ratio}(\omega)}{\omega - \omega_o} d\omega . \tag{6.9}$$

These relationships have been advantageous for determining the phase from amplitude characteristics, generally easier to obtain experimentally (McDaniel and Clarke, 2001). Another application of minimum phase systems is related to the filtering of a room response or acoustic channel, for speech dereberveration. It is well-known that a conjugate filter can be applied using the complex conjugate of the room frequency response (Preis, 1982),

$$H(\omega) H^*(\omega) = \left| H(\omega) \right|^2 , \tag{6.10}$$

where the gain is incremented and the phase response is equalized as intended. Nevertheless, the required inverse filter is not always realizable. Furthermore, this implies that the system response is known. If the room impulse response is minimum phase, an inverse filter can be found solely from the magnitude response. For a non minimum phase response an inverse filter may be unstable or violate causality (Neely and Allen, 1979). It was found that phase behaviour was largely determined by room dimensions, with wall reflectivity modulating reverberation. A minimum phase inverse filter applied on a mixed phase response retains artifacts (sometimes perceived as “bell chimes”) due to remaining all pass components (Cahill and Lawlor, 2008, Neely and Allen, 1979). Efforts to eliminate these artifacts have included the use of data analysis techniques such as Non-Negative Matrix Factorization, applied at a post-processing stage (Cahill and Lawlor, 2008).

6.2 Phase distortion correction techniques

In order to ameliorate waveform distortion in audio engineering and underwater acoustics, equalization techniques have been developed to correct the effects of electronic circuitry, particularly when coupled to narrow-band transducers operating near resonance. Reduction of gross phase shifts was initially achieved in amplifiers and transducers by means of network improvements, such as increasing input inductance and diminishing transformer leakage inductance and distributed capacitance (Hilliard, 1964). More recently, efforts to correct phase distortions have included, for example, hardware and software equalization methods that compensate for the known effects of the system by pre-distorting emitted signals (Assous et al., 2007). Another approach is the use of block equalisation based on software and passive matching networks connected to the transducer in order to maximise efficiency over a larger bandwidth (Doust and Dix, 2001). This is explored in detail in the following section.

6.2.1 Filter-derived matched circuits

Broadband matching networks have been investigated as a way to enhance phase response flatness while providing power matching (P.R. Atkins et al., 2008b). It has been found that additional high frequency roll off can substantially flatten the response (Hurrell, 2004). Such networks are based on the electrical lumped-element transducer model (Stansfield, 1991), with values determined through impedance measurements. The simplest electrical-analogue model for a transmit transducer operating near resonance is shown in Fig. 6.1. Radiation and loss resistance are represented by R_{rad}. The motional inductance and capacitance are L_{mot} and C_{mot}, whilst the shunt capacitance is C_s, also referred as the dielectric clamped capacitance. For simplicity, a parallel loss resistance component has not been included.

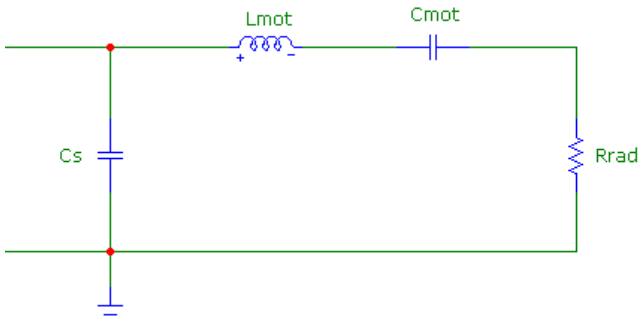

FIG. 6.1. Classical transducer equivalent circuit

When operated in a transmit mode, a matching circuit would be added to cancel the reactive part of the input impedance, thus providing a more favourable load for the power amplifier. Such matching circuits are traditionally designed using a band-pass filter assumption, in order to improve the response characteristics of the transducer (Doust and Dix, 2001, Stansfield, 1991). In this case, the aim is to linearise the phase response over the largest possible bandwidth. The transducer is incorporated into the design as a half section of the intended band-pass filter. Admittance, *Y*, is defined in terms of conductance, *G*, and susceptance, *B*, such as (Guillemin, 1953)

$$Y = G + jB, \tag{6.11}$$

and is measured in units of Siemens. This complex quantity is used to characterize resonant transducers and the associated equivalent electrical networks. Admittance measurements were taken from the TC2130 transducer, using a HP4291A impedance analyzer (Agilent Technologies, Santa Clara, USA). As developed in (Stansfield, 1991), the input admittance of the transducer equivalent circuit in Fig. 5.1 is determined from the parallel combination of the

shunt capacitance, C_s, with the admittance of the series LCR arm formed by L_{mot}, C_{mot} and R_{rad}. From basic network theory the resulting input admittance, Y_{in}, is given by

$$Y_{in} = \frac{1}{R_{rad}\left(1+Q_M^2\Omega_\omega{}^2\right)} + j\omega\left[C_s - \frac{\omega_s C_{mot} Q_M^2 \Omega_\omega{}^2}{\omega\left(1+Q_M^2\Omega_\omega{}^2\right)}\right], \tag{6.12}$$

with ω_s is the angular resonant frequency,

$$\Omega_\omega = \frac{\omega}{\omega_s} - \frac{\omega_s}{\omega}, \tag{6.13}$$

and

$$Q_M = \frac{\omega_s L_{mot}}{R_{rad}}. \tag{6.14}$$

The real component of Eq. 6.12 corresponds to the conductance, and the imaginary part to the susceptance. Values are selected to produce curves fitted to experimental results, specifically, in the frequency range marked by the 3 dB points of the conductance peak. Resulting quantities, obtained with a minimization routine (Matlab 'fminsearch' function), constitute the specific equivalent electrical circuit. Frequency was limited to the area near the main resonance, thus a second resonance was not considered when adjusting the admittance curves. The measured and modelled admittances are presented in Figs. 6.2, 6.3 and 6.4, while the transducer equivalent circuit is shown in Fig. 6.5. The second resonance is prominent in each of the plots. The peak conductance value (minimum impedance) occurs at the transducer main resonant frequency. The eccentricity of the loop in Fig. 6.4 is a consequence of device loading, since light damping approximates a circular shape (Stansfield, 1991).

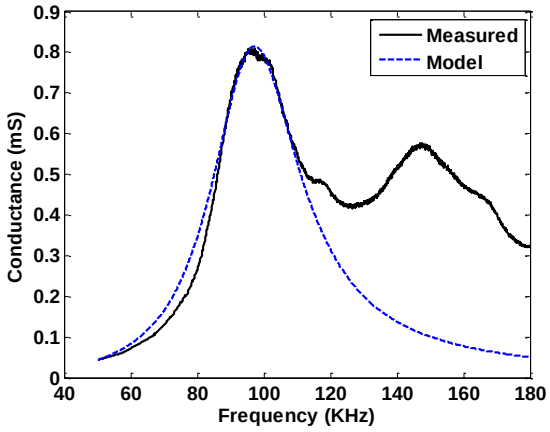

FIG. 6.2. Experimental and modelled conductance.

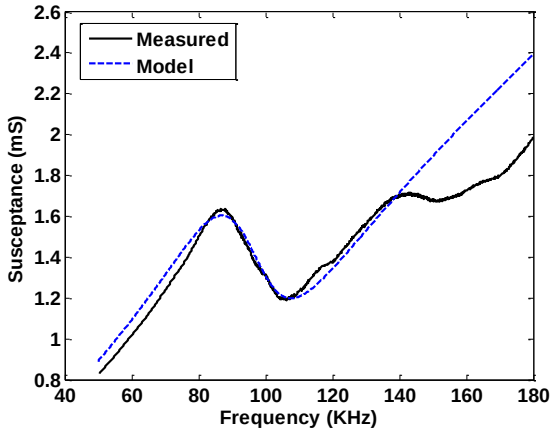

FIG. 6.3. Experimental and modelled susceptance.

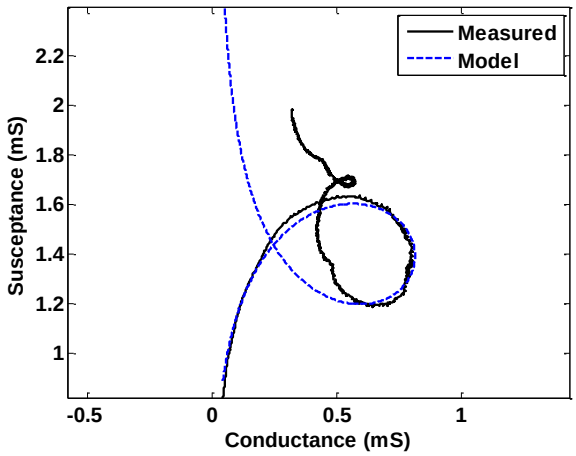

FIG. 6.4. Experimental and modelled admittance loops.

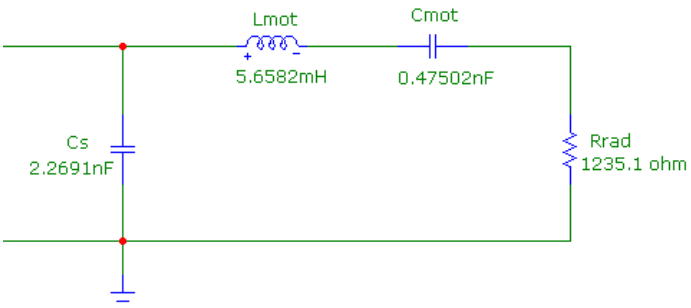

FIG. 6.5. Transducer equivalent circuit for the Reson TC2130

Butterworth and Bessel (or Bessel-Thomson) filter architectures were selected for their superior phase response linearity, although only the Bessel type was originally aimed to have a maximally-flat response (Van Valkenburg, 1982). Synthesis of the double-terminated Butterworth and Bessel, 3rd order band-pass networks was based on methods and tables from standard filter theory texts (Chen, 1995, Huelsman, 1993). Detailed filter-design calculations are presented in Appendix A.1.

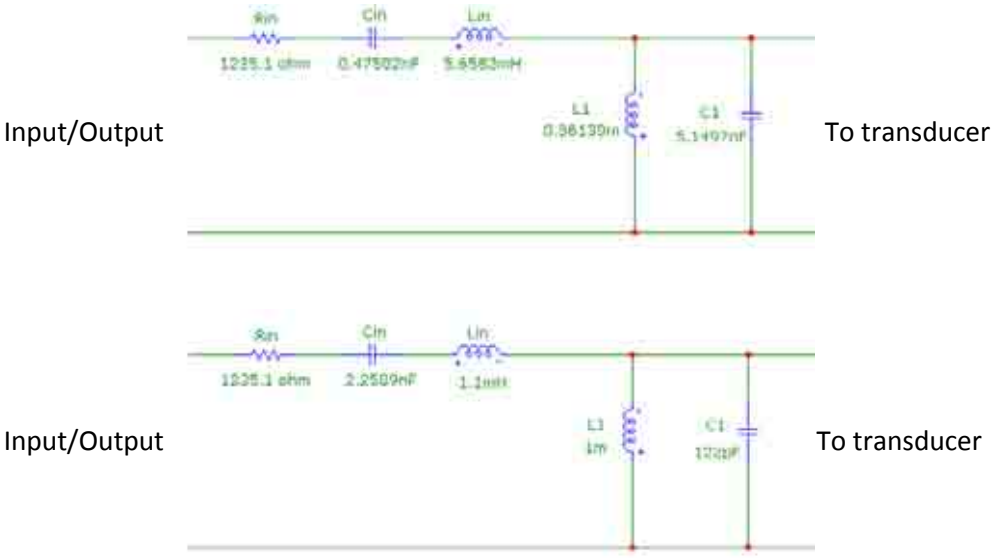

FIG. 6.6. Top, Butterworth-derived matching circuit.

Bottom, Bessel-derived matching circuit

Resulting circuits, Fig. 6.6, were built, connected to the transducer circuit, measured and evaluated analytically. The admittance data obtained from each case of matching is displayed in Fig. 6.7, along with the curves from the models extracted from circuit loop analysis.

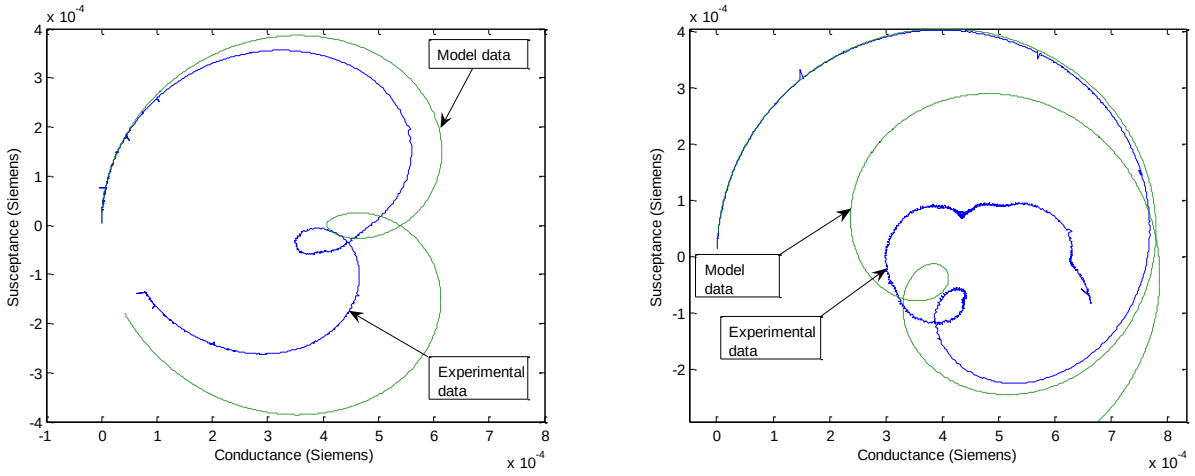

FIG. 6.7. Admittance loops of transducer with bandpass matching filter. Left, Butterworth-derived. Right, Bessel-derived.

A performance comparison between the two matching schemes and the unmatched transducer was made in terms of bandwidth and phase linearity. Fig. 6.8 shows the three transfer functions in amplitude, with their 3-db points marked. We can see that the unmatched transducer, and the Butterworth matching have approximately the same bandwidth, about 35 kHz; although the Butterworth-matched case is significantly flatter in the interval. The transfer function of the Bessel-matched case is wider, particularly toward the higher frequencies, with a total bandwidth of about 68 kHz. In the phase response plots, it can be clearly noticed that the Bessel exhibits a response that is closer to linear for a larger frequency range. The improvements, however, would be less significant if the relevant bandwidth to be used were narrower.

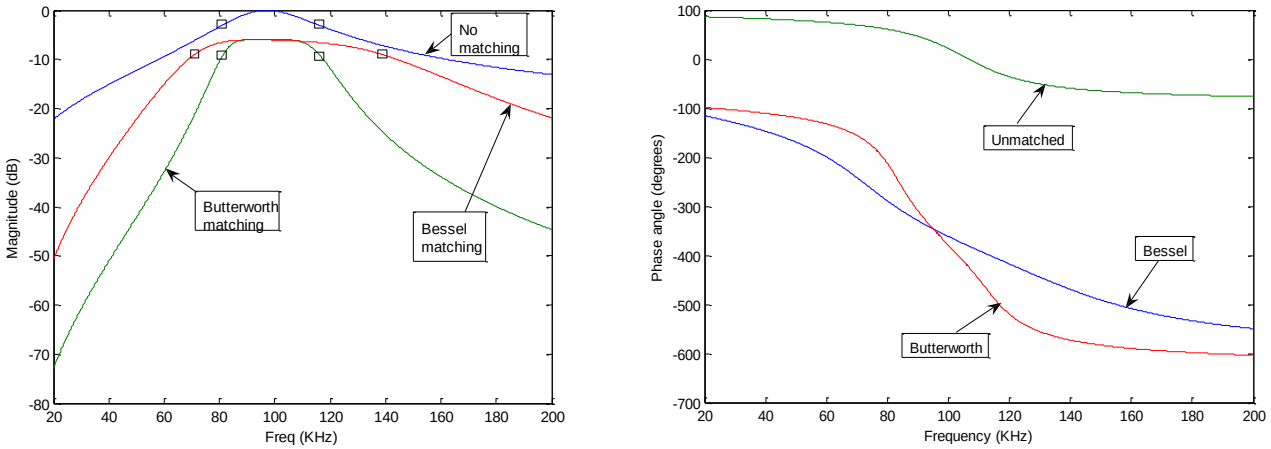

FIG. 6.8. Predicted magnitude (Right) and phase (Left) response.

The 3 dB points are marked in the magnitude response.

Traditional studies of matching transducers have been mostly focused in the efficient transfer of power and the enlargement of bandwidth, without taking phase into consideration. In this respect the development presented above, particularly aimed at the phase response, could be a valuable contribution. However, this only considers the transfer function of the transducer, which is less useful. Supporting electronics such as transmitter and receiver amplifiers and filters add phase distortion (as seen in Fig. A.10 in the Appendix). A complete system vision would appear to be the best approach, with each individual system block compounded into a black box containing all of them. Furthermore, the corrective measures discussed above may not be particularly convenient for application in commercial scientific sonars, since they rely on additional hardware, software compensation and special transmission signals that may be less energy efficient, leading to a reduced noise-limited range performance. A more general treatment of phase distortion, instead of a case-by-case approach would be advantageous to sonar users and designers.

6.3 Phase calibration approaches

The role of waveform distortion and phase spectra becomes more relevant with increased bandwidth. As Doust and Dix pointed out, in addition to larger bandwidth, enhanced resolution also requires waveform fidelity (Doust and Dix, 2001). Consequently, phase calibration of acoustic systems has been given more attention for devices operating in higher-frequency regimes. For example, calibration techniques for medical ultrasound imaging systems have been developed. In these applications, calibration performance is driven by the exacting phase flatness criteria of industry standards, extending above and below the working frequency of the device (Wilkens and Koch, 2004). Furthermore, the importance of determining peak pressures of nonlinear fields, which requires knowledge of the amplitude and phase response, has been stressed (Bloomfield et al., 2011, Cooling and Humphrey, 2008). In general, full transducer characterization in amplitude and phase can lead to improved performance in ultrasound imaging systems (P.L.M.J. van Neer et al., 2011b).

6.3.1 Phase calibration methods in ultrasound

Suitable hydrophones with flat phase response become difficult to achieve as bandwidth increases. In this context, primary and secondary calibration techniques have been extended to include phase. As desirability of phase calibration is appreciated more, these methods have been implemented by internationally-recognized metrological institutes, such as the Physikalisch-Technische Bundesanstalt (PTB) (Ludwig and Brendel, 1988, "Status Report PTB", 2008), while other techniques, previously amplitude-only, have also been adapted for the treatment of phase (Cooling and Humphrey, 2008). In general, correction approaches based on deconvolution operations, can be conducted in the frequency domain by means of a

complex division (Wilkens and Koch, 2004). Then narrow band procedures expressed through the sensitivity relationship (Hurrell, 2004, Ludwig and Brendel, 1988)

$$p_a(t) = \frac{V_{open}(t)}{M_s(f_{awf})}, \tag{6.15}$$

need to be extended. In Eq. 6.15, previously introduced in Chapter 2 (Eq. 2.7), $p_a(t)$ is the free-field acoustic pressure as averaged in the face of the transducer, $V_{open}(t)$ is the open circuit voltage at the transducer terminals, and $M_s(f_{awf})$ is the sensitivity at the working frequency f_{awf}. This approach requires knowledge of the broadband hydrophone complex transfer function, which can be obtained through various techniques as summarized in (Ludwig and Brendel, 1988). Recently, primary ultrasound calibration has been obtained with optical interferometry, where the acoustic field induces a displacement in a pellicle which is then measured with an optical beam. Secondary calibration relies on techniques such as time-delay spectrometry (TDS) (Wilkens and Koch, 2004), as developed by (Heyser et al., 1989). TDS is a swept-frequency ultrasonic technique with improved processing gain due to selective discrimination of arrival times from the relevant range, which ensures direct path, free-field conditions. This is particularly advantageous when acute attenuation degrades imaging at relatively longer ranges, or when acoustic measurements are performed in reverberant environments. TDS is a fundamentally coherent technique based on the matched filtering of time-delayed signals and processing of the complex analytical function (Heyser et al., 1989). TDS can be applied to calibration through substitution with reference hydrophones and it has been adapted to include phase response (Christian Koch, 2003, Ch. Koch and Wilkens, 2004). TDS has been coupled with heterodyning or time-gating experimental schemes, using an optical hydrophones as reference (Ch. Koch and Wilkens, 2004, Wilkens

and Koch, 2004). Another approach is finite-difference modelling of acoustic fields propagating nonlinearly (Cooling and Humphrey, 2008), where the field measured at an specific position is compared with a simulated field. This method relies on a reference hydrophone for field characterization, but this does not require *a priori* knowledge of phase response. Similarly, models have been applied to predict the acoustic backscattering from a flat reflector (P.L.M.J. van Neer et al., 2011b). Phase is referenced to the start of the vibration due to the stimulus, a fixed point in the time response that is not a function of frequency.

Ultrasound calibration techniques have reached frequencies as high as 100 MHz for amplitude (Umchid et al., 2009) and phase (Bloomfield et al., 2011), with challenges exacerbated in the MHz regime. For example, dimensions of typical hydrophones, greater or comparable to the wavelength, can introduce undesirable effects upon phase measurements. This is due to diffraction by the hydrophone, and by spatial averaging across the geometry of the active element (Cooling et al., 2011). Efforts have been made to minimize these problems with the design of smaller sensitive elements (Ludwig and Brendel, 1988). It has been recently observed that these effects also caused by waveform characteristics, undergoing varying degrees of interference (Cooling et al., 2011). It has been pointed out that spatial averaging effects can be removed if the hydrophone has at least a half-wavelength resolution, which at a 100 MHz means a 7 μm aperture (Umchid et al., 2009). Another source of error can be introduced by misalignment and uncertainties in range and sound speed, which can be severe due to the high frequencies involved. For example, in the phase calibration using a flat reflector, it has been estimated that at 4 MHz an uncertainty of ±0.1 m in the speed of sound leads to an uncertainty in the phase response of ±6.5º. Furthermore, a distance uncertainty of just ±0.1 mm leads to a phase uncertainty of ±97º (P. L. M. J. van Neer et al., 2011a).

6.3.2 Phase calibration methods in sonar

For the case of hydrophones operating in the range of sonar frequencies, the long-established calibration method of free-field, three transducer reciprocity (Bobber, 1970) is predominant. Extension of this procedure to incorporate phase (Luker and Van Buren, 1981), constitutes the basis used by the National Physical Laboratory, in the United Kingdom (Hayman and Robinson, 2007). However, this technique is also extremely sensitive to positioning accuracy and thus demands a typical alignment accuracy of better than one-hundredth of a wavelength (Pocwiardowski et al., 2006). This was recognized early on, and this method was recommended for frequency ranges below 500 kHz, since the alignment issues become unsustainable above 1 MHz (Ludwig and Brendel, 1988). An optical method developed in China, HAARI (Yuebing and Yongjun, 2003), has similar performance but lower uncertainty levels, since the hydrophone is not required to rotate. Nevertheless, the technique relies on a laser Doppler vibrometer, complicating its implementation outside a laboratory environment.

One of the aims of this work is to extend the standard-target method to incorporate phase response along with amplitude, in order to obtain full system characterization. The inclusion of phase response to the standard-target method is also applicable to the calibration of multibeam sonar systems, with the estimation of individual phase responses of array elements. This is essential for the maintenance of sidelobe rejection performance within a beamformer (Hayman and Robinson, 2007, Pocwiardowski et al., 2006), which can undermine the directionality of a multibeam sonar and impact its quantitative capabilities (Cochrane et al., 2003). In more general terms, the calibration of phase is relevant to underwater acoustic applications where the integrity of the temporal wave is important, such as in verifying the performance of specific waveforms, or in maintaining processing gain within a matched filter.

6.4 **Dual-frequency phase calibration**

As previously discussed in the context of ranging applications, multi-frequency transmissions can be useful for determining distance, calculating it as a phase difference between the frequency components. For these applications, phase shifts induced by the target are not considered. The alternative approach could be adopted where the range variable is removed, and the remaining phase shift is related only to the target and system effects. This possibility renders dual-frequency transmission signals suitable for phase calibration, suggesting their practicality in the extension of the standard-target method to include phase simultaneously with amplitude and without changing basic experimental settings (Islas-Cital et al., 2011b). Range only needs to be approximated in order to calculate the target strength, but it does not affect phase measurements. Although phase is computed with an ambiguity in factors of 2π, the phase characteristics of the target are uncovered, which leads to the extraction of the complete system response, as expressed in Eq. 6.15, by means of the standard-target method.

In general terms, the scaled differential phase terms calculated and measured in this work are then defined as

$$\Delta\varphi_{meas}(f) = \frac{N\varphi_{meas}(f_1) - M\varphi_{meas}(f_2)}{M} \tag{6.16}$$

and

$$\Delta\varphi_{model}(f) = \frac{N\varphi_{model}(f_1) - M\varphi_{model}(f_2)}{M}, \tag{6.17}$$

where the subscripts ‘meas’ and ‘model’ refer to measured and modelled quantities, respectively. The resulting phase difference, subsequently referred only as ‘target phase,’ is used. It can argued that ‘absolute’ phase is in general not a meaningful term, since phase is always defined as difference (Hurrell, 2004). These phases can be subsequently incorporated as a calibration data set into an experimental active sonar system simultaneously transmitting two frequency modulated waveforms with the same spectral separation value μ.

For amplitude calibration, one or both received frequency components can be used, since superposition applies and a condition of zero co-channel interference has been established. The system frequency response *H(f)*, which in this case includes the transducer and supporting electronics as well as transmission losses, is extracted by a division in the frequency domain such as

$$H(f) = \frac{V_r(f)}{V_t(f)F_{bs}(f)} \ , \tag{6.18}$$

where all the variables are complex and a function of frequency *f*, while V_r is the received voltage, V_t is the transmitted voltage, and F_{bs} is the backscattered form function in the far field. Although the function *H(f)* is correspondingly complex and contains phase information, it remains ambiguous in range.

If we consider the amplitude ratio of the measured received and transmitted voltages as the experimental value to be recorded, the generality of the deconvolution method can be better illustrated as

$$V_{ratio}(f) = F_{bs}(f)H(f), \tag{6.19}$$

in which the expected value of the form function $F_{bs}(f)$ is affected by the response of the system, yielding the actual measured value. For the case of phase the same relationship applies, but the measured and modelled phases are determined using dual-frequency transmission pulses. Thus the expression that corresponds to Eq. 6.19 is

$$\Delta\varphi_{meas}(f) = \Delta\varphi_{mod}(f) + \Phi(f), \tag{6.20}$$

since phase angles can be added or subtracted instead of multiplied or divided, where $\Phi(f)$ is a function of the range-corrected value of the system phase response $angle\left(H(f)\right)$ (Cooling and Humphrey, 2008). The system phase response can then be removed from subsequent measurements such that

$$\Delta\varphi_{cal}(f) = \Delta\varphi_{meas}(f) - \Phi(f), \tag{6.21}$$

in order to achieve a calibrated response, $\Delta\varphi_{cal}$, that can be compared with a predicted target phase. A simplified block diagram summarizing the procedures followed in this work and described in the previous paragraphs is shown in Fig. 6.9, with the steps added for phase calibration enclosed in parenthesis and dashed lines.

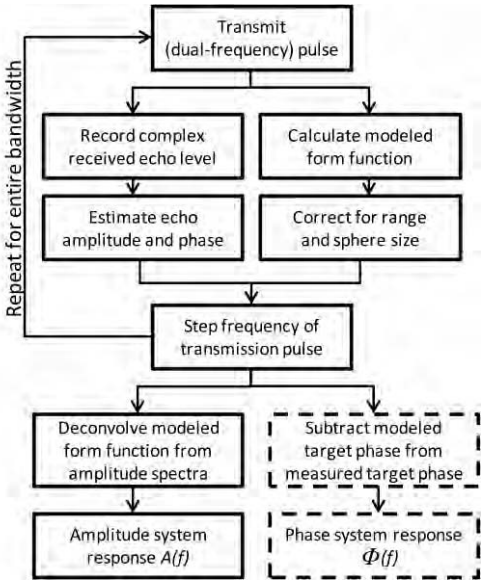

FIG. 6.9. Block diagram of the processing applied to the first set of backscattering measurements, in order to obtain the system amplitude and phase response. Subsequent measurements on other spheres followed the same steps, but the known effects of the system can now be removed in order to extract the calibrated target response. Dashed line boxes are for phase calibration only.

6.4.1 System response analysis

The extracted amplitude and phase responses are presented in Fig. 6.10, both referenced to the lower frequency, as done throughout in this work. As previously mentioned, a black box approach was adopted, in which a system transfer function represents all the stages contained in the two-way signal path. Therefore, all the hardware involved in the transmission and detection of the electroacoustical signal are included, as well as the purely acoustical effects of the water tank. Nevertheless, the magnitude characteristics (top panel) show that the dominant factor is the transducer, as proven by the close resemblance to the manufacturer's data. For the case of phase, no equivalent specifications were available.

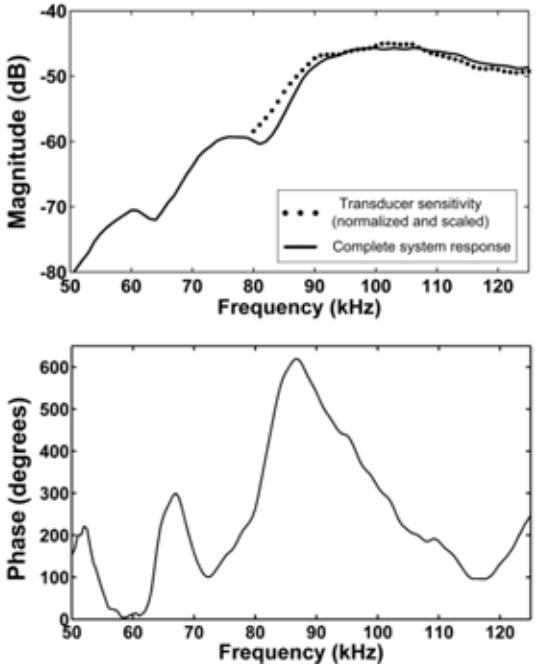

FIG. 6.10. Top panel: Measured amplitude response of complete system, 20log(*A(f)*), including transducer, supporting electronics and propagation losses in the tank (solid line), and transducer sensitivity from manufacturer's datasheet (dotted line). Lower panel: Measured dual-frequency phase response of the system, $\Phi(f)$, with μ = 1.2. Calibration target was the 20 mm tungsten carbide sphere with cobalt binder.

The measured unwrapped differential phase response for the complete system (lower panel), presents rapid changes of phase versus frequency, particularly around system poles and even where the magnitude curve is substantially flat. The approximate correspondence of peaks in the phase plot to points of inflection in the amplitude indicate minimum phase characteristics (Heyser, 1969a), in combination with additional all-pass components (Blauert and Laws, 1978). These departures from a linear phase response, likely to appear in most practical systems due to the presence of various modes and inter-element coupling (P. R. Atkins et al., 2007b), further demonstrate the need for compensation.

6.4.2 Phase calibration accuracy

Calibration error was estimated from the difference between the measured and modelled responses, using RMS values. The agreement between measured and modelled phase is shown in Fig. 6.11. As in the case of amplitude, it is clear that the agreement also tends to deteriorate as more resonances are included. For example, the RMS error across the bandwidth is 9.6° for the 22-mm-diameter sphere, while it is 14.5° for the 25-mm-diameter sphere and 18.3° for the 30-mm-diameter sphere. Therefore, due to phase sensitivity to target composition, errors in the determination of these values can lead to calibration inaccuracies. It can be noticed in all plots that the lower-frequency section of the spectra is more conspicuously affected by noise, as the transducer sensitivity degrades as a function of frequency. Effects related to phase unwrapping are seen as 360° shifts. In the case of the 40-mm-diameter sphere, the measured data follow replicas of the modelled response scaled by 360°. Abrupt peaks in the curves are caused by the excitation of elastic resonances of the spheres (Flax et al., 1978), as seen in all cases except for the 22-mm-diameter sphere. It will be noted that a major advantage of the dual transmission frequency, standard-target method is that phase calibration errors do not increase as a function of frequency, only as a function of decreased signal-to-noise ratio and sphere resonances. This is further evidenced with the measured phase standard deviation, $SD_{meas}(f)$, presented in Fig. 6.12. The inter-ping variation of phase response also follows the system signal-to-noise ratio.

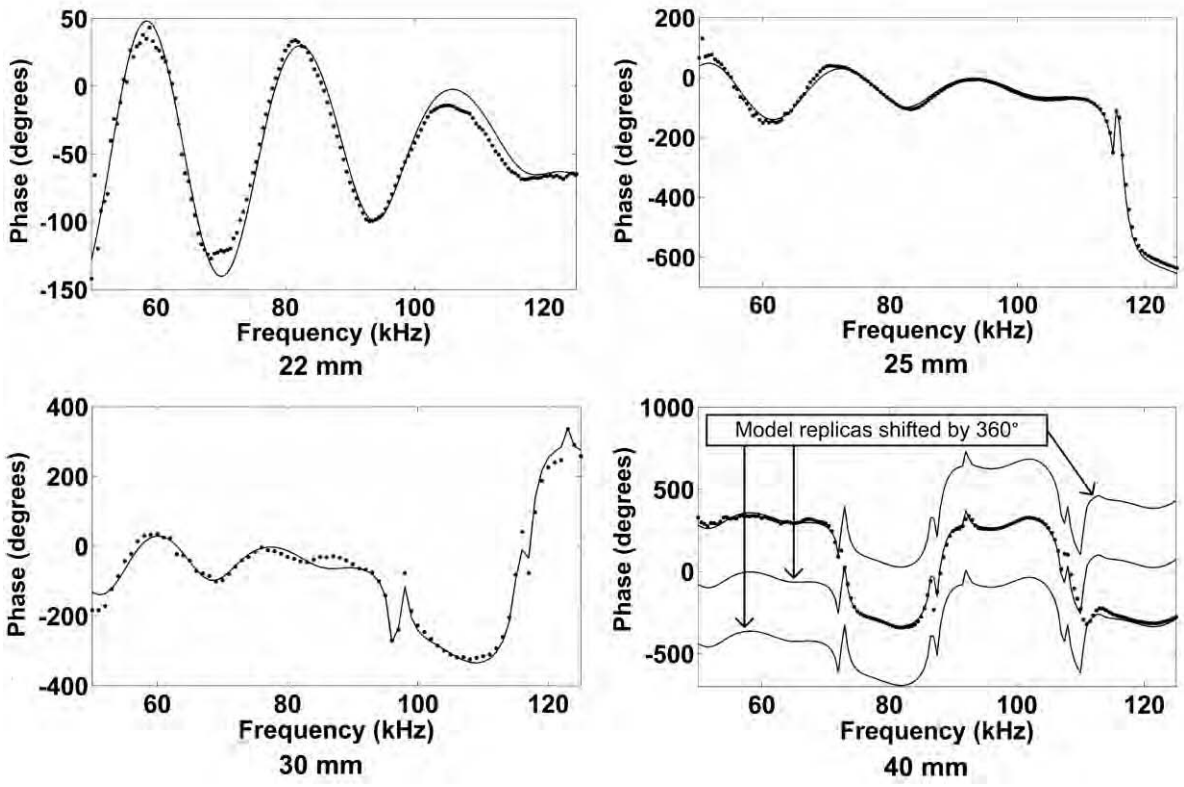

FIG. 6.11. Resulting agreement after calibration between modelled and experimental phase responses, $\Delta\varphi_{mod}(f)$ and $\Delta\varphi_{cal}(f)$. Diameter of the spheres is indicated below each panel. Point plots correspond to calibrated measured data, solid lines to model. For the 40-mm-diameter sphere, modelled responses are replicated and shifted by 360°. μ = 1.2 in all cases.

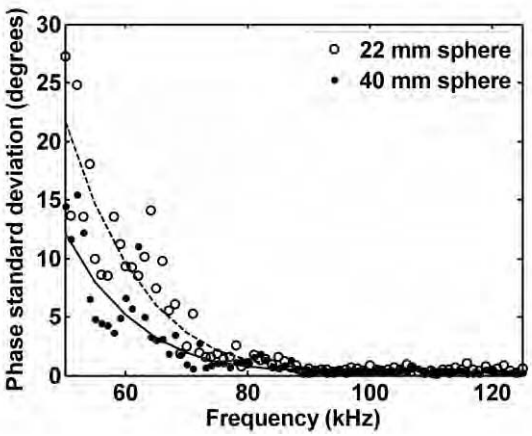

FIG. 6.12. Inter-ping standard deviation of measured target phase, $SD_{meas}(f)$. Experimental data from 22 mm and 40 mm spheres with μ = 6/5 = 1.2 shown together with polynomial fits.

6.4.3 Phase calibration degradation

As mentioned previously, some of the issues affecting the accuracy and repeatability of amplitude calibration can also degrade the phase calibration procedure. Nevertheless, the exactitude of phase calibration is also challenged by particular problems. For example, the presence of bubbles on the surface of the spheres can be an extraneous source of potential errors, since gas enclosures introduce acoustically-soft characteristics to acoustically-hard targets. In this respect, the practice of wetting and soaking (applying soap and immersing in water before placement in the water tank) the targets largely precludes the formation of bubbles and reduces stabilization time. Additional errors in phase determination can occur in reverberant environments where multipaths may contaminate the measured phase (Yimin Zhang et al., 2008). Moreover, operations such as frequency multiplication, performed on the processing of the dual sub-bands, can potentially magnify the effects of phase noise (Lance et al., 1984), caused by fluctuations in oscillators and synthesizers as well as external independent noise sources. In selecting the frequency separation values, the approach of maintaining spectrally independent sub-bands has been adopted, in order to avoid the correlation of noise. This approach is also advantageous in that it denies spectral overlapping (aliasing) issues. The processing strategy may also be viewed as that of multiplying both sub-band spectral components such that a common phase comparison frequency is employed. Overall system phase-noise performance is improved when a lower phase comparison frequency is used, corresponding to a large value of μ, as the available bandwidth permits. This behaviour is illustrated in Fig. 6.13, again in terms of phase standard deviation, where curve fitted to data sets from the same sphere (22 mm), but with different μ values, are shown.

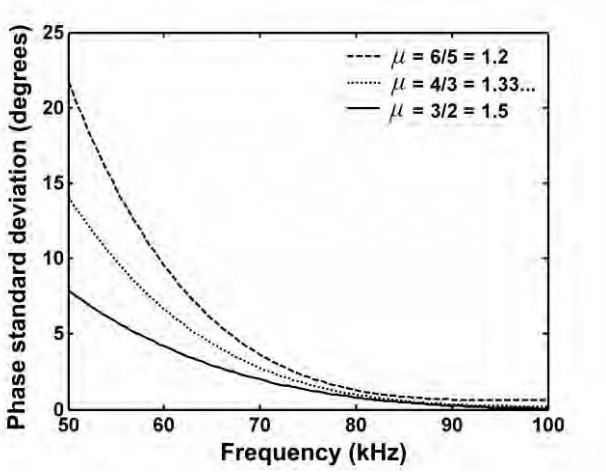

FIG. 6.13. Curve fits to measured phase standard deviation, $SD_{meas}(f)$, from the 22 mm sphere at three different spectral separation values.

As expected, dual-frequency phase measurements obtained with a spectral factor of 1.5 present overall lower instability than those with 1.33 and 1.2. The system's intrinsic and measured phase deviations, $SD_{int}(f)$ and $SD_{meas}(f)$ respectively, are related through the spectral separation such that

$$SD_{int}(f) = \frac{SD_{meas}(f)}{N+M}. \tag{6.22}$$

The previous expression links the expected noiseless system phase response, termed 'intrinsic', with the measured values, which are prone to phase noise and, as demonstrated, to the spectral separation factor. Eq. 6.22 was proven empirically for the three curves in Fig. 6.13, which approximately converge to the expected intrinsic response.

6.4.4 Calibration repeatability

Successive calibrations were performed in order to evaluate repeatability and systematic errors. A 20 mm TC/Co sphere was removed and inserted again four times, with measurements performed overnight every 24 hours. Frequency covered 50 to 125 kHz with 500 Hz steps. Twenty pings were averaged. Temperature and receiver battery voltage were monitored at every frequency step. As seen in Fig. 6.14, amplitude standard deviation for the entire bandwidth was near 0.1 dB, whilst for phase it was in the order of 5°. Since temperature had an approximate standard deviation of 0.10° throughout, and receiver battery voltage variation is negligible, most of the variation could be ascribed to target stabilization and the dissolution of bubbles potentially attaching to the spheres, as discussed for the case of an amplitude-only procedure.

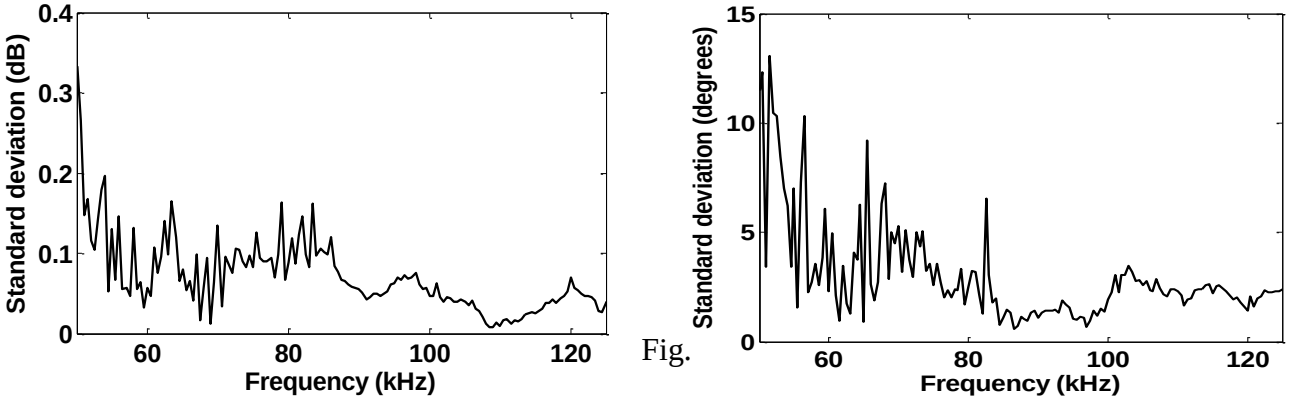

Fig.

FIG. 6.14. Standard deviation of magnitude (left) and phase (right) system response, averaged over four successive calibrations.

6.5 **Summary**

The system phase response of electroacoustic systems has been introduced, together with concepts used in its analysis, such as group delay. Phase distortion issues have been described and correction techniques reviewed. The approach of designing broadband matching electrical networks for phase response linearization has been more closely detailed. Two filter-derived matching circuits have been derived for the Reson TC 2130 transducer, using admittance measurements to obtain its equivalent circuit. A full-system phase calibration approach has been advocated, with previous works reviewed, which are mainly found in the field of ultrasound medical imaging. For the case of sonar, an extension to the standard-target calibration method to include the phase response has been advanced. This method is based on the use of dual-frequency signals and frequency domain processing to remove the range factor. The amplitude and phase system response of the laboratory tank sonar system is extracted. The accuracy and repeatability of this approach are discussed.

7. AMPLITUDE AND PHASE SCATTERING FROM CANONICAL TARGETS

This chapter presents scattering results using the calibrated sonar system described. Amplitude and phase characteristics of canonical sonar targets are analyzed. Phase features are connected to relevant echo formation mechanisms. Potential target identification applications are discussed.

7.1 Target phase representation

As discussed in Section 3.4 the phase of an echo can be displayed in different manners in order to better exploit the contained information. Underwater acoustics scattering papers representing the target response in amplitude and phase are not abundant. Some of these works have been reviewed in the preceding sections. In many cases, this phase does not allow for intuitive physical interpretation and thus contributes little to the analysis of received signals. It was recently proposed to present the derivatives of form function angles. These formats are sensitive to elastic resonances (Mitri et al., 2008), and thus to the subjacent echo formation mechanisms (Yen et al., 1990). The idea has been applied to the Method of Isolation and Identification of Resonances (MIIR), where the ratio between the imaginary and real part of the spectrum has been shown to be valuable for resonance examination (Maze, 1991, Rembert et al., 1990). Finally, in system analysis applications, trends generated by the unwrapped phase have been studied in terms of system poles and zeroes (Lyon, 1983). However, target phase spectrum in this format is difficult to compare directly with model computations, which complicates results interpretation. In the next section the usefulness of the dual-frequency target phase presentation will be explored using canonical scatterers.

7.2 Solid spheres

The phase response of solid spheres was already briefly examined in Section 6.4.2, in the context of phase calibration accuracy. The angle of the calibrated form function can be directly presented, together with that of the theoretically-predicted case, via the Goodman-Stern model script. Recalling the definition of the acoustic form function in the far field, F_{bs}, in terms of the spectra of the incident, P_{inc}, and and scattered pressure, P_{scat}, we have

$$F_{bs}(ka) = \left(\frac{2R}{a}\right)\left(\frac{Pscat}{Pinc}\right)e^{-jkR}, \tag{7.1}$$

where k is the wave number, a is the radius of the sphere and R is the range to the target. The term e^{-jkR} is sometimes not included in definitions that only consider the amplitude of the form function. It adds a pure phase delay corresponding to the distance and it could be used to determine the modelled pressure at a given point in space.

7.2.1 Rigid behaviour

For a perfectly rigid sphere, the phase of the specular contribution, φ_{spec}, has been determined from purely geometric arguments as (P. L. Marston, 1992)

$$angle\left(\varphi_{spec}(ka)\right) = -2ka\sin\left(\theta/2\right) \tag{7.2}$$

where the incidence angle θ is 180° for the backscattering case (refer to geometry shown in Fig. 2.1).

For this experiment the range, R, was estimated to be approximately 2.17 m to the centre of a sphere suspended at the fixed XY table holding. The unwrapped and unwrapped phase of the form function, angle(F_{bs}), of a 22 mm TC/Co sphere (rigid behaviour) is presented in Fig. 7.1. It can be noticed that linear mismatch exists, which can be ascribed to expected inaccuracies in the estimation of range. A correction factor was applied in order to remove the difference with a value of R – 0.0062, for this case, with the resulting phases shown in Fig. 7.2, together with the geometrical approximation calculated from Eq. 7.2. The figure of 0.0062 was obtained empirically. This exercise is an attempt of achieving an absolute calibration, continued later in in Fig. 7.4, and done for illustration purposes.

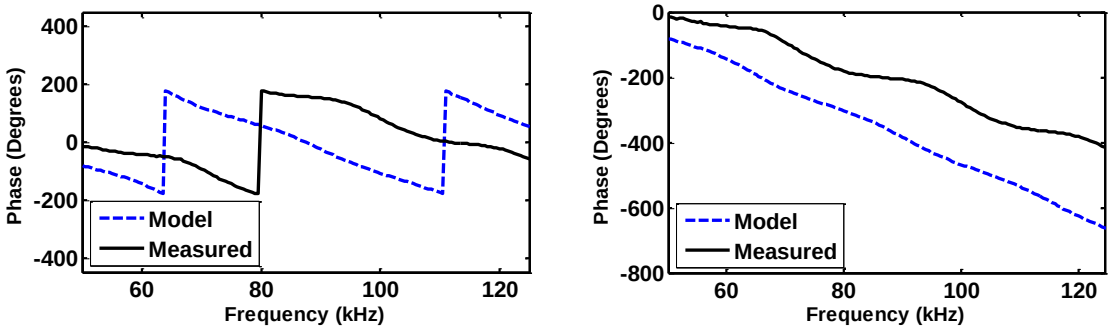

FIG. 7.1. Wrapped (left) and unwrapped (right) absolute form function phase of a 22 mm TC/Co sphere. Without range correction factor.

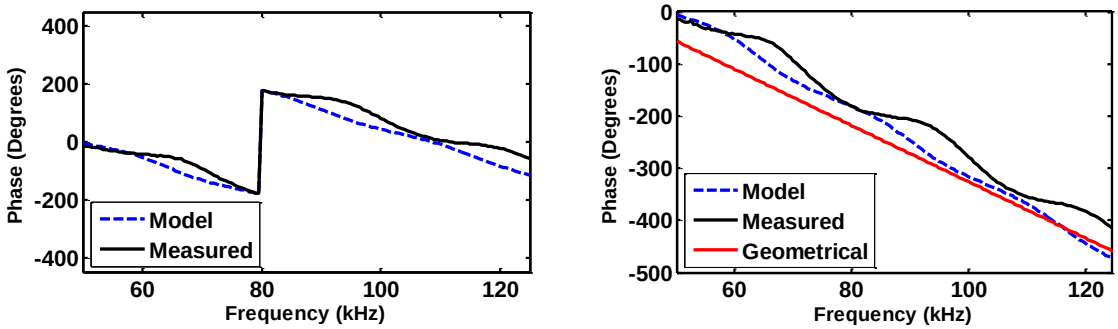

FIG. 7.2. Wrapped (left) and unwrapped (right) absolute form function phase of a 22 mm TC/Co sphere. With range correction factor. Geometrical approximation included in red.

The sensitivity of the phase of the form function to a correction of 6.2 mm is evident, thus illustrated the desirability of removing the range factor from the determination and representation of phase. As mentioned in Section 3.4, the rate-of-change of phase has been used in this capacity, essentially removing range. The discrete derivative (Matlab function 'diff') was applied to the unwrapped, corrected curves of Fig. 7.2 (Right), with the results shown in Fig. 7.3. This approach was applied by (Mitri et al., 2008) with the rate-of-change of phase, *RCP*, as

$$RCP = \frac{diff\left\{UW\left[angle\left(f_{bs}\left(f\right)\right)\right]\right\}}{diff\left(f\right)}, \tag{7.3}$$

with units are given in degrees per segment (Hz) in the manner of (Yen et al., 1990).

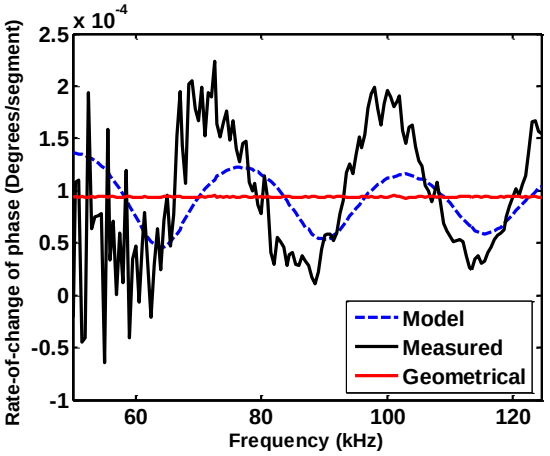

FIG. 7.3. Rate-of-change of phase from the 22 mm TC/Co sphere.

Although the peaks of the oscillations fairly coincide, a slight difference in the slope remains. One of the disadvantages of the use of the derivative is the noisy nature of the curves computed from experimental data, as clearly observed in Fig. 7.3. Furthermore, in some cases this approach can potentially obscure the underlying physical phenomenon or provide

insufficient information. For example, in elastic scattering the resonances are only seen as noise-like sharp spikes. An alternative representation could be found by directly fitting a line to the corrected range-corrected curves of Fig. 7.2 and then subtracting it. This was performed with Matlab's 'polyfit' function, resulting in the curves of Fig. 7.4.

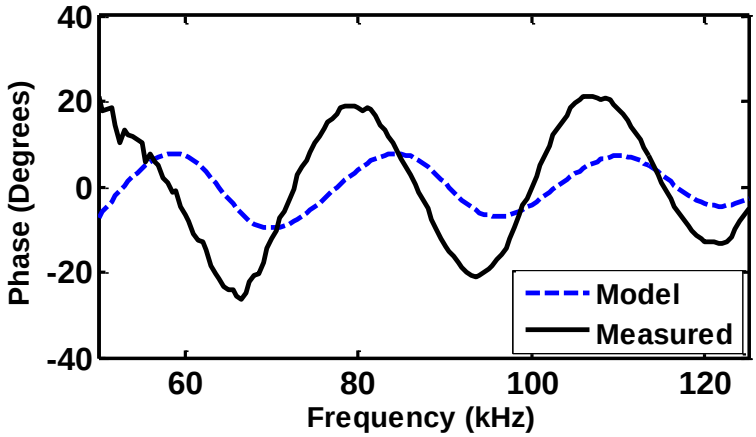

FIG. 7.4. Slope-corrected absolute form function phases from Fig. 7.2 (right plot), corresponding to the 22 mm TC/Co sphere.

It can be observed that the slopes of both the modelled and measured responses have been brought to zero, although the oscillations do not quite agree. These locations are not affected by the range correction factor applied prior to slope removal. The lack of agreement of Fig. 7.4 shows the difficulties in achieving an accurate absolute phase calibration, even when empirical correction factors are added. In contrast, it has been demonstrated that the dual-frequency method allows for accurate comparison between modelled and measured data. Two more examples of agreement are given in Fig. 7.5, with a total RMS error of 18° for the 15 mm case, and 10.5° for the 20 mm case. The mean value for the 15 mm sphere is approximately -54°, and -46.6° for the 20 mm, which are relatively near the 0° (no phase shift) expected from an ideal point scatterer.

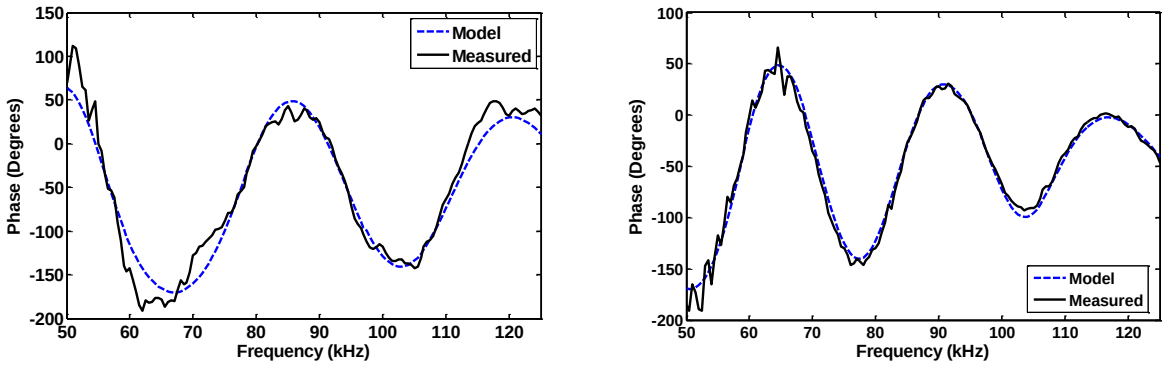

FIG. 7.5. Dual-frequency phase measurements.

Left, 15 mm dia. TC/Co sphere. Right, 20 mm dia. TC/Co sphere.

It is known that the smooth oscillations seen in the amplitude and phase spectra of a rigid target are due to Franz (creeping) wave diffractions, which are linked to the zeroes of the transfer function (Hirobayashi and Kimura, 1999). Since their period frequency, f_{Franz}, is given by the path length, it can be obtained from the following expression (Medwin and Clay, 1998)

$$f_{Franz} = \frac{1.22c}{2\pi a}, \tag{7.4}$$

which for a speed of sound c=1468 m/s, and a sphere with radius a = 10 mm, is approximately equal to 28500 Hz. This corresponds well to the period observed experimentally and shown in Fig. 7.6. Also, the period can be approximately estimated from the time difference, Δt, between consecutive arrivals. This difference can be observed in Fig. 7.7 and results in

$$f_{Franz} = \frac{1}{\Delta t} = \frac{1}{35\mu\sec} \approx 28600\ Hz \tag{7.5}$$

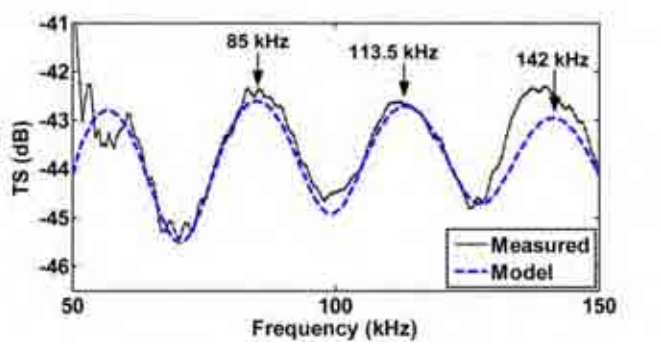

FIG. 7.6. Target strength of a 20 mm diameter tungsten carbide sphere.

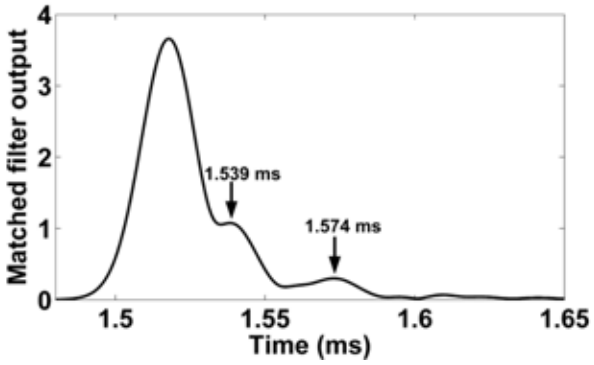

FIG. 7.7. Matched filter envelope output of echo from the 20 mm diameter TC/Co.

It has been proposed that the backscattered pressure approximates a minimum phase behaviour as the evaluation point moves away from the target and into the far field. In the near field, the backscattered field has been determined to be non-minimum phase (Hirobayashi and Kimura, 1999). Although his was not verified, it is believed that it deserves more attention, in order to determine the characteristics of scattered sound fields in underwater acoustics.

7.2.2 Elastic behaviour

For the case of a larger metallic spheres geometrical approximations are ill-fitted, because of the presence of mechanical resonances in the frequency range, which correspond to poles in the transfer function. This can be observed in the form function unwrapped phase trends of Fig. 7.8, where the deviation could be analogous to the findings of Lyon, who established that system phase deviates from propagation phase as more poles and zeroes are present, with poles corresponding to resonances (Lyon, 1983). As previously mentioned, the rate-of-change of phase is very sensitive to some target elastic resonances, and this is clearly noticed in Fig. 7.9.

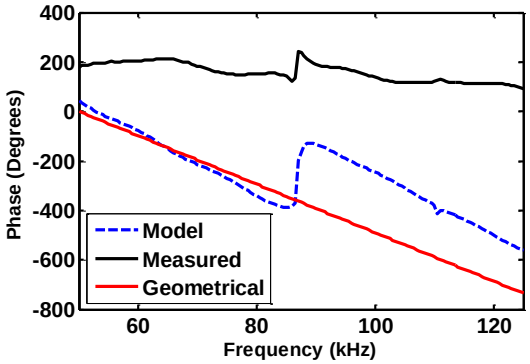

FIG. 7.8. Unwrapped phase from 40 mm TC/Co with correction.

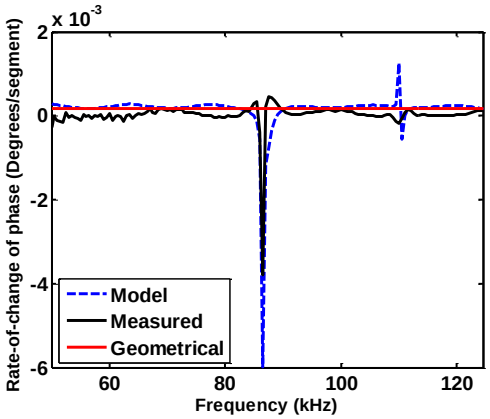

FIG. 7.9. Rate-of-change of phase for the 40 mm TC/Co sphere.

As previously observed, the dual-frequency phase of elastic targets presents large jumps, and random 360° ambiguity factors. These characteristics appear to diminish the usefulness of the method, as it is difficult to ascertain the level of agreement. In this respect, plotting replicas of one of the curves, scaled by 360° factors, can make the coincidence more obvious. This was adopted for the 40 mm sphere in Fig. 6.4, but the computation of a quantitative error figure is still impeded. However, compensation of existing 360° factors is relatively simple, and an algorithm was implemented for that purpose. After one of the curves is arbitrarily chosen to be the template and placed along the 0° phase line, the other is corrected at each frequency point and the separating phase ambiguity is removed, either adding or subtracting 360° factors. When no real agreement exists, this algorithm produces a disjointed curve with several phase wrapping jumps. This prevents false conclusion of agreement to be reached. After correction, remaining error is then found in the range from 0 to 360°. In Fig. 7.10 the input (left panel) and output (right panel) of this procedure are presented. Although the multiple changes are abrupt, particularly for the larger spheres, the agreement hinted in the original image is confirmed after correction. This permits quantitative comparison, and, for example, the total RMS error is 32.2° for the 40 mm sphere, and 76° for the 84 mm sphere. The larger error in the 84 mm case is explained by the higher number of resonances, since it is at the drastic jumps where most of the disagreement occurs. In this respect, the frequency resolution of 500 Hz may not be fine enough to capture every resonance. Furthermore, some peaks in the predicted curve do not appear in the experimental data. Measurements for the 40 mm sphere were obtained in the stepped-frequency mode, whilst the 84 mm target was insonified with an LFM pulse. As previously discussed, the LFM approach is much faster, with the whole bandwidth measured in a few seconds. On the contrary, the stepped frequency method can last several hours (depending on the frequency step and the number of pings).

Although suffering from lower SNR, a chirp signal can acquire, almost instantly, rich information from the echoes received. Data can then be simultaneously presented in the time-domain, as well as in amplitude and phase spectra, as demonstrated in Fig. 7.11.

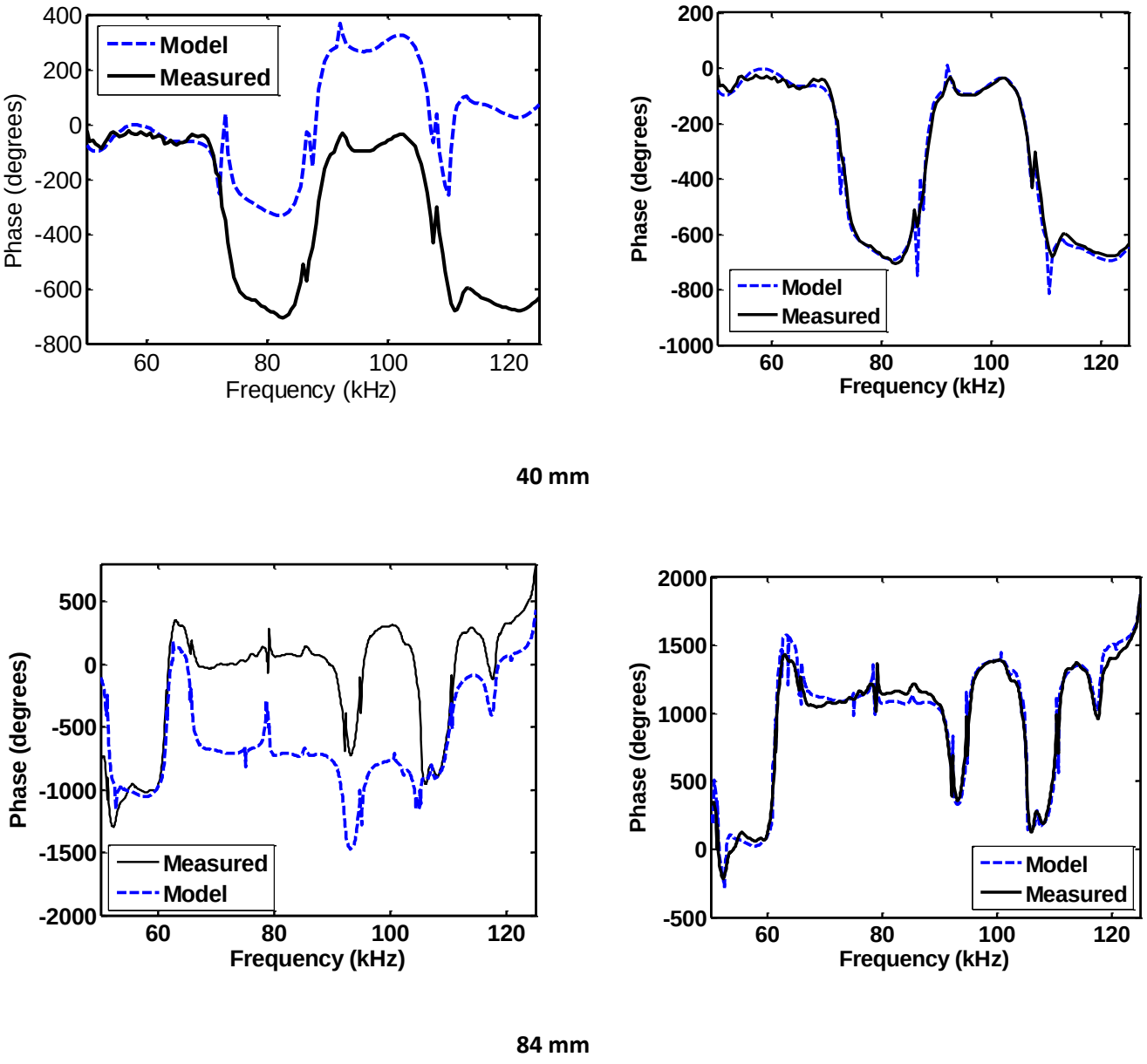

FIG. 7.10. Dual-frequency differential target phase from elastic metallic spheres. Original (left) and corrected for phase ambiguity (right). Top, 40 mm, diameter measured with stepped-frequency CW pulses. Bottom, 84 mm diameter, measured with LFM pulse.

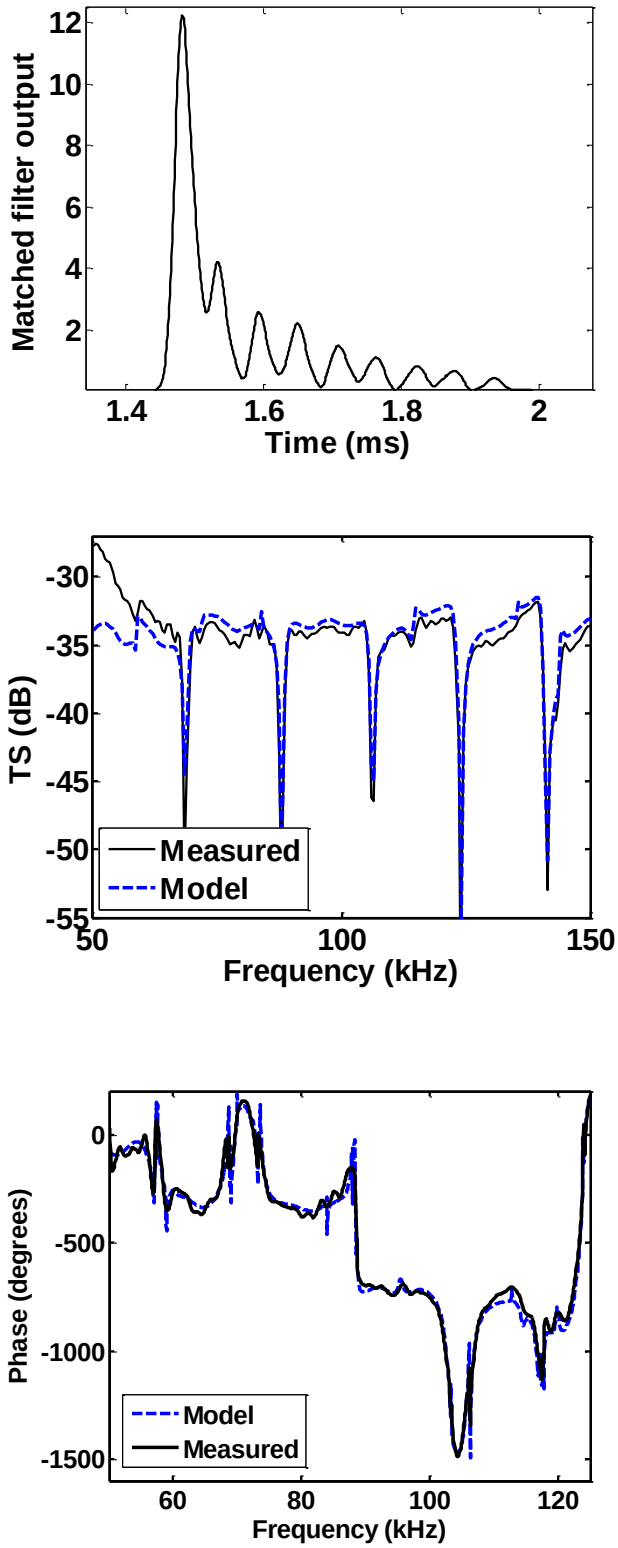

FIG. 7.11. Scattering from 75 mm TC/Co sphere.

Top, frequency domain. Middle, amplitude spectra. Bottom, phase spectra.

7.2.3 Experiments with two solid spheres

In order to further explore the usability of dual-frequency target phase, a series of experiments with simultaneous insonification of two spheres were performed. Two targets with the same dimensions, but different material properties, were insonified simultaneously with an LFM pulse, as depicted in Fig. 7.12. The spheres were a 24 mm in diameter tungsten carbide spheres, one with nickel binder and the other with cobalt binder.

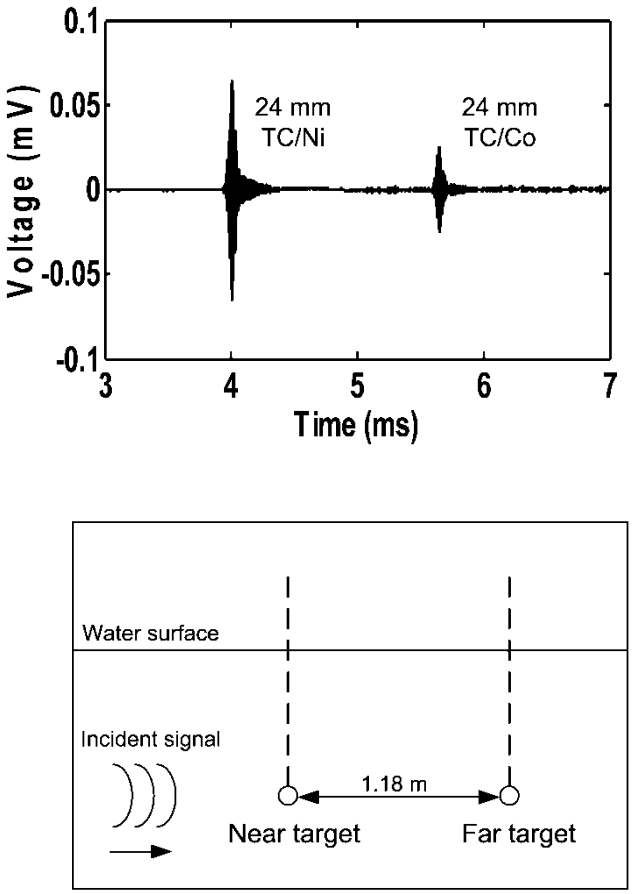

FIG. 7.12. Dual-target arrangement for simultaneous insonification. Top, raw received echoes from a 24 mm diameter TC/Ni and a 24 mm diameter TC/Co sphere placed along the horizontal axis and separated by approximately 1.18 m, as shown in the bottom.

Calibrated dual-frequency phase from the arrangement shown in Fig. 7.13 demonstrate that this approach eliminates range effects, as the response of the two targets coincides, as seen in Fig. 7.13. The plot does not show the frequency range from 50 to 60 kHz because of poor SNR associated with pulse measurements and no averaging used in this instance.

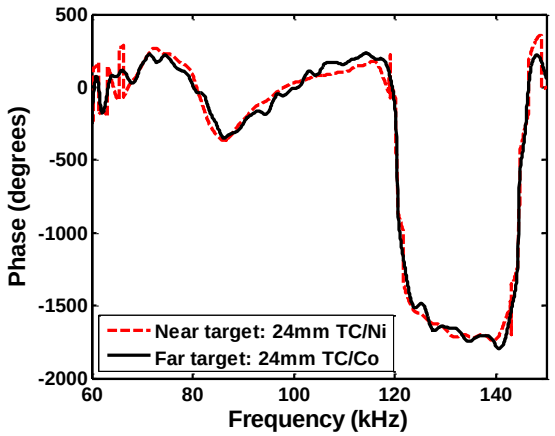

Fig. 7.13. Near and far target differential phase for simultaneous insonification of a 24 mm TC/Ni and a 24 mm TC/Co sphere, with their received echoes shown in Fig. 7.12.

Agreement in phase for this LFM measurement appears to be better than TS, as seen by the noisy far-target curve of Fig. 7.14 (top panel), where the low SNR seriously deteriorates agreement. Variability of phase measurements is mostly determined by signal-to-noise ratio, but the spectral separation chosen has an impact as well, due to phase noise. Phase measurements averaging 100 LFM pings with a 100 μsec duration presented an standard deviation of approximately 6° in this experiment.

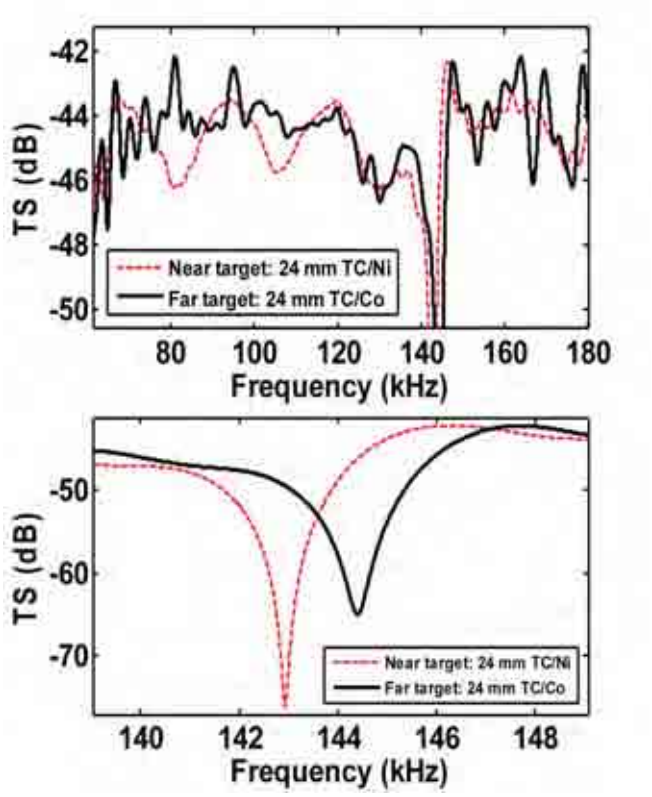

FIG. 7.14. Target strength from the two horizontally-aligned targets insonified by the LFM pulse. Top panel, wide spectral response. Lower panel, resonant notches.

Differences in the frequency locations of the resonant notches, apparent in the lower panel of Fig. 7.14, can confuse the identification of the spheres as having the different dimensions. A joint scrutiny of amplitude and phase responses could help to correctly identify the received echoes as produced by geometrically-identical targets with slightly different material characteristics. This is compared to Fig. 7.15, with calibrated TS and phase from two TC spheres different in size and material properties. The TS plot (top panel) shows two resonant notches located well apart, which is confirmed in the phase graph (lower panel). In this case, both representations indicate that echoes were produced by spheres significantly different in dimensions and physical characteristics.

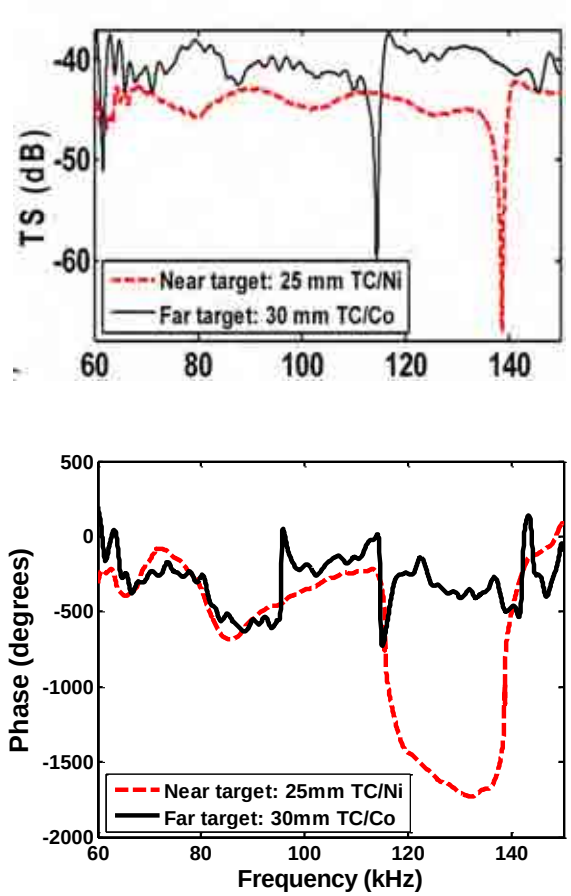

FIG. 7.15. Scattering from a 25 mm TC/Ni and a 30 mm TC/Co sphere insonified simultaneously. Top, target strength. Bottom, differential target phase.

7.3 Air-filled shells

7.3.1 Table-tennis balls

Acoustic scattering from table tennis balls has been studied in the past, for potential usage as calibration targets (V.G. Welsby and Hudson, 1972). It was advanced that these targets could approximate a perfectly reflecting target, although they were later abandoned due to the difficulty of predicting the exact characteristics of the plastic (nitrate cellulose). This is observed in Fig. 7.16 were the predicted TS and phase do not present the same characteristics as the measured values.

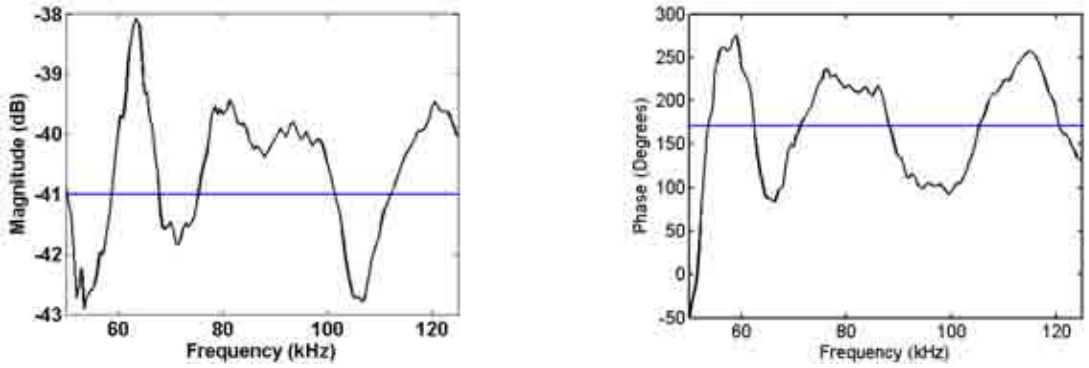

FIG. 7.16. Scattering from ping pong ball. Left, target strength, right, phase. Black line, measured values, blue line predicted values.

Welsby and Hudson estimated the target strength to be -42 dB, but this was done reportedly done for a ball with a radius of 1.6 cm (V.G. Welsby and Hudson, 1972). This could be a mistake since, as far as the author's knowledge, official ping pong balls passed from a radius of 1.9 cm to the current 2.0 cm. The mean value of the differential phase 180°, which agrees with the phase polarity reversal expected from an acoustically 'soft' target. Although a different μ value changes the location of peaks and valleys, the value still oscillates around a mean of 180°. The acoustic field scattered from acoustically 'soft' objects has been determined to have a minimum phase property (Hirobayashi and Kimura, 1999). Verification of this claim was left for future work.

7.3.2 Ceramic shells

A ceramic air-filled shell made of 99.9% pure alumina (Al_2O_3) was used. These flotation spheres (Deepsea Power & Light, San Diego, CA, USA) have high buoyancy and extreme pressure resistance, for use in depths greater than 4000 m. The target, shown in Fig. 7.17, has a nominal outer diameter of 91.44 mm (±0.2 mm) and a thickness of 1.3 mm. Material is specified to be non-porous. Air inside is at an approximate pressure of 0.5 atm (P. R. Atkins et al., 2007c). The acoustic properties of these specific shells have been previously assessed as potential calibration targets (P. R. Atkins et al., 2007c, Francis et al., 2007).

FIG. 7.17. Air-filled ceramic shell.

Broadband target strength measurements are presented in Fig. 7.18, together with predicted values using the Faran model. The agreement was enhanced by parameter optimization through multivariate minimization in Matlab. Shear wave velocity in the shell and shell thickness were the most important factors affecting the model fit to the experimental data. Automatic minimization was therefore run with shell thickness and shear wave velocity as the free parameters. The process, applied in the frequency range with higher SNR (from above 60 kHz) yielded a shear wave value, C_T = 6350 m/s. The longitudinal wave speed was, CL = 11011 m/s (as in (Francis et al., 2007)). The resulting shell thickness was 1.346 mm, although the thickness has been found to be inhomogeneous (P. R. Atkins et al., 2007c).

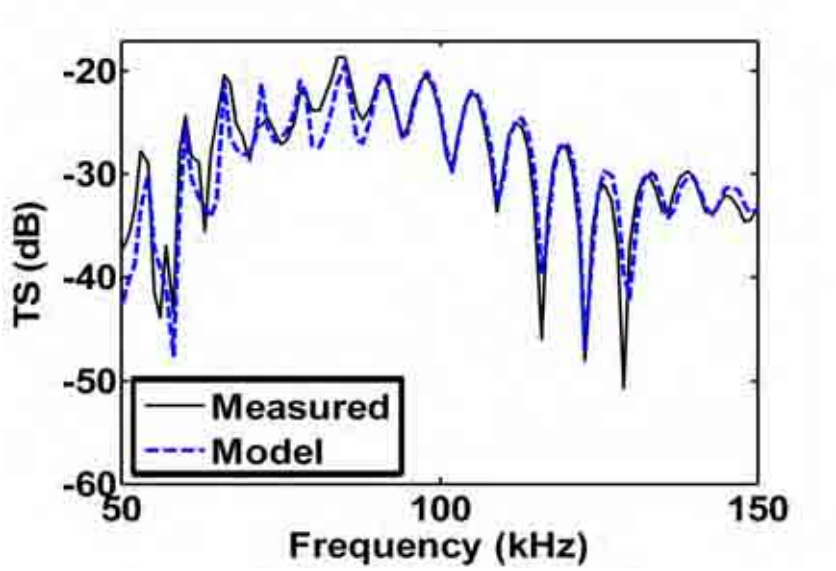

FIG. 7.18. Modelled and calibrated TS for the 91.44 mm diameter ceramic air-filled shell.

As in the case of the solid sphere, oscillations seen in Fig. 7.18 have also been ascribed to interference between specular reflection and various types of circumferential waves, travelling inside or outside the shell at speeds determined by the frequency and vibration mode (Shirley and Diercks, 1970). These waves have been identified as the diffracted Franz waves observed in solid spheres, as well as flexural symmetric and anti-symmetric Lamb waves of order zero, s_0 and a_0 respectively (Ayres et al., 1987). For a water-filled shell additional waves travelling through the interior and bouncing repeatedly on the concave boundaries can also be found, especially in lower frequencies enhancing penetration (R. Hickling and Means, 1968). The air-filled shell presents a high impedance contrast target that negates transmission (Shirley and Diercks, 1970), and behaves similarly to a shell containing a vacuum (Diercks and Hickling, 1967). In the time domain, the front-face echo, occurring at 1.59 ms, is followed by a larger peak corresponding to the flexural surface wave travelling along the outside of the

circumference with a speed close to 2000 m/s. In a similar experiment, analogous behaviour was reported by (Mikeska, 1970).

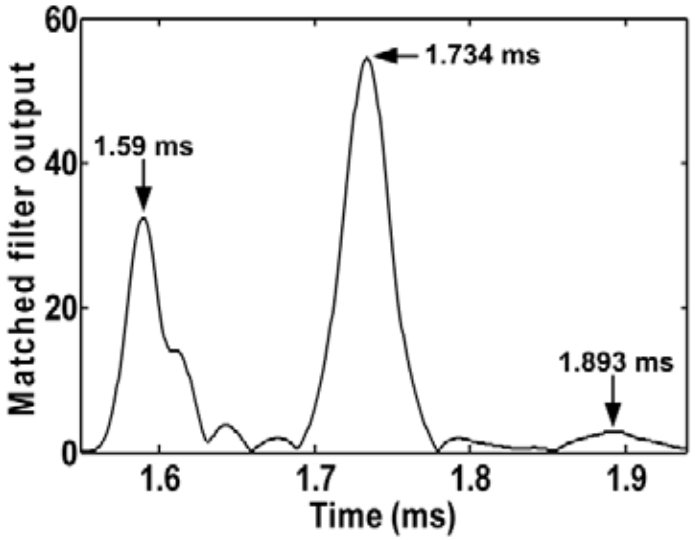

FIG. 7.19. Ceramic shell time domain response.

The discussed echo formation mechanisms, active in the air-filled thin shell, are more clearly observed in the extended modelled response presented in Fig. 7.20. From this plot it can be noted that the entire measured range of Fig. 7.18 forms a protuberance in the response. This corresponds to a zone of strong flexures caused by the anti-symmetrical Lamb waves (Ayres et al., 1987), also denoted as the midfrequency enhancement (Gaunaurd and Werby, 1991). After that section, a periodic pattern caused by the Lamb s_0 contributions is observed (Ayres et al., 1987).

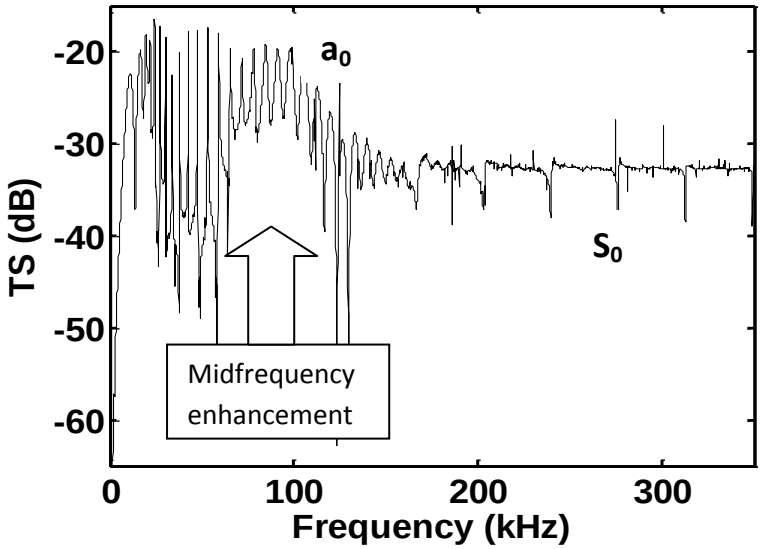

FIG. 7.20. Extended modelled TS for the 91.44 mm diameter ceramic air-filled shell.

The modelled and measured phase responses, shown in Fig. 7.21, are in fair agreement over a considerable bandwidth segment (60 to 150 kHz), with an RMS error of 82° after the ambiguity-correction algorithm was applied (Fig. 7.21, bottom). The mechanism causing a rapid phase ramp roughly between 100 and 120 kHz cannot be clearly identified solely from the TS plot, not in Fig. 7.18, nor Fig. 7.20. This indicates that relevant acoustic phenomena could be more strongly manifested in the phase component.

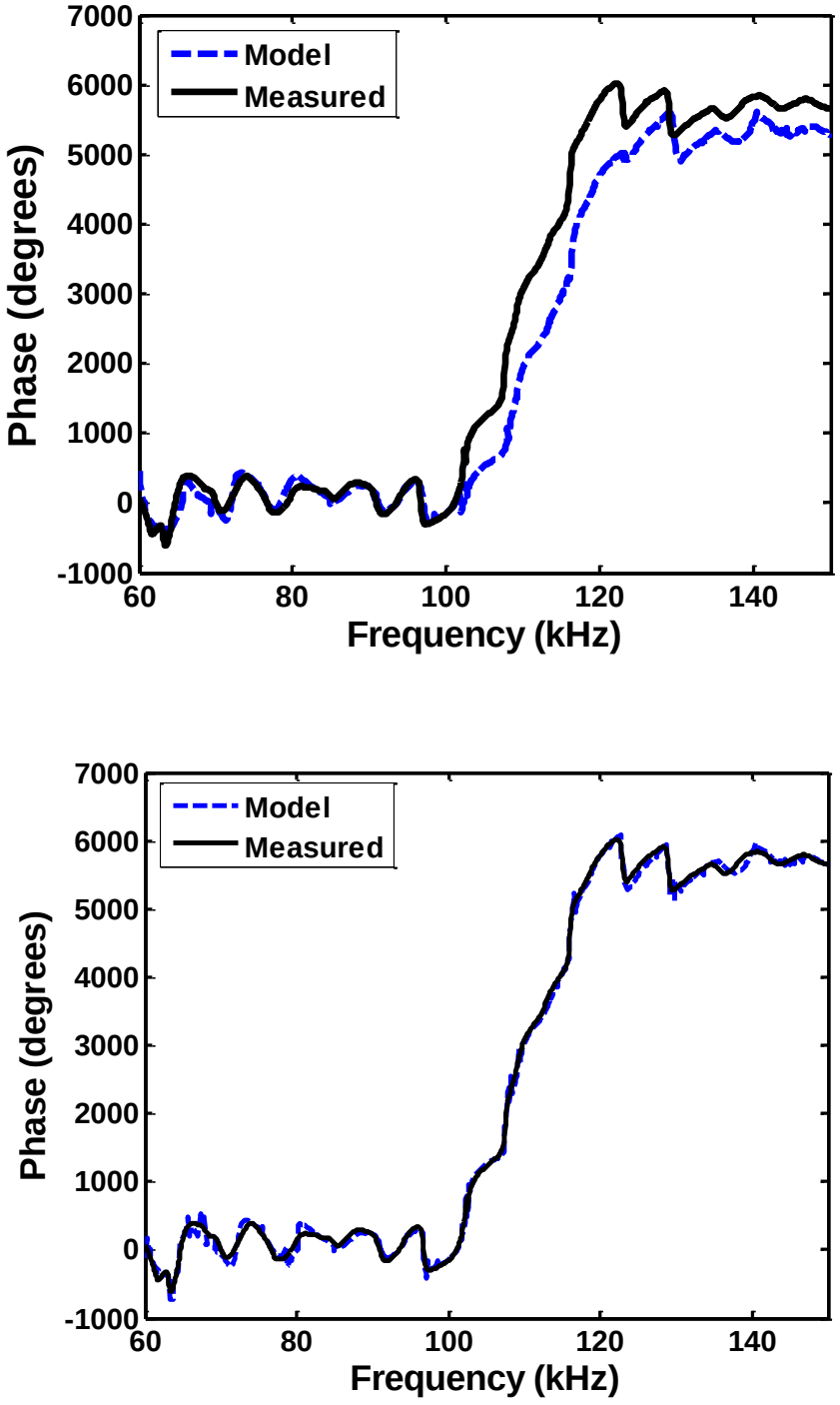

Fig. 7.21. Modelled and calibrated phase for the 91.44 mm diameter ceramic air-filled shell. Top, unwrapped phases. Bottom, unwrapped phases and application of the 360° ambiguity correction method described in Section 7.22.

As discussed previously, resonant scattering theory explains scattering from a shell as an elastic behaviour superimposed on a background. For a thin shell, the correct background has been shown to approximate an acoustically soft background at low frequencies and a rigid background at high frequencies (Werby, 1991). It appears that the abrupt phase increase may be connected to the transition to a rigid background. As previously discussed, Hickling represented the behaviour of a rigid scatterer using the phase of the form function. For a solid sphere, shown in the right panel of Fig. 7.22, this curve converged to a position in the reflector. The modelled form function of the shell has been represented in the same manner in Fig. 7.21, left panel. The transition frequency, near 123 kHz, approximates the start of the ramp in the dual-frequency plot (near 100 kHz), after the spectral separation, μ=1.2, has been accounted for. Verification of a potential sensitivity of target phase to the acoustical background could be attained by studying shells with different materials and thickness.

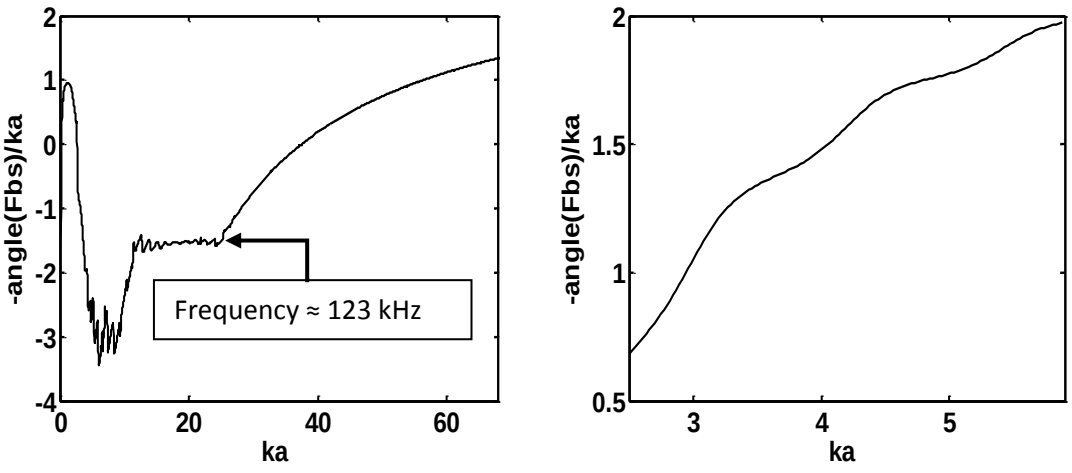

FIG. 7.22. Hickling's representation of the phase of the form function.
Left, ceramic air-filled shell. Right, solid 20 mm TC/Co sphere.

7.4 Finite solid cylinders

A series of acoustic measurements were conducted on bluntly truncated metallic cylinders with circular cross-section. A selection of these results is presented in this section. The cylinders were suspended with loops of strings attached to the end, submerged horizontally and rotated in the horizontal plane. Measured backscattering was compared with theoretical solutions. As discussed in Section 2.4.7, finite cylinders can be modelled by the exact solution to the infinite cylinder, whilst the ends do not substantially intervene. Stanton's finite cylinder model was found to be unreliable for cases departing from broadside incidence. In addition, hybrid Finite Element/Boundary Element (FE/BE) numerical calculations were developed by Dr. Trevor Francis, using various mesh resolutions in order to encompass the relevant frequency range. Finally, a Finite Element model was developed in COMSOL by Ms. Nuria González (González Salido, 2012).

7.4.1 Broadside and end-on incidence

Initial measurements were conducted without tilt or rotation applied. A set of cylinders was obtained from an 2 cm-diameter stainless steel rod that was cleanly subdivided in segments. Since the exact steel alloy was unknown, material parameters were initially approximated from tables and subsequently optimized by fitting the resonant notches, in the manner used for solid spheres. The resulting values were a density of 7910 kg/m^3, a longitudinal wave speed, C_L, of 5400 m/s, and transversal (shear) wave speed, C_T, of 3100 m/s. The resulting target strength agreement for broadside incidence is presented in Fig. 7.23, for a 12 cm long steel cylinder. As expected, the TS for an infinite cylinder is larger, but the FEM (COMSOL), BEM, and measured TS values fairly agree. As in the case of the sphere, resonant minima have been linked to the frequencies of eigenvibration (Bao et al., 1990).

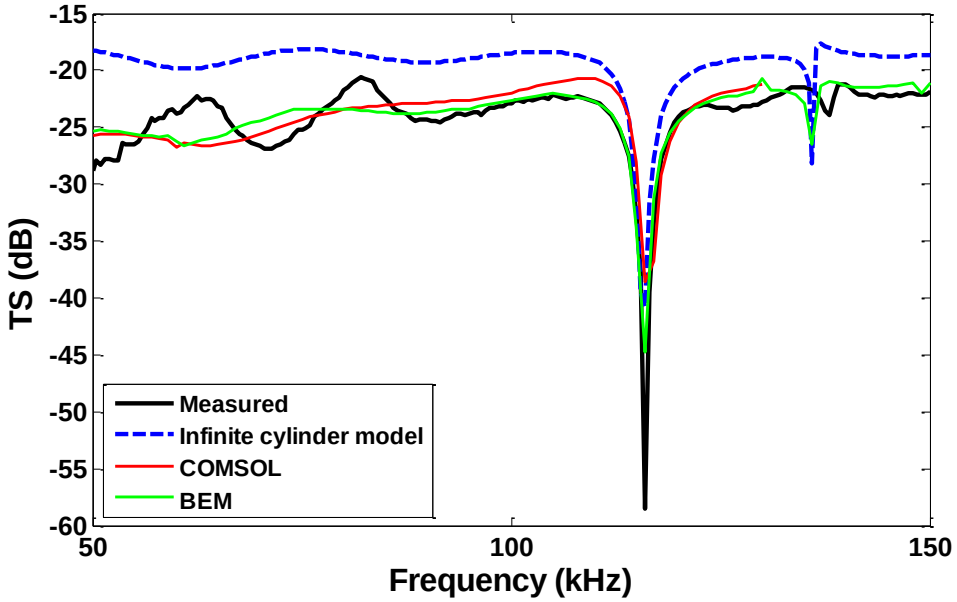

FIG. 7.23. Target strength from a steel cylinder of length, L=12 cm, and radius, a=1 cm. Broadside incidence.

Target phase, measured and calculated with the infinite cylinder model, is shown in Fig. 7.24 for the 12 cm-long steel cylinder, and in Fig. 7.25 for the 24 cm-long steel cylinder (from the same rod). Agreement was not excellent and the curves could not be submitted to the ambiguity correction algorithm. Although the phase trends appear, in general, similar, exact coincidence is not achieved. This is particularly evident in the rigid oscillations at lower frequencies. Nevertheless, the two resonances present are detected in the 12 cm case (less frequency range in the other plot). Frequency discrepancies in the diffraction-induced features may indicate variations in the path length covered by the circumferential waves. This can be caused by slight unwanted tilt angles in the vertical axis or inexact orientation angles. It may be noted that the disagreement in the rigid oscillations also occurs in the TS plot of fig. 7.23. Dual-frequency phase obtained from the BEM model with 1000 Hz steps and μ = 1.2 is also shown in Fig. 7.24. More frequencies and better resolution are needed properly evaluate it. The construction of an even finer mesh for higher frequencies may be necessary.

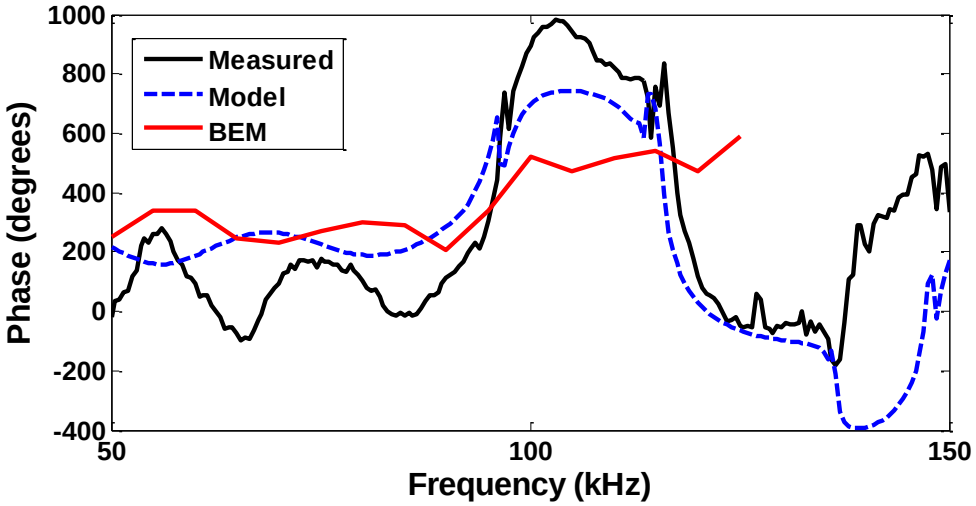

FIG. 7.24. Target phase from a steel cylinder of length, L=12 cm, and radius, a=1 cm. Infinite cylinder model. Broadside incidence.

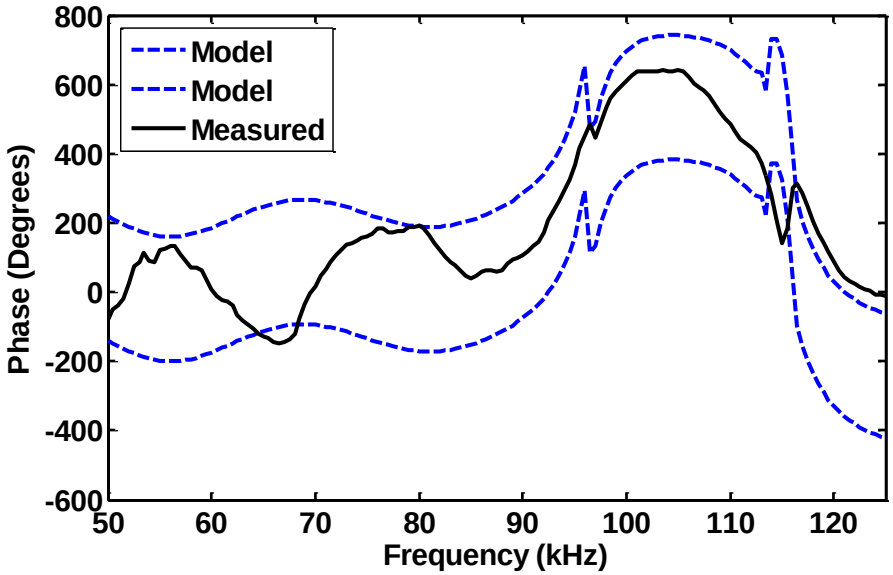

FIG. 7.25. Target phase from a steel cylinder of length, L=24 cm, and radius, a=1 cm. Infinite cylinder model in blue, with 360°-scaled replicas. Broadside incidence.

Backscattering from cylinder end-on incidence is presented in Fig. 7.26. It is well known that enhancements may occur in this case, due to waves propagating in meridional and helical paths along the cylinder and reflecting back off the far end (Gipson and Marston, 1999, P.L. Marston, 1997).

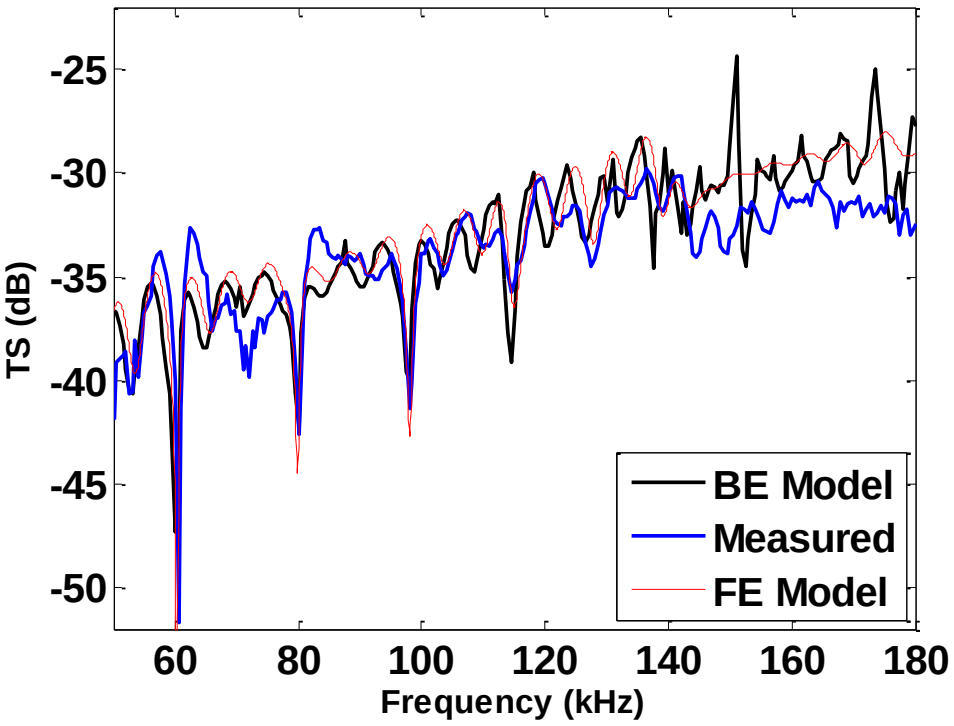

FIG. 7.26. Target strength from 12 cm-long steel cylinder for end-on incidence.

7.4.2 Oblique incidence

As previously discussed in section 2.3.2.4 concerning target orientation, finite cylinders are useful to study the effects of oblique incidence on an elongated body. The rotational device described in Section 4.4 was used to rotate the targets in the horizontal plane, as illustrated in Fig. 7.27, where the axis of the cylinder forms an angle ψ with normal sound incidence.

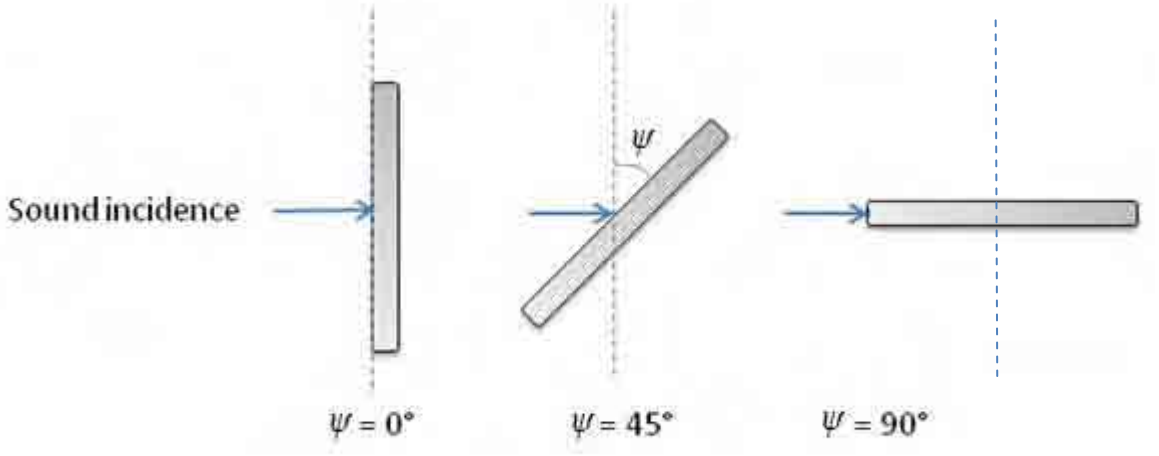

FIG.7.27. Cylinder rotation and angle of incidence.

Since neither the infinite cylinder model (Li and Ueda, 1989), nor Stanton's finite cylinder model (Stanton, 1988b), consider end contributions, these theoretical solutions become less applicable as the target is rotated. It has been determined, through comparison with T-matrix solutions, that Stanton's finite cylinder model is valid up to a 20° angle deviation from broadside (Partridge and Smith, 1995). However, experimental results in the present work indicate that the range of agreement may be even smaller in practice. For this reason, a Boundary Element Model (BEM), developed by Dr. Trevor Francis, was used to compare directivity patterns. Due to the computational costs of the fine mesh required for higher frequencies, a first approximation to the problem covered a range of frequency from 50 to 150 kHz, in 1000 Hz steps. This frequency interval corresponds to a rigid scattering regime. Extremely high rotation resolution of 0.25° could be achieved. BEM target strength results for the 12 cm long steel cylinder described in the previous section are presented in Fig. 7.28, where 180° corresponds to broadside incidence and 90° is end-on incidence. Patterns are broadly in agreement in the measured and simulated plots. Rotation resolution in the

measured values, 1.8°, may be too poor to show the clearly defined bands seen in the BEM results. Frequency resolution can also be considered poor, with steps of 1 kHz for the BEM model and 500 Hz for the measurements. A possible experimental source of error could be the stabilization time in between movement. For this data, the time was set to be 5 minutes. It is unknown if the interval is too short, and subtle movements (not visible from the top of the tank) remain in the cylinder, as it is perturbed by the rotation.

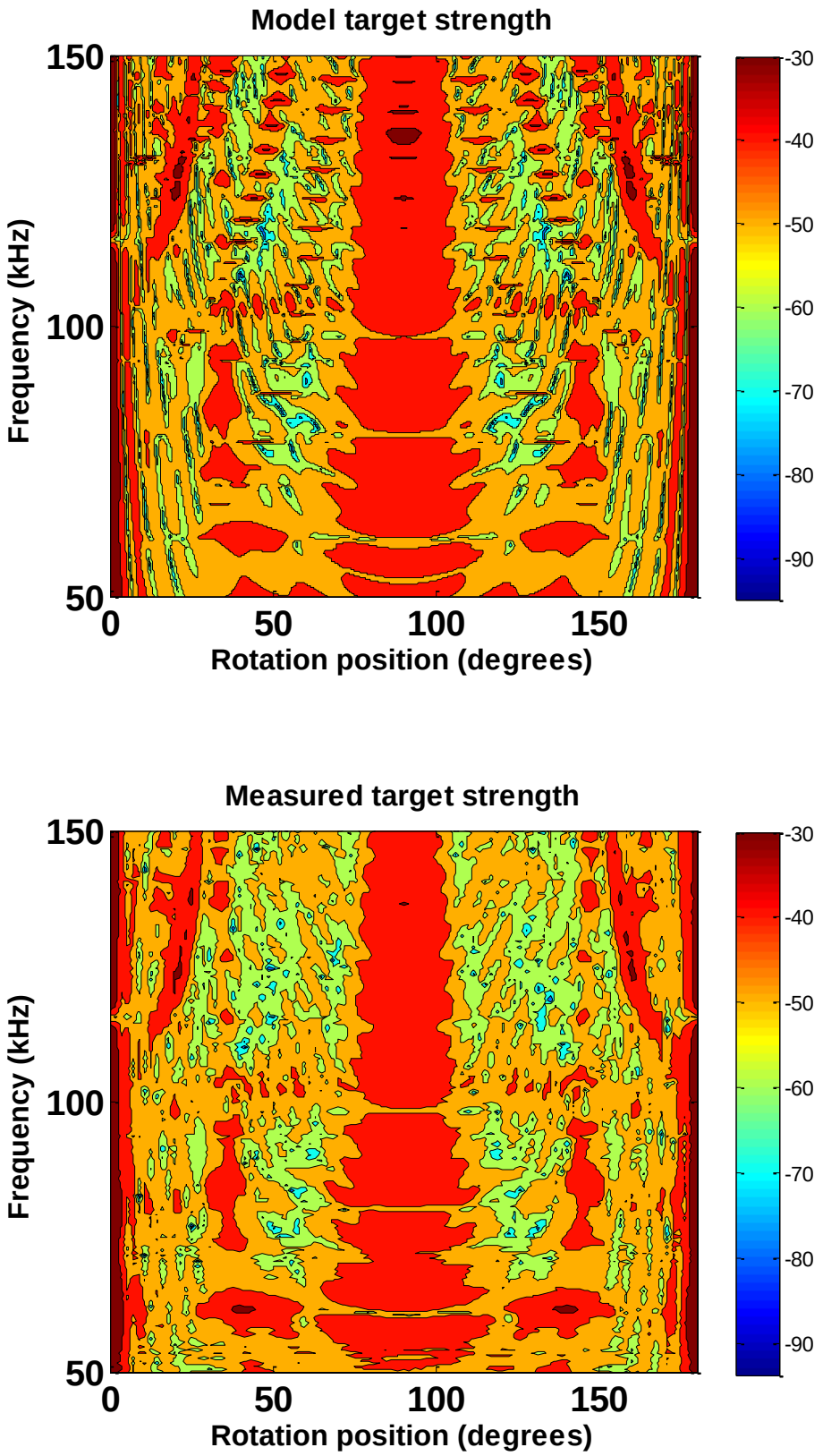

FIG.7.28. TS as a function of orientation and frequency. Angles of 0° and 180° in the rotation axis correspond to broadside incidence. Top, BEM model. Bottom, measured.

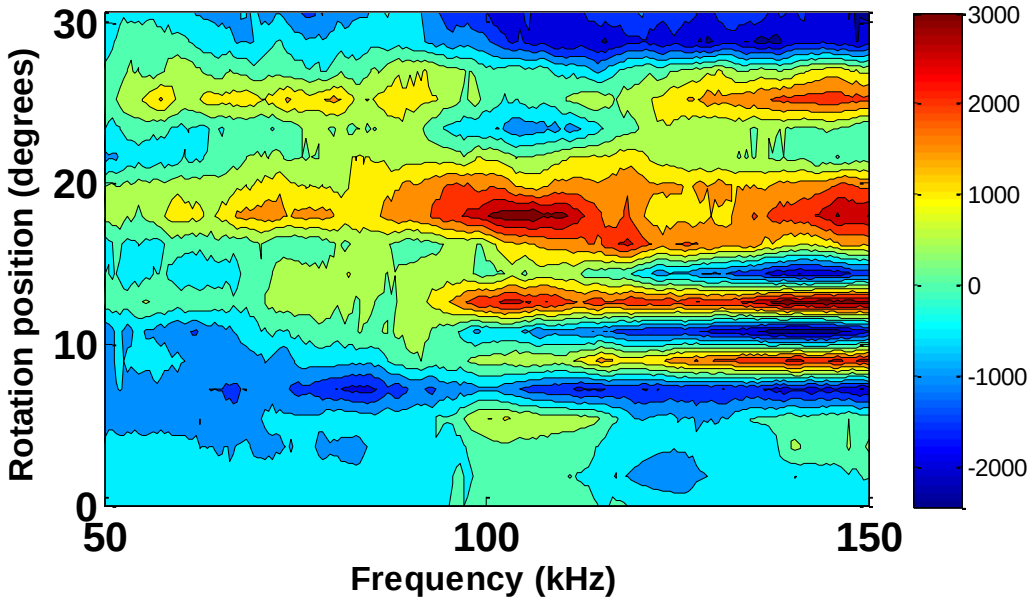

FIG.7.29. Target phase as a function of orientation and frequency. Steel 12 cm cylinder. Rotation from broadside (0°) incidence to 31.8°.

The target phase shown in Fig. 7.29 is complicated to interpret. Target phase characteristics from the BEM calculations did not agree with the measured values. It is thought that a correction factor is missing, although the exact formulation was not found at the time of submission. Without theoretical confirmation of target phase (beyond the approximation at broadside incidence) it is difficult to draw clear and reliable conclusions from Fig. 7.29. However, based on the most dramatic phase changes with respect to frequency at a given rotation position, some hypotheses could be advanced. For example, the bands where the phase abruptly changes could be related to the coupling angles of longitudinal, shear, or Rayleigh waves. This could be the case around 14° which is close to the longitudinal wave coupling angle. Near 28° we see another band that could be related to the shear wave coupling angle. However, the strong change close to 18° is not clearly explained. This approach is similar to that of (Mitri, 2010).

7.5 Prolate spheroid

An aluminium prolate spheroid, pictured in Fig. 7.30, was machined at the workshop of the University of Birmingham and used as an acoustic target. A BEM model was developed by Dr. Trevor Francis in order to predict the rigid response of this target. Comparison is shown in Fig. 7.31.

FIG.7.30. Machined aluminium prolate spheroid.

Although exact agreement is not achieved, the main arch patterns are present in both graphs, and TS levels are similar. However, measurements show a much greater level of detail due to the resonant effects. Target phase was not calculated.

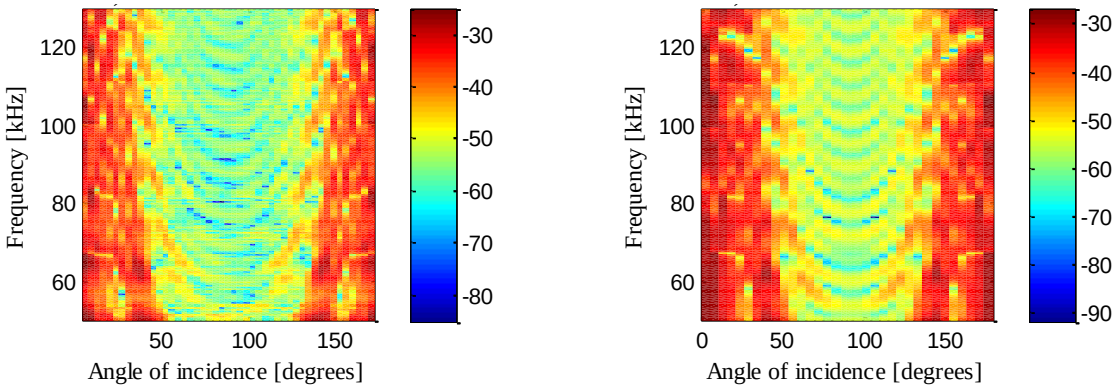

FIG.7.31. TS from aluminium prolate spheroid rotated 180°.

Left, measured. Right, BEM model.

8. CONCLUSIONS AND FURTHER WORK

8.1 Conclusions

This work has examined potential improvements to scientific sonar performance, aimed at fisheries and marine oceanography, with potential future applications to automatic target identification. From a broad perspective, this work contributes towards the efforts to enhance information levels utilized by sonar processors. It is clear that increasingly higher bandwidth capability, together with reliable, broadband calibration procedures have been very important in the technological development of sonar. It is in this context where the present work aims to contribute.

The detailed analysis on the variations in tungsten carbide spheres has demonstrated that even the most robust targets can potentially contribute to calibration degradation. The corrosion processes occurring in cobalt-based spheres was particularly interesting. Using tungsten carbide spheres with nickel binder can be advantageous since their corrosion resistance is evidently superior. This finding elicited the interest of assessing the possibility for acoustic detection of subtle surface changes induced by corrosion. Preliminary results appear promising, but more tests have to be conducted in order to reach conclusive results. The usage of phase in this context remained pending.

For improved range-resolution performance, phase distortion issues need to be taken into account, since they can potentially undermine the integrity of the probing waveform. Full-

system calibration, based on a complex deconvolution operation, appears to be the most flexible and suitable approach. Currently, correction of sonar phase response for underwater acoustics is relatively rare. Consequently, few methods are available, in contrast to the field of ultrasound medical imaging where this has been achieved successfully up to a frequency of 100 MHz. For this reason, the proposed extension to the standard-target method, incorporating phase would seem to be useful.

Parallel extraction of both the amplitude and phase response of a laboratory broadband sonar system has been demonstrated. The procedure described is relatively simple and does not require specialized facilities for precise alignment or substantial hardware modifications. It can be easily applied to stepped, continuous wave transmission or broadband systems incorporating pulse compression techniques. As expected, the extracted phase response exhibits non-minimum phase characteristics that imply potential distortion.

Target phase agreement between measurement and theoretical calculations has been demonstrated. This has proven useful for identification and added understanding of scattering processes. This additional parameter could add an extra dimension for characterization of scatterers. The subjacent principle is that phase contains information about the target, which may add to that in the amplitude. For example, target phase manifests spatial decorrelation or temporal incoherence, which is exacerbated by dispersive characteristics, resonances, and target size.

The implementation of numerical BEM or FEM solutions was promising. The limited results presented in this work are of preliminary nature and more intensive efforts are planned in this respect. As expected, the main obstacles in this approach are the enormous requirements for computing power, which slow down the development process and restrict the range of targets that are convenient for practical simulation.

Results presented in Chapter 7 mainly have illustrative roles. The next step is the full interpretation and understanding of features in the target phase space, jointly with the amplitude spectra and the time-domain response.

8.2 Further work

It is envisioned that this work could serve as an initial effort towards the study and usage of signal phase in underwater acoustics, as conducted in this laboratory. Some related research lines and specific topics considered worthy of more detailed investigation are outlined below. Some of these points were addressed in this thesis but afford further development. Others, while not directly pursued, elicited interest during the course of this research. An overarching theme is to achieve an improvement in the interpretation of target phase.

- *Optimized phase unwrapping and phase ambiguity correction algorithms.*
- *Development of FEM/BEM numerical scattering solutions for elastic prolate spheroids.*
- *Algorithms for 'soft' and 'hard' classification.*
- *Further investigation of the response as transfer function, with the analysis of*

poles and zeroes.

- *Minimum and non-minimum phase characteristics of scattered acoustic fields.*
- *Investigation of the relationship between target phase and orientation of elongated objects.*
- *Application of target phase for the localisation of flaws or embedded gas enclosures.*
- *Acoustic backscattering measurements on marine organism such as shrimp.*
- *Closer investigation of acoustic scattering from cylinders with various angles of insonification. Relationship of target phase and echo enhancements.*

A. APPENDICES

A.1 Transducer modelling and filter-derived matching circuits

Determination of the transducer equivalent circuit model through admittance measurements was described in Section 6.2.1. In this Appendix, more details and background on the design of the matching band-pass filters are included.

A.1.1 Transfer functions

The complete filter-derived matching circuits is originated from the transducer model, reproduced again in Fig. A.1.1.

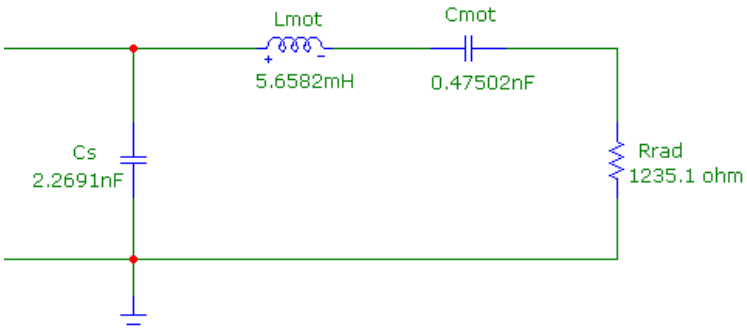

FIG. A.1. Reson TC2130 transducer circuit equivalent.

The transfer functions of the equivalent circuit, presented in Fig. 6.8, were obtained through impedance loop analysis, including an input resistance, R_{in}, as shown in Fig. A.2.

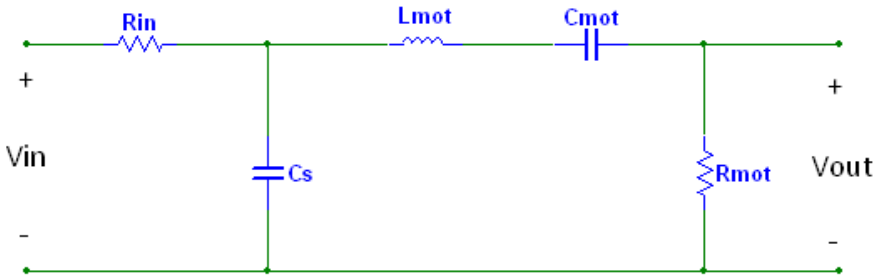

FIG. A.2. Generalized equivalent circuit with input resistance, Rin.

From impedance loop analysis in the complex frequency domain,

$$V_{out} = \frac{\left(\frac{1}{C_s s}\right)V_{in}}{R_{in} + \frac{1}{C_s s}} = \frac{V_{in}}{1 + R_{in}C_s s} \tag{A.1}$$

and

$$\frac{V_{out}}{V_{in}} = \frac{R_{mot}\left(\frac{1}{1 + R_{in}C_s s}\right)}{\frac{1}{C_{mot}s} + L_{mot}s + R_{mot}} = \frac{R_{mot}C_{mot}s}{\left(1 + R_{in}C_s s\right)\left(\frac{1}{C_{mot}s} + L_{mot}s + R_{mot}\right)}. \tag{A.2}$$

Multiplying and re-arranging,

$$\frac{V_{out}}{V_{in}} = \frac{R_{mot}C_{mot}s}{\left(C_{mot}L_{mot}R_{in}C_s\right)s^3 + \left(C_{mot}R_{mot}R_{in}C_s + C_{mot}L_{mot}\right)s^2 + \left(C_{mot}R_{mot} + R_{in}C_s\right)s + 1} \tag{A.3}$$

The response of this transfer function was analyzed through Bode plots, using the Matlab function 'bode.' The complete equivalent circuit, resulting when the matching network is added to the transducer, is presented in Fig. A.3.

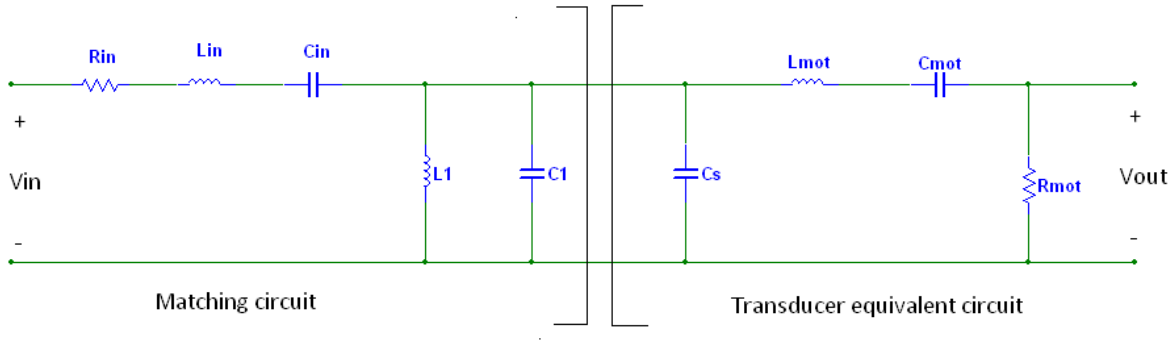

FIG. A.3. Transducer connected to matching circuit.

The complete transfer function was also obtained from impedance loop analysis in the complex frequency (Laplace) domain. It was of the form

$$\frac{V_{out}}{V_{in}} = \frac{Ns^3}{As^6 + Bs^5 + Cs^4 + Ds^3 + Es^2 + Fs + G} \tag{A.4}$$

These coefficients are algebraically long and cumbersome. They were introduced in the extract of the Matlab script included in the following page. The notation mostly follows the labels of Fig. A.3, with the capacitances in parallel, C_1 and C_s, joined in the variable 'C1plusCs.' For shortness, the subscript 'mot' (motional) is been reduced to 'm.' Expressions have been divided in smaller parts, using temporary variables that are later added. The resulting polynomials for the numerator and denominator form a transfer function model using the Matlab command 'tf.' Finally, magnitude and phase of the transfer function are obtained for the delimited frequency range ('wlim' = 'ω_{lim}') using the 'bode' function.

Matlab implementation of transfer function of matched transducer (from Fig. 10.3)

```
%Numerator
N = Rm / (Lm*Lin*C1plusCs);

%Denominator
%S^6
A = 1;

%S^5
B = (Rin/Lin) + (Rm/Lm);

%S^4
X1 = (Lin + L1) / L1;
X2 = C1plusCo / Cin;
T = X1 + X2;

X3 = Lin*C1plusCo;
X  = T / X3;

C  = X + ((Rm*Rin)/(Lm*Lin)) + (1 / (Cm*Lm));

%S^3
Y1 = Rin / (L1*Lin*C1plusCo);
Y2 = n*T;
Y3 = Rin / (Cm*Lm*Lin);
D = Y1 + Y2 + Y3;

%S^2
Z1 = 1 /(Cin*Lin*L1*C1plusCo);
Z2 = (Rm*Rin) / (L1*Lm*Lin*C1plusCo);
Z3 = T / (Cm*Lm*Lin*C1plusCo);
E = Z1 + Z2 + Z3;

%S^1
V1 = Rm  / (L1*Lm*Lin*Cin*C1plusCo);
V2 = Rin / (L1*Lm*Lin*Cm*C1plusCo);
F = V1 + V2;

%S^0
G = 1 / (L1*Lm*Lin*Cm*Cin*C1plusCo);


NUM = [n 0 0 0];
DEN = [A B C D E F G];


g = tf(NUM,DEN);


fstart = 50000;
fend = 180000;

wlim = {(2*pi*fstart),(2*pi*fend)};
[mag, phase,w1] = bode(g,wlim1);
```

A.1.2 Synthesis of filter-derived matching networks

The subject of filter-derived transducer matching circuits was treated in Section 6.2.1. The synthesis strategy was based on prototype networks, and frequency and impedance de-normalization, as described in standard filter books (Chen, 1995, Huelsman, 1993, Van Valkenburg, 1982). The aim is to compute the values of the lumped passive elements of the filter-derived matching networks shown previously, with a generalized transfer function described by Eq. 10.4. A flowchart taken from (Huelsman, 1993) is presented in Fig. A.4, which shows the flexible filter design process adopted.

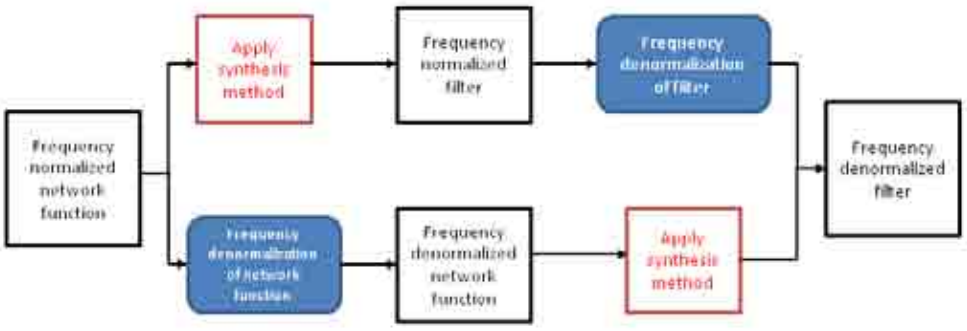

FIG. A.4. Filter design flowchart.

For synthesis, the typical prototype is the low-pass filter, which can be modified into high-pass, or placed in series with others to form band-pass and band-stop responses. One of the synthesis approaches adopted is exemplified next, for the case of the Butterworth-derived matched filter. The normalized network function for a 3rd order Butterworth low-pass filter, with cut-off frequency ω_c = 1 rad/sec is (Huelsman, 1993)

$$N_{LP}(s) = \frac{1}{s^3 + 2s^2 + 2s + 1}, \tag{A.5}$$

where p is the normalized, and s the de-normalized, complex-frequency variables. The passive realization (doubly-terminated, lossless ladder) of the network function is presented in Fig. A.5.

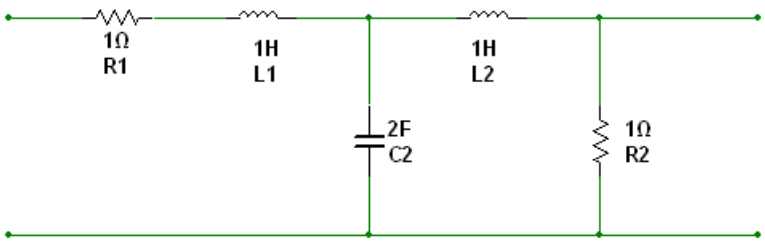

FIG. A.5. Normalized 3rd order Butterworth passive low-pass filter, with cut-off frequency ω_c = 1 rad/sec.

The next step is frequency de-normalization, through the relation

$$s = \Omega_n p \,, \tag{A.6}$$

where the de-normalization constant, Ω_n, also applies for impedance transformations. Substituting in the normalized network function (Eq. A.5) we obtain

$$N_{LP}(s) = \frac{1}{\left(\frac{s}{\Omega_n}\right)^3 + 2\left(\frac{s}{\Omega_n}\right)^2 + 2\left(\frac{s}{\Omega_n}\right) + 1} = \frac{\Omega_n^{\,3}}{s^3 + 2\Omega_n s^2 + 2\Omega_n^{\,2} s + \Omega_n^{\,3}} \,. \tag{A.7}$$

At this point, one possible synthesis method is to introduce the desired frequency characteristics into Ω_n, such as

$$\Omega_n = \left[\frac{2\pi}{Normalized\ Frequency\left(rad/\sec\right)}\right]\left[Desired\ central\ \ frequency\left(Hz\right)\right], \tag{A.8}$$

therefore $\Omega_n = 200000\pi$ (for a central frequency of 100 kHz) and

$$N_{LP}\left(s\right) = \frac{\Omega_n^{\ 3}}{s^3 + 400000\pi s^2 + 2\left(400000\pi\right)^2 s + \left(400000\pi\right)^3}. \tag{A.9}$$

The circuit realization of the de-normalized, low-pass network function is achieved by applying the same de-normalization constant to the passive components in Fig. A.1.4, namely C/Ω_n, and L/Ω_n, while R remains unchanged. However, the resulting network still needs to be converted to band-pass. This can be achieved converting a single capacitor to a parallel LC element, and a single inductor to a series LC element. This has been named the "leapfrog" method, which is considered particularly suitable for band-pass realizations (Van Valkenburg, 1982).

The alternative approach, illustrated in Fig. A.3, is the direct transformation from normalized low-pass to band-pass. This involves the change of variable

$$s = \frac{p^2 + \omega_r^{\ 2}}{B_W\left(p\right)}, \tag{A.10}$$

where ω_r, is the central frequency and BW is the bandwidth, which is equal for the low-pass and band-pass cases. Therefore, the de-normalized, band-pass transfer function becomes

$$N_{BP}(p)=\frac{1}{\left(\frac{p^2+\omega_r{}^2}{B_W(p)}\right)^3+2\left(\frac{p^2+\omega_r{}^2}{B_W(p)}\right)^2+2\left(\frac{p^2+\omega_r{}^2}{B_W(p)}\right)+1}, \tag{A.11}$$

and

$$N_{BP}(p)=\frac{(B_W p)^3}{p^6+2B_W p^5+\left(2B_W{}^2+3\omega_r{}^2\right)p^4+\left(B_W{}^3+4B_W\omega_r{}^2\right)p^3+\left(3\omega_r{}^4+2B_W{}^2\omega_r{}^2\right)p^2+2B_W\omega_r{}^4 p+\omega_r{}^6} \tag{A.12}$$

A synthesis possibility is to equate the resulting transfer function to the general transfer function presented in Eq. A.4. This can be implemented under a narrow-band approximation which affects the change of variable introduced with Eq. A.10 (Huelsman, 1993).

Matching filter-derived networks requires that component values of the prototypes are changed to those of the transducer model. This can be done because impedance scaling does not affect the transfer function (H.Y. Lam, 1979). Therefore, *R* becomes *AR*, *L* becomes $AL'/2\pi f$ and *C* becomes $C'/2\pi fA$, with *L'* and *C'* as the prototype values.

A.2 Full-wave modal analysis

Modal solutions to the scattering of sound by elastic objects were introduced in Section 2.4.5. Further details on the implementation of these theoretical solutions are given in this Appendix. These solutions are based on Bessel functions, either using the original phase angle approach taken by (Faran, 1951) or a matrix form chosen by (Goodman and Stern, 1962). A compromise between precision and computational speed occurs on the selection of the number of terms to be included in the calculation. Necessarily, the summands are finite and the series is truncated. It can be assumed that the higher-order terms do no contribute significantly and can be eliminated (Stanton, 1988a). However, a minimum number of terms has to be reached in order to ensure convergence. The main guiding criteria, as applied in previous works (Stanton, 1988a), was the optimized agreement with measured data. For the case of the elastic shell it was found that 20 terms were not enough. In general, 40 terms were used in the entire summation.

A.2.1 Bessel functions

Bessel functions originate as solutions to Bessel's differential equation, of paramount importance in applied mathematics (Kreyszig, 1999). Solving the Helmholtz equation in spherical coordinates, an approach adopted by (Goodman and Stern, 1962), results in spherical Bessel functions of the first, j_n, and second kind, y_n. Relationship with ordinary Bessel functions, J_n and Y_n, is given by (Abramowitz and Stegun, 1972)

$$j_n(x) = \sqrt{\frac{\pi}{2x}} J_{n+\frac{1}{2}}(x), \tag{A.13}$$

and

$$y_n(x) = \sqrt{\frac{\pi}{2x}} Y_{n+\frac{1}{2}}(x), \tag{A.14}$$

where n is the partial wave, x is a ka (k, wave number, a radius for spheres and cylinders). These identities were implemented, since Matlab only provides standard Bessel functions of the first kind, J_n (Matlab: *besselj*), modified first kind, I_n (Matlab: *besseli*), second kind, Y_n (Matlab: *bessely*), modified second kind, K_n (Matlab: *besselk*), and third kind, H_n, (Matlab: *besselh*). Derivative of Bessel function of the first kind is given by

$$J'_n(x) = \left(\frac{n}{x}\right) J_n(x) - J_{n+1}(x), \tag{A.15}$$

and

$$J''_n(x) = \frac{\left(n^2 - x^2\right) J_n(x) - nJ_n + xJ_{n+1}(x)}{x^2}. \tag{A.16}$$

A.2.2 Matlab implementation of modal solutions: cylinder

More details about the Matlab modal solution script for cylinder scattering are included. Plane wave scattering on an infinite cylinder was discussed in Section 2.4.7, and illustrated in Fig. 2.3, with ψ as the angle of incidence with respect to the cylinder axis. The scattered pressure, P_{scat}, is given by

$$P_{scat} = P_o e^{ik\sin\theta} \sum_{n=0}^{\infty} C_n H_n^{(2)}\left(kR\cos\theta\right)\cos\left(n\theta\right), \tag{A.17}$$

where P_o is the incident pressure amplitude, R is the range to the target, k is the wavenumber, n is the order of the partial wave, $H_n^{(2)}$, is the second kind Hankel function, and C_n contains the unknown coefficients to be computed. After applying boundary conditions, the coefficients are of the form (Flax et al., 1980, Li and Ueda, 1989)

$$C_n = \varepsilon_n \left(-i\right)^n \frac{J_n\left(x_c\right)Q_n - x_c J'_n\left(x_c\right)S_n}{H_n^{(2)}\left(x_c\right)Q_n - x_c H_n^{(2)}{}'\left(x_c\right)S_n}, \tag{A.18}$$

with ε_n as the Newmann factor, and $x_c = k\ a\ cos(\theta)$. Q_n and S_n are notations used by (Li and Ueda, 1989) and are solved from Bessel functions. The Matlab script section presented in the following page contains the expressions for Q_n and S_n, as given by Li and Ueda (Li and Ueda, 1989). The function J( ) is the Bessel function of the first kind, with dJ( ), and d2J( ) as the first and second derivatives.

Matlab implementation of modal solution for cylinder scattering (Li and Ueda, 1989)

```
tdeg = IncAngle;                %Incidence angle in degrees
trad = tdeg*(pi/180);

f0 = freq1;                     % Initial frequency
f1 = freq2;                     % Last frequency
df = stepfreq;                  % Step frequency

nfreq = round((f1-f0)/df)+1;

for j = 1:nfreq                 %Frequency loop

      freq(j) = f0 + (j-1)*df;
      om = 2*pi*freq(j);        %om = 'omega' = ω

      k  = om / c;        % c = Speed of sound in water;
      k1 = om / cl;       %cl = Longitudinal wave speed in the cylinder;
      k2 = om / ct;       %ct = Shear wave speed in the cylinder;
      x    =  k*a;        % a = cylinder radius
      x1   = k1*a;
      x2   = k2*a;

      p = sqrt( ((k1)^2) - (k*sin(trad))^2 );
      q = sqrt( ((k2)^2) - (k*sin(trad))^2 );
      x1p = p*a;
      x2q = q*a;
      xs = k*sin(trad)*a;
      xc = k*cos(trad)*a;

   for n = 0:mm                 % Partial wave order loop, mm is maximum

      Gn = x1p*dJ(n,x1p)-J(n,x1p);
      Wn = (n+1)*J(n+1,x2q)-x2q*dJ(n+1,x2q);
      Rn = (-(x2q^2) + (xs^2) + (n^2) + n)*J(n+1,x2q) + n*x2q*dJ(n+1,x2q);
      Fn = x2q*dJ(n,x2q) - (n^2)*J(n,x2q) + ((x2q^2)/2)*(J(n,x2q));
      Zn = (xs^2)*(-2*(n^2)*J(n,x2q)*Gn + 4*x1p*dJ(n,x1p)*Fn);
      Yn = 2*n*Gn*Rn - (xs^2)*2*x2q*dJ(n,x1p)*Wn;
      Xn = 2*Fn*Rn + (xs^2)*n*J(n,x2q)*Wn;

      Sn = ((v/(1-(2*v)))*((x1^2)*J(n,x1p)) - (x1p^2)*d2J(n,x1p))*Xn +
            n*(J(n,x2q)-x2q*dJ(n,x2q))*Yn - x2q*dJ(n+1,x2q)*Zn;

      Qn = (rho3*(x2^2)/(rho1*2))*(x1p*dJ(n,x1p)*Xn + n*J(n,x2q)*Yn +
            J(n+1,x2q)*Zn);

      %For the Newmann factor, Єn
      if(n==0)
            Cn = 1*(((-1i)^n)*( (J(n,xc)*Qn - xc*dJ(n,xc)*Sn) /
            ((H2(n,xc)*Qn)    - xc*dH2(n,xc)*Sn) ));
      else
            Cn = 2*(((-1i)^n)*( (J(n,xc)*Qn - xc*dJ(n,xc)*Sn) /
            ((H2(n,xc)*Qn) - xc*dH2(n,xc)*Sn) ));
      end

   end
end
```

The alternative expression for C_n, based on phase-angle shift is

$$C_n = -\varepsilon_n \left(-i\right)^{n+1} \sin\left(\eta_n\right) e^{(i\eta_n)}. \tag{A.19}$$

Expressions leading to η_n, initially given by Faran and in this case taken from (Stanton, 1988b) are presented below,

$$\tan\eta_n = \tan\delta_n\left(x_c\right)\frac{\tan\alpha_n\left(x_c\right)+\tan\Phi_n}{\tan\beta_n\left(x_c\right)+\tan\Phi_n}, \tag{A.20}$$

$$\tan\delta_n\left(x\right) = \frac{-J_n\left(x\right)}{N_n\left(x\right)}, \tag{A.21}$$

$$\tan\alpha_n\left(x\right) = \frac{-xJ'_n\left(x\right)}{J_n\left(x\right)}, \tag{A.22}$$

$$\tan\beta_n\left(x\right) = \frac{-xN'_n\left(x\right)}{N_n\left(x\right)}, \tag{A.23}$$

$$\tan\zeta_n\left(x_1,\sigma\right) = -\left(\frac{x_2^2}{2}\right)\left\{\frac{\left[\dfrac{\tan\alpha_n\left(x_1\right)}{\tan\alpha_n\left(x_1\right)+1} - \dfrac{n^2}{\tan\alpha_n\left(x_2\right)+n^2-\dfrac{1}{2}x_2^2}\right]}{\left[\dfrac{\tan\alpha_n\left(x_1\right)+n^2-\dfrac{1}{2}x_2^2}{\tan\alpha_n\left(x_1\right)+1} - \dfrac{n^2\left(\tan\alpha_n\left(x_2\right)+1\right)}{\tan\alpha_n\left(x_2\right)+n^2-\dfrac{1}{2}x_2^2}\right]}\right\}. \tag{A.24}$$

Scattered pressure for the finite cylinder of length L is given by Stanton as

$$P_{scat} = P_o \frac{e^{ikR}}{R}\left(\frac{-L_{cyl}}{\pi}\right)\frac{\sin\Delta}{\Delta}\sum_{n=0}^{\infty}\varepsilon_n \sin(\eta_n) e^{-i\eta_n}\cos(n\theta), \tag{A.25}$$

where $\Delta = kL_{cyl}\cos\theta$.

A.3 LFM pulse compression and processing

Receiver processing and structure was presented in Section 4.7.4 and Fig. 4.12. Parts of this development were also published in a conference paper (Islas-Cital et al., 2011a). The transmitted linear-frequency modulated (LFM) pulse is defined as

$$v_t(t) = w(t)V_t e^{j(\omega_o t + \frac{1}{2}\alpha_{LFM} t^2)}, \tag{A.26}$$

where *w(t)* is window function, V_t is the transmitted peak voltage, ω_o is the centre frequency in radians, t is time, and α_{LFM} is the sweep rate or chirp rate, defined as

$$\alpha_{LFM} = \frac{B_w}{T_{pulse}}, \tag{A.27}$$

with B_w as the bandwidth, and T_{pulse} as pulse duration. With an ideal point scatterer and assuming no Doppler effects, a returned echo is a delayed, scaled replica of the transmitted signal. However, realistic targets add a characteristic phase angle to the propagation phase, such that the echo is

$$v_r(t) = V_{\max} e^{j[(\omega_o (t-\tau) + \alpha (t-\tau)^2 + \varphi]}, \tag{A.28}$$

where φ is the target-induced phase. The two-way propagation delay, τ, is defined as

$$\tau = \frac{2R}{c}, \tag{A.29}$$

where R is the range from the transducer to the target, and c is the speed of sound in the water. For frequency-domain processing Fourier transforms are applied to the replica and received signal. The spectrum of the transmitted signal is

$$P_t(\omega) = \int_{-\infty}^{\infty} p_t(t) e^{-j\omega t} dt = \int_{-\infty}^{\infty} e^{j\left(\omega_o t + \alpha_{LFM} t^2\right)} e^{-j\omega t} dt = \int_{-\infty}^{\infty} e^{-j\left[(\omega-\omega_o)t - \alpha_{LFM} t^2\right]} dt\,, \tag{A.30}$$

resulting in

$$V_t(\omega) = \frac{V_{\max}}{2}\sqrt{\frac{\pi}{\alpha_{LFM}}} e^{-j\left[\frac{(\omega_o-\omega)^2}{2\alpha_{LFM}}\right]} \left[F(\eta_1) + F(\eta_2)\right], \tag{A.31}$$

where the terms $[F(\eta_1)+ F(\eta_2)]$ are the Fresnel integrals (Cook, 1960, Glisson et al., 1970). In practice, the matched or compression filter is designed to match only the squared-law phase component in Eq. 10.3.6, discarding a residual phase from the Fresnel integrals (Cook, 1960, F. Lam and Szilard, 1976). Similarly, the spectrum of the received signal $P_r(\omega)$ contains the following phase

$$angle\left(P_r(\omega)\right) = \frac{(\omega_o - \omega)^2}{2\alpha_{LFM}} + \tau\omega - \varphi\,. \tag{A.32}$$

The correlator operation, defined as

$$C(\omega) = P_r(\omega) P_t^*(\omega)\,, \tag{A.33}$$

then eliminates the quadratic phase component introduced by modulation, leaving a phase angle that augments linearly with frequency due to propagation, and a phase angle φ induced by the target. This is expressed as

$$angle(C(\omega)) = -\tau\omega + \varphi(\omega) = -2Rk + \varphi(\omega), \quad \text{(A.34)}$$

with k as the wave number. Therefore, the spectrum of the correlator contains a linear phase component and a phase shift, $\varphi(\omega)$, corresponding to the target.

A.4 Sonar system design

An active sonar system was built using a Reson TC-2130 as receiver/transmitter. The sonar system is composed of transmitter, receiver and duplexer. Signals sent and received were generated and read with the NI-6251 data acquisition card, using the NI-DAQmx drivers and software (National Instruments, Austin, TX, USA). The NI-DAQmx software uses a multithreaded driver designed to ease the programming of concurrent I/O operations. In this respect, synchronization is also simplified, with trigger signals being selectable by software, either from internally-available clocks or externally routed references. Further information and examples of the NI-DAQmx software syntax is given in Appendix A.5.

A.4.1 Duplexer

The interchange between transmission and reception using a single transducer was achieved by means of optical switches and digital control signals. Isolation diodes commonly used in traditional receivers were avoided to rule out nonlinear effects. The chosen optical switches were the Panasonic AQY221X2S, RF PhotoMOS (see datasheet extract in the next page). The passage of current through drain and source in the MOS transistors was controlled with digital signals at the anode and cathode of the internal LEDs. The switching circuit section is shown in Fig. A.6.

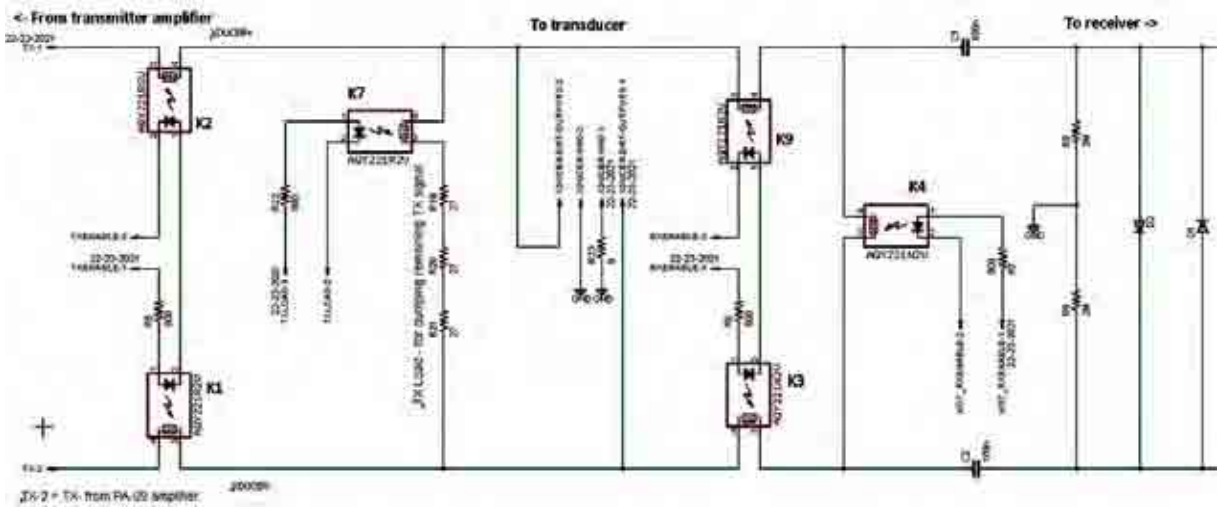

FIG. A.6. Switching section. Transducer, in the middle, is connected through optical switches to differential transmit signals from the left and to the receiver amplifier, to the right.

Transmit enable switches, K1 and K2 in Fig. A.5, were placed at each path of the differential signal. After each transmission, the transducer is connected to a 81 Ω discharge load through K7. Receive mode is enabled with switches K3 and K9 (seen in the schematic to the right of the transducer) at the differential lines, and working in complementary operation with K4, which interconnects the terminals of the receive amplifiers during transmission. The grounding scheme of the whole system is illustrated in Fig. A.7.

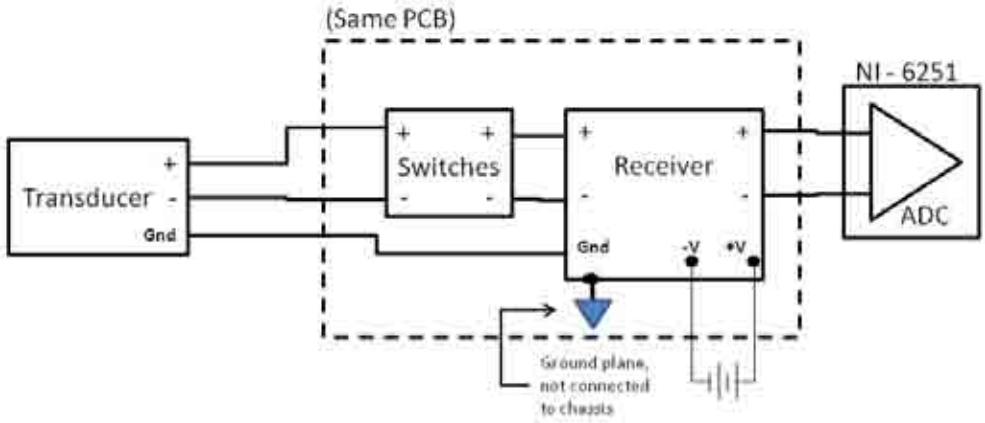

FIG. A.7. Sonar receiver grounding scheme.

A.4.2 Receiver

Low-level received signals were amplified with precision, dual-channel instrumentation amplifiers. This type of differential amplifiers offered desirable characteristics, most importantly, enhanced common mode noise rejection (Albaugh, 2006). As seen in Fig. A.6, signals were coupled to the amplifiers by means of 100 nF capacitors (C1 and C2) and 2 MΩ resistors (R8 and R9), providing DC current paths to ground. The PCB design accommodates two alternative options for the instrumentation amplifier device to be used, as seen in the schematic presented in Fig. A.8. Either of the two options can be populated, and the corresponding signal paths opened by means of jumpers (R1 and R2). Pads for each device were placed on the opposite faces of the PCB, as shown in the photographs presented in Fig. A.9. The output of the amplifiers was filtered with a low-pass LC ladder, with a cut-off frequency of 300 kHz.

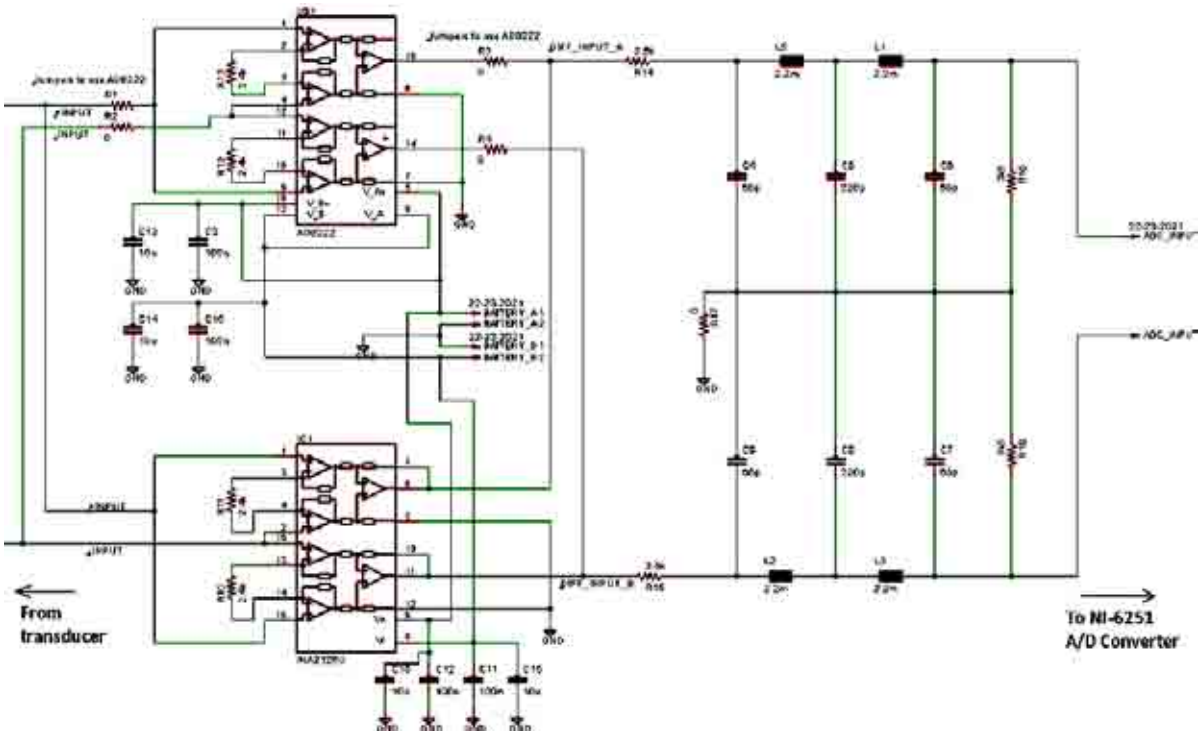

FIG. A.8. Receiver schematic.

The two instrumentation amplifiers considered were the INA2128 (Texas Instruments, Dallas, TX, USA) and the AD8222 (Analog Devices, Norwood, MA, USA). Both are dual channel precision devices, based on 3-op amp architectures (Albaugh, 2006). For the construction of the prototype, implementation of the INA2128 was easier due to its SOIC package, in contrast to the 1.4x4 mm footprint area and LFCSP packaging of the AD8222. Operation and performance tests resulted satisfactory, and thus the INA2128 was maintained. The INA2128 has a maximum offset voltage of 50 μV and a low drift of 0.5 μV/°C maximum, as specified in the included datasheet. Supply voltage of ±12 V was provided from a battery reference voltage, precluding the effects of line noise.

A.4.3 Printed circuit board (PCB) design

The duplexer circuit was built into the same enclosure and printed circuit board (PCB) as the receiver amplifier and filters. Design of the PCB was performed using the freeware layout editor software, Eagle, Version 5.4.0 (Cadsoft, Leeds, UK). Prototype PCBs were manufactured in April 2010 by Beta Layout Ltd (Beta Layout Ltd., Shannon, Ireland). This common PCB is shown in Figs. A.9 and A.10. It can be noticed that the receiver section was physically separated from the duplexer section, in order to avoid the digital noise induced by the switching signals. Efforts were made to achieve an optimal grounding scheme, following guidelines found in (Ott, 1988). Copper ground planes were placed in both sides, in a 3.6 cm square covering the receiver section. The planes were connected with multiple vias distributed randomly in the area, thus providing several return paths and reducing the length of potential ground loops.

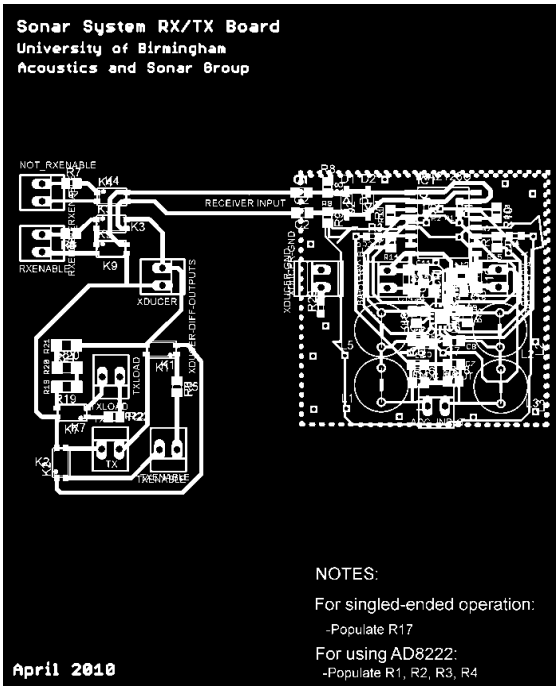

FIG.A.9. PCB design in the Eagle software.

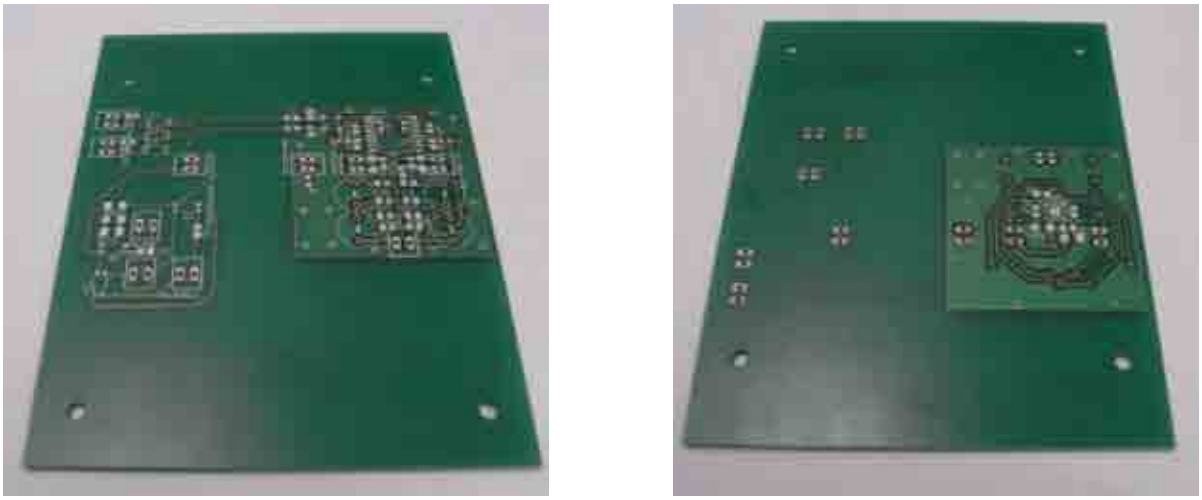

FIG. A.10. Both sides of PCB containing duplexer and receiver circuits.

A.4.4 Transmitter

Amplification of transmitted signals was performed with an Apex PA09 power operational amplifier (Cirrus Logic, Austin, Texas, USA). This is a MOS device, with high gain-bandwidth product and low noise, as described in the datasheet included in following page. The amplifier supply voltage, approximately ±38.7 V, was derived from a ±55 V unregulated power supply (RS Components stock number 591-950), using adjustable linear voltage regulators (LM317 and LM337). This was necessary since the maximum amplifier supply range is ±40 V. The schematic of the transmitter circuit is shown in Fig. A.11, alongside with its performance simulation, performed in Multisim (National Instruments, Austin, TX, USA). The PA09 amplifier is sealed in an 8-pin TO-3 package. An external phase compensation capacitor with a value of 10 pF is connected between pins 7 and 8. The PCB for the PA09 power amplifier, mounted on a heat-sink, is shown in Fig. A.12. It was installed, together with the power supply supporting circuitry, in a metallic enclosure, as shown in Fig. A.13.

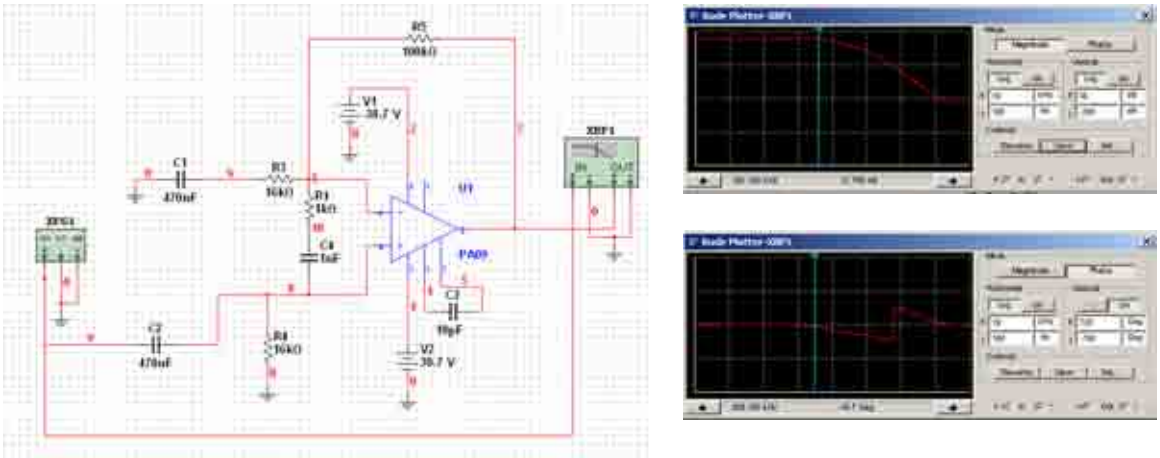

FIG. A.11. Amplifier schematic and performance simulation.

FIG. A.12. PA09 amplifier PCB.

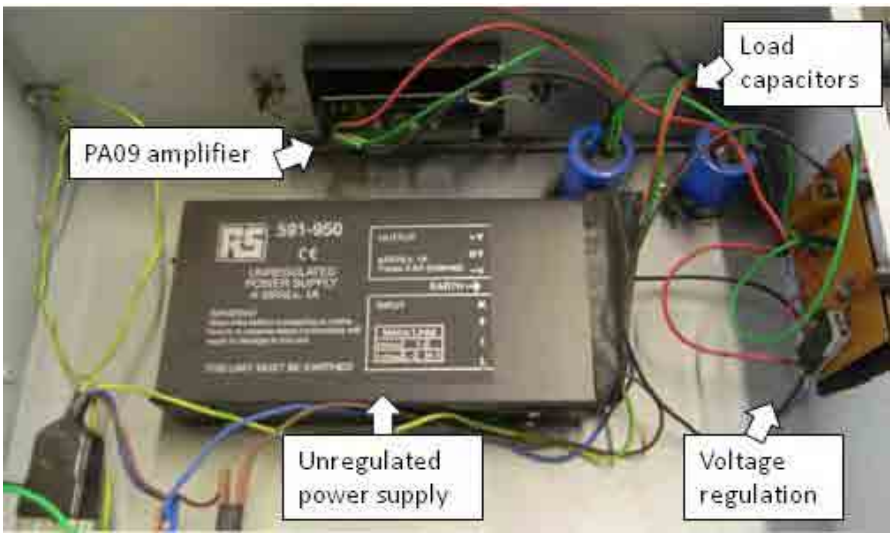

FIG. A.13. Transmission signal amplification.

A.5 Target rotation

The target rotation device was briefly introduced in Section 4.4. The motor (RS 440-458) is a 4-phase hybrid stepper motor, as described in the datasheet included in this Appendix. Rotation step is 1.8°. The motor was operated in a full-step excitation mode, controlled digitally from the NI-6251 data acquisition card, through a L298N full-bridge driver. A table containing the excitation sequence is presented below, with the digital NI-6251 outputs (P2.0 to P2.5) connected to L298N inputs, and activating motor coils labelled with a 4-wire configuration.

Table A.1. Rotation excitation sequence.

NI – 6251 digital output	*P2.0*	*P2.1*	*P2.2*	*P2.3*	*P2.4*	*P2.5*	*Decimal value of digital bus state*
L298N Input/ Output	*Enable A*	*Enable B*	*Input 1 / Red wire*	*Input 2 / Black wire*	*Input 3 / Green wire*	*Input 4 / Yellow wire*	
Excitation sequence (clockwise rotation) ↓	1	1	1	0	1	0	23
	1	1	0	1	1	0	27
	1	1	0	1	0	1	43
	1	1	1	0	0	1	39

The excitation sequence was written into a digital bus connected to the driver. This was accomplished through the Matlab script included in the following page. A finite number of steps was obtained by dividing the desired rotation by the step resolution (1.8°). A complete arc was reached with a for loop covering the total number of steps. Short pauses (0.3 seconds) were applied between steps, and a longer stabilization pause of the order of a few minutes after each rotation, before acoustic acoustical measurements.

Motor rotation Matlab script section

```
samples = 512;

%Motor excitation sequence from digital outputs (from table)
MotorPosition = [23 27 43 39];

% 'RotationStepDegrees' is the chosen rotation resolution
MotorStep = round(RotationStepDegrees/1.8);

%rotate after measurements have been made at the starting position (run=1)
if(run>1)

    CurrPos =  mod(CurrPos + RotationStepDegrees,360);

    fprintf(strcat('Moving motor to: ', int2str(CurrPos), ' degrees...'));

    pos = prevpos;

%MoveMotor
for(k=1:MotorStep)

    MotorControlOutput(1:samples) = uint8(MotorPosition(pos));

%Write signal to motor controller
SamplesPerChannelWritten = libpointer('int32Ptr',0);

[Status,c,d] =
calllib('nicaiu','DAQmxWriteDigitalU8',TaskHandle6Numeric,samples,int32(1),
double(10),DAQmx_Val_GroupByScanNumber,MotorControlOutput,SamplesPerChannel
Written, []);

    if Status ~= 0,
        fprintf('Error in DAQmxWriteDigitalU8 - motor control   Status =
%d\n',Status);

        return
    end %End of error check

    pos = pos + 1;
    if(pos==5)
        pos=1;
    end

    pause(0.3); %pause between individual steps

end %End of motor step movement


fprintf(strcat('Waiting : ', int2str(RotationWaitTime), ' minutes for
stabilization...'));

%pause after the established rotation sector is completed, stabilization
period
pause(RotationWaitTime*60);
```

A.6 Temperature measurement

Temperature was measured with a TMS Europe, Pro-Track 223, with a 3-wire platinum resistance thermocouple. This was calibrated, by TMS Brockwell Calibration, to an uncertainty of ±0.075°C. A copy of the calibration certificate is included in the following page. The link between the temperature data logger, was established through serial communications. Two steps were necessary since the instrument has an RS485/422 interface. First, this protocol was converted to RS232 with a K2-ADE converted (KK Systems Ltd., Brighton, UK). Then, RS232 was converted to USB with a DX-UBDB9 (Dynex, Richfield, MN, USA). This is illustrated in Fig. A.14.

FIG. A.14. Temperature measurement system and communications link.

Communication is established and verified at the beginning of the script as follows:

```
sPort = serial('COM5', 'BaudRate', 9600, 'Parity', 'none', 'StopBits',
1,'FlowControl', 'hardware', 'Terminator', 'CR/LF');

fopen(sPort);

% Initiation Command - expect 'OK' from unit)
cmd = [';000CONFIG' char(13) char(10)];

fwrite(sPort,cmd,'char');      % Write to serial port

% Read from serial port by checking BytesAvailable
a=char(fread(sPort,sPort.BytesAvailable))';

if(a(2) == 'O')
    fprintf('Serial communication with temperature meter established\n');
    else
        fprintf('Error in serial communication with temperature meter\n');
        return
end
```

A.7 NI-DAQmx driver software for the NI-6251 data acquisition card

NI-DAQmx is a proprietary software interface for National Instruments multifunction data acquisition cards. Besides operating in the associated National Instruments graphical control environment, LabView, NI-DAQmx can work with standard programming languages such as C/C++. Implementation in Matlab is based on C/C++ functions and syntax, as described in the NI-DAQmx C Reference Help, included in the installation suite. Implementation is task-based, with general and specific parameters defined.

General parameter definition

```
DAQmx_Val_Cfg_Default = int32(-1);         %%Default
DAQmx_Val_RSE = int32(10083);              %%RSE
DAQmx_Val_NRSE = int32(10078);             %%NRSE
DAQmx_Val_Diff = int32(10106);             %%Differential
DAQmx_Val_PseudoDiff = int32(12529);       %%Pseudodifferential
DAQmx_Val_ChanPerLine = int32(0);          %%One Channel For Each Line */
DAQmx_Val_ChanForAllLines = int32(1);      %%One Channel For All Lines */

% Units
DAQmx_Val_Volts = int32(10348);            %%Volts
DAQmx_Val_FromCustomScale = int32(10065); %%From Custom Scale

% Active Edge
DAQmx_Val_Rising = int32(10280);           %%Rising
DAQmx_Val_Falling = int32(10171);          %%Falling

% Sample Mode
DAQmx_Val_FiniteSamps = int32(10178);      %%Finite Samples
DAQmx_Val_ContSamps = int32(10123);        %%Continuous Samples
DAQmx_Val_HWTimedSinglePoint = int32(12522);%%Hardware Timed Single Point

% Fill Mode
DAQmx_Val_GroupByChannel = uint32(0);      %%Group by Channel
DAQmx_Val_GroupByScanNumber = uint32(1);   %%Group by Scan Number
```

Task creation

```
%% Create new tasks
TaskHandle1 = libpointer('uint32Ptr',0);
TaskHandle2 = libpointer('uint32Ptr',0);
TaskHandle3 = libpointer('uint32Ptr',0);
TaskHandle4 = libpointer('uint32Ptr',0);
TaskHandle5 = libpointer('uint32Ptr',0);
TaskHandle6 = libpointer('uint32Ptr',0);

RXSignalInputTaskName  = 'AnalogInputTask';
TXSignalOutputTaskName = 'AnalogOutputTask';
ControlSignalsTaskName = 'DigitalOutputTask';
BatteryAInputTaskName  = 'BatteryAInputTask';
BatteryBInputTaskName  = 'BatteryBInputTask';
MotorTaskName          = 'MotorControlTask';
```

Task handle assigned to specific tasks (one example)

```
[Status,TaskNameText,TaskHandle1] =
calllib('nicaiu','DAQmxCreateTask',RXSignalInputTaskName,TaskHandle1);
```

Analog input channel creation

Function: DAQmxCreateAIVoltageChan - *Creates channel(s) to* measure voltage *and adds the channel(s) to the* task *you specify with* **taskHandle.**

```
minADVal = double(DCOffset-ADMaxVal);
maxADVal = double(DCOffset+ADMaxVal);

% Create a NIDAQmx Task TaskHandle1 - reading of transducer voltage
[Status,ChannelNameText,c,d]  =
calllib('nicaiu','DAQmxCreateAIVoltageChan',TaskHandle1Numeric,char(AIConfi
gStrings(NumberOfRXChannels)),'',DAQmx_Val_Diff,minADVal,maxADVal,DAQmx_Val
_Volts,'');

% Create a NIDAQmx Task TaskHandle1 - reading of battery voltage A
[Status,ChannelNameText,c,d]  =
calllib('nicaiu','DAQmxCreateAIVoltageChan',TaskHandle4Numeric,'Dev1/ai1','
',DAQmx_Val_Diff,0,10,DAQmx_Val_Volts,'');

% Create a NIDAQmx Task TaskHandle1 - reading of battery voltage B
[Status,ChannelNameText,c,d]  =
calllib('nicaiu','DAQmxCreateAIVoltageChan',TaskHandle5Numeric,'Dev1/ai3','
',DAQmx_Val_Diff,0,10,DAQmx_Val_Volts,'');
```

Analog output channel creation

Function: DAQmxCreateAOVoltageChan - *Creates channel(s) to generate voltage and adds the channel(s) to the task you specify with* **taskHandle**.

```
minDAVal = double(-10);
maxDAVal = double(10);

% Generate a D/A output channel - for transmitted signal into transducer
[Status,ChannelNameText,c,d]  =
calllib('nicaiu','DAQmxCreateAOVoltageChan',TaskHandle2Numeric,'/Dev1/ao0',
'',minDAVal,maxDAVal,DAQmx_Val_Volts,'');
```

Digital output channel

Function: DAQmxCreateDOChan - *Creates channel(s) to generate digital signals and adds the channel(s) to the task you specify with* **taskHandle**. *You can group digital* lines *into one* digital channel *or separate them into multiple digital channels. If you specify one or more entire* ports *in* **lines** *by using port physical channel names, you cannot separate the ports into multiple channels.*

```
% Digital output channel - for duplexer control
[Status, DigitalOutputChannelNamesText]  =
calllib('nicaiu','DAQmxCreateDOChan',TaskHandle3Numeric,'/Dev1/port0','',DA
Qmx_Val_ChanForAllLines );

% Digital output channel - for motor rotation control
[Status, DigitalOutputChannelNamesText]  =
calllib('nicaiu','DAQmxCreateDOChan',TaskHandle6Numeric,'/Dev1/port2','',DA
Qmx_Val_ChanForAllLines );
```

Timing and triggering for analog input reading

```
% Set up the on-board timing with internal clock source
ActiveEdge = DAQmx_Val_Rising;          % Sampling edge
SampleMode = DAQmx_Val_FiniteSamps;     % Collect a finite number of
samples

SamplesToAcquire = uint64(RXSamplesPerChannel);
[Status,ClockSource] =
calllib('nicaiu','DAQmxCfgSampClkTiming',TaskHandle1Numeric,'OnboardClock',
RXSamplingFrequency,ActiveEdge,SampleMode,SamplesToAcquire);

%  Define the parameters for a digital edge start trigger for output.
% Set the analog output to trigger off the AI start trigger.
% This is an internal trigger signal.
[Status,a] =
calllib('nicaiu','DAQmxCfgDigEdgeStartTrig',TaskHandle2Numeric,'/Dev1/ai/St
artTrigger',DAQmx_Val_Rising);
```

Digital output sent to duplexer

Function: DAQmxWriteDigitalU8 - *Writes multiple 8-bit unsigned integer samples to a task that contains one or more digital output channels. Use this format for devices with up to 8 lines per port.*

```
DigitalOutput = zeros(1,TXSamplesPerChannel);

% Make  control signals
InitialRelayDeadTime = 1e-3;
InitialDeadTimeSamples = floor(InitialRelayDeadTime*TXSamplingFrequency);

RelayDeadTime = 0.4e-3;
RelayDeadTimeSamples = floor(RelayDeadTime*TXSamplingFrequency);

LoadRelayActiveTime = 0.5e-3;
LoadRelayActiveTimeSamples = loor(LoadRelayActiveTime*TXSamplingFrequency);

%Timing
DurationOfTXEnable = InitialDeadTimeSamples + ActualTXSamples +
RelayDeadTimeSamples;
LoadActiveInterval = LoadRelayActiveTimeSamples;
StartOfRXInterval = DurationOfTXEnable+LoadActiveInterval;

%First timing section - A
DigitalOutput(1:DurationOfTXEnable) = uint8(9);

%Second timing section - B
DigitalOutput((DurationOfTXEnable+1):(DurationOfTXEnable+LoadActiveInterval
)) = uint8(10);

%Third timing section - C
DigitalOutput((StartOfRXInterval+1):(TXSamplesPerChannel)) = uint8(4);

%Write enable signal through digital output
SamplesPerChannelWritten = libpointer('int32Ptr',0);

[Status,c,d] =
calllib('nicaiu','DAQmxWriteDigitalU8',TaskHandle3Numeric,int32(TXSamplesPe
rChannel),int32(0),double(10),DAQmx_Val_GroupByScanNumber,DigitalOutput,Sam
plesPerChannelWritten, []);
```

Signal transmission

Function: DAQmxWriteAnalogF64 - *Writes multiple floating-point samples to a task that contains one or more analog output channels.*

```
% Transmission of analog signal - Insert weighted TX waveform

TXSignal(InitialDeadTimeSamples:(InitialDeadTimeSamples+ActualTXSamples-1))
= ReplicaSignal;

fprintf('Transmitting signal\n');


% Write samples to task
SamplesPerChannelWritten = libpointer('int32Ptr',0);

[Status,a,b] =
calllib('nicaiu','DAQmxWriteAnalogF64',TaskHandle2Numeric,int32(TXSamplesPe
rChannel),int32(0),double(10),DAQmx_Val_GroupByChannel,TXSignal,SamplesPerC
hannelWritten,[]);
```

B. REFERENCES

Abramowitz, M. and Stegun, I. (eds.) (1972) **Handbook of mathematical functions with formulas, graphs, and mathematical tables***,* Washington, D.C.: U.S. Dept. of Commerce.

Albaugh, N.P. (2006) **The instrumentation amplifier handbook**. Tucson, AZ, USA: Burr-Brown Corporation.

Allen, J.S., Kruse, D.E. and Ferrara, K.W. (2001) Shell waves and acoustic scattering from ultrasound contrast agents. **IEEE Trans. Ultrason., Ferroelect., Freq. Contr.***,* 48: (2): 409-418.

Altes, R.A. (1995) Signal processing for target recognition in biosonar. **Neural Networks***,* 8: (7/8): 1275-1295.

Amin, M., Zemany, P., Setlur, P. and Ahmad, F. (2006) Moving target localization for indoor imaging using dual frequency CW radars. **4th IEEE Workshop on Sensor Array and Multichannel Processing** Waltham, MA, USA IEEE.

Anderson, M.E., Soo, M.S.C. and Trahey, G.E. (1998) Microcalcifications as elastic scatterers under ultrasound. **IEEE Transactions on Ultrasonics, Ferroelectrics, and Frequency Control***,* 45: (4): 925-934.

Anderson, V.C. (1950) Sound scattering from a fluid sphere. **J. Acoust. Soc. of America***,* 22: (4): 426-431.

Andreeva, I.B. and Tarasov, L.L. (2003) Scattering of acoustic waves by small crustaceans. **Acoustical Physics***,* 49: (2): 125-128.

Anson, L.W., Chivers, R.C. and Puttick, K.E. (1995) On the feasibility of detecting pre-cracking fatigue damage in metal-matrix composites by ultrasonic techniques. **Composites Science and Technology***,* 55: 63-73.

Aoki, I. and Inagaki, T. (1993) Acoustic surveys of abundance and distribution of the Japanese sardine Sardinops melanostictus in the spawning grounds off southern Kyushu, Japan. **Nippon Suisan Gakkaishi***,* 59: (10): 1727-1735.

Arons, A.B. and Yennie, D.R. (1950) Phase distortion of acoustic pulses obliquely reflected from a medium of higher sound velocity. **J. Acoust. Soc. Am.***,* 22: (2): 231-237.

Ashley, J.R. (1966) Phase shift in audio systems. **IEEE Trans. Audio and Electroacoustics***,* 14: 50.

Assous, S., Hopper, C., Lovell, M., et al. (2010) Short pulse multi-frequency phase-based time delay estimation. **J. Acoust. Soc. Am.***,* 127: (1): 309-315.

Atkins, P.R., Collins, T. and Foote, K.G. (2007a) Transmit-signal design and processing strategies for sonar target phase measurement. **IEEE J. Sel. Topics Signal Process.***,* 1: (1): 91-104.

Atkins, P.R., Foote, K.G. and Collins, T. (2007) Practical implications of sonar target-phase measurement classifiers. **Institute of Acoustics International Conference on Detection and Classification of Underwater Targets** Edinburgh, Scotland 29: 163-172.

Atkins, P.R., Islas-Cital, A. and Foote, K.G. (2008) Sonar target-phase measurement and effects of transducer matching. **J. Acoust. Soc. Am.**, 123: (5): 3949.

Au, W.W.L. (1994) Comparison of sonar discrimination: Dolphin and an artificial neural network. **J. Acoust. Soc. Am.**, 95: (5): 2728-2735.

Au, W.W.L. and Benoit-Bird, K.J. (2003) Acoustic backscattering by Hawaiian lutjanid snappers. II. Broadband temporal and spectral structure. **J. Acoust. Soc. Am.**, 114: (5): 2767-2774.

Au, W.W.L., Branstetter, B.K., Benoit-Bird, K.J., et al. (2009) Acoustic basis for fish prey discrimination by echolocating dolphins and porpoises. **J. Acoust. Soc. Am.**, 126: (1): 460-467.

Au, W.W.L. and Simmons, J.A. (2007) Echolocation in dolphins and bats. **Phys. Today**, 60: (9): 40-45.

Aw, P.K., Tan, A.L.K., Tan, T.P., et al. (2008) Corrosion resistance of tungsten carbide based cermet coatings deposited by high velocity oxy-fuel spray process. **Thin Solid Films**, 516: 5710-5715.

Ayres, V.M., Gaunaurd, G.C. and Tsui, C.Y. (1987) The effects of Lamb waves on the sonar cross-sections of elastic spherical waves. **Int. J. Solids Structures**, 23: (7): 937-946.

Azimi-Sadjadi, M.R., Yao, D., Huang, Q., et al. (2000) Underwater target classification using wavelet packets and neural networks. **IEEE Transactions on Neural Networks**, 11: (3): 784-794.

Bamber, J. and Phelps, J. (1977) The effective directivity characteristic of a pulsed ultrasound transducer and its measurement by semi-automatic means. **Ultrasonics**, 169-174.

Bao, X.L., Cao, H. and Uberall, H. (1990) Resonances and surface waves in the scattering of an obliquely incident acoustic field by an infinite elastic cylinder. **J. Acoust. Soc. Am.**, 87: (1): 106-110.

Barlow, A.J. and Yazgan, E. (1966) Phase change method for the measurement of ultrasonic wave velocity and a determination of the speed of sound in water. **Brit. J. Appl. Phys.**, 17: 807-819.

Barr, R. (2001) A design study of an acoustic system suitable for differentiating between orange roughy and other New Zealand deep-water species. **J. Acoust. Soc. Am.**, 109: (1): 164-178.

Barr, R. and Coombs, R.F. (2005) Target phase: An extra dimension for fish and plankton target identification. **J. Acoust. Soc. Am.**, 118: (3): 1358-1371.

Beedholm, K. and Mohl, B. (1998) Bat sonar: An alternative interpretation of the 10-ns jitter result. **J. Comp. Physiol. A**, 182: 259-266.

Benoit-Bird, K.J., Au, W.W.L. and Kelley, C.D. (2003) Acoustic backscattering by Hawaiian lutjanid snappers. I. Target strength and swimbladder characteristics **J. Acoust. Soc. Am.**, 114: (5): 2757-2766.

Biernat Jr., S. (1995) Carbide coatability. **Cutting tool engineering**, 47: (2).

Biot, M.A. (1957) General theorems on the equivalence of group velocity and energy transport. **The Physical Review***,* 105: (4): 1129-1137.

Blackstock, D.T. (2000) **Fundamentals of physical acoustics**. New York: John Wiley and Sons.

Blauert, J. and Laws, P. (1978) Group delay distortions in electroacoustical systems. **J. Acoust. Soc. Am.***,* 63: (5): 1478-1483.

(2011) **Advanced Metrology for Ultrasound in Medicine** Teddington, UK Journal of Physics: Conference Series.279

Bobber, R.J. (1970) **Underwater electroacoustic measurements**. Washington, D.C.: Naval Research Laboratory.

Bordier, J.M., Fink, M., Le Brun, A. and Cohen-Tenoudji, F. (1992) The random phase transducer in ultrasonic non-destructive testing of coarse grain stainless steel: An original tool to characterize multiple scattering effects. **IEEE Ultrasonics Symposium** Tucson, AZ. 2: 877-882.

Braithwaite, H. (1973) Discrimination between sonar echoes from fish and rocks on the basis of hard and soft characteristics. **J. Sound Vib.***,* 27: (4): 549-557.

Brill, D., Gaunaurd, G.C., Strifors, H., et al. (1991) Backscattering of sound pulses by elastic bodies underwater. **Applied Acoustics***,* 33: 87-107.

Brillouin, L. (1960) **Wave propagation and group velocity**. London: Academic Press.

Burwen, D.L., Nealson, P.A., Fleischman, S.J., et al. (2007) The complexity of narrowband echo envelopes as a function of fish side-aspect angle. **ICES J. Mar. Sci.***,* 64: 1066-1074.

Cahill, N. and Lawlor, R. (2008) A novel approach to mixed phase room impulse response inversion for speech dereverberation. **IEEE International Conference on Acoustics, Speech and Signal Processing***.* Las Vegas, NV.

Carlson, A.B. (1986) **Communication systems: An introduction to signals and noise in electrical communication**. London: McGraw-Hill.

Chan, F. and Rabe, E. (1997) A non-linear phase-only algorithm for active sonar signal processing. **MTS/IEEE Oceans** Halifax, Canada. 506-511.

Chen, W.K. (1995) **The circuits and filters handbook**. Boca Raton, Florida, USA: CRC Press.

Chestnut, P., Landsman, H. and Floyd, R.W. (1979) A sonar target recognition experiment. **J. Acoust. Soc. Amer.***,* 66: (1): 140-147.

Chinnery, P.A. and Humphrey, V.F. (1998) Fluid column resonances of water-filled cylindrical shells of elliptical cross section. **J. Acoust. Soc. Am.***,* 103: (3): 1296-1305.

Chu, D. and Stanton, T.K. (1998) Application of pulse compression techniques to broadband acoustic scattering by live individual zooplankton. **J. Acoust. Soc. Am.***,* 104: (1): 39-55.

Chu, D. and Ye, Z. (1999) A phase-compensated distorted wave Born approximation representation of the bistatic scattering by weakly scattering objects: Application to zooplankton. **J. Acoust. Soc. Am.**, 106: (4): 1732-1743.

Clay, C.S. (1983) Deconvolution of the fish scattering PDF from the echo of the PDF for a single transducer sonar. **J. Acoust. Soc. Am.**, 73: (6): 1989-1994.

Clay, C.S. and Heist, B.G. (1984) Acoustic scattering by fish: Acoustic models and a two-parameter fit. **J. Acoust. Soc. Am.**, 75: (4): 1077-1083.

Clay, C.S. and Horne, J.K. (1994) Acoustic models of fish: The Atlantic cod (*Gadus morhua*). **J. Acoust. Soc. Am.**, 96: (3): 1661-1668.

Cochrane, N.A., Li, Y. and Melvin, G.D. (2003) Quantification of a multibeam sonar for fisheries assessment applications. **J. Acoust. Soc. Am.**, 114: (2): 745-758.

Cole, P. and Watson, J. (2005) "Acoustic emission for corrosion detection". **Third Middle East Nondestructive Testing Conference and Exhibition**. Bahrain.

Cook, C.E. (1960) Pulse compression: Key to more efficient radar transmission. **Proc. IRE**, 48: 310-316.

Cooling, M.P. and Humphrey, V.F. (2008) A nonlinear propagation model-based phase calibration technique for membrane hydrophones. **IEEE Trans. Ultrason., Ferroelect., Freq. Contr.**, 55: 84-93.

Cooling, M.P., Humphrey, V.F. and Wilkens, V. (2011) "Hydrophone area-averaging correction factors in nonlinearly generated ultrasonic beams". **Advanced Metrology for Ultrasound in Medicine**. Teddington, UK, Journal of Physics: Conference Series.

Coombs, R. and Barr, R. (2004) Acoustic remote sensing of swimbladder orientation and species mix in the oreo population on the Chatham Rise. **J. Acoust. Soc. Am.**, 115: (4): 1516-1524.

Cotté, B., Culver, R.L. and Bradley, D.L. (2007) Scintillation index of high frequency acoustic signals forward scattered by the ocean surface. **J. Acoust. Soc. Am.**, 121: (1): 120-131.

Daigle, G.A. (1987) Impedance of grass-covered ground at low frequencies measured using a phase difference technique. **J. Acoust. Soc. Am.**, 81: (1): 62-68.

Dardy, H.D., Bucaro, J.A., Schuetz, L.S., et al. (1977) Dynamic wide-bandwidth acoustic form-function determination. **J. Acoust. Soc. Am.**, 62: (6): 1373-1376.

Delaney, J.R. and Barga, R. (2009) "A 2020 vision for ocean science". **The fourth paradigm** Microsoft Research 27-38.

Demer, D.A. and Conti, S.G. (2003) Reconciling theoretical versus empirical target strengths of krill: Effects of phase variability on the distorted-wave Born approximation. **ICES J. Marine Science**, 60: 429-434.

Demer, D.A., Cutter, G.R., Renfree, J.S., et al. (2009) A statistical-spectral method for echo classification. **ICES Journal of Marine Science**, 66: 1081-1090.

Deneuville, F., Duquennoy, M., Ouaftouh, M., et al. (2008) Wide band resonant ultrasound spectroscopy of spheroidal modes for high accuracy estimation of Poisson coefficient of balls. **The Rev. Sci. Instrum***,* 79: 1-5.

Deuser, L.M., Middleton, D., Plemons, T.D., et al. (1979) On the classification of underwater acoustic signals. II. Experimental applications involving fish. **J. Acoust. Soc. Am.***,* 65: (2): 444-455.

Diercks, K.J. and Hickling, R. (1967) Echoes from hollow aluminum spheres in water. **J. Acoust. Soc. Am.***,* 41: (2): 380-393.

Dietzen, G.C. (2008) **Acoustic scattering from sand dollars (Dendraster excentricus): Modeling as high aspect ratio oblate objects and comparison to experiment**. Master of Science, Massachusetts Institute of Technology.

Do, M.A. and Surti, A.M. (1982) Accumulative uncertainties in the quantitative evaluation of signals from fish. **Ultrasonics***,* 20: (5): 217-223.

Doane, J.W., Gray, M.D. and Capall, J.J. (2006) Nondestructive inspection system for corrosion detection in fuel tank liners. **J. Acoust. Soc. Am.***,* 120: (5): 3115.

Doonan, I., Bull, B., Dunford, A., et al. (2001) "Acoustic estimates of the biomass of aggregations of orange roughy in the Spawning Box and on the Northeastern and Eastern Hills, Chatham Rise, July 2000". Wellington, Ministry of Fisheries.

Doust, P.E. and Dix, J.F. (2001) The impact of improved transducer matching and equalisation techniques on the accuracy and validity of underwater acoustic measurements. **Proc. Institute of Acoustics***,* 23, Pt 2: 100-109.

Dragonette, L.R., Numrich, S.K. and Frank, L.J. (1981) Calibration technique for acoustic scattering measurements. **J.Acoust.Soc.Am.***,* 69: (4): 1186-1189.

Dunn, J.H., Howard, D.D. and King, A.M. (1959) Phenomena of scintillation noise in radar-tracking systems. **Proc. of the IRE***,* 47: (5): 855-863.

Ehrenberg, J.E. (1979) A comparative analysis of in situ methods for directly measuring the acoustic target strength of individual fish. **IEEE Journal of Oceanic Engineering***,* 4: (4): 141-152.

Fan, Y., Honarvar, F., Sinclair, A.N., et al. (2003) Circumferential resonance modes of solid elastic cylinders excited by obliquely incident acoustic waves. **J. Acoust. Soc. Am.***,* 113: (1): 102-113.

Faran, J., James J. (1951) Sound scattering by solid cylinders and spheres. **J. Acoust. Soc. Am.***,* 23: (4): 405-418.

Fernandes, P.G. (2009) Classification trees for species identification of fish-school echotraces. **ICES Journal of Marine Science***,* 66: 1073-1080.

Feuillade, C. (2004) Animations for visualizing and teaching acoustic impulse scattering from spheres. **J. Acoust. Soc. Am.***,* 115: (5): 1893-1904.

Feuillade, C. and Clay, C.S. (1999) Anderson (1950) revisited. **J. Acoust. Soc. Am.***,* 106: (2): 553-564.

Feuillade, C., Meredith, R.W., Chotiros, N.P., et al. (2002a) Time domain investigation of transceiver functions using a known reference target. **J.Acoust.Soc.Am.**, 112: (6): 2702-2712.

Feuillade, C., Meredith, R.W., Chotiros, N.P., et al. (2002b) Time domain investigation of transceiver functions using a known reference target. **J. Acoust. Soc. Am.**, 112: (6): 2702-2712.

Fink, M., Mallart, R. and Cancre, F. (1990) The random phase transducer: A new technique for incoherent processing - Basic principles and theory. **IEEE Trans. Ultrason., Ferroelect., Freq. Contr.**, 37: (2): 54-69.

Flax, L., Dragonette, L.R. and Uberall, H. (1978) Theory of elastic resonance excitation by sound scattering. **J. Acoust. Soc. Am.**, 63: (3): 723-731.

Flax, L., Gaunaurd, G.C. and Uberall, H. (1981) "Theory of resonance scattering". In Mason, W.P. & Thurston, R.N. (Eds.) **Physical Acoustics**. London, Academic Press 191-294.

Flax, L., Varadan, V.K. and Varadan, V.V. (1980) Scattering of an obliquely incident acoustic wave by an infinite cylinder. **J. Acoust. Soc. Am.**, 68: (6): 1832-1835.

Fofonoff, N.P. and Millard Jr., R.C. (1983) "Algorithm for computation of fundamental properties of seawater". UNESCO Technical papers in marine science. Report Number 44.

Folds, D.L. (1971) Target strength of focused liquid-filled spherical reflectors. **J. Acoust. Soc. Am.**, 49: (5): 1596-1599.

Foote, K.G. (1980) Importance of the swimbladder in acoustic scattering by fish: A comparison of gadoid and mackerel target stregths. **J. Acoust. Soc. Am.**, 67: (6): 2084-2089.

Foote, K.G. (1982) Optimizing copper spheres for precision calibration of hydroacoustic equipment. **J. Acoust. Soc. Am.**, 71: (3): 742-747.

Foote, K.G. (1983a) Linearity in fisheries acoustics, with addition theorems. **J. Acoust. Soc. Am.**, 73: (6): 1932-1940.

Foote, K.G. (1983b) Maintaining precision calibrations with optimal copper spheres. **J. Acoust. Soc. Am.**, 73: (3): 1054-1063.

Foote, K.G. (1990) Spheres for calibrating an eleven-frequency acoustic measurement system. **J. Const. Int. Explor. Mer**, 46: 284-286.

Foote, K.G. (1996) Coincidence echo statistics. **J. Acoust. Soc. Am.**, 99: (1): 266-271.

Foote, K.G. (1998) Measurement of morphology and physical properties of zooplankton. **IEEE Recent advances in sonar applied to biological oceanography** London. 1-6.

Foote, K.G., Chu, D., Hammar, T.R., et al. (2005) Protocols for calibrating multibeam sonar. **J. Acoust. Soc. Am.**, 117: (4): 2013-2027.

Foote, K.G. and Francis, D.T. (2002) Comparing Kirchhoff-approximation and boundary-element models for computing gadoid target strengths. **J. Acoust. Soc. Am.**, 111: (4): 1644-1654.

Foote, K.G., Francis, D.T.I. and Atkins, P.R. (2007) Calibration sphere for low-frequency parametric sonars. **J. Acoust. Soc. Am.**, 121: (3): 1482-1490.

Foote, K.G., Knudsen, H.P., Vestnes, G., et al. (1987) Calibration of acoustic instruments for fish density estimation: A practical guide. **Coop. Res. Rep. Const. Int. Explor. Mer.** , 144: 69.

Foote, K.G. and MacLennan, D.N. (1984) Comparison of copper and tungsten carbide calibration spheres. **J. Acoust. Soc. Am.**, 75: (2): 612-616.

Francis, D.T.I., Foote, K.G. and Atkins, P.R. (2007) "Robustness of target strength of an immersed, hollow ceramic flotation sphere of constant shell thickness". **MTS/IEEE Oceans 2007**. Vancouver, Canada.

Fraser, D.B. and LeCraw, R.C. (1964) Novel method of measuring elastic and anelastic properties of solids. **The Rev. Sci. Instrum**, 35: (9): 1113-1115.

Furusawa, M. (1988) Prolate spheroidal models for predicting general trends of fish target strength. **J. Acoust. Soc. Jpn.**, 9: (1): 13-24.

Gammell, P.M. (1981) Improved ultrasonic detection using the analytic signal magnitude. **Ultrasonics**, 19: 73-76.

Gaunaurd, G.C. (1985) Sonar cross sections of bodies partially insonified by finite sound beams. **IEEE J. Oceanic Eng.**, 10: (3): 213-230.

Gaunaurd, G.C. and Werby, M.F. (1991) Sound scattering by resonantly excited, fluid-loaded, elastic spherical shells. **J. Acoust. Soc. Am.**, 90: (5): 2536-2550.

Gdeisat, M. and Lilley, F. (2011) **Phase unwrapping** [online]. 19/Apr/2011 Liverpool John Moores University [Accessed 10/July/2011 2011]

Gerlich, D. and Kennedy, G.C. (1979) The elastic moduli and their pressure derivatives for tungsten carbide with different amounts of cobalt binder. **J. Appl. Phys.**, 50: (3331-3333).

Gipson, K. and Marston, P.L. (1999) Backscattering enhancements due to reflection of meridional leaky Rayleigh waves at the blunt truncation of a tilted solid cylinder in water: Observations and theory. **J. Acoust. Soc. Am.**, 106: (4): 1673-1680.

Giryn, A. (1982) A species classifier of sea creatures compiled on the basis of their echo sounder signals. **IEEE Trans. Pattern Analysis and Machine Intelligence**, 4: (6): 666-671.

Glisson, T.H., Black, C.I. and Sage, A.P. (1970) On sonar signal analysis. **IEEE Trans. on Aerospace and Electronic Systems**, 6: (1): 37-50.

Godø, O.R. (2009a) "Technology answers to the requirements set by the ecosystem approach". **The future of fisheries science in North America**. Springer.

Godø, O.R. (2009b) "Technology answers to the requirements set by the ecosystem approach". **The future of fisheries science in North America**. Springer 373-403.

Goodman, R.R. and Stern, R. (1962) Reflection and transmission of sound by elastic spherical shells. **J. Acoust. Soc. Am.**, 34: (3): 338-344.

González Salido, N. (2012) Análisis numérico mediante elementos finitos de la dispersión acústica producida por cuerpos elásticos de dimensiones finitas. Master, Universidad Politecnica de Valencia.

Gorska, N. and Ona, E. (2003) Modelling the acoustic effect of swimbladder compression in herring. **ICES J. Marine Science**, 60: 548-554.

Gorska, N., Ona, E. and Korneliussen, R.J. (2005) Acoustic backscattering by Atlantic mackerel as being representative of fish that lack a swimbladder. Backscattering by individual fish. **ICES J. Mar. Sci.**, 62: 984-995.

Gudra, T., Opielinski, K.J. and Jankowski, J. (2010) Estimation of the variation in target strength of objects in the air. **Phyisics Procedia**, 3: 209-215.

Guillemin, E.A. (1953) **Introductory circuit theory**. London: John Wiley & Sons.

Hackman, R.H. and Todoroff, D.G. (1985) An application of the spheroidal-coordinate-based transition matrix: The acoustic scattering from high aspect ratio solids. **J. Acoust. Soc. Am.**, 78: (3): 1058-1071.

Haslett, R.W.G. (1962) The back-scattering of acoustic waves in water by an obstacle: II. Determination of the reflectivities of solids using small specimens. **Proc. Phys. Soc.**, 79: 559-571.

Haslett, R.W.G. (1969) The target strengths of fish. **J. Sound Vib.**, 9: (2): 181-191.

Hassab, J.C. (1978) Homomorphic deconvolution in reverberant and distortional channels: An analysis. **J. Sound Vib.**, 58: (2): 215-231.

Hayman, G. and Robinson, S.P. (2007) "Phase calibration of hydrophones by the free-field reciprocity method in the frequency range 10 kHz to 400 kHz".

Hazen, E.L. and Horne, J.K. (2003) A method for evaluating the effects of biological factors on fish target strength. **ICES J. Mar. Sci.**, 60: 555-562.

He, H. and Lyon, R.H. (1996) Group delay in resonant scattering. **J. Acoust. Soc. Am.**, 99: (3): 1465-1474.

He, P. (1999) Direct measurements of ultrasonic dispersion using a broadband transmission technique. **Ultrasonics**, 37: 67-70.

Henderson, M.J., Horne, J.K. and Towler, R.H. (2007) The influence of beam position and swimming direction on fish target strength. **ICES J. Mar. Sci.**, 65: 226-237.

Heyser, R.C. (1969a) Loudspeaker phase characteristics and time delay distortion: Part 1. **J. of the Audio Eng. Soc.**, 17: (1): 30-41.

Heyser, R.C. (1969b) Loudspeaker phase characteristics and time delay distortion: Part 2. **J. of the Audio Eng. Soc.**, 17: (2): 130-137.

Heyser, R.C. (1984) Determining the acoustic position for proper phase response of transducers. **J. Audio Eng. Soc.**, 32: (1/2): 23-25.

Heyser, R.C., Hestenes, J.D., Rooney, J.A., et al. (1989) Medical ultrasound imager based on time delay spectrometry. **Ultrasonics**, 27: 31-38.

Hickling, R. (1962a) **Acoustic radiation and reflection from spheres**. PhD, California Institute of Technology.

Hickling, R. (1962b) Analysis of echoes from a solid elastic sphere in water. **J. Acoust. Soc. Am.**, 34: (10): 1582-1592.

Hickling, R. (1964) Analysis of echoes from a hollow metallic sphere in water. **J. Acoust. Soc. Am.**, 36: (6): 1124-1137.

Hickling, R. and Means, R.W. (1968) Scattering of frequency-modulated pulses by spherical elastic shells in water. **J. Acoust. Soc. Am.**, 44: (5): 1246-1252.

Hilliard, J.K. (1964) Notes on how phase and delay distortions affect the quality of speech, music and sound effects. **IEEE Trans. Audio**, 12: 23-25.

Hirobayashi, S. and Kimura, H. (1999) Phase characteristics of scattering transfer functions of a sphere. **Electronics and Communications in Japan**, 82: (8): 50-61.

Hobæk, H, and Nesse, T.L. (2006) Scattering from spheres and cylinders: Revisited. **29th Symposium on Physical Acoustics** Norwegian Physical Society. 1-16.

Hoffman, J.F. (1971) Classification of spherical targets using likelihood ratios and quadrature components. **J. Acoust. Soc. Amer.**, 49: (1): 23-30.

Horne, J.K. (2000) Acoustic approaches to remote species identification: A review. **Fish. Oceanogr.**, 9: (4): 356-371.

Horne, J.K. and Clay, C.S. (1998) Sonar systems and aquatic organisms: Matching equipment and model parameters. **Can. J. Fish. Aquat. Sci.**, 55: 1296-1306.

Horner, J.L. and Gianino, P.D. (1984) Phase-only matched filtering. **Applied Optics**, 23: (6): 812-816.

Hsieh, C.P. and Khuri-Yakub, B.T. (1992) Surface defect inspection of spherical objects by the resonant sphere technique. **Appl. Phys. Lett.**, 60: (15): 1815-1817.

Huang, C.F., Young, M.S. and Li, Y.C. (1999) Multiple-frequency continuous wave ultrasonic system for accurate distance measurement. **Review of Scientific Instruments**, 70: (2): 1452-1458.

Huang, K. and Clay, C.S. (1980) Backscattering cross sections of live fish: PDF and aspect. **J. Acoust. Soc. Am.**, 67: (3): 795-802.

Huang, K.N. and Huang, Y.P. (2009) Multiple-frequency ultrasonic distance measurement using direct digital frequency synthesizers. **Sensors and Actuators A**, (149): 42-50.

Huelsman, L.P. (1993) **Active and passive analog filter design**. New York: McGraw Hill.

Humphrey, V.F., Robinson, S.P., Smith, J.D., et al. (2008) Acoustic characterization of panel materials under simulated ocean conditions using a parametric array source. **J. Acoust. Soc. Am.***,* 124: (2): 803-814.

Hurrell, A. (2004) Voltage to pressure conversion: are you getting 'phased' by the problem? **Journal of Physics: Conference Series: Advanced Metrology for Ultrasound in Medicine***,* 1: 57-62.

Imaizumi, T., Furusawa, M., Akamatsu, T., et al. (2008) Measuring the target strength spectra of fish using dolphin-like short broadband sonar signals. **J. Acoust. Soc. Am.***,* 124: (6): 3440-3449.

Islas-Cital, A., Atkins, P.R., Foo, K.Y., et al. (2011a) "Broadband amplitude and phase sonar calibration using LFM pulses for high-resolution study of hard and soft acoustic targets". **Oceans 2011**. Santander, Spain.

Islas-Cital, A., Atkins, P.R., Foo, K.Y., et al. (2011b) Phase calibration of sonar systems using standard targets and dual-frequency transmission pulses. **J. Acoust. Soc. Am.***,* 130: (4): 1-8.

Jech, J.M. and Horne, J.K. (2002) Three-dimensional visualization of fish morphometry and acoustic backscatter. **ARLO***,* 3: (1): 35-40.

Jin, G. and Tang, D. (1996) Uncertainties of differential phase estimation associate with interferometric sonars. **IEEE J. Oceanic Eng.***,* 21: (1): 53-63.

Johannesson, K.A. and Mitson, R.B. (1983) "Fisheries acoustics : A practical manual for aquatic biomass estimation". In Nations, F.a.A.O.o.t.U. (Ed.) Rome.

Jones, B.A., Lavery, A.C. and Stanton, T.K. (2009) Use of the distorted wave Born approximation to predict scattering by inhomogeneous objects: Application to squid. **J. Acoust. Soc. Am.***,* 125: (1): 73-88.

Jonzén, N., Cardinale, M., Gardmark, A., et al. (2002) Risk of collapse in the estern Baltic cod fishery. **Marine Ecology Progress Series***,* 240: 225-233.

Kaduchak, G. and Marston, P.L. (1993) Observation of the midfrequency enhancement of tone bursts backscattered by a thin spherical shell in water near the coincidence frequency. **J. Acoust. Soc. Am.***,* 93: (1): 224-230.

Kim, D., Greenleaf, J.F., Kinter, T.M., and Kinnick, R. R. (1990) Detection of specular reflectors and suppression of speckle by phase filtering. **Annual International Conf. IEEE Eng. in Medicine and Biology Soc.** 12: 331-332.

Kimura, T., Wadaka, S., Misu, K., Nagatsuka, T., Tajime, T., and Koike, M. (1995) A high resolution ultrasonic range measurement method using double frequencies and phase detection. **Proc. IEEE Ultrason. Symp.** 1 : 737-741.

Kloser, R.J. and Horne, J.K. (2003) Characterizing uncertainty in target-strength measurements of a deepwater fish: orange roughy (*Hoplostethus atlanticus)*. **ICES J. Mar. Sci.***,* 60: 516-523.

Kloser, R.J., Williams, A. and Koslow, J.A. (1997) Problems with acoustic target strength measurements of a deepwater fish, orange roughy (Hoplostethus atlanticus, Collett). **ICES Journal of Marine Science***,* 54: 60-71.

Koch, C. (2003) Amplitude and phase calibration of hydrophones by heterodyne and time-gated time-delay spectrometry. **IEEE Trans. Ultrason., Ferroelect., Freq. Contr.***,* 50: (3): 344-348.

Koch, C. and Wilkens, V. (2004) Phase calibration of hydrophones: Heterodyne time-delay spectrometry and broadband pulse technique using an optical reference hydrophone. **Journal of Physics: Conference Series: Advanced Metrology for Ultrasound in Medicine** 1: 14-19.

Korneliussen, R.J., Diner, N., Ona, E., et al. (2008) Proposals for the collection of multifrequency acoustic data. **ICES J. Mar. Sci.***,* 65: 982-994.

Koslow, J.A. (2009) The role of acoustics in ecosystem-based fishery management. **ICES Journal of Marine Science***,* 66: 966-973.

Kreyszig, E. (1999) **Advanced engineering mathematics**. 8th.Singapore: John Wiley & Sons.

Lacker, S.G. and Henderson, T.L. (1990) Wideband monopulse sonar performance: Cylindrical target simulation using an acoustic scattering center model. **IEEE J. Oceanic Eng.***,* 15: (1): 32-43.

LaFollett, J.R., Williams, K.L. and Marston, P.L. (2011) Boundary effects on backscattering by a solid aluminum cylinder: Experiment and finite element model comparison (L). **J. Acoust. Soc. Am.***,* 130: (2): 669-672.

Lam, F. and Szilard, J. (1976) Pulse compression techniques in ultrasonic non-destructive testing. **Ultrasonics***,* 14: (3): 111-114.

Lam, H.Y. (1979) **Analog and digital filters: Design and realization**. Englewood Cliffs, N.J., U.S.A.: Prentice-Hall.

Lance, A.L., Seal, W.D. and Labbar, F. (1984) Phase noise and AM noise measurements in the frequency domain. **Infrared and Millimeter Waves***,* 11: 239-289.

Laugier, P., Fink, M. and Abouelkaram, S. (1990) The random phase transducer: A new technique for incoherent processing - Experimental results. **IEEE Trans. Ultrason., Ferroelect., Freq. Contr.***,* 37: (2): 70-78.

Lavery, A.C., Chu, D. and Moum, J.N. (2010) Measurements of acoustic scattering from zooplankton and oceanic microstructure using a broadband echosounder. **ICES Journal of Marine Science***,* 67: (2): 379-394.

Lavery, A.C., Stanton, T.K., McGehee, D.E., et al. (2002) Three-dimensional modeling of acoustic backscattering from fluid-like zooplankton. **J. Acoust. Soc. Am.***,* 111: (3): 1197-1210.

Lawson, G.L. and Rose, G.A. (2000) Seasonal distribution and movements of coastal cod (Gadus Morhua L.) in Placentia Bay, Newfoundland. **Fisheries Research***,* 49: 61-75.

Lee, C.C., Lahham, M. and Martin, B.G. (1990) Experimental verification of the Kramers-Kronig relationship for acoustic waves. **IEEE Trans. Ultrason., Ferroelect., Freq. Contr.**, 37: (4): 286-294.

Lee, K.I. (2007) Frequency dependencies of phase velocity and attenuation coefficient in a water-saturated sandy sediment from 0.3 to 1.0 MHz. **J. Acoust. Soc. Am.**, 121: (5): 2553-2558.

LeFeuvre, P., Rose, G.A., Hale, R., et al. (2000) Acoustic identification in the Northwest Atlantic using digital image processing. **Fisheries Research**, 47: 137-147.

Legouis, T. and Nicolas, J. (1987) Phase gradients method of measuring the acoustic impedance of materials. **J. Acoust. Soc. Am.**, 81: (1): 44-50.

Leroy, C.C., Robinson, S.P. and Goldsmith, M.J. (2008) A new equation for the accurate calculation of sound speed in all oceans. **J. Acoust. Soc. Am.**, 124: (5): 2774-2782.

Lew, H. (1996) "Broadband active sonar: implications and constraints". Melbourne, Australia

Li, T.B. and Ueda, M. (1989) Sound scattering of a plane wave obliquely incident on a cylinder. **J. Acoust. Soc. Am.**, 86: (6): 2363-2368.

Lim, R. (2010) "Sonar detection and classification of underwater UXO and environmental parameters". SERDP.

Llort, G and Sintes, C. (2009) Statistical modeling of interferometric signals in underwater applications. **Signal Processing, Sensor Fusion, and Target Recognition XVIII** Orlando, FL, USA SPIE.

Logerwell, E.A. and Wilson, C.D. (2004) Species discrimination of fish using frequency-dependent acoustic backscatter. **ICES J. Mar. Sci.**, 61: 1004-1013.

Love, R.H. (1977) Target strength of an individual fish at any aspect. **J. Acoust. Soc. Am.**, 62: (6): 1397-1403.

Lu, H.J. and Lee, K.T. (1995) Species identification of fish shoals from echograms by an echo-signal image processing system. **Fisheries Research**, 24: 99-111.

Ludwig, G. and Brendel, K. (1988) Calibration of hydrophones based on reciprocity and time delay spectrometry. **IEEE Trans. Ultrason., Ferroelect., Freq. Contr.**, 35: (2): 168-174.

Luker, L.D. and Van Buren, A.L. (1981) Phase calibration of hydrophones. **J. Acoust. Soc. Am.**, 70: (2): 516-519.

Lurton, X. (2002) **An introduction to underwater acoustics**. Chichester, UK: Praxis Publishing.

Lyon, R.H. (1983) Progressive phase trends in multi-degree-of-freedom systems. **J. Acoust. Soc. Am.**, 73: 1223-1228.

Lyon, R.H. (1984) Range and frequency dependence of transfer function phase. **J. Acoust. Soc. Am.**, 76: (5): 1433-1437.

MacLennan, D.N. and Dunn, J.R. (1984) Estimation of sound velocities from resonance measurement on tungsten carbide calibration spheres. **Journal of Sound and Vibration***,* 97: (2): 321-331.

MacLennan, D.N. and Holliday, D.V. (1996) Fisheries and plankton acoustics: past, present and future. **ICES J. Mar. Sci.***,* 53: 513-516.

Marston, P.L. (1992) "Geometrical and catastrophe optics methods in scattering". In Pierce, A.D. & Thurston, R.N. (Eds.) **High frequency and pulse scattering***.* London, Academic Press 1-234.

Marston, P.L. (1997) Approximate meridional leaky ray amplitudes for tilted cylinders: End-backscattering enhancements and comparisons with exact theory for infinite solid cylinders. **J. Acoust. Soc. Am.***,* 102: (1): 358-369.

Martin Traykovski, L.V., O'Driscoll, R.L. and McGehee, D.E. (1998) Effect of orientation on broadband acoustic scattering of Antarctic krill *Euphausia superba*: Implications for inverting zooplankton spectral acoustic signatures for angle of orientation. **J. Acoust. Soc. Am.***,* 104: (4): 2121-2135.

Matsumoto, H. (1990) Characteristics of SeaMarc II phase data. **IEEE J. Oceanic Eng.***,* 15: (4): 350-360.

Maze, G. (1991) Acoustic scattering from submerged cylinders. MIIR Im/Re: Experimental and theoretical study. **J. Acoust. Soc. Am.***,* 89: (6): 2559-2566.

McClatchie, S., Macaulay, G., Coombs, R.F., et al. (1999) Target strength of an oily deep-water fish, orange roughy (*Hoplostethus atlanticus)* I. Experiments. **J. Acoust. Soc. Am.***,* 106: (1): 131-142.

McClatchie, S., Thorne, R.E., Grimes, P., et al. (2000) Ground truth and target identification for fisheries acoustics. **Fisheries Research***,* 47: 173-191.

McCutcheon, S.C., Martin, J.L. and Barnwell, T.O.J. (1993) "Handbook of hydrology". In Maidment, D.R. (Ed.) **Handbook of hydrology***.* New York, McGraw-Hill.

McDaniel, J.G. and Clarke, C.L. (2001) Interpretation and identification of minimum phase reflection coefficients. **J. Acoust. Soc. Am.***,* 110: (6): 3003-3010.

Medwin, H. and Clay, C.S. (1998) **Fundamentals of Acoustical Oceanography**. San Diego, CA: Academic Press.

Meghanathan, N. and Nayak, L. (2010) Steganalysis algorithms for detecting the hidden information in image, audio and video cover media. **International Journal of Network Security & Its Application***,* 2: (1): 43-55.

Mercier, N., Belleval, J.F.d. and Lanceleur, P. (1993) Characterization of flaws using the poles and zeros of the transfer function of the corresponding ultrasonic system. **Ultrasonics***,* 31: (4): 229-235.

Mikeska, E.E. (1970) Scattering of Linear FM acoustic pulses from aluminum spheres in water. **J. Acoust. Soc. Am.***,* 48: (1): 357-361.

Misund, O.A. (1997) Underwater acoustics in marine fisheries and fisheries research. **Reviews in Fish Biology and Fisheries***,* 1-34.

Mitri, F.G. (2010) Acoustic backscattering enhancements resulting from the interaction of an obliquely incident plane wave with an infinite cylinder. **Ultrasonics***,* 50: 675-682.

Mitri, F.G., Greenleaf, J.F., Fellah, Z.E.A., et al. (2008) Investigating the absolute phase information in acoustic wave resonance scattering. **Ultrasonics***,* 48: 209-219.

Miyanohana, Y., Ishii, K. and Furusawa, M. (1993) Spheres to calibrate echo sounders in any frequency. **NIppon Suisan Gakkaishi***,* 59: (6): 933-942.

Montes-García, P., Castellanos, F. and Vásquez-Feijoo, J.A. (2010) Assessing corrosion risk in reinforced concrete using wavelets. **Corrosion Science***,* 52: 555-561.

Moss, C.F. and Simmons, J.A. (1993) Acoustic image representation of a point target in the bat *Eptesicus fuscus*: Evidence for sensitivity to echo phase in bat sonar. **J. Acoust. Soc. Am.***,* 93: (3): 1553-1562.

Muller, M.W., Allen III, J.S., Au, W.W.L., et al. (2008) Time-frequency analysis and modeling of the backscatter of categorized dolphin echolocation clicks for target discrimination. **J. Acoust. Soc. Am.***,* 124: (1): 657-666.

Nash, R.D.M., Sun, Y. and Clay, C.S. (1987) High resolution acoustic structure of fish. **J. Const. Int. Explor. Mer***,* 43: 23-31.

Neely, S.T. and Allen, J.B. (1979) Invertibility of a room impulse response. **J. Acoust. Soc. Am.***,* 66: (1): 165-169.

Nesse, T.L., Hobæk, H. and Korneliussen, R.J. (2009) Measurements of acoustic-scatternig spectra from the whole and parts of Atlantic mackerel. **ICES Journal of Marine Science***,* 66: 1169-1175.

Neubauer, W.G., Vogt, R.H. and Dragonette, L.R. (1974) Acoustic reflection from elastic spheres. I. Steady-state signals. **J. Acoust. Soc. Am.***,* 55: (6): 1123-1129.

Frank, L.J., and Dragonette, L.R. (1982) Acoustic classification of submerged targets. **IEEE International Conference on Acoustics, Speech, and Signal Processing** 7 : 327-330.

Numrich, S.K. and Uberall, H. (1992) "Scattering of sound pulses and the ringing of target resonances". In Pierce, A.D. & Thurston, R.N. (Eds.) **High frequency and pulse scattering***.* London, Academic Press 235-318.

Numrich, S.K., Varadan, V.V. and Varadan, V.K. (1981) Scattering of acoustic waves by an finite elastic cylinder immersed in water. **J. Acoust. Soc. Am.***,* 70: (5): 1407-1411.

O'Donell, M. and Miller, J.G. (1981) Quantitative broadband ultrasonic backscatter: an apporach to nondestructive evaluation in acoustically inhomogeneous materials. **J. Appl. Phys.***,* 52: (2): 1056-1065.

Ona, E., Mazauric, V. and Andersen, L.N. (2009) Calibration methods for two scientific multibeam systems. **ICES J. Mar. Sci.***,* 66: 1326-1334.

Oppenheim, A.V. and Lim, J.S. (1981) The importance of phase in signals. **Proc. of the IEEE***,* 69: (5): 529-541.

Ott, H.W. (1988) **Noise reduction techniques in electronics systems**. 2nd.New York: John Wiley & Sons, Inc.

Papoulis, A. (1962) **The Fourier integral and its applications**. London: McGraw-Hill.

Paraskevas, I. and Chilton, E. (2004) Combination of magnitude and phase statistical features for audio classification. **Acoustics Research Letters Online***,* 5: (3): 111-117.

Partridge, C. and Smith, E.R. (1995) Acoustic scattering from bodies: Range of validity of the deformed cylinder method. **J. Acoust. Soc. Am.***,* 97: (2): 784-795.

Peters, F. and Petit, L. (2003) A broad band spectroscopy method for ultrasound wave velocity and attenuation measurement in dispersive media. **Ultrasonics***,* 41: 357-363.

Pezeshki, A., Azimi-Sadjadi, M.R. and Scharf, L.L. (2007) Undersea target classification using canonical correlation analysis. **IEEE Journal of Oceanic Engineering** 32: (4): 948-955.

Piersol, A.G. (1981) Time delay estimation using phase data. **IEEE Trans. on Acoustics, Speech, and Signal Processing***,* 29: (3): 471-477.

Piquette, J.C. and Paolero, A.E. (2003) Phase change measurement, and speed of sound and attenuation determination, from underwater acoustic panel tests. **J. Acoust. Soc. Am.***,* 113: (3): 1518-1525.

Foote, K.G. (2006) Optimizing two targets for calibrating a broadband multibeam sonar. **IEEE Oceans** Boston. 1-4.

Preis, D. (1982) Phase distortion and phase equalization in audio signal processing: A tutorial review. **J. Audio Eng. Soc.***,* 30: (11): 774-794.

Radtke, D.B., Davis, J.V. and Wilde, F.D. (2005) Specific electric conductance. **U.S. Geological Survey Techniques of Water-Resources Investigations** [Accessed August].

Ramp, H.O. and Wingrove, E.R. (1961) Principles of pulse compression. **IRE Trans. Military Electronics***,* 5: (2): 109-116.

Reeder, D.B. and Stanton, T.K. (2004) Acoustic scattering by axisymmetric finite-length bodies: An extension of a two-dimensional conformal mapping method. **J. Acoust. Soc. Am.***,* 116: (2): 729-746.

Rembert, P., Lenoir, O., Izbicki, J.L., et al. (1990) Experimental analysis of phase spectrum of cylindrical or plane targets: a new global method of isolation of resonances. **Physics Letters A***,* 143: (9): 467-472.

Rihaczek, A.W. and Hershkowitz, S.J. (1996) Man-made target backscattering behavior: Applicability of conventional radar resolution theory. **IEEE Trans. on Aerospace and Electronic Systems***,* 32: (2): 809-824.

Roberts, P.L.D. and Jaffe, J.S. (2007) Multiple angle acoustic classification of zooplankton. **J. Acoust. Soc. Am.**, 121: (4): 2060-2070.

Roitblat, H.L., Au, W.W.L., Nachtigall, P.E., et al. (1995) Sonar recognition of targets embedded in sediment. **Neural Networks**, 8: (7/8): 1263-1273.

Rose, G.A. and Porter, D.R. (1996) Target-strength studies on Atlantic cod (*Gadus morhua*) in Newfoundland waters. **ICES J. Mar. Sci.**, 53: (259-265).

Ross, R.A. and Bechtel, M.E. (1968) Scattering-center theory and radar glint analysis. **IEEE Trans. on Aerospace and Electronic Systems**, 4: (5): 756-762.

Rudgers, A.J. (1969) Acoustic pulses scattered by a rigid sphere immersed in a fluid. **J. Acoust. Soc. Am.**, 45: (4): 900-910.

Sachse, W. and Pao, Y.H. (1978) On the determination of phase and group velocities of dispersive waves in solids. **J. Appl. Phys.**, 49: (8): 4320-4327.

Sancho-Knapik, D., Alvarez-Arenas, T.G., Peguero-Pina, J.J., et al. (2011) Air-coupled broadband ultrasonic spectroscopy as a new non-invasive and non-contact method for the determination of leaf water status. **J. Exp. Bot.**, 62: (10): 3637-3645.

Schornich, S. and Wiegrebe, L. (2008) Phase sensitivity in bat sonar revisited. **J. Comp. Physiol. A**, 194: 61-67.

Shirley, D.J. and Diercks, K.J. (1970) Analysis of the frequency response of simple geometric targets. **J. Acoust. Soc. Am.**, 48: (5): 1275-1282.

"Short report for CCAUV". (2008). Status Report PTB. Physikalisch-Technische Bundesanstalt.

Silbiger, A. (1963) Scattering of sound by an elastic prolate spheroid. **J. Acoust. Soc. Am.**, 35: (4): 564-570.

Simmonds, E.J., Armstrong, F. and Copland, P.J. (1996) Species identification using wideband backscatter with neural network and discriminant analysis. **ICES Journal of Marine Science**, 53: 189-195.

Simmonds, J. and MacLennan, D.N. (2005) **Fisheries acoustics**. 2nd.Oxford, UK: Blackwell Science.

Skolnik, M.I. (1962) **Introduction to radar systems**. 2nd.London: McGraw-Hill.

Skudrzyk, E. (1971) **The foundations of acoustics**. New York: Springer-Verlag.

Soria, M., Freon, P. and Gerlotto, F. (1996) Analysis of vessel influence on spatial behaviour of fish schools using a multi-beam sonar and consequences for biomass estimates by echo-sounder. **ICES J. Mar. Sci.**, 53: 453-458.

Spagnolini, U. (1995) 2-D phase unwrapping and instantaneous frequency estimation. **Ieee Trans. on Geoscience and Remote Sensing**, 33: (3): 579-589.

Spence, R.D. and Granger, S. (1951) The scattering of sound from a prolate spheroid. **J. Acoust. Soc. Am.**, 23: (6): 701-706.

Stansfield, D. (1991) **Underwater electroacoustic transducers**. Bath, UK: Bath University Press.

Stanton, T.K. (1988a) Sound scattering by cylinders of finite length. I. Fluid cylinders. **J. Acoust. Soc. Am.**, 83: (1): 55-63.

Stanton, T.K. (1988b) Sound scattering by cylinders of finite length. II. Elastic cylinders. **J. Acoust. Soc. Am.**, 83: (1): 64-67.

Stanton, T.K. (1989) Sound scattering by cylinders of finite length. III. Deformed cylinders. **J. Acoust. Soc. Am.**, 86: (2): 691-705.

Stanton, T.K. and Chu, D. (2000) Review and recommendations for the modelling of acoustic scattering by fluid-like elongated zooplankton: Euphausiids and copepods. **ICES J. Mar. Sci.**, 57: 793-807.

Stanton, T.K. and Chu, D. (2008) Calibration of broadband active acoustic systems using a single standard spherical target. **J. Acoust. Soc. Am.**, 124: (1): 128-136.

Stanton, T.K., Chu, D., Jech, M., et al. (2010) New broadband methods for resonance classification and high-resolution imagery of fish with swimbladders using a modified commercial broadband echosounder. **ICES J. Mar. Sci.**, 67: 365-378.

Stanton, T.K., Chu, D. and Wiebe, P.H. (1998a) Sound scattering by several zooplankton groups. II. Scattering models. **J. Acoust. Soc. Am.**, 103: (1): 236-253.

Stanton, T.K., Chu, D., Wiebe, P.H., et al. (1993a) Average echoes from randomly oriented random-length finite cylinders: Zooplankton models. **J. Acoust. Soc. Am.**, 94: (6): 3463-3472.

Stanton, T.K., Chu, D., Wiebe, P.H., et al. (1998b) Sound scattering by several zooplankton groups. I. Experimental determination of dominant scattering mechanisms. **J. Acoust. Soc. Am.**, 103: (1): 225-235.

Stanton, T.K. and Clay, C.S. (1986) Sonar echo statistics as a remote-sensing tool: volume and seafloor. **IEEE Journal of Oceanic Engineering**, 11: (1): 79-96.

Stanton, T.K., Clay, C.S. and Chu, D. (1993b) Ray representation of sound scattering by weakly scattering deformed fluid cylinders: Simple physics and application to zooplankton. **J. Acoust. Soc. Am.**, 94: (6): 3454-3462.

Stanton, T.K., Reeder, D.B. and Jech, J.M. (2003) Inferring fish orientation from broadband-acoustic echoes. **ICES J. Marine Science**, 60: 524-531.

Stodolsky, D.S. (1970) The standardization of monaural phase. **IEEE Trans. Audio and Electroacoustics**, 18: (3): 288-299.

Tappan, P.W. (1965) More on phase distortion (The Editor's Corner). **IEEE Trans. Audio**, 13: 1-3.

Tesei, A., Guerrini, P. and Zampolli, M. (2008) Tank measurements of scattering from a resin-filled fiberglass spherical shell with internal flaws. **J. Acoust. Soc. Am.***,* 124: (2): 827-840.

Ting, C.S. and Sachse, W. (1978) Measurement of ultrasonic dispersion by phase comparison of continuous harmonic waves. **J. Acoust. Soc. Am.***,* 64: (3): 852-857.

Tolstoy, I. and Clay, C.S. (1966) **Ocean acoustics: Theory and experiment in underwater sound**. London, United Kingdom: McGraw-HIll

Traykovski, L.V.M., O'Driscoll, R.L. and McGehee, D.E. (1998) Effect of orientation on broadband acoustic scattering of Antarctic krill *Euphausia superba*: Implications for inverting zooplankton spectral acoustic signatures for angle of orientation. **J. Acoust. Soc. Am.***,* 104: (4): 2121-2135.

Tribus, M. and McIrvine, E.C. (1971) Energy and information. **Sci. Am.***,* 225: (3): 179-188.

Tucker, D.G. and Barnickle, N.J. (1969) Distinguishing automatically the echoes from acoustically 'hard' and 'soft' objects with particular reference to the detection of fish. **J. Sound. Vib.***,* 9: (3): 393-397.

Turin, G.L. (1960) An introduction to matched filters. **IRE Trans. Information Theory***,* 6: (3): 311-329.

Uberall, H., Dragonette, L.R. and Flax, L. (1977) Relation between creeping waves and normal modes of vibration of a curved body. **J. Acoust. Soc. Am.***,* 61: (3): 711-715.

Uberall, H., Moser, P.J., Merchant, B.L., et al. (1985) Complex acoustic and electromagnetic resonance frequencies of prolate spheroids and related elongated objects and their physical interpretation. **J. Appl. Phys.***,* 58: (6): 2109-2124.

Uberall, H., Ripoche, J., Maze, G., et al. (1996) "The resonances: From nuclear physics to underwater acoustics". In Guran, A.;Ripoche, J. & Ziegler, F. (Eds.) **Acoustic interactions with submerged elastic structures. Part I: Acoustic scattering and resonances***.* Singapore, World Scientific 1-14.

Uberall, H., Stoyanov, Y.J., Nagl, A., et al. (1987) Resonance spectra of elongated elastic objects. **J. Acoust. Soc. Am.***,* 81: (2): 312-316.

Umchid, S., Gopinath, R., Srinivasan, K., et al. (2009) Development of calibration techniques for ultrasonic hydrophone probes in the frequency range from 1 to 100 MHz. **Ultrasonics***,* 49: 306-311.

Vagle, S., Foote, K.G., Trevorrow, M.V., et al. (1996) A technique for calibration of monostatic echosounder systems. **IEEE J. Oceanic Eng.***,* 21: (3): 298-305.

van Neer, P.L.M.J., Vos, H.J. and de Jong, N. (2011) Reflector-based calibration of ultrasound transducers. **Ultrasonics***,* 51: 1-6.

Van Valkenburg, M.E. (1982) **Analog filter design**. New York: CBS College Publishing.

Veksler, N. (1996) "RST and peripheral waves". In Guran, A.;Ripoche, J. & Ziegler, F. (Eds.) **Acoustic interactions with submerged elastic structures. Part I: Acoustic scattering and resonances**. Singapore, World Scientific 15-43.

Wang, H. and Cao, W. (2001) Improved ultrasonic spectroscopy methods for characterization of dispersive materials. **IEEE Trans. Ultrason., Ferroelect., Freq. Contr.**, 48: (4): 1060-1065.

Wang, L. and Walsh, S.J. (2006) Measurement of phase accumulation in the transfer functions of beams and plates. **J. Sound Vib.**, 290: 763-784.

Waterman, P.C. (1969) New formulation of acoustic scattering. **J. Acoust. Soc. Am.**, 45: (6): 1417-1429.

Welsby, V.G. and Goddard, G.C. (1973) Underwater acoustic target strength of nets and thin plastic sheets. **Journal of Sound and Vibration**, 28: (1): 139-149.

Welsby, V.G. and Hudson, J.E. (1972) Standard small targets for calibrating underwater sonars. **J. Sound Vib.**, 20: (3): 399-406.

Werby, M.F. (1991) The acoustical background for a submerged elastic shell. **J. Acoust. Soc. Am.**, 90: (6): 3279-3287.

Werby, M.F. and Evans, R.B. (1987) Scattering from objects submerged in unbounded and bounded oceans. **IEEE J. Oceanic Eng.**, 12: (2): 380-394.

Wheeler, H.A. (1939) The interpretation of amplitude and phase distortion in terms of paired echoes. **Proc. of the IRE**, 27: 359-384.

Wiener, F.M. (1941) Phase distortion in electroacoustic systems. **J. Acoust. Soc. Am.**, 13: (2): 115-123.

Wiener, F.M. (1947) Sound diffraction by rigid spheres and circular cylinders. **J. Acoust. Soc. Am.**, 19: (3): 444-451.

Wilkens, V. and Koch, C. (2004) Amplitude and phase calibration of hydrophones up to 70 MHz using broadband pulse excitation and an optical reference hydrophone. **J. Acoust. Soc. Am.**, 115: (6): 2892-2903.

Williams, K.L., Kargl, S.G., Thorsos, E.I., et al. (2010) Acoustic scattering from a solid aluminum cylinder in contact with a sand sediment: Measurements, modeling and interpretation. **J. Acoust. Soc. Am.**, 127: (6): 3356-3371.

Yang, M., Hill, S.L., Bury, B., et al. (1994) A multifrequency AM-based ultrasonic system for accuracy distance measurement. **IEEE Trans. on Instrumentation and Measurement**, 43: (6): 861-866.

Yao, J. and Ida, N. (1990) "Delay estimation using maximum entropy derived phase information". In Fougere, P.F. (Ed.) **Maximum entropy and Bayesian methods**. Amsterdam, The Netherlands, Kluwer Academic Publishers 309-324.

Yaoita, A., Adachi, T. and Yamaji, A. (2005) Determination of elastic moduli for a spherical specimen by resonant ultrasound spectroscopy. **NDT and E International**, 38: 554-560.

Yen, N.-c., Dragonette, L.R. and Numrich, S.K. (1990) Time-frequency analysis of acoustic scattering from elastic objects. **J. Acoust. Soc. Am.**, 87: (6): 2359-2370.

Yovel, Y., Franz, M.O., Stilz, P., et al. (2011) Complex echo classification by echo-locating bats: A review. **J. Comp. Physiol. A***,* 197: (5): 475-490.

Yuebing, W. and Yongjun, H. (2003) The application of optical interferometry in the measurement of hydrophones. **Institute of Acoustics Conference on Calibration and Measurement in Underwater Acoustics** London, Institute of Acoustics. 25 : 10-18.

Zadler, B.J., Le Rousseau, J.H.L., Scales, J.A., et al. (2004a) Resonant ultrasound spectroscopy: Theory and application. **Geophys. J. Int.***,* 156: 154-169.

Zakharia, M.E., Magand, F., Hetroit, F., et al. (1996) Wideband sounder for fish species identification at sea. **ICES Journal of Marine Science***,* 53: 203-208.

Zhang, H., Chimenti, D.E. and Zeroug, S. (1998) Transducer misalignment effects in beam reflection from elastic structures. **J. Acoust. Soc. Am.***,* 104: (4): 1982-1991.

Zhang, Y., Amin, M. and Ahmad, F. (2008) Time-frequency analysis for the localization of multiple moving targets using dual-frequency radars. **IEEE Signal Processing Letters***,* 15: 777-780.

Zhao, Z. and Hou, Z.Q. (1984) The generalized phase spectrum method for time delay estimation. **IEEE International Conference on Acoustics, Speech, and Signal Processing**, 459-462.

Zhu, X., Li, Y.L., Yong, S., et al. (2009) A novel definition and measurement method of group delay and its applications. **IEEE Trans. on Instrumentation and Measurement***,* 58: (1): 229-233.